2nd International Workshop on Rocket Combustion Modeling

Atomization, Combustion and Heat Transfer

M3 Micro Combustor
OH Emission - Triple Injector Flame

March 25 - 27, 2001
Lampoldshausen, Germany

20020531 120
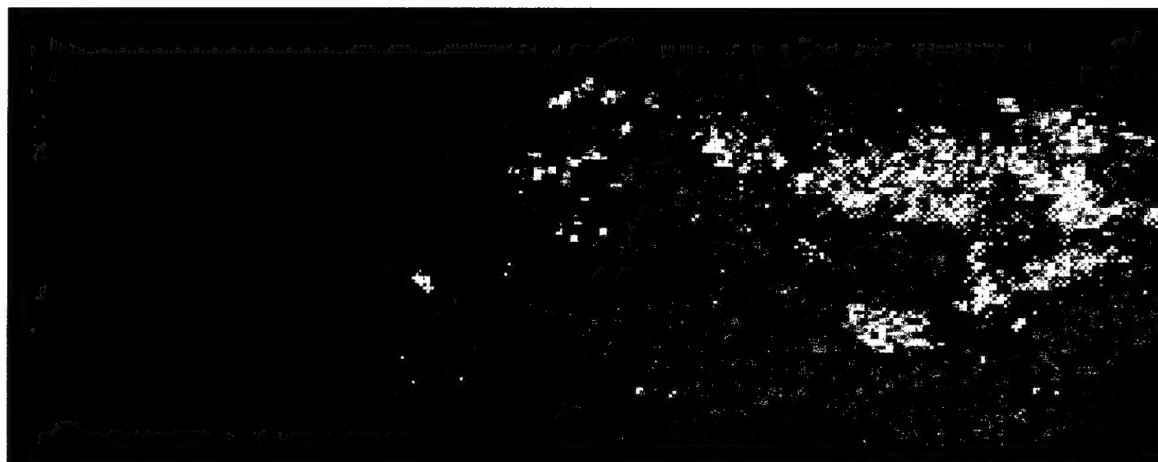
AQ F02-08-1614

Proceedings of the

2nd International Workshop Rocket Combustion Modeling

Atomization, Combustion and Heat Transfer

OH Emission: Triple Injector Flame
M3 Micro Combustor

Edited by
Oskar J. Haidn

DLR

REPORT DOCUMENTATION PAGE

Form Approved OMB No. 0704-0188

1. REPORT DATE (DD-MM-YYYY)	2. REPORT TYPE	3. DATES COVERED (From – To)
14-03-2002	Conference Proceedings	3 May 2001 - 4 May 2001

4. TITLE AND SUBTITLE

2nd International Workshop on Rocket Combustion Modeling

5a. CONTRACT NUMBER
F61775-01-WF023

5b. GRANT NUMBER

5c. PROGRAM ELEMENT NUMBER

6. AUTHOR(S)

Dr. Oskar J. Haidn, editor

5d. PROJECT NUMBER

5d. TASK NUMBER

5e. WORK UNIT NUMBER

7. PERFORMING ORGANIZATION NAME(S) AND ADDRESS(ES)
German Aerospace Center
Langer Grund
Lampoldshausen 74239
Germany

8. PERFORMING ORGANIZATION REPORT NUMBER

N/A

9. SPONSORING/MONITORING AGENCY NAME(S) AND ADDRESS(ES)

European Office of Aerospace Research and Development
PSC 802 BOX 14
FPO 09499-0014

10. SPONSOR/MONITOR'S ACRONYM(S)
EOARD

11. SPONSOR/MONITOR'S REPORT NUMBER(S)
CSP 01-5023

12. DISTRIBUTION/AVAILABILITY STATEMENT

Approved for public release; distribution is unlimited.

13. SUPPLEMENTARY NOTES

14. ABSTRACT

The Final Proceedings for 2nd International Workshop on Rocket Combustion Modeling, 3 May 2001 - 4 May 2001

The aim of the workshop is to present the state-of-the art in computational fluid dynamics (CFD) tools used for liquid rocket propulsion purposes. The tools should be affordable, fast and reliable for predictive design of cryogenic liquid rocket components.

15. SUBJECT TERMS
EOARD, Chemical Propulsion, Combustion, high pressure combustion, atomization, heat transfer

16. SECURITY CLASSIFICATION OF:			17. LIMITATION OF ABSTRACT	18, NUMBER OF PAGES	19a. NAME OF RESPONSIBLE PERSON
a. REPORT	b. ABSTRACT	c. THIS PAGE	UL		Ingrid Wysong
UNCLAS	UNCLAS	UNCLAS			**19b. TELEPHONE NUMBER** (Include area code) +44 (0)20 7514 4285

Standard Form 298 (Rev. 8/98)
Prescribed by ANSI Std. Z39-18

Introductory Remarks

What can research laboratories and universities do in order to provide industry with affordable, fast but also reliable predictive tools for the design of components for cryogenic liquid rocket engines?

Although there is rather a strong competition in the global space transportation market between the industries in Europe, Russia and the United States of America, rocket engineers and scientists are nevertheless very interested in a continuous exchange of ideas across all borders. Increasing demand for both shorter development times and higher performance of the propulsion systems of launch vehicles have drastically reduced nowadays margins in the design process. With still substantial gaps in the knowledge base of the dominating physical phenomena in liquid rocket engines, the scientific community tends towards joint international efforts in order to approach these complex problems. Only during continuous discussions about the validity of different physical models, applicability of numerical solution procedures and the precision of experimental data available for verification, the scientists and engineers usually gain a much deeper insight in the problems they are dealing with and come up with new ideas.

The idea of providing a stimulating podium for the said exchange of views in mind, CNES, DLR, CNRS, ONERA and SNECMA send out invitations for the first workshop on Rocket Combustion Modelling to take place at ONERA Toulouse in 1998. Needless to say that the outcome of the workshop was to the benefit of all participants. After now three years of improvement of physical models, numerical schemes as well as experimental data, the organisers envisaged a second workshop with at this time a much broader participation, particularly from Russia and the United States. The comments of the participants during and after the meeting clearly showed that the objectives of the workshop were met.

This is exactly the place to say a warm "thank you very much" to all the authors and co-authors who have not hesitated to perform not only the sometimes tedious computations but also have agreed to provide a written version of their contribution. Furthermore, let me especially thank Mohammed Habiballah from ONERA Chattilon, Wolfgang Mayer from DLR Lampoldshausen and Jean-Louis Thomas from Snecma Moteurs Vernon who did an excellent job describing the test cases for the workshop.

Last but not least, I would like to thank the sponsoring organisations EOARD and DLR for their support of the workshop.

On behalf of the organising committee

Lampoldshausen, November 2001   Oskar J. Haidn

Table of Content

List of Authors

Bellan, J.,	Jet Propulsion Laboratory, Pasadena
Blouquin, R.,	Bertin Technolgies, Paris
Bodele, E.,	LCSR, Centre National de la Recherche Scientifique, Orleans
Branam, R.,	Air Force Research Laboratory, Edwards AFB
Burnley, V.,	Air Force Research Laboratory, Wright Patterson AFB
Chen, Y.S.,	ESI Inc., Huntsville
Cheng, G.,	SECA Inc., Huntsville
Dupoirieux, F.,	ONERA Chatillon, Paris
Durand, P.,	CNES, Evry
Farmer, R.,	SECA Inc., Huntsville
Gökalp, I.,	LCSR, Centre National des Recherche Scientifiques, Orleans
Görgen, J.,	Astrium GmbH, Ottobrunn
Gorokhovski, M.,	CORIA, Centre National des Récherche Scientifiques, Rouen
Gutheil, E.,	Institute for Scientific Computing, Heidelberg
Habiballah, M.,	ONERA Chatillon, Paris
Haidn, O.J.,	DLR Lampoldshausen
Harstad, K.,	Jet Propulsion Laboratory, Pasadena
Hussong, J.,	DLR Stuttgart
Knab, O.,	Astrium GmbH, Ottobrunn
Legrand, L.,	CNES, Evry
Lequette, L.,	Bertin Technologies, Paris
Mayer, W.O.H.,	DLR Lampoldshausen
Oefelein, J.,	Sandia National Laboratories, Livermore
Okong'o, V.N.,	Jet Propulsion Laboratory, Pasadena
Pourouchottamane, M.,	ONERA Chattilon, Paris
Saucereau, D.,	SNECMA Moteurs, Vernon
Schneider, G.,	DLR, Lampoldshausen
Slavinskaya, N.A.,	Central Institute of Aviation Motors, Moskau
Sokolova, I.A.,	Institute of Mathematical Modeling, Russian Academy of Science, Moskau
Telaar, J.,	DLR, Lampoldshausen
Thomas, J.-L.,	SNECMA Moteurs, Vernon
Vingert, L.,	ONERA Palaiseau, Paris
Vuillermoz, P.,	CNES, Evry
Zurbach, S.,	SNECMA Moteurs, Vernon

TRANSPORT PROPERTIES AND THERMODYNAMIC PROCESSES FOR LIQUID FUELS AND GAS MIXTURES of N_2, O_2, H_2 and H_2O

I.A. Sokolova*, N.A. Slavinskaya**, O.J. Haidn***

*Institute for Mathematical Modeling Russian Academy of Science,
Miusskaya pl.4-A, 125047, Moscow, sokolova@imamod.ru
**Central Institute of Aviation (CIAM), Aviamotornaya st.2, Russia, 111250 Moscow, slan@orc.ru
***German Aerospace Center (DLR), Langer Grund, 74239 Lampoldshausen, oskar.haidn@dlr.de

Abstract

This report deals with problems of transport properties in gas dynamic flows at high pressures and densities and, in particular, with transport properties of Hydrogen, Nitrogen, Water and Oxygen. The behavior of these substances at high pressures and/or low temperatures is quite different from perfect gas behavior. Especially near its critical points or lines of phase changes, thermodynamic properties, equations of state and transport properties as well exhibit proper characters while the specified conditions are taking place. An overview of models in use to predict the transport properties for the species given above in various phase states is carried out and different theoretical approaches are investigated. A generalization of the models requires the knowledge of all these properties in the widest possible range of temperatures and pressures. Therefore, the inclusion of limiting states' data (dilute gas, saturation and melting regime) into a multi-property analysis is essential, especially while extending these correlations beyond the range of experimental data.

A novel method for the prediction of viscosity and thermal conductivity on the basis of an unique equation for gas and liquid is presented which bases on the model of effective kinetic diameter of hard spheres. Furthermore, the kinetic effects on the droplet surface under high ambient temperature are considered. Temperature and concentration jumps were used to describe non-equilibrium boundary conditions on an evaporating liquid oxygen (LOX) droplet. The influence of calculation errors on the values of these jumps is evaluated.

Introduction

The properties of matters in various phase states may be divided into two kinds, equilibrium properties and transport properties. A great progress has been made in the recent years in studying equilibrium properties, although inconsistency between calculated properties is often a problem in industrial thermophysical properties simulations because typically different prediction methods are used for different phase states. Hence, it may happen that equations for liquids are used for the prediction of properties in a region where the vapor pressure equation indicates a gas phase should be present. Therefore, a consistent method for the prediction of all the properties based on a single set of fundamental parameters is the most preferable. A generalized equation of state can be used accurately to predict equilibrium properties of fluids and dense gases.

Furthermore, transport properties of matters in different thermo-physical states are also important features required in various engineering design problems such as simulations of viscous flows through channels and combustion chambers of various technical devices such as flows in rocket engines, chemical reactors or shock tubes. The governing equations for these gasdynamic systems are the Navier-Stokes equations with mass diffusion, heat flux, pressure tensor expressions. All the coefficients in these equations have to be known precisely since they have a very strong influence on the accuracy and the consistency of the simulations.

The object of our investigations presented here is (1), to provide adequate thermo-physical property data, mainly transport properties, covering the largest possible range of temperatures and densities, and (2), to demonstrate a model of vaporization accounting for thermal non-equilibrium boundary conditions on the surface of a liquid droplet.

Thermodynamic properties

Under various boundary conditions different physical phases such as dense gases and liquids usually co-exist, i.e. the flow of a mixture of cold gaseous hydrogen, superheated steam and liquid oxygen in a cryo-genic liquid rocket engine. Although mixtures of layers of liquids and dense gases may be treated as a continuum, the properties of substances under high pressure and low temperature are quite different from those of a perfect gas. Hence, thermodynamic properties, equations of state and transport properties as well have their particular characteristics at specific conditions.

The conventional interpretation of the specific characteristics of thermo-physical properties of matters under different boundary conditions of pressures and temperatures generally makes use of well-known phase diagram of states. Figures 1 and 2 shown typical phase diagrams for N_2 and H_2.
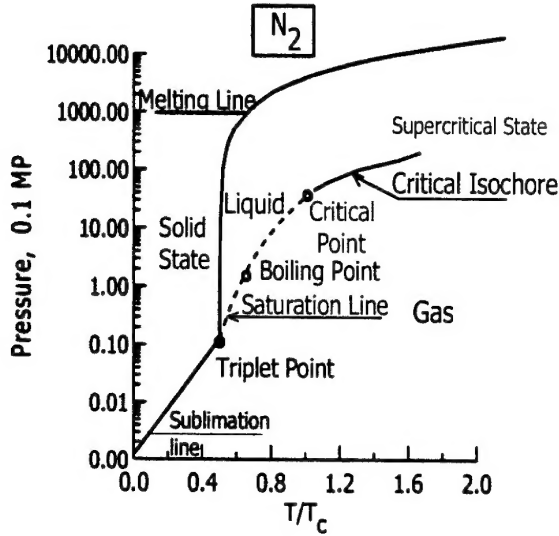
Fig. 1: Phase diagram of N_2 Fig. 2: Phase diagram of H_2
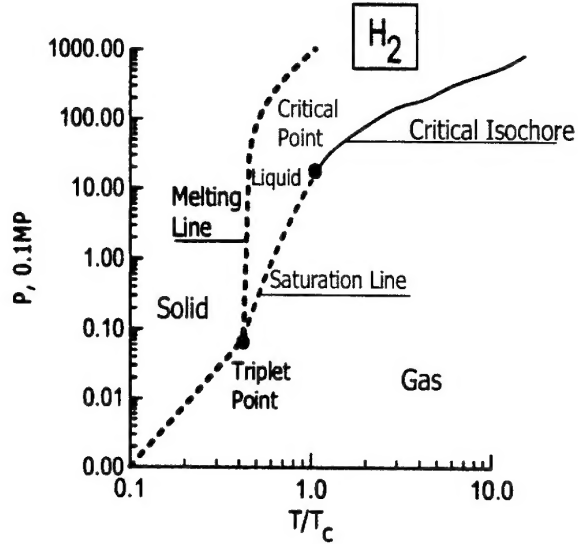
All three different physical phases: gas, liquid and solid states are realized under different pressures as the temperature varies. The triple point (TP) is the point of co-existence of all three phases. The melting line (ML) is the boundary line between the liquid and the solid state. The sublimation line separates the co-existence of gas and solid states. The saturation line (SL) is the boundary line between gas and liquid, along which specific volumes of gas and liquid co-exist at given temperatures and pressures. The critical point (CP) is characterized by the critical values of temperature T, pressure P and density ρ_c. The CP is the final point on the SL, where the density (or the specific volume) of a dense gas becomes equal to the density (or the specific volume) of a liquid. Above this point, phase transitions don't happen anymore. The distinctions between gas and liquid have all disappeared above CP, and the specific dense gas behavior is close to that of a liquid. In other words, it is impossible to distinguish between gas or liquid exists. The choice of boundary between gas and liquid has become a matter of convention and usually the critical iso-chore is used.

	$T_{melt.}$ K	$T_{boil,}$ K	$T_{crit,}$ K	$P_{crit,}$ 0.1 MPa	$\rho_{crit.}$ kg/m^3
p- H_2	13.8	20.28	32.98	12.93	31.4
n- H_2	13.95	20.38	33.23	13.16	31.6
N_2	63.15	77.35	126.25	33.96	304
O_2	54.35	90.18	154.60	50.9	406
Air			132.62	37.85	302.56
H_2O	273.	374.12	647.3	221.39	317.8

Table 1: Critical parameters of substances of interest

A brief summary of the critical parameters for some of the substances of interest is given in Table 1, much more details can be found in [1]. Although the critical parameters for various matters differ widely the particular behavior of thermodynamic (transport) properties near critical areas is quite similar.

Various papers have been devoted to the investigation of equations of state for simple fluid-gas substances such as H_2, O_2, N_2, or H_2O in wide ranges of temperature and pressure. The outcome of both experimental and theoretical treatments made it possible to work out accurate correlations for basic tables of thermodynamic properties, including specific volume (V), enthalpy (h), entropy (S), and specific thermal capacity (C_p) in terms of temperature T and pressure P, as unique reference sources of data [1][2][3]. As an example, the specific behavior of factor compressibility Z for Oxygen is shown in Figure 3, with p the pressure and V the specific volume.
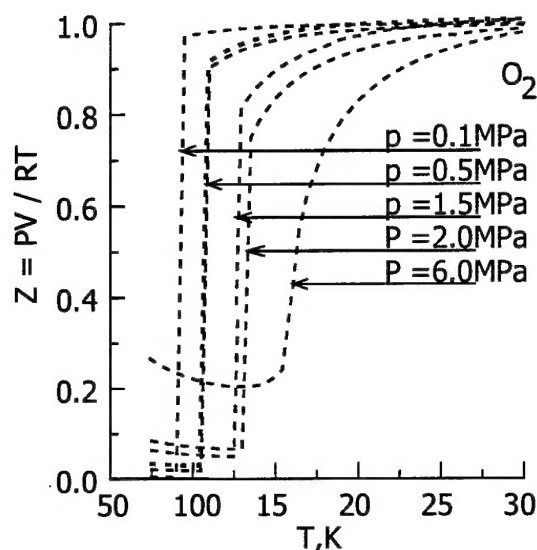
Fig. 3: Compressibility factor $Z = \dfrac{pV}{RT}$
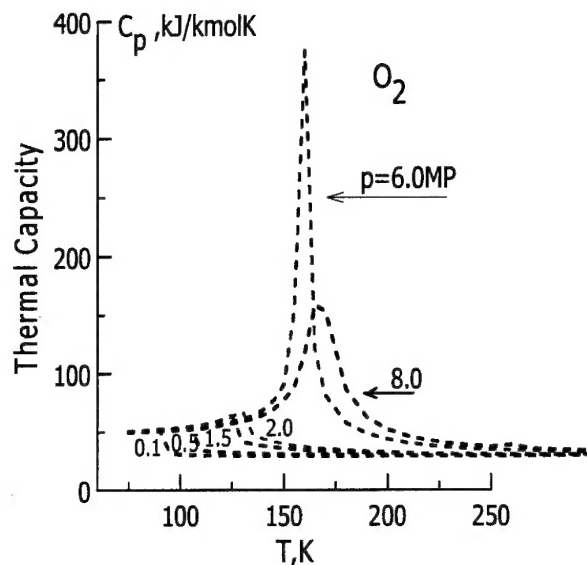
Fig. 4: Thermal Capacity near critical point

Near CP, a steep increase of the compressibility factor Z and an anomaly of the thermal capacity can be observed. Fluctuations in density, molar fractions and other physical values cause a delay of diffusion, a growth of viscosity and thermal conductivity and give rise to other problems. The thermodynamic properties near CP were investigated for H_2, O_2, N_2, and H_2O thoroughly and may be found in [1] or [3]. An example for the anomalous behavior of the specific thermal capacity of O_2 near critical region is shown in Figure 4.

Transport Properties

For dense gases, viscosity, thermal conductivity and thermal diffusion as well are the functions of temperature and pressure (density). Atypical diagram of the reduced viscosity $\eta *$ in terms of reduced density $\rho *$ and temperature T^* is shown on Figure 5. Areas of moderate dense gas (G) and liquid (L) are pointed out. The line relating to the diluted gas limit (DGL), the saturation line (SL) and the melting line (ML) are mapped on the diagram as the bounding lines of the $\eta * - \rho * - T *$ surface. The picture clearly shows the complex behavior of the viscosity in terms of density and temperature.

Generally, analytical expressions are used for application oriented calculations. Hence, accurate correlations are needed. The analytical generalization of experimental data includes property data in the as wide as possible range of temperature and density. Therefore, data near critical areas, saturation line and melting are very important in any multi-property analysis, especially when the correlations are to be extended onto areas which lack experimental data. Additionally, data of viscosity and thermal conductivity in the dilute gas limit is needed as well.

3
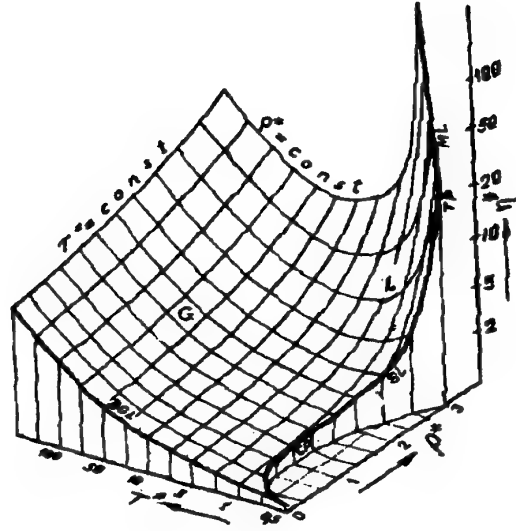
Fig. 5: Reduced viscosity $\eta^* = \eta/\eta_o$ in terms of reduced temperature, $T^* = T/T_c$ and density, $\rho^* = \rho/\rho_c$. G is the gas state; L is the liquid state; CP is the critical point; TP is the triple point; SL is the saturation line; ML is the melting line; DGL is the dilute gas limit

The investigation of viscosity and thermal conductivity in the regions of saturation and melting provides a means for extension into the range of extra-large pressures. Results obtained from fundamental theory studies are included as well into the treatment of data. Viscosity and thermal conductivity of the main components of interest (nitrogen, oxygen, hydrogen and water) are reviewed here. Experimental studies of the transfer coefficients for most matters are primarily limited to temperatures below *1000 – 1200 K* due to high chemical activities of the substances. Hence, the most extensive measurements of viscosity and thermal conductivity have been performed for less chemical active substances such as nitrogen or air. Generally, properties of the most chemical active molecule oxygen are less known. Table 2 gives a summary of the current boundaries of temperature and pressure of the experiment data for viscosity and thermal conductivity for some basic components.

	Viscosity				Thermal conductivity			
	Rarified Gas 0.1 MPa	SL	Dense Gas		Gas, 0.1 MPa	SL	Dense Gas	
	$\Delta T, K$	$\Delta T, K$	$\Delta T, K$	$\Delta p, MPa$	$\Delta T, K$	$\Delta T, K$	$\Delta T, K$	$\Delta p, MPa$
H_2	300-1000	14-32.976	to 1000	to 100	to 830	14-32[*)]	to 1000	to 100
N_2	400-2000	65-124	to 900	0.1-80	273-1373	65-124	300-430	to 10
		~126.5	~300	to 200			~300	0.1-1000
O_2	400-1960	55-150 ~70	300-525	0.1-80	300-1000	55-150	~300	to 360
Air	400-2000	70-128	300-523	0.1-80	300-1200	70-128	300-1200	0.1-100
							~300	to 360
H_2O	~1000	273.16-643.16	273-1000	0.1-80	~1000	273.16-643.16	~300	0.1-100

Table 2: Temperature and pressure limits reached in experimental investigations of viscosity and thermal conductivity

The recommended data for viscosity and thermal conductivity, as correlated tables data are included in the Standard Reference Data (GOST Standard, Russia, NIST Data and others) [4-6].
All major theoretical approaches in use for computing viscosity and thermal conductivity and diffusion at

4

high pressures are quasi-empirical. Due to the specific behavior of the transport properties at high densities it is recommended to perform predictions based on theoretical approaches only when experimental data is missing. Viscosity and thermal conductivity coefficients in the limiting case of zero density may be calculated applying Boltzmann equation and Chapman-Enskog method [7] using potential functions to account for particle interaction. Such data are suitable for comparison in wide ranges of temperature at low densities. The complementary data in the limit of the saturation line and the melting area may be important for correlation at high density.

Quasi-theoretical approaches

One of the wide-spread methods for the prediction of transport properties at high densities is a particular method of excess functions. Usually, the excess of viscosity and thermal conductivity is represented by a power low [8,9]. The main suggestion is that the expression for the viscosity or thermal conductivity coefficient consists of the two terms, with one of them a function of temperature and the other a function of density:

$$\eta(T,\rho) = \eta_o(T) + \Delta\eta\ (\rho) \tag{1}$$

$$\lambda(T,\rho) = \lambda_o(T) + \Delta\lambda(\rho) \tag{2}$$

The usual practice is to express the excessive values of $\Delta\eta\ (\rho)$ and $\Delta\lambda(\rho)$ in terms of a serial expansion of density:

$$\Delta\eta(\rho) = a_1\rho + a_2\rho^2 + a_3\rho^3 + a_4\rho^4 + a_5\rho^5 \tag{3}$$

$$\Delta\lambda(\rho) = b_1\rho + b_2\rho^2 + b_3\rho^3 + b_4\rho^4 + b_5\rho^5 \tag{4}$$

Although some results of the correlations (1)-(4) are in good agreement with experiments, the method of excess function holds only within certain limits. In reality, the functions $\Delta\eta\ (\rho)$ and $\Delta\lambda(\rho)$ are derived for either normal or large temperatures and do not hold for small temperatures and high densities. The method of excess viscosity or thermal conductivity yields reliable results only in the region of equidistant isotherms. But this equidistance is lost at high density and at low temperatures near the critical area. The isotherms of the reduced viscosity of hydrogen are shown in Figure 6. It can be seen that the error near the critical range may exceed 40%.
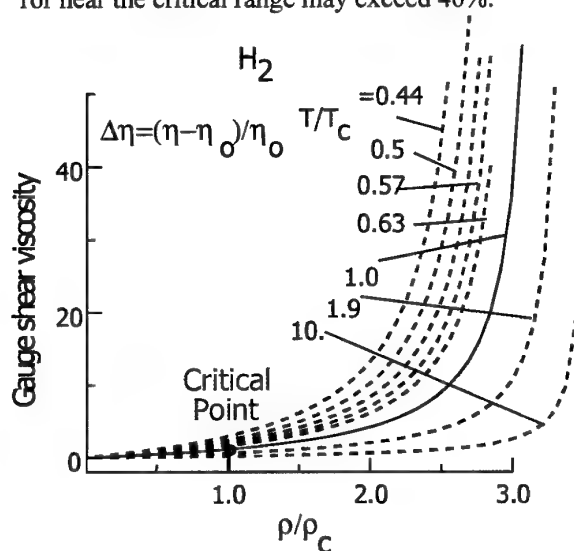

Fig. 6: Excess viscosity of Hydrogen reduced to dilute gas limit in terms of reduced of density.
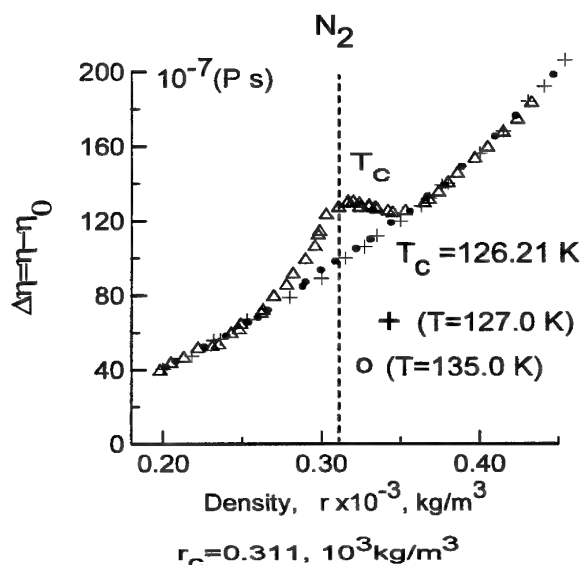
Fig. 7: Excess viscosity of Nitrogen near critical point

The behavior of the excess viscosity of nitrogen near the critical area is shown in Figure 7. The enhancement of the viscosity along the critical isotherm above the regular part is about 37%. Despite these shortcomings, it is obvious that the method of excess functions is quite useful in some cases.

Generalization on the base of Enskog equation

There are a variety of models proposed in the form of reduced density and reduced temperature. The most reasonable equations for the prediction of properties in wide areas of temperatures and pressures usually base on modifications of Enskog kinetic theory for hard spheres. Among them a unique equation for viscosity has been proposed [10,11]. This single equation describes the viscosity of both diluted gases and liquids. The fitting parameters of the equation have been derived using the most recent data of viscosity of diluted gases, of the two phases on saturation line, near the melting line and for dense states. Details of study are omitted here.

The quasi-theoretical equation of viscosity includes two terms, a kinetic part and a collision part, as

$$\mu = \mu_{kin} + \mu_{col},$$ (5)

with μ_{kin} the kinetic part and μ_{col} the collision part of the viscosity taking into account the different mechanisms of impulse transfer. These parts are functions of reduced temperature and density (ρ / ρ_s) with ρ_s the density of the dense gas on the line of melting.

A series of calculations using the proposed equation of viscosity have been performed and the results are compared with direct computer simulations. This comparison confirmed the validity of this quasi-theoretical equation [10,11]. A set of the results obtained is shown in Figures 8 - 10. While Figures 8a and 8b show the isobars and isochores of viscosity of H_2, Figures 9 and 10 present the isochores of the viscosity of N_2 and O_2, respectively. Generally, the deviations of the results are in almost all cases less than a few percent.
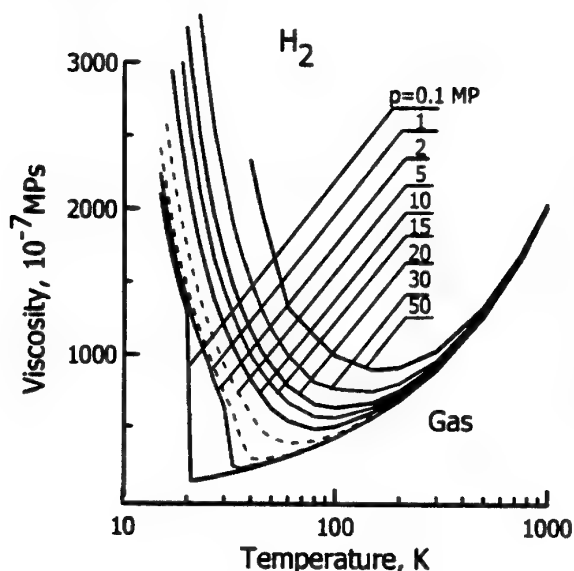
Fig. 8a: Viscosity isobars of H_2. Dotted lines are placed near critical pressure
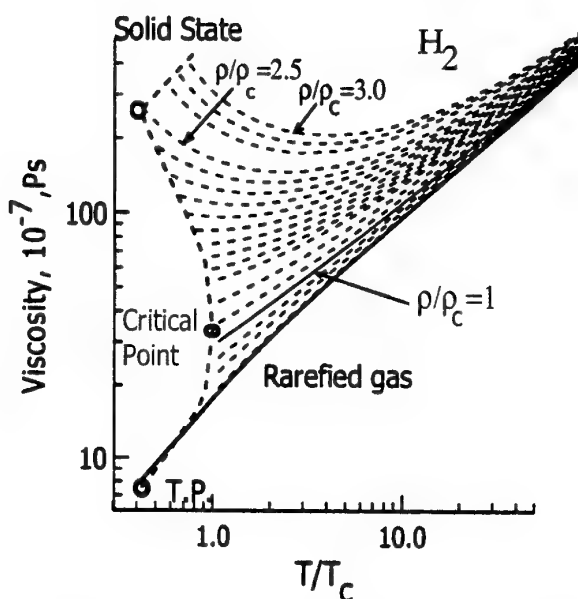
Fig. 8b: Viscosity isochores of H_2. Triplet Point (T.P.) and Critical Point (CP) are given on the saturation line

Model of the effective diameter sphere

Although the empirical correlation relies on direct experiments [11] is very useful and provides the basis for comparison and of reference, it cannot be applied for cases such as the dense states of H_2O or for mixtures of gases and liquids. Furthermore, a generalization of this correlation for other substances than the

6

experimentally investigated ones is questionable. Therefore, the only way of overcome these kind of difficulties is to predict the transport properties on the basis of kinetic theory.
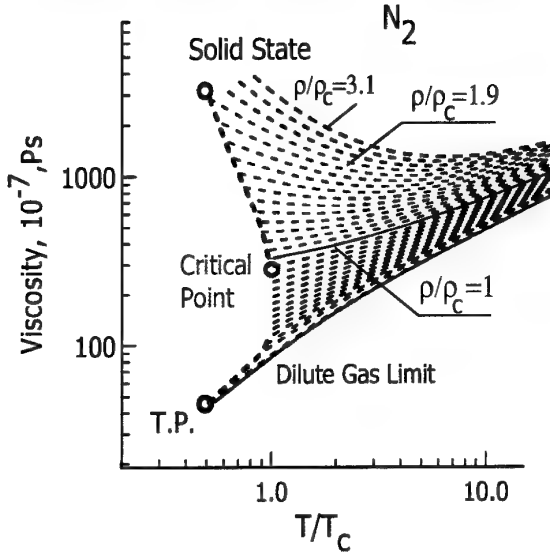
Fig. 9: Viscosity isochore of N_2.
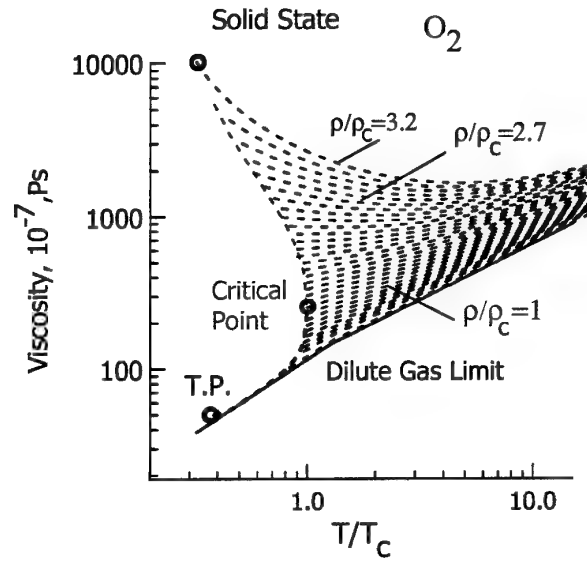
Fig.10: Viscosity isochore of O_2.

A novel model for the prediction of the viscosity of dense gases and liquids in a wide range of density and temperature is proposed [12-13], which bases on specific characteristics of particle interaction in a dense environment.
Both, the kinetic theory foundation and the generalization of the Enskog model for dense gases and fluids make use of the model of a hard sphere. They are unreliable for real fluids because the actual interactions between the particles are not taken into account. However, if the model of effective diameter of a sphere is applied properly using effective potential of the particle interaction, the transport properties of real fluids may be predicted successfully. The formalism of the Enskog hard sphere theory remains the same, but the real character of particle interaction is considered properly by the effective diameter σ_{ceff}.

Molecular dynamics (MD) [14-15] simulations show that the effective pair potential in dense media is a truncated function of the distance between the pairs due to a screening effect of neighboring particles. Therefore, the MD calculations were carried out based on the Lennard-Jones model with either a cut-off at some distance: $r \sim (2.5\text{-}3.0)\ \sigma_o$ or applying other modifications such as the (exp-6-8) truncated model.

Nevertheless, any truncation at a constant distance is valid only for liquids.

The Enskog equation of viscosity consists of two terms

$$\mu = \mu_{kin}\ (\sigma_{kin}\ ) + \mu_{col}\ (\sigma_{col}\ ), \tag{6}$$

with σ_{kin} the effective kinetic diameter (the parameter of impulse transfer along the particle's trajectory) and σ_{col} the effective collision diameter (the parameter of impulse transfer by the particles collision). At any temperature both parameters show systematic differences. Similar results are obtained for diffusion and thermal conductivity.

A new model of the effective kinetic diameter is proposed which assumes that this effective kinetic diameter is a function of temperature and density. This model describes the decrease of the free path of particles with increasing density. The interaction between particles is taken as Lennard-Jones (LJ) potential with a shielding function to account for environmental effects. The cut-off parameter is determined in terms of density and temperature and takes the overlapping of long-range attractive forces of closely packed of molecules into account.

We will describe the interaction of particles taking into account the overlapping of distance fields due to close molecular packing at higher densities taking the effective potential in form of a reference potential model with an exponential screening function

$$U(r) = \left[U_{rep}(r) + U_{att}(r) \right] \exp\left(-\left(\frac{r}{b_{cut}} \right)^2 \right),$$ (7)

with b_{cut} the cut-off parameter, which accounts for screening interaction of the particles. The mean distance between the particles $s = n^{-1/3}$ is taken as a screening parameter. Thus,

$$b_{cut} = s \quad \text{or} \quad b_{cut} / \sigma_o = b_{cut}^* = (n\sigma_o^3)^{-1/3} = \left(n^* \right)^{-1/3},$$ (8)

with n the number density, σ_o the parameter of the potential function (LJ in this case). In the case of low density the potential is transformed into the reference potential function.

The results of numerical simulation using the effective kinetic diameter coincide with the results of MD calculations for the limit of high density states as well as with kinetic diameter simulations of a dilute gas in the limiting case of DGL. For dense gases the effective kinetic diameter results show excellent agreement with results determined from viscosity experiments for argon, nitrogen and other gases.

For a given density, the effective kinetic diameter is derived from relation

$$\sigma_{kin}(T^*, b\rho) = \left[\Omega^{(2,2)}(T, b_{cut}) \right]^{1/2} = \sigma_0 \left[\Omega^{(2,2)^*}(T^*, n^*) \right]^{1/2}, \quad b\rho = \frac{2}{3}\pi n^*,$$ (9)

with $\Omega^{(2,2)}$ the Ω-collision integrals of Cowling, b the volume of hard spheres .

The model of the effective kinetic diameter uses no empirical parameters and can therefore be applied for viscosity calculations when experimental data are missing. Since this approach accounts for density variations, it is most suited for property calculations with varying densities. The model can be used to predict transport properties of dilute gases, dense gases and liquids on the basis of a single equation.
A comparison of our predicted N_2 viscosities at *100 MPa* with data taken from the NIST is shown in Figures 11a and b show. The agreement between the direct theory (present calculation) and the correlation data (NIST) is quite reasonable. The increase of the deviation with decreasing temperature at very low temperatures may be related to the LJ reference potential function whose parameters are not reasonably suited for low temperatures.
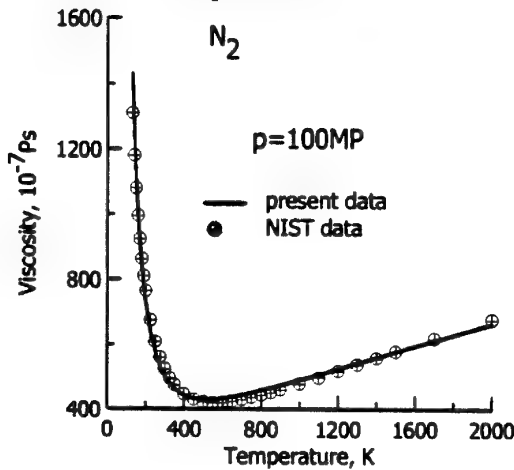

Fig. 11-a: Viscosity on N_2 : present calculation
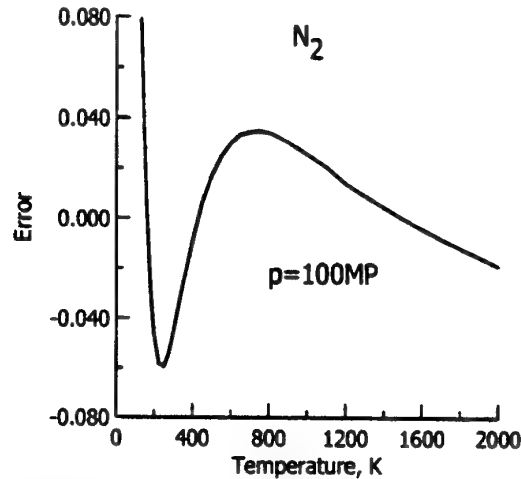(solid curve) and NIST data (circles)

Fig. 11-b: Error of viscosity,
$\Delta = [\eta(present)-\eta(NIST)]/\eta(present)$

Thermal non-equilibrium processes

The main processes in cryogenic liquid rocket engine systems are droplet vaporization and spray combustion including liquid jet atomization, spray formation, vaporization, multiphase flow mixing, ignition and combustion in a high pressure high temperature environment. The time scales of liquid jet atomization, evaporation, convection and mixing are such that oxygen droplets may penetrate into the flame front and enter the reactant which is mainly superheated steam for the propellant combination LOX/GH$_2$.

Any evaporation process involves heat and mass transfer from the hot surrounding gases to the droplet surface and vice versa. For an accurate prediction of these fluxes transport coefficients and thermodynamic properties of both fluids are needed. However, investigations have shown that not only conservation equations, equation of state (EQS), transport and thermodynamic properties must be modeled accurately, but also interface processes have to be taken into account. Typically, thermal equilibrium conditions on the droplet interface is assumed which may not hold at very large temperature and concentration gradients. Therefore, a model, which accounts for thermal non-equilibrium at the droplet surface, is necessary.

When the radius r of a spherical droplets is small and comparable with the mean free path λ of the molecules in the surrounding gas ($0.01 < Kn < 0.2$, $Kn=\lambda/2r$) the discrete molecular structure is considered in a slip-flow regime. Foundations of the basic Boltzmann equation are valid for small Kn numbers, and the Navier-Stokes equations (the governing equations for continuum) may be used for all the entire regime except the layer close to the interface. This Knudsen layer is specified as collisionless molecular flow regime. Its thickness is of the order of the mean free path of the molecules and therefore, the individual behavior of the molecules has to be considered. One way of correct simulation of the flow in the entire domain is to extrapolate the boundary conditions. The boundary conditions on the solid surface under continuum assumptions are modified by jump conditions of thermodynamic and gasdynamic values. The linear extrapolation of the real temperature field to the surface gives the unknown boundary ambient gas temperature T_e (0) as shown in Figure 12.

The solution of Navier-Stokes energy equation with this boundary condition T_e (0) coincides with the true solution outside the Knudsen layer. The difference between the liquid surface temperature T_{in} and the extrapolated gas temperature T_e (0) on the surface $\Delta T_j = T_{in} - T_e$ (0) is the temperature jump. The same assumption is taken for concentrations of evaporated components. Accordingly, the difference $\Delta Y = Y_g^1 - Y_d^1$ is the concentration jump.
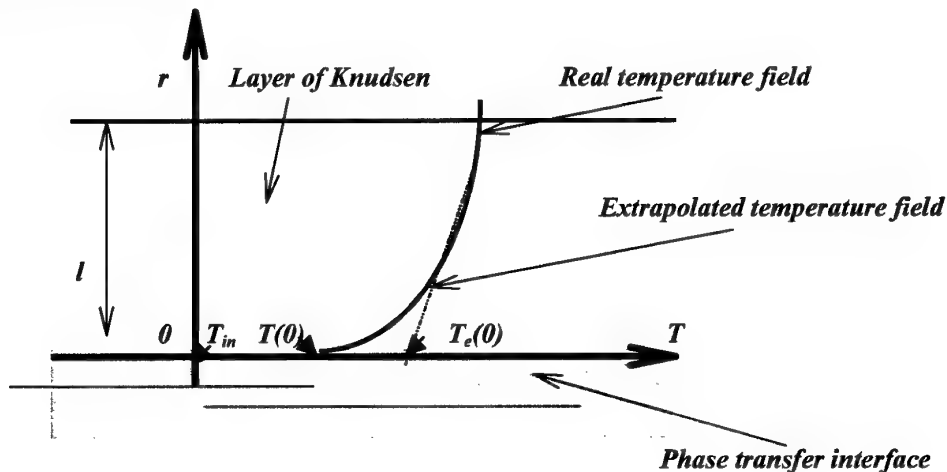
Figure 12: Schematic of temperature distribution around a droplet

We will consider here a model for single drop evaporation in a stagnant environment in an infinite volume. The special problem of the vaporization processes of liquid oxygen droplet (LOX) in superheated steam (GH$_2$O) is investigated. The conservation equations are used for oxygen droplet evaporating in steam under the following conditions: droplet radius $\sim$ $10 \div 100 \mu m$, temperature $\sim$ $1500 \div 2000$ K and pressure $1 \div 10$ MPa. Knudsen number falls in the range $0.01 < Kn < 0.15$. Since there are large gradients of

temperature and concentrations on the droplet surface, the boundary conditions for conservation equations must be investigated.

Droplet evaporation modeling of LOX in water steam (GH$_2$O) has some specific characters. The critical parameters of H$_2$O are considerable higher as compared to O$_2$. If surface temperature of the droplet is lower than *100 K* then according to the phase-equilibrium concept, the water vapor around the droplet condenses and freezes at its surface. However, an ice layer on a LO$_2$ droplet has never been observed so far in experiments. Evidently, the processes in the ultimate boundary layer of LO$_2$ and GH$_2$O may be in thermal non-equilibrium [16-18].

Model of quasi steady – state vaporization

If the characteristic time of molecular transfer is smaller than characteristic time of droplet evaporation, than the fields of temperature and concentration are invariant at constant droplet radius, and the quasi steady – state vaporization model may be used. It includes the following assumptions:

- the temperature of droplet is constant, uniform and equal to the wet-bulb temperature, i.e. droplet heating is neglected;
- the ambient gas has negligible solubility in the liquid and only oxygen diffuses from the surface;
- the radial motion of the liquid surface is assumed to be small;
- the pressure is equal to the ambient pressure everywhere;
- radiation, Dufour and Soret effects are negligible;
- density of gas phase is constant.

The governing system of equations is simplified further neglecting diffusion of the gas into the liquid droplet, chemical reactions and viscous dissipation. To determine the temperature and concentration jumps, Yalamov's approach is applied [19 – 21].

The resulting simplified system of equations is as follows [22 – 23]

$$R_u T = \left(p + \frac{a(T)}{V(V+b)} \right)(V - b), \tag{10}$$

$$v \frac{dY_1}{dr} = \frac{1}{r^2 \rho_m} \frac{\partial}{\partial r} (\rho_m D_{12} r^2 \frac{dY_1}{dr}), \tag{11}$$

$$\frac{1}{r^2} \frac{\partial}{\partial r} (r^2 \rho_m v) = 0, \tag{12}$$

$$\rho_m C_V \frac{d\,T}{dr} = \frac{1}{r^2} \frac{d}{dr} \left(r^2 \lambda_m \frac{dT}{dr} \right) + \left(C_{V_1} - C_{V_2} \right) \rho_m D_{12} \frac{dY_1}{dr} \frac{dT}{dr} - \frac{p}{r^2} \frac{d}{dr} (r^2 v). \tag{13}$$

The boundary conditions for the gas phase are as follows:

For $r = r_d$:

$$\rho_m v = j, \quad Y_1 v - D_{12} \frac{dY_1}{dr} = j \frac{1}{\rho_m}, \tag{14}$$

$$\lambda_m \frac{dT}{dr} = jl, \tag{15}$$

$$(T_e^g - T_d^l)\,\big|_{r=r_d} = K_T^{(T)}\frac{\partial T^g}{\partial r}\,\big|_{r=r_d} + K_T^{(n)}T_\infty\frac{\partial Y_1}{\partial r}\,\big|_{r=r_d},$$

$$\left(Y_e^g - Y_1^d\right)\big|_{r=r_d} = K_n^{(n)}\frac{\partial Y_1}{\partial r}\,\big|_{r=r_d} + \frac{K_n^{(T)}}{T_\infty}\frac{\partial T^l}{\partial r}\,\big|_{r=r_d}$$

(16)

For $r = \infty$:

$$T = T_0,\; Y_1 = Y_{1\infty}.\; Y_1 = \frac{\rho_1}{\rho_m},\quad \rho_m = \rho_1 + \rho_2,\; R = Y_1 R_1 + (1-Y_1)R_2,\; C_V = Y_1 C_{V_1} + (1-Y_1)C_{V_2}.\quad (17)$$

T_e^g, Y_e^g are temperature and concentration of oxygen in the gas phase on the droplet surface; T_d^l, Y_1^l are temperature and concentration of oxygen in the liquid on the droplet surface. ρ_m is the mass density of the mixture, v the radial velocity; Y_i, D_{12} are the mass fraction and the binary diffusion coefficients for each species, S_y is a term which stands for different effects, for example, Dufour, Soret effects, inertia source term ,etc..; h_m, h_i are the mixture and the specific enthalpies, λ_m is the thermal conductivity of the mixture; $\Delta\overline{H} = \overline{h}_1^{vap} - \overline{h}_1^{liq}$ is the specific enthalpy of vaporization of species ; $K_T^{(T)}, K_n^{(n)}$ are coefficients of temperature and concentration jumps, $K_T^{(n)}, K_n^{(T)}$ cross coefficients.

Furthermore, we will introduce the following the non - dimensional parameters:

$$\xi = \frac{r}{r_0},\; \theta = \frac{T}{T_0},\; \delta = \frac{\rho}{\rho_0},\; L = \frac{1}{R_0 T_0},\; \Lambda = \frac{\lambda_m}{p_0 R_0 D_{12_0}},\; \overline{D} = \frac{D_{12}}{D_{12_0}},$$

$$R_0 = (1-Y_{10})R_2 + Y_{10}R_1,\; \overline{R}_i = \frac{R_i}{R_0},\; C_{p_i} = \frac{C_{p_i}}{R_0},\; C_p = \frac{C_p}{R_0},\; \overline{p} = \frac{p}{p_0},$$

(18)

$$C_V = C_p - \overline{R},\; \eta = \frac{1}{\xi},\; \overline{R}_e = (1-Y_e^g)\overline{R}_2 + Y_e^g\overline{R}_1$$

After integration of the system of governing equation and some additional mathematical simplifications an analytical solution of the steady - state evaporation problem is derived. The equations for the temperature

$$A(1-\theta) + \left(B + \frac{\gamma_1}{\gamma_0}A\right)\ln\frac{\gamma_0 - \gamma_1}{\gamma_0\theta - \gamma_1} = \gamma_0\eta,$$

(19)

$$\gamma_0 = J\left(C_{V_1} + \overline{R}_2\right),\; \gamma_1 = \theta_d\gamma_0 - LJ,$$

(20)

$$\lambda_m = AT + B.$$

(21)

and concentration distributions

$$\frac{\overline{D}}{\overline{R}\Lambda\theta}\frac{dY_1}{d\theta} = \frac{1-Y_1}{\left(C_{V_1} + \overline{R}_2\right)(\theta_d - \theta) - L}$$

(22)

can be integrated analytically for $\overline{D} = const$:

$$\frac{1}{\overline{R}_1}\ln\frac{\left[Y_1\overline{R}_1+(1-Y_1)\overline{R}_2\right](1-Y_{1\infty})}{(1-Y_1)}=\frac{A}{\overline{D}\left(C_{V_1}+\overline{R}_2\right)}$$

$$\left\{\frac{1}{2}\left(1-\frac{\gamma_1}{\gamma_0}\right)^2-\frac{1}{2}\left(\theta-\frac{\gamma_1}{\gamma_0}\right)^2+\left(2\frac{\gamma_1}{\gamma_0}+\frac{B}{A}\right)(1-\theta)+\frac{\gamma_1}{\gamma_0}\left(\frac{\gamma_1}{\gamma_0}+\frac{B}{A}\right)\ln\frac{\gamma_0-\gamma_1}{\gamma_0\theta-\gamma_1}\right\}.$$

(23)

For the power dependence of $\overline{D}$ on temperature, the analytical solution depends on the power of temperature. For $D=D_0\left(\dfrac{T}{T_0}\right)^{1.75}$ the equation for concentration distribution can be written as

$$\frac{1}{\overline{R}_1}\ln\frac{\left[Y_1\overline{R}_1+(1-Y_1)\overline{R}_2\right](1-Y_{1\infty})}{(1-Y_1)}=\frac{4A}{B}\left(\theta^{\frac14}-\theta_e^{\frac14}\right)-\frac{2}{B\xi^3}(Ac+B)\cdot\left\{\frac12\ln\left|\frac{\xi+\theta^{\frac14}}{\xi-\theta^{\frac14}}\right|+arctg\frac{\theta^{\frac14}}{\xi}\right\}\Bigg|_{\theta_e}^{\theta}$$

(24)

with

$$\xi=\left(\theta_e-\frac{L}{C_{V_1}-\overline{R}_2}\right).$$

(25)

This system of the algebraic equations for the temperature and concentration fields in the neighborhood of the droplet is closed by the expressions for θ_e, Y_e^g, which are determined from the temperature and jumps conditions.

Finally the system of algebraic equations for determination T_e^s, Y_e^g, Q^m is the following

$$(T_e^g-T_d^l)\big|_{r=r_d}=-K_T^{(T)}\left(\frac{Q^T-Q^m h_1}{4\pi r_d^2\lambda_e}\right)+K_T^{(n)}T_\infty\left(\frac{Q^m(1-Y_e^g)}{4\pi r_d^2\rho_m D_{12}}\right),$$

(26)

$$\left(Y_e^g-Y_1^d\right)\big|_{r=r_d}=K_n^{(n)}\left(\frac{Q^m(1-Y_e^g)}{4\pi r_d^2\rho_m D_{12}}\right)-\frac{K_n^{(T)}}{T_\infty}\left(\frac{Q^T-Q^m h_1}{4\pi r_d^2\lambda_e}\right)$$

$$Q^m=\frac{4\pi r_d}{(l-h_1)}\left[B(T_e^g-T_0)+\frac{A}{2}\left(T_e^{g2}-T_0^2\right)\right],\quad Q^T=lQ^m,$$

(27)

with Q^m,Q^T, the integral mass and heat fluxes and l the heat of evaporation.

To calculate the concentration and temperature jumps according to Yalamov and co-workers [21] we simplify the jumps coefficients, as given below:

$$K_T^{(T)}=\Psi_1^{(0)}\frac{\lambda}{2kn_0\Delta_{\frac12}}\left(\frac{\pi}{2kT_0}\right)^{\frac12}$$

(28)

$$K_T^{(n)} = \Psi_2^{(a)} \frac{n_0^2}{n_{01}n_{02}} \left(\frac{m_1}{2kT_0}\right)^{\frac{1}{2}} D_{12} - \frac{n_0^2(m_1+m_2)}{4\rho_0^2\gamma_0} \left(\frac{\pi}{2kT_0}\right)^{\frac{1}{2}} \times \left(m_2^{\frac{3}{2}} - m_1^{\frac{3}{2}}\right)\left(D_{12} - D_{12}^{[1]}\right)\left(\frac{104}{25\pi}\right)$$

(29)

$$K_n^{(n)} = \Psi_3^{(a)} \frac{n_0^2}{n_{01}n_{02}} \left(\frac{m_1}{2kT_0}\right)^{\frac{1}{2}} D_{12} + \left[\frac{4n_0^2(m_1+m_2)}{5\rho_0 n_{01}\gamma_0} \left(\frac{m_1}{2kT_0}\right)^{\frac{1}{2}}\right] \times$$
$$\times \left(D_{12} - D_{12}^{[1]}\right)$$

(30)

$$K_n^{(T)} = -\Psi_1^{(a)} \frac{\lambda}{2kT\Delta_{-\frac{1}{2}}} \left(\frac{\pi}{2kT_0}\right)^{\frac{1}{2}} - \frac{26}{25}\frac{n_{02}}{\rho_0^2}\frac{(m_1+m_2)(m_2^{\frac{3}{2}} - m_1^{\frac{3}{2}})\lambda}{k\gamma_0\sqrt{2\pi kT_0}} \times$$
$$\times \left(\frac{\left(D_{12} - D_{12}^{[1]}\right)}{D_{12}}\right)$$

(31)

$$\Delta_{-\frac{1}{2}} = \frac{n_{01}}{n_0}m_1^{-\frac{1}{2}} + \frac{n_{02}}{n_0}m_2^{-\frac{1}{2}}, \quad \Delta_{\frac{1}{2}} = \frac{n_{01}}{n_0}m_1^{\frac{1}{2}} + \frac{n_{02}}{n_0}m_2^{\frac{1}{2}}, \quad \gamma_0 = \left(1 - \frac{2}{5}\frac{\Omega_{12}^{(1,2)}}{\Omega_{12}^{(1,1)}}\right)^{-1}$$

(32)

$$\Psi_1^{(a)} = \frac{1}{2} + \frac{52}{25\pi} + \left(\frac{52}{25\pi}\right)\frac{n_{01}n_{02}\left(m_1^{\frac{3}{2}} - m_2^{\frac{3}{2}}\right)}{\rho_0^2\sqrt{m_1 m_2}},$$

(33)

$$\Psi_2^{(a)} = -\left(2 - \frac{5}{2}\right) \times \frac{n_{01}\sqrt{\pi}}{4n_0\Delta_{-\frac{1}{2}}m_1^{\frac{1}{2}}} + \frac{2}{5}\frac{\rho_{01}}{\rho_0\sqrt{\pi}},$$

(34)

$$\Psi_3^{(a)} = \left(2 - \frac{5}{2}\right) \times \frac{n_{01}\sqrt{\pi}}{8n_0\Delta_{-\frac{1}{2}}m_1^{\frac{1}{2}}} + \frac{2}{\sqrt{\pi}} - \frac{2\rho_{01}}{5\rho_0\sqrt{\pi}} + \left(\frac{1}{2}\right)\sqrt{\pi},$$

(35)

$$\Psi_4^{(a)} = \frac{3}{4} + \frac{52}{25\pi} + \left(\frac{52}{25\pi}\right)\frac{n_{01}n_{02}\left(m_1^{\frac{3}{2}} - m_2^{\frac{3}{2}}\right)}{\rho_0^2\sqrt{m_1 m_2}} - \frac{4}{5}\frac{n_0 m_1^{\frac{3}{2}}}{\rho_0\pi}\Delta_{-\frac{1}{2}}$$

(36)

with n_0 - molecular mixture concentration, n_{0i} - molecular concentration of ith component, $n_0 = n_{01} + n_{02}$, m_i - mass of a molecule; D_{12} - coefficient of binary diffusion, $D_{12}^{[1]}$ - coefficient of binary diffusion first approach; k - Boltzmann constant; T_0 - temperature of a droplet and $\Omega_{ij}^{(l,s)}$ - collision integrals.

The radius of evaporating droplet is determined by equation

$$r^2\frac{dr}{dt} = -\frac{Q^m}{4\pi\rho_l}.$$

(37)

After integrating

13

$$r\frac{dr}{dt}=-\frac{1}{(l-h_1)\rho_l}\left[B(T_e^g-T_0)+\frac{A}{2}(T_e^{g^2}-T_0^2)\right],\tag{38}$$

$$r_o^2-r_d^2=-\frac{2}{(l-h_1)\rho_l}\left[B(T_e^g-T_0)+\frac{A}{2}(T_e^{g^2}-T_0^2)\right]\Delta t\tag{39}$$

follows.

Numerical results

A series of computations have been performed to investigate the influence of various physical phenomena on the distributions of the temperature and the concentration. We computed concentration and temperature jumps on the surface of an evaporating single oxygen droplet in steam for initial droplet radii of *10, 25* and *50 μm* for *T = 1500÷2500K* and *P = 0.1 and 4 MPa.*

It is found that the initial droplet size as well as the pressure and temperature of the surroundings have a significant influence on the droplet behavior [17]. Due to the lack of experimental data for the binary system LOX/GH$_2$O we have tested the model comparing our results with experimental data [24] for the system LOX/N$_2$, see Figure 12. The results are in a good agreement. The predicted lifetimes of LOX droplets in steam for various pressures and steam temperatures are shown in Figure 13 for different initial droplet radii.

The temperature jumps on the boundary surface of droplet and surroundings were computed using different assumptions about thermodynamic and transport properties behavior. The physical properties in terms of temperature and density were taken in the first case. In a second case, the averaged mean values were used [18]. The corresponding temperature jumps on the droplet surface are demonstrated in Figures 14a,b for different droplet radii and two ambient pressures *p = 0.1* and *4 MPa* at various initial steam temperatures *T$_o$*. It is evident from the figures that the usage of simple approximations for the thermodynamic and transport properties may cause significant errors.
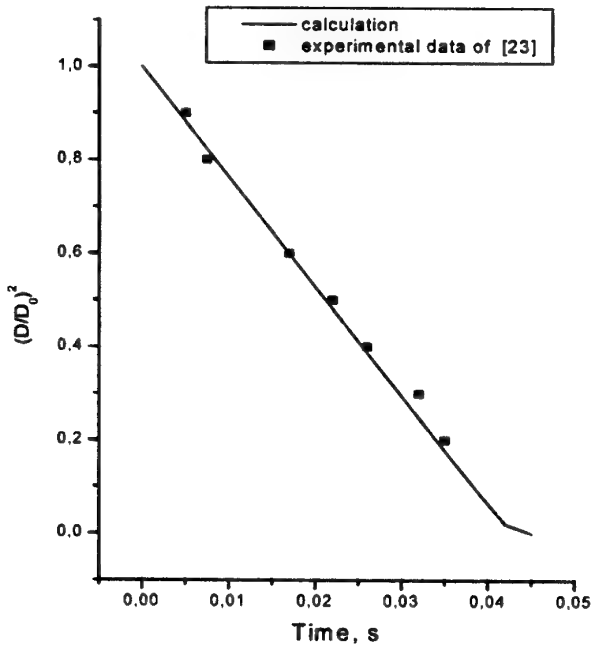

Fig. 12: Averaged Variation of *(D/D$_0$)^2* over time for the system LOX/N$_2$; *P = 0.1 MPa, T$_{N2}$ = 300K*
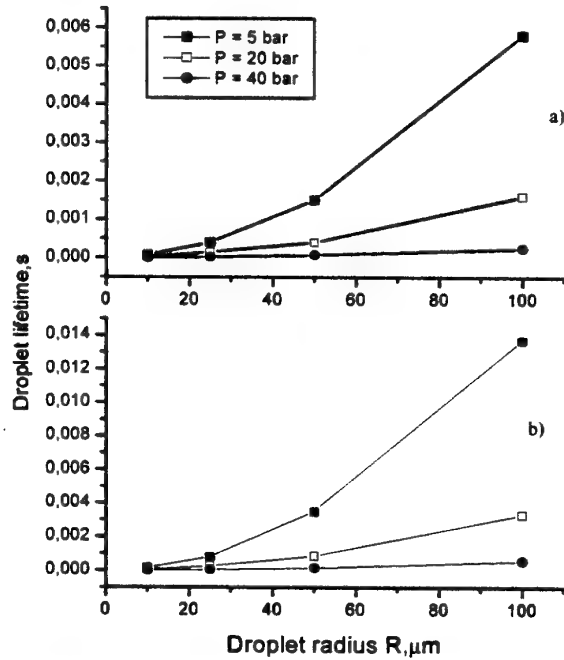
Fig. 13: Droplet lifetime over initial droplet radius for the system LOX/GH$_2$ for various pressures and initial steam temperatures
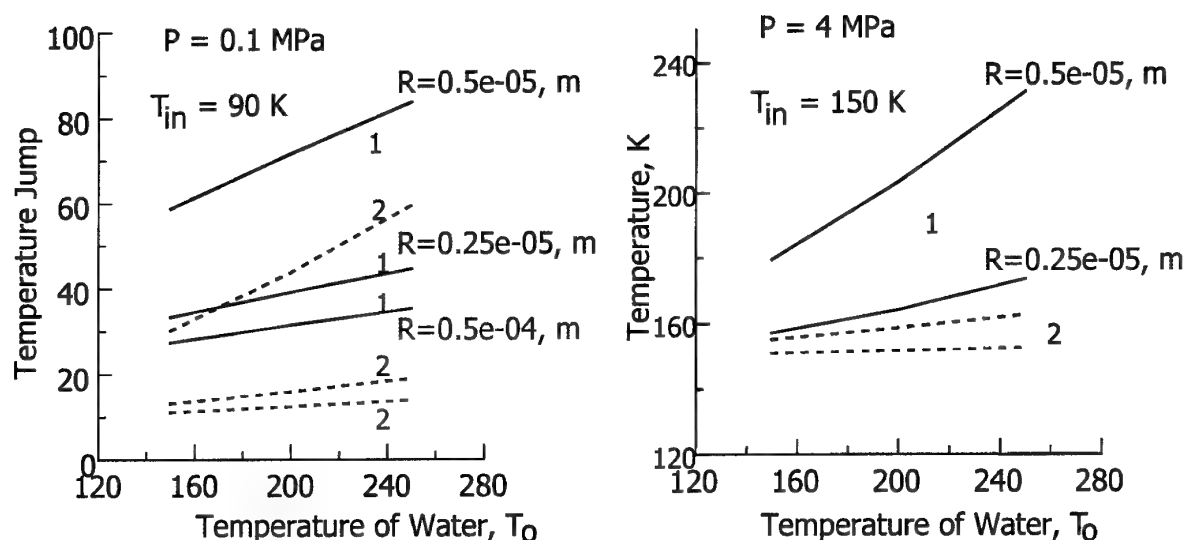a) *T$_{GH2O}$=1500 K* and b) *T$_{GH2O}$=1000 K*

Fig. 14 a,b: Temperature jumps on the boundary surface of droplet and surroundings for a) $P = 0.1$ MPa, $T_{in} = 90$ K and b) $P = 4$ MPa, $T_{in} = 150$ K: Solid curves (1) are the computations with real properties; dotted curves (2) are the computations with averaged constant properties at various droplet radii R. T_0 is the initial temperature of surroundings, T_{in} is the temperature of liquid droplet surface

Conclusions

It has been shown that viscosity and thermal conductivity of fluids strongly depend on density and temperature and that the prediction of transport properties which bases on simple models of power expansion of density yield erroneous results if applied beyond certain limits. The proposed effective kinetic diameter model makes it possible to describe the viscosity of liquids and gases in wide ranges of temperature and density. The performed numerical studies confirmed that the new model is the less computing resources compared with the MD simulations, which requires many hours of computations per individual data point and many days for mixtures. Computations, which base on the effective kinetic diameter model, can be done with less effort.

The vaporisation model which accounts for thermal non-equilibrium boundary conditions at the droplet surface and describes thermodynamic processes on the interface more accurately but relies heavily on exact transport properties.

References

[1] N.B. Vargaftic. Handbook. Thermo-Physical Properties of Gases and Liquids. Moscow, Nauka., 1972.

[2] V.N. Zubarev, A.D. Kozlov, V.M. Kuzneszov, L.V. Sergeeva, et.al. Handbook. Thermophysical properties of industrial important gases at high pressures and high temperatures, Moscow, Energoizdat. 1989.

[3] NIST. Thermo-physical properties of pure fluids Database, Original development by R.D. McCarty and V.App, NBS Technical Note 1097. May 1986.

[4] J.O. Hirschfelder, C.F. Curtis, R.B. Bird, Molecular Theory of Gases and Liquids, New York, Wiley, 1954.

[5] Nitrogen. Viscosity and thermal conductivity coefficients at temperatures 65-1000K and pressures from limiting dilute gas to 200 MPa. SCSD 89-85. State Committee on Standard DATA. Standard and Reference Data TABLES. Moscow.

[6] Oxygen. Viscosity and thermal conductivity coefficients at temperatures 70-500K and pressures from limiting dilute gas to 100 MPa. SCSD 93-86. State Committee on Standard DATA. Standard and Reference Data TABLES. Moscow.

[7] Normal Hydrogen. Viscosity and thermal conductivity coefficients at temperatures 14-1500K and pressures from limiting dilute gas to 100 MPa. SCSD 182-87. State Committee on Standard DATA. Standard and Reference Data TABLES. Moscow.

[8] N.B. Vargaftic, L.P. Filippov, A.A. Tarzimanov, E.E. Tozskiy. Handbook on the Thermo-conductivity of Liquids and Gases. Moscow, Energoizdat. 1990.

15

[9] R.C. Reid, J.M. Prausnitz, B.E. Poling. The Properties of Gases and Liquids. 4th Ed. McGraw Hill, New York, 1987.

[10] E. Liousternik, M.P.Voronin. Universal equation for viscosity of liquids and gases. Thermo-Physics of High Temperatures, V.21, N3, 1983.

[11] M.P. Voronin. Mathematical description diagram of viscosity. Ph.D. Thesis, IHT, Moscow, 1984.

[12] I.A. Sokolova, V.E. Liousternik. Model and Simulation Method for Study of Dense Fluids. Shock Compression of Condensed Matters - 1995. Proceedings of the Conference of the APS Topical Group on Shock Compression of Condense Matters. Seattle, Washington, 1995. Ed. S.C. Shmidt. W.C. Tao. AIP Conference Proceedings. 370. Part 1., 1996., p.167-170.

[13] I.A. Sokolova, V.E. Lusternik. Numerical analysis of density dependence for effective transport kinetic diameter for real fluids. Lecture Notes in Computer Science. V.1196, Springer-Verlag, 1997. Eds: L.Vulkov, J.Wasniewski, P.Ya., p. 474-481.

[14] M. Schoen, C. Hoheisel. The shear viscosity of a Lennard-Jones fluid calculated by equilibrium MD. Molec. Physics. 1985. V.53, N3., p.653

[15] J.J. Erpenbeck. Transport coefficients of hard-sphere mixtures. III. Diameter ratio 0.4 and mass ratio 0.03 at high fluid density. Physical Review E. V.1993. 48, N1, p.223-232.

[16] Slavinskaya N.A., Haidn O. J., O_2 -H_2O vapor–liquid phase equilibria, Proc. of Spray 99, Bremen, 1999.

[17] N.A. Slavinskaya, O.J. Haidn. Numerical modeling of isolated oxygen droplet evaporation in steam: A First approach, Proc. of 16th ILASS Europe, Darmstadt, Germany, 2000.

[18] N.A. Slavinskaya, O.J. Haidn. Numerical modeling of liquid oxygen evaporation in steam using non-equilibrium boundary conditions, AIAA 2001-0335, 2001.

[19] S.K. Loaylka. Temperature jump in a gas mixture. Phys. of Fluids, 1974, vol. 17, No. 15, p.897.

[20] C. Shen. The concentration - jump coefficient in a rarefied binary gas mixture. J. Fluid Mech., 1983, vol. 137, pp. 221-231.

[21] I.Y. Yalamov, V.S. Galojan. The droplet's dynamic in azeotropic viscosity medium. Erevan, Luis, 1985.

[22] I.K. Rakhmatulina. The investigation of non - steady heat transfer under evaporation, condensation and burning of drops. Ph.D., Institute of Mechanics of Lomonosov Univ., 1977.

[23] T. Elperin, B. Krasovitov. Radiation, thermal diffusion and kinetic effects in evaporation and combustion of large and moderate size fuel droplets, Int. J. Mass Transfer, 1995, Vol. 38, N 3, pp. 409-418

[24] X. Chesneau, C. Chauveau, I. Gökalp. Experiments on high pressure vaporization of liquid oxygen droplets. AIAA-94-0688, 1994.

A Perspective on LES and its Application to Liquid Rocket Combustion Systems

Joseph C. Oefelein
Sandia National Laboratories
Combustion Research Facility
Livermore, California 94551-0960

Abstract

This paper provides a perspective on Large Eddy Simulation (LES) and its application to liquid rocket injection, mixing and combustion processes. Simulating these processes involves a variety of challenges which include all of the classical closure problems inherent to the treatment of turbulence and combustion, and a unique set of problems imposed by the introduction of thermodynamic nonidealities and transport anomalies. Emphasis is placed on 1) the fundamental issues and limiting extremes, 2) the theoretical and numerical framework developed to handle these difficulties, and 3) a series of results which give insight into the intricate nature of the problem and current state of the art with respect to LES. The discussion is framed in the context of the three workshop test cases, with conclusions drawn accordingly.

Introduction

Simulating injection, mixing and combustion processes in cryogenic rocket engines poses a variety of challenges which include all of the classical closure problems inherent to the treatment of combustion, and a unique set of problems imposed by the introduction of thermodynamic nonidealities and transport anomalies. Flow conditions within the chamber are inherently turbulent, and combined demands associated with performance and heat transfer typically result in the specification of operating pressures and temperatures that produce local transcritical [1] and supercritical conditions.

From the classical point of view, reacting multiphase flows introduce the complicating factors of chemical kinetics, highly nonlinear source terms, and a variety of subgrid-scale (*sgs*) velocity and scalar mixing interactions. Flow field evolution is affected by compressibility effects (volumetric changes induced by changes in pressure) and variable inertia effects (volumetric changes induced by variable composition and/or heat addition). The resultant coupling yields an array of fluid dynamic, thermochemical, thermodynamic and transport processes which are dominated by widely disparate time and length scales.

The situation becomes more complex at elevated pressures due to the inherent decrease in turbulence scales and difficulties which arise as fluid states approach and/or exceed local critical conditions. Near the critical point, propellant mixture properties begin to exhibit liquid-like densities, gas-like diffusivities and pressure-dependent solubilities. Surface tension and heat of vaporization approach zero, and the isothermal compressibility and constant pressure specific heat increase significantly. These phenomena, coupled with extreme local property variations, have a significant impact on the evolutionary dynamics of a given system.

This paper presents a perspective on the Large Eddy Simulation (LES) technique and its application to the injection, mixing and combustion processes described above. After establishing the key phenomenological trends and flow characteristics, the implications, modeling options, and tradeoffs are outlined and the general requirements for LES are discussed and contrasted with the Reynolds-Averaged Navier-Stokes (RANS) approach. A series of case studies are then presented which highlight various aspects of the problem and the utility of LES as a fundamental tool. The discussion is framed in the context of the three workshop test cases, with conclusions drawn accordingly.

---

[1] A liquid propellant at subcritical temperature in a high-pressure supercritical environment.
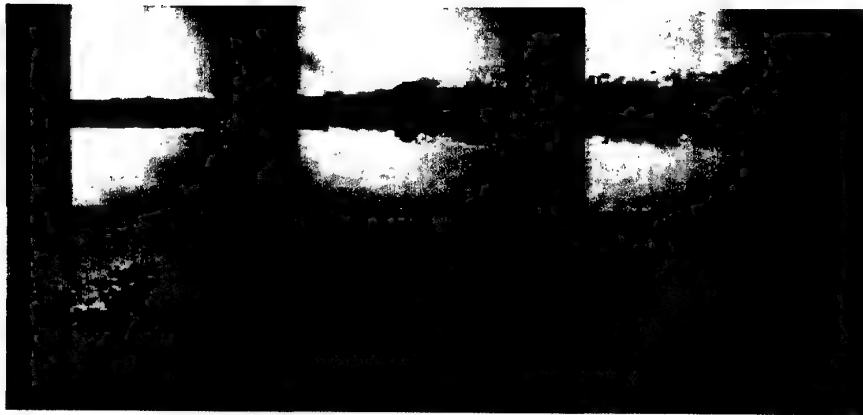
1

Figure 1: Reacting shear-coaxial liquid-oxygen–hydrogen injector operating at 1.5 *MPa* (15 atm). From Mayer and Tamura (1996). Used with permission.
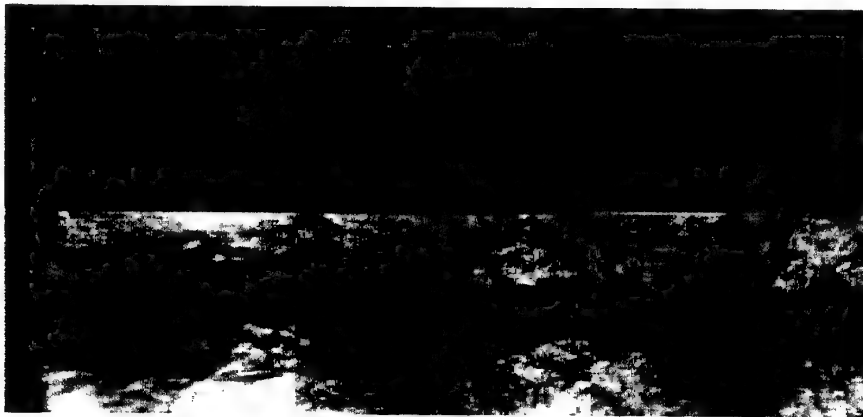

Figure 2: Reacting shear-coaxial liquid-oxygen–hydrogen injector operating at 4.5 *MPa* (44 atm). From Mayer and Tamura (1996). Used with permission.

Phenomenological Trends

Recent experiments have provided a much clearer understanding of the phenomenological conditions which exist as a function of chamber pressure. Depending on the injector type, fluid properties, and flow characteristics, two limiting extremes may exist. At subcritical chamber pressures, injected liquid jets undergo the classical cascade of processes associated with atomization. Dynamic forces and surface tension promote the formation of a heterogeneous spray which evolves continuously. Spray flames form as a consequence which are lifted away from the injector face in a manner consistent with the combustion mechanisms exhibited by local drop clusters. When chamber pressures approach or exceed the critical pressure of a particular propellant, however, injected liquid jets undergo a transcritical change of state as interfacial fluid temperatures rise above the critical temperature of the local mixture. For this situation, diminished intermolecular forces promote diffusion dominated processes prior to atomization and respective jets vaporize forming a continuous fluid in the presence of exceedingly large gradients. Well mixed diffusion flames evolve as a consequence which are anchored by small but intensive recirculation zones generated by the shearlayers imposed by adjacent propellant streams.

The flow visualization studies conducted by Mayer and Tamura (1996) illustrate these trends for the case of a liquid-oxygen–gaseous-hydrogen shear-coaxial injector element. The two extremes are shown in Figs. 1 and 2,
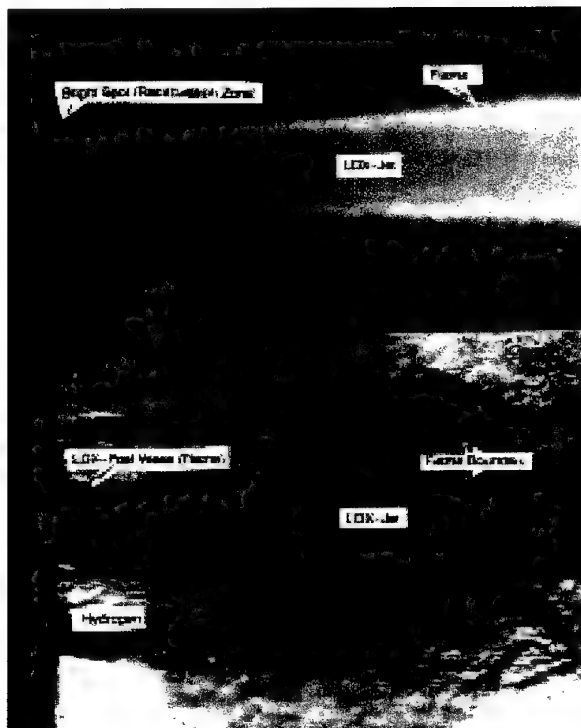
Figure 3: Near injector region of a reacting liquid-oxygen–gaseous-hydrogen shear-coaxial injector, flame (top) and corresponding flow field (bottom). Oxygen and hydrogen velocities are 30 and 300 m/s, respectively, oxygen and hydrogen injection temperatures are 100 K and 300 K, oxygen jet diameter is 1 mm, chamber pressure is 4.5 MPa (44 atm). From Mayer and Tamura (1996). Used with permission.

respectively. Note that the critical pressure and temperature of oxygen are p_c = 5.04 MPa (49.7 atm) and T_c = 155 K, respectively. The critical pressure and temperature of hydrogen are p_c = 1.30 MPa (12.8 atm), T_c = 33.2 K. When liquid-oxygen is injected at low-subcritical pressures (Fig. 1) atomization occurs forming a distinct spray as described above. Ligaments are detached from the jet surface forming spherical drops which subsequently breakup and vaporize. As the chamber pressure approaches the thermodynamic critical pressure of the liquid-oxygen (Fig. 2), the number of drops present diminishes. Here, the injected jet exhibits a pure diffusion mechanism at a pressure of 4.5 MPa, which is slightly below the thermodynamic critical pressure of oxygen, and significantly above that of hydrogen. Experimental results have revealed that flame attachment occurs instantaneously after ignition in the small but intensive recirculation zone which forms just downstream of the annular post. A well mixed diffusion flame forms within this region producing a wake that separates the oxygen stream from the hydrogen-rich outer flow. The conditions imposed for Test Cases RCM-2 and RCM-3 are phenomenologically analogous to those of Figs. 1 and 2.

Flow Characteristics

Simulating either of the two extremes described above with either LES or RANS based methods requires a detailed representation of the broadband turbulence coupled with appropriate multiphase, thermochemical, thermodynamic and transport models. Modeling subcritical atomization and dense spray processes similar to those depicted in Fig. 1 are still one of the most difficult and evasive topics of research. At this point only relatively crude highly empirical models exist. Dilute spray models, however, are more prevalent and can be very accurate at low subcritical pressures. Results shown in subsequent sections will demonstrate the effectiveness of LES in treating dilute spray dynamics in a configuration which eliminates the ambiguities associated with atomization. Simulating the transcritical jet, on the other hand, does not require use of an atomization model, but does require a detailed representation of the physical properties.

3

Because the fluid is much denser, the broadband turbulence characteristics which must be considered are clearly evident in Fig. 2. Figure 3 is a visualization which illustrates the near injector region of this case in the vicinity of the liquid-oxygen post. The mean flame characteristics are shown on the top of the figure, and the corresponding flow field is shown on the bottom. The oxygen and hydrogen velocities for this case are 30 and 300 m/s, respectively, the oxygen and hydrogen injection temperatures are 100 K and 300 K, the oxygen jet diameter is 1 mm, and the mean chamber pressure is 4.5 MPa (44 atm). Figures 4 and 5 show the corresponding thermophysical behavior of of oxygen and hydrogen over the regimes of interest. Plots of density, specific heat, viscosity, and thermal conductivity are given on the interval $40 \leq T \leq 1000 \, K$ for pressures of 1, 10, 50, 100, 200, and 400 atmospheres. Note that at 1000 K and above, both oxygen and hydrogen exhibit ideal gas behavior and the pressure effect is negligible. As the temperature is decreased below 1000 K, however, significant nonidealities are introduced, with property variations associated with oxygen producing the most significant effects.

Figure 6 shows the trends associated with the kinematic viscosity. The effect of pressure on this quantity is particularly significant and has a direct impact on the characteristic scales associated with the turbulence field. For both oxygen and hydrogen, an increase in pressure from 1 to 100 atmospheres results in a corresponding reduction in the kinematic viscosity of up to three orders of magnitude. This implies a three order of magnitude increase in the characteristic Reynolds number. Based on Kolmogorov's universal equilibrium theory (Tennekes and Lumley 1972, Hinze 1975), the order of magnitude of the Kolmogorov microscale, denoted here as η_t, and the Taylor microscale, denoted here as λ_t, are related to the Reynolds number by

$$\frac{\eta_t}{l_t} \sim Re_t^{-\frac{3}{4}} \qquad \frac{\lambda_t}{l_t} \sim Re_t^{-\frac{1}{2}} \tag{1}$$

Here the Reynolds number is defined as $Re_t = q_t l_t / \nu$ where $q_t = \sqrt{2k_t/3}$. The term q_t represents the turbulence intensity, k_t the *sgs* kinetic energy, and l_t the integral length scale. The relations given by Eq. (1) indicate that a three order of magnitude decrease in the kinematic viscosity results in 2.25 and 1.5 order of magnitude decreases in the Kolmogorov and Taylor microscales, respectively. These reductions have a direct impact on the overall grid density required to resolve key processes.

Figure 7 shows the trends associated with the effective mass diffusivity. When the pressure is increased from 1 to 100 atmospheres, both oxygen and hydrogen exhibit a two order of magnitude decrease in the mass diffusion rate over the full range of temperatures plotted. Oxygen exhibits a decrease of up to 4 orders of magnitude at temperatures below the critical mixing temperature. The diminished mass diffusion rates coupled with the liquid-like densities which dominate at high pressures significantly alter the coupling associated with local combustion characteristics in the vicinity of the liquid-oxygen jet.

Qualitative analysis of Fig. 3 correlated with the trends shown in Figs. 4–7 suggests that there are at least seven fundamentally important flow characteristics which must be accounted for: 1) dense near-critical and supercritical fluid mixture properties, 2) transient broadband turbulent mixing over a wide range of scales, 3) high pressure chemical kinetics, 4) strong multicomponent property gradients, 5) dominant preferential diffusion processes, 6) anomalous multiphase interfaces, and 7) geometrically dominated (wall-bounded) three-dimensional evolution. Treating this set of characteristics represents a minimal requirement for any simulation-based or modeled treatment of the flow. In general, the intricate multiple-time, multiple-length scale coupling must be resolved (or modeled) to represent the physics. A time-accurate treatment of turbulence, thermochemistry, thermodynamics and transport properties are essential, and disparate turbulence and molecular transport processes must be treated simultaneously. Algorithm design and high-performance massively parallel computing are also essential elements.

Modeling Options and Tradeoffs

There are currently three basic choices with regard to the simulation approach. The widely used Reynolds-Averaged Navier-Stokes (RANS) approximation, Large Eddy Simulation (LES) and Direct Numerical Simulation (DNS). The least numerically intensive is RANS. For this approach, all turbulent motions are modeled. The closure is empirical and based on scaling arguments which apply only in the time-averaged limit. In general, predictions are highly sensitive to models and model constants, and respective constants must be adjusted and tuned for every flow. LES is a much more numerically intensive methodology, but offers a higher degree of accuracy in return. For this approach,
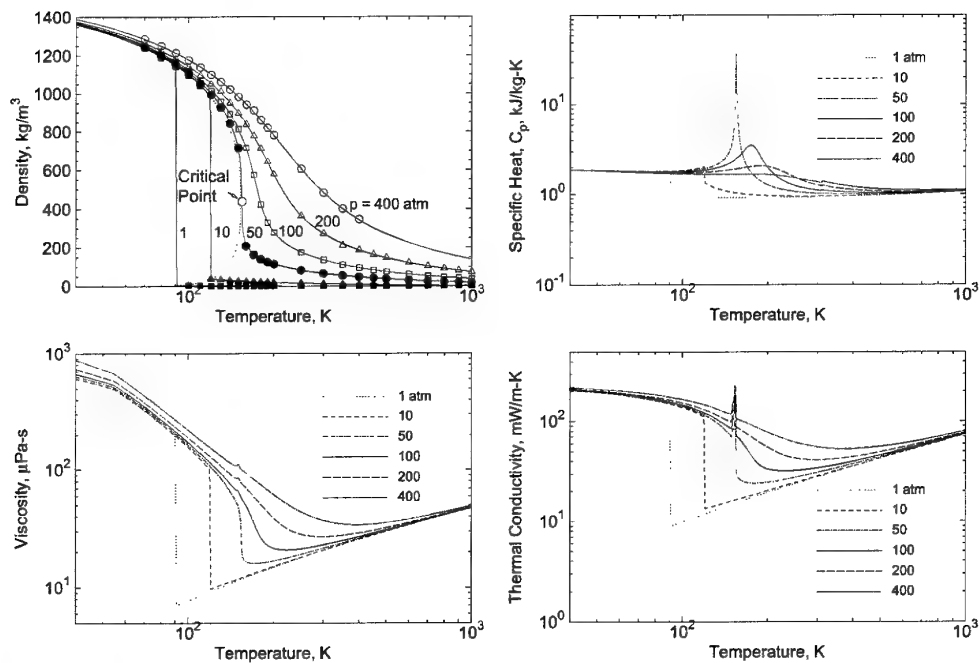
Figure 4: Density (compared with experimental data points obtained by Vargaftik (1975)), specific heat, viscosity, and thermal conductivity versus temperature over the interval $40 \leq T \leq 1000$ and pressures of 1, 10, 50, 100, 200, and 400 atmospheres for pure oxygen.
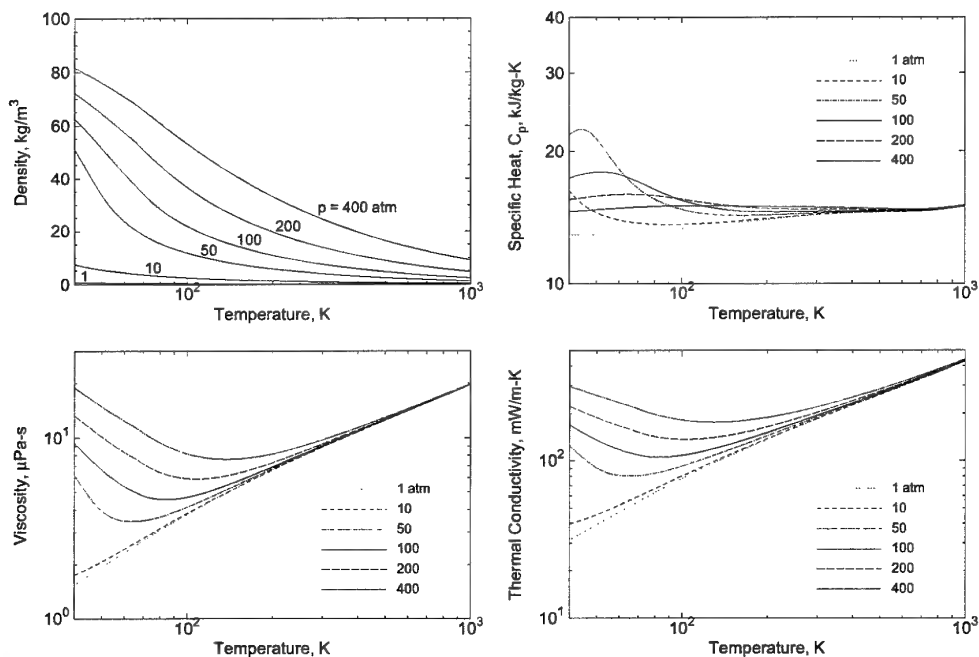
Figure 5: Density, specific heat, viscosity, and thermal conductivity versus temperature over the interval $40 \leq T \leq 1000$ and pressures of 1, 10, 50, 100, 200, and 400 atmospheres for pure hydrogen.

5

Figure 6: Kinematic viscosity of pure oxygen (left) and pure hydrogen (right) over the temperature interval $40 \leq T \leq 1000$ and pressures of 1, 10, 50, 100, 200, and 400 atmospheres.

Figure 7: Effective mass diffusivity of pure oxygen (left) and pure hydrogen (right) over the temperature interval $40 \leq T \leq 1000$ and pressures of 1, 10, 50, 100, 200, and 400 atmospheres.
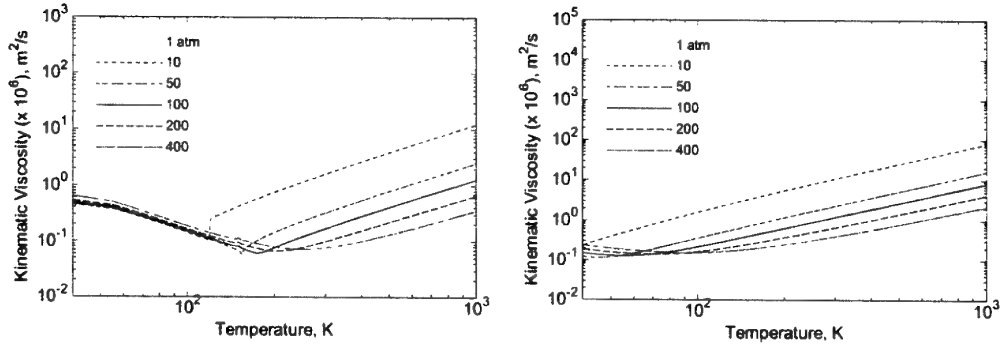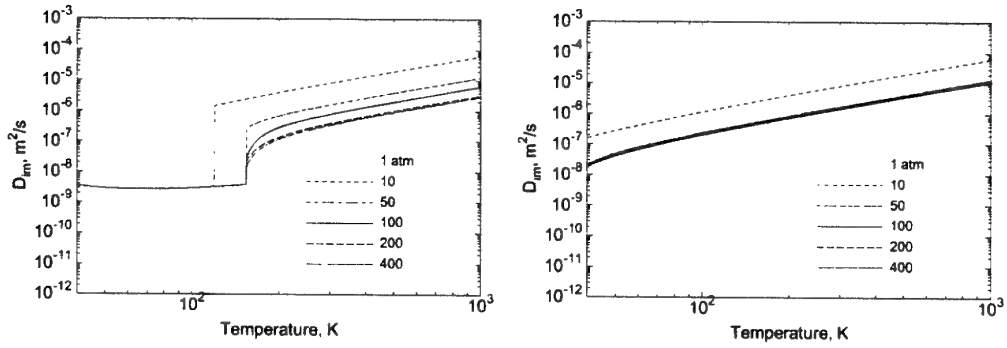
the large energetic scales are resolved, and the subgrid-scales are modeled. In contrast to RANS, LES closures are time-accurate, the models tend to be more universal, and it is not necessary to adjust constants for every flow. With the appropriate grid constraints in place, the use of dynamic modeling eliminates the need for any model constants. The enhanced accuracy, however, comes with a much stricter set of algorithmic requirements. Similarly, DNS is the most numerically intensive. For this approach, all scales are resolved, and no modeling is required, but the method is severely CPU limited.

There are three baseline considerations which currently dictate the selection of RANS versus LES versus DNS as a solution method: 1) the time required to get a solution, 2) the accuracy of a solution, and 3) the feasibility of obtaining a solution. Performing a DNS which meets the seven criteria listed in the previous section is clearly not feasible at this point in time. Thus, tradeoffs typically revolve around RANS versus LES, with DNS being used as a more fundamental tool for studying extremely small-scale phenomena in highly idealized domains. This in itself is limiting, and care must be taken to insure DNS simulations of this type are truly relevant to the flow phenomena of interest. LES, by definition, is an inherently three-dimensional simulation methodology (as is DNS), and LES grid requirements are much stricter than those for RANS. Well proportioned LES grids are typically sized a factor of four coarser in each coordinate direction than an equivalent well sized DNS grid with the equivalent order of accuracy. Examples of well sized LES grids are given in subsequent sections. RANS is by far the fastest solution technique, but also the least accurate since the entire system is essentially a model. However, the speed and minimal resources with which RANS solutions can be obtained is often an invaluable and necessary engineering tool. A secondary consideration is the fact that the LES methodology imposes a much stricter set of numerical requirements and constraints.

General Requirements for LES

Improvements in computational speed and capacity over the past several years has made the application of LES feasible for increasingly complex flows. This method has now been used successfully as both as a complementary tool for understanding turbulence and for modeling the effects of turbulence in a variety of engineering applications. With the advent of massively parallel computer hardware, LES now provides a means to study coupled combustion, transport and multiphase processes in parameter spaces that are unattainable using direct numerical simulation (DNS) techniques, with a degree of fidelity that can be far more accurate than other conventional methods.

Modeling Issues

During the past decade, considerable progress has been made in LES. Early works relied heavily on the use of the Smagorinsky eddy viscosity model (Smagorinsky 1963). A key breakthrough in the field of *sgs* modeling resulted from the introduction of the dynamic modeling procedure (Germano, Piomelli, Moin and Cabot 1991, Moin, Squires, Cabot and Lee 1991, Lilly 1992, Zang, Street and Koseff 1993, Vreman, Geurts and Kuerten 1994). In this approach constants which appear in the base *sgs* models are computed dynamically as functions of space and time providing the proper local amount of *sgs* scalar mixing and dissipation. Another important idea in *sgs* modeling involves the use of scale-similarity laws which assume that the largest of the unresolved scales have similar structure to the smallest of the resolved scales. Among these models, only that proposed by Bardina, Ferziger and Reynolds (1983) satisfies the important physical constraint of Galilean invariance (Speziale 1985).

Dynamic modeling coupled with scale similarity ideas have been very useful in *sgs* modeling of nonreacting flows. This concept is currently being exploited in LES of reacting flows. Erlebacher, Hussaini, Speziale and Zang (1992) were one of the first to propose a compressible generalization of the dynamic Smagorinsky model and couple this to the scale-similarity model to obtain the *sgs* mass and energy fluxes. These ideas have now been extended to multicomponent mixtures (Oefelein 2001). With this framework in place, the role of combustion models are to account for the effect of *sgs* fluctuations in the thermochemical variables and filtered chemical source terms over a wide range of pressures. Achieving this closure hinges on the specification of accurately reduced kinetics mechanisms coupled to an accurate representation of *sgs* scalar mixing processes.

7

Numerical Constraints

It is well known that numerical dissipation and dispersion errors can have significantly devastating effects on *sgs* models. The presence of these errors depletes energetic turbulence scales at the mid- to high-wavenumbers and consequently competes with the models. When this occurs, the *sgs* models themselves often have no effect on the flow, and the contamination often to leads erroneous conclusions. To avoid this situation, numerical methods used for LES must provide spatially "non-dissipative" spectrally clean damping characteristics out to the smallest wavenumbers coupled with simultaneous local conservation of mass, momentum and total-energy. Conservation of kinetic energy is particularly important when dynamic modeling is used.

Co-located schemes with explicit artificial dissipation terms added for stabilization purposes have historically failed to provide the appropriate spectral characteristics. This is easily shown if one compares the magnitude of the residual associated with the artificial dissipation terms of a given scheme to that associated with a given *sgs* model. The former is always orders of magnitude greater, even for higher-order schemes. Unfortunately, this fact precludes a wide class of flow solvers, including the trivial conversion of most RANS based codes. Staggered grid algorithms fashioned after the pioneering work of Harlow and Welch (1965), on the other hand, have been shown to give acceptable spectral characteristics. Specialized schemes of this type are currently the workhorse of the LES community.

Because of the obvious advantages, grid stretching functions are widely used for LES just as they are for RANS calculations. One additional constraint associated with LES, however, is that the energetic scales must be resolved on grids that minimize commutation errors. This requirement imposes strict grid stretching constraints which precludes the use of typical RANS grids. Instead, grids must be constructed with much more restricted grid stretching and grid aspect ratios. The stretching ratio associated with adjacent cells in a given coordinate direction should never exceed 10 percent, and grid aspect ratios greater than 100 are rarely acceptable. The issues outlined above represent minimal requirements and non-adherence can lead to diminished broadband resolution and significant high wavenumber contamination.

Phenomenological Case Studies

Development efforts conducted by Oefelein (2001) over the past several years have led to a massively parallel software package which incorporates the general requirements for LES described in the previous section. The effort was driven by two mutually dependent objectives. The first was to develop improved models suitable for performing high-fidelity LES of the complex phenomena described above. The second was to develop a high-performance parallel algorithm which supported the implementation of large-scale simulations. Emphasis was placed on a general treatment of phenomenologically complex reacting multiphase flows, including the seven fundamentally important flow characteristics described above. These flow characteristics are:

1. Dense near-critical and supercritical fluid mixture properties.

2. Broadband turbulent mixing over a wide range of scales.

3. High pressure chemical kinetics.

4. Strong multicomponent property gradients.

5. Dominant preferential diffusion processes.

6. Anomalous multiphase interfaces.

7. Geometrically dominated (wall-bounded) three-dimensional evolution.

The baseline Eulerian–Lagrangian framework solves the filtered conservation equations of mass, momentum, total-energy and species using a staggered grid methodology analogous to that pioneered by Harlow and Welch (1965) in generalized curvilinear coordinates. Dual-time stepping is used with a unified all Mach number preconditioning technique. The algorithm accommodates fully implicit time advancement using a fully explicit multistage scheme in pseudo-time. This scheme exhibits excellent parallel efficiency and scalability attributes. The implicit formulation is

A-stable which allows one to set the time step based solely on accuracy considerations. It accommodates arbitrary equations of state, thermochemical, thermodynamic and transport processes, and provides full thermophysical coupling over a wide range of conditions. It accommodates intermediate complex geometric features while maintaining the accuracy of structured spatial stencils. The parallel paradigm employs distributed-memory message-passing using MPI, the single-Program–Multiple-Data (SPMD) model and structured multiblock domain decomposition.

Following are three examples which give insight into the intricate nature of the problem and the current state of the art with respect to LES. The first is an early set of results which illustrate the prevalence of items 1-7 listed above when modeling high pressure mixing and combustion in liquid-oxygen (LOX), hydrogen systems. These results represent a first preliminary attempt at simulating these phenomena and demonstrate a capability to handle the extreme complex thermophysical flow characteristics. The second example is an LES of a low-Mach-number, high-Reynolds-number, particle-laden channel flow. This is an extremely difficult case to handle with a compressible flow solver. The results demonstrate a capability to handle these extremes, the ability of LES to capture transient broadband turbulent mixing over a wide range of scales, and also the ability to resolve the geometrically dominated (wall-bounded) three-dimensional evolution of the flow. The last set of results also demonstrates these advantages in a more complex geometry, and additionally the ability of LES to simulate spray characteristics and particle dispersion.

High-Pressure Mixing and Combustion in $LOX–H_2$ Systems

Figure 8 shows contours of density, temperature, and H_2, O_2, OH and H_2O mass fractions in the near-field injector region of a hydrogen–liquid-oxygen shear layer. The two streams are separated by a 0.5 *mm* LOX post. The pressure is 10.1 *MPa* (100 atm). The hydrogen (upper stream) and oxygen (lower stream) velocities are 125 and 30 m/s, respectively. The injection temperatures are 150 *K* and 100 *K*. These early calculations were performed using the theoretical-numerical framework developed by Oefelein (1997) and represent a first attempt at simulating such processes. The matrix of conditions considered were fashioned after the flow visualization studies conducted by Mayer and Tamura (1996). Emphasis was placed on the near-field flow processes in the vicinity of the post. The conditions selected produce a supercritical hydrogen stream and a liquid-oxygen stream which undergoes a transcritical change of state within the mixing layer. Inlet velocity profiles were generated assuming fully developed turbulent flow and a heat conduction model was applied to the splitter plate to provide a realistic energy flux distribution at the walls. Nonreflecting outflow conditions were imposed at the exit and inviscid, adiabatic, and noncatalytic conditions were imposed at the transverse boundaries.

These results illustrate the prevalence of items 1-7 listed above. Transcritical mixing induces a vortical structure within the injected hydrogen stream which is analogous to that produced by a backward facing step. This structure emanates from the boundary layer upstream of the post and is amplified by interactions within the shear layer and coalescence downstream with adjacent vortices. The oxygen stream, on the other hand, proceeds unimpeded in an essentially straight line. Because of the liquid-like characteristics of the oxygen stream, an extremely large density gradient exists within this region. Note that the change in density is on the order of 1000 to 1. Diminished mass diffusion rates are also evident. The combined effect produces a fuel rich flame which anchors itself to the oxygen jet and behaves in a qualitatively similar manner as the diffusion dominated flame depicted in Figs. 2 and 3. Combustion occurs at near stoichiometric conditions and produces a wake which effectively separates the hydrogen and oxygen streams as the flow evolves downstream. Results highlight the effect of the momentum flux ratio on flame-holding dynamics, the dominating effect of the density gradient, and the impact of diminished mass diffusion rates which accompany the liquid-like behavior of near-critical fluids.

Low-Mach-Number, High-Reynolds-Number (Particle-Laden) Channel Flow

Three particularly relevant effects induced by interphase coupling are turbulence modulation which involves the damping of gas phase turbulence by particulates accommodating to turbulent motion, turbulence generation which involves the production of gas phase turbulence due to the presence of particle wakes, and liquid deformation and breakup processes and the resultant effect on interphase exchange processes. As part of an effort to treat these phenomena systematically a series of LES calculations are being performed using the algorithmic framework describe above and compared to the experimental data acquired by Kulick, Fessler and Eaton (1994). These experiments characterize the interactions between various particle loading conditions and the fluid turbulence in the well-defined confines of a turbulent channel. Particles are selected to respond to some, but not all scales of turbulent motions. Gas phase velocities were measured to investigate the means by which particles attenuate turbulence.
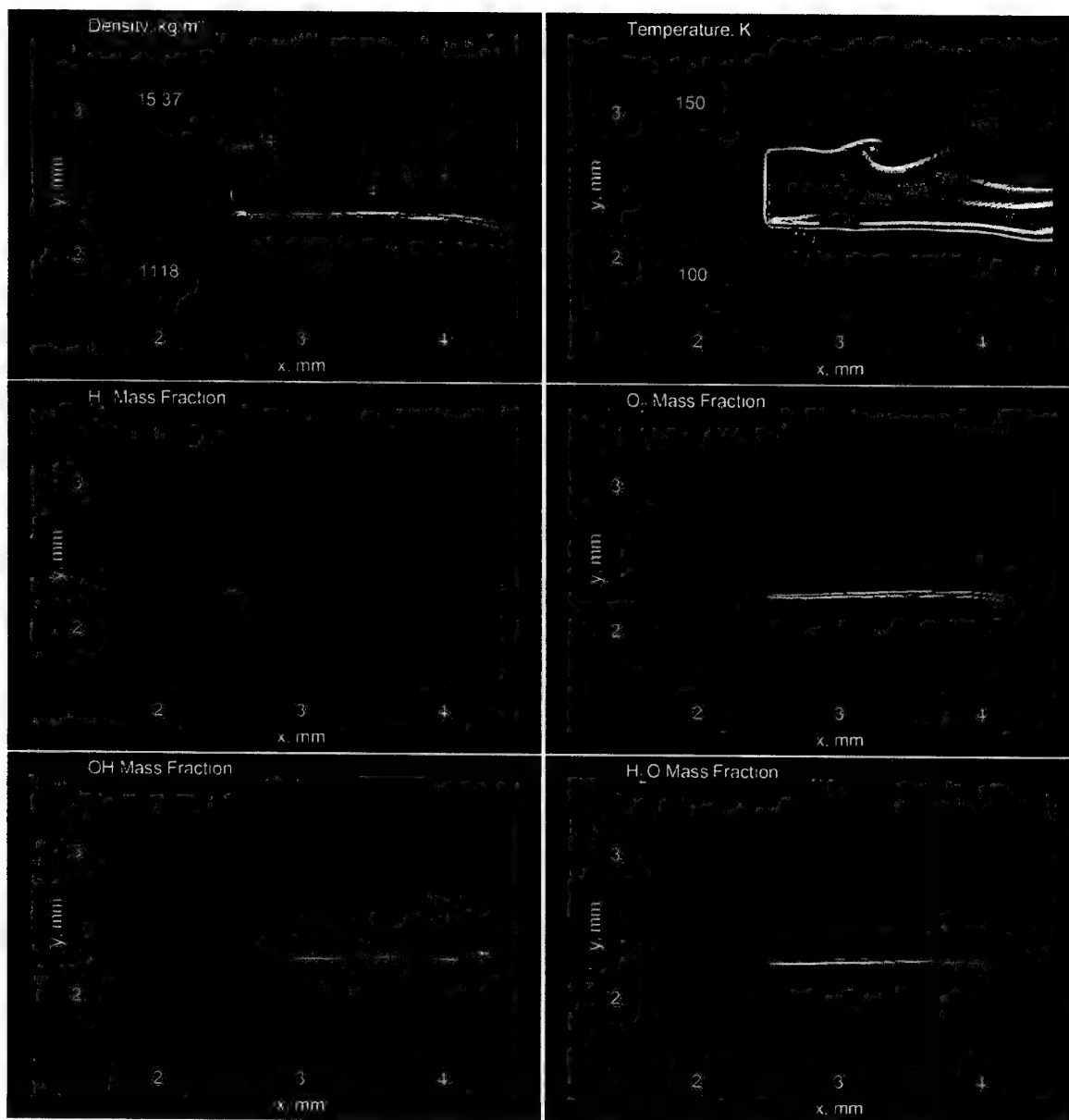
Figure 8: Contours of density, temperature, and H_2, O_2, OH and H_2O mass fractions in the near-field injector region. Chamber pressure is 10.1 *MPa* (100 atm), hydrogen (upper stream) and oxygen (lower stream) velocities are 125 and 30 m/s, respectively, and injection temperatures are 150 *K* and 100 *K*.
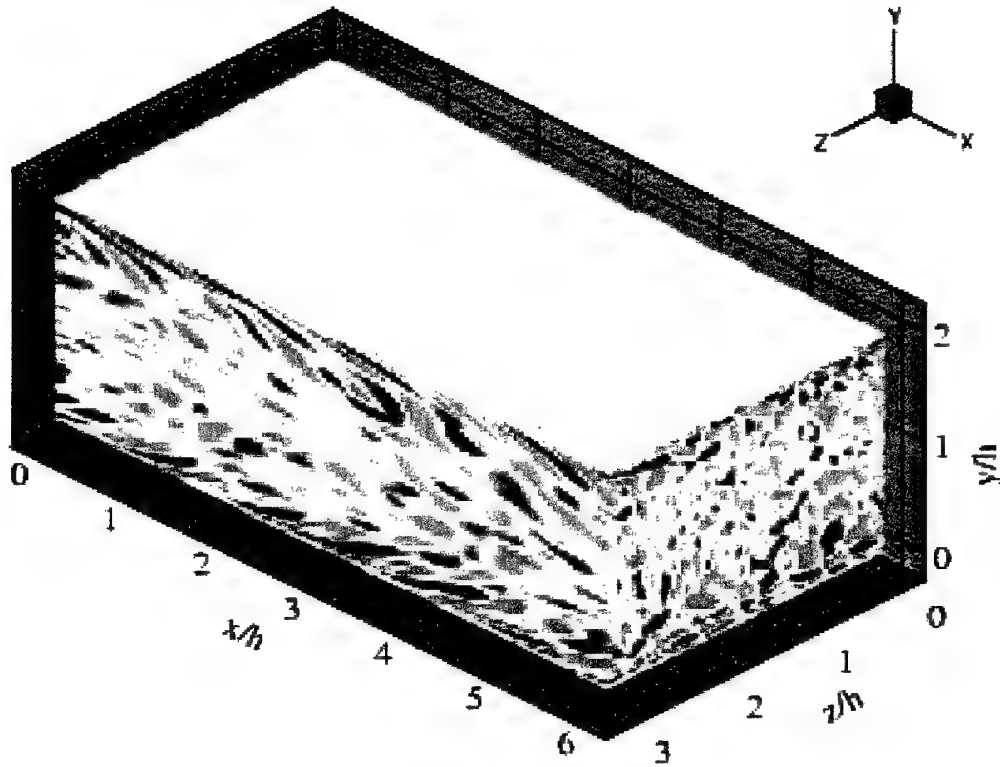
Figure 9: Instantaneous contours of the streamwise component of vorticity in a high Reynolds number, particle laden channel. Half-height is $h = 20\ mm$, mean centerline velocity is $U_{cl} = 10.5\ m/s$, Reynolds number based on h is $\mathrm{Re}_h = 13800$, friction velocity is $u_\tau = 0.49\ m/s$ and Reynolds number based on u_τ is $\mathrm{Re}_\tau = 645$.
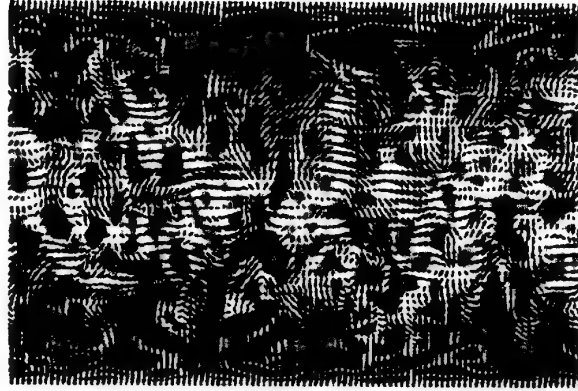
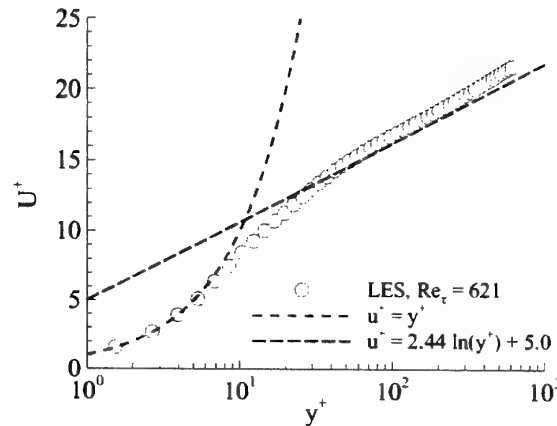Figure 10: Velocity vectors and contours of the streamwise component of vorticity in the $y - z$ plane.

Figure 11: Time-averaged streamwise component of velocity compared with classic law-of-the-wall profiles.

Figure 9 shows the instantaneous contours of the streamwise component of vorticity in the turbulent low-Mach-number, high-Reynolds-number, particle laden channel of Kulick et al. (1994). The channel half-height is $h = 20\ mm$. The mean centerline velocity is $U_{cl} = 10.5\ m/s$ and the Reynolds number based on h is $\mathrm{Re}_h = 13800$. The friction velocity is $u_\tau = 0.49\ m/s$ and Reynolds number based on u_τ is $\mathrm{Re}_\tau = 645$. The domain dimensions in the streamwise, transverse (wall-normal), and spanwise directions, respectively are $6h \times 2h \times 3h$. The primary grid is composed of 100^3 hexahedral cells.

This second set of results demonstrate the ability of LES to capture transient broadband turbulent mixing over a wide range of scales and the ability to resolve the geometrically dominated three-dimensional evolution of turbulent flows. It also demonstrates the ability of the algorithmic framework to handle low-Mach-number flows in the incompressible limit. The detailed broadband structure associated with the baseline conditions described above are shown in Fig. 10. Here velocity vectors are plotted with contours of the streamwise component of vorticity in the $y - z$ plane. Figures 11 and 12 show the time-averaged streamwise component of velocity compared with classic law-of-the-wall profiles and the streamwise and wall-normal root-mean-square components of velocity compared with experimental data points obtained by Kulick et al. (1994). These results are typical when dynamic modeling is used with an appropriately sized grid.

Swirling Particle-Laden Flow in Coannular Dump-Combustor

In addition to broadband turbulence structure, this last set of results demonstrates the ability of LES to simulate spray characteristics and particle dispersion. Obtaining high-fidelity solutions of reacting sprays hinges on the application
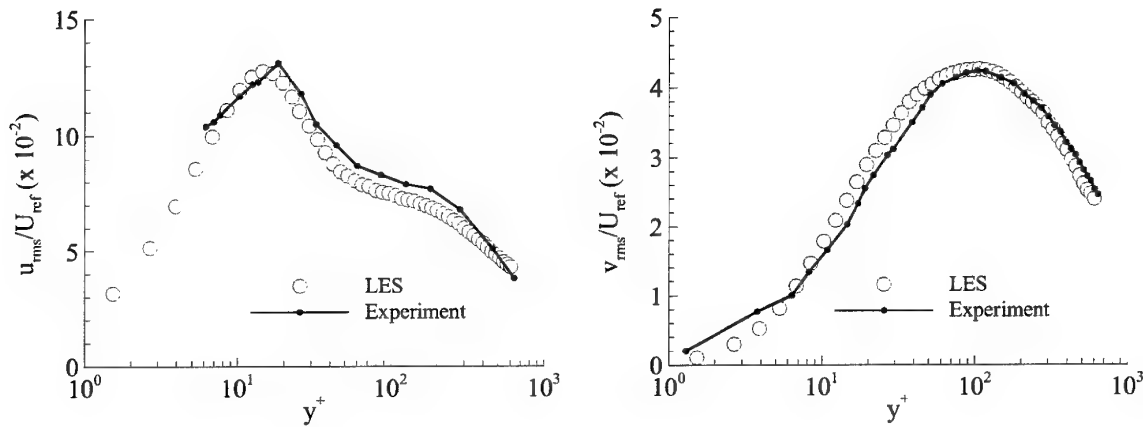
12

Figure 12: Streamwise and wall-normal root-mean-square components of velocity compared with experimental data points obtained by Kulick et al. (1994).
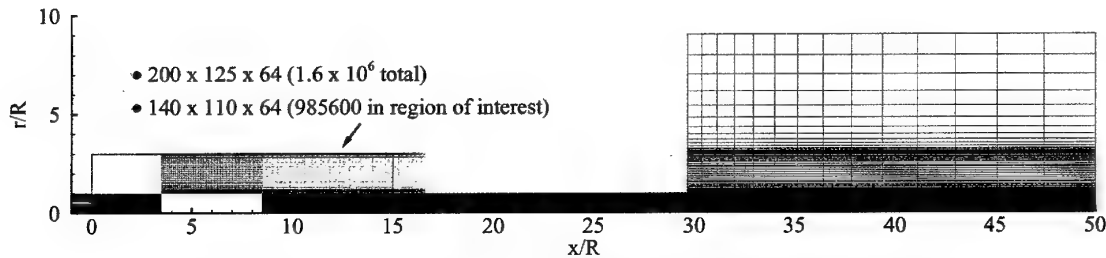

Figure 13: Cross-section of the computational domain and grid employed.

of methods and models which accurately describe momentum coupling and subgrid-scale modulation of turbulence, mass and energy coupling and subgrid-scale scalar mixing, and the combustion processes induced as a consequence. As part of an effort to treat these phenomena systematically a series of LES calculations have been performed and compared to the experimental data acquired by Sommerfeld et al. (Sommerfeld and Qiu 1991, Sommerfeld, Ando and Wennerberg 1992, Sommerfeld and Qiu 1993). These experiments characterize a swirling particle-laden flow in a model coannular combustion chamber and effectively isolate the effects related to momentum coupling. The primary objectives here were to gain a clearer understanding of the effectiveness and feasibility of current models and to gain a quantitative understanding of potential model limitations by analyzing the characteristic fluid dynamic scales of importance.

Sommerfeld et al. provides detailed measurements of swirling particle-laden flow in a chamber which consists of a sudden pipe expansion with a centered (primary) and annular (secondary) jet discharging into a cylindrical test section. A cross-section of the computational domain is given in Fig. 13. The region of interest is shown in Fig. 14. The primary jet has a radius of $r/R = 0.5$ and is laden with glass beads with a mean particle diameter of 45 μm distributed between 20 and 80 μm. The secondary jet extends over a radial interval of $0.59 \leq r/R \leq 1$ and is injected with a swirling azimuthal velocity component. The relevant flow conditions and particle properties are summarized in Table 1. Particles are injected in the primary jet in equilibrium with the gas-phase in a manner that matches the experimental distribution. A series of one-component phase-Doppler anemometer measurements were made along cross-sections at the 8 axial locations indicated. Gas-phase and particle-phase mean and rms velocity components were acquired along with simultaneous measurements of the particle size and mass flux distributions.

Figure 15 shows 1 mm thick cross-sections of the instantaneous particle distributions for Case 2 superimposed on the corresponding turbulent velocity field. For plotting purposes, the superimposed particle distribution shown is quite thick relative to the particle size distribution. One should not infer from this figure that collisions are important. Analysis of the particle number densities throughout the flowfield indicate that they are not. At any instant in time there are approximately 2.5 million particles being tracked, with two-way coupling applied between the gas and particles.
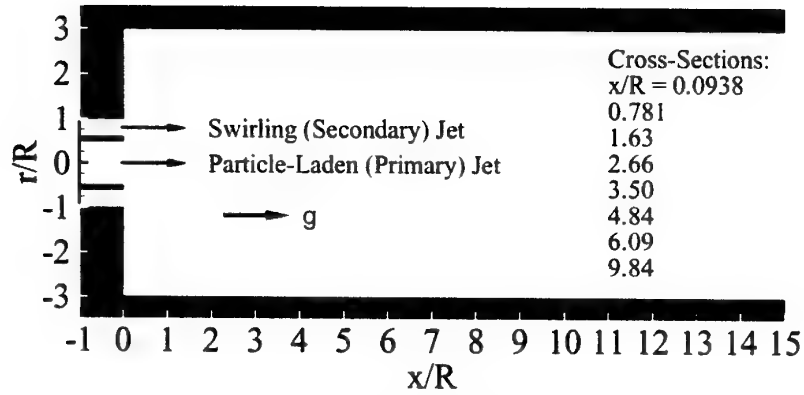
13

Figure 14: Region of interest in the Sommerfeld configuration.

Table 1: Flow conditions and particle properties used in the Sommerfeld experiments.

	Case 1	Case 2
Gas Phase (Air):		
Flow rate in primary jet, g/s	9.9	6.0
Flow rate in secondary jet, g/s	38.3	44.6
Inlet Reynolds number[a]	26200	27250
Swirl number	0.47	0.49
Temperature, K	300	
Particle Phase:		
Loading ratio in primary jet	0.034	0.17[b]
Flow rate, g/s	0.34	1.0
Mean diameter, μm	45.5	
Density ratio, ρ_p/ρ_f	2152	

[a] Based on total volume flow rate.
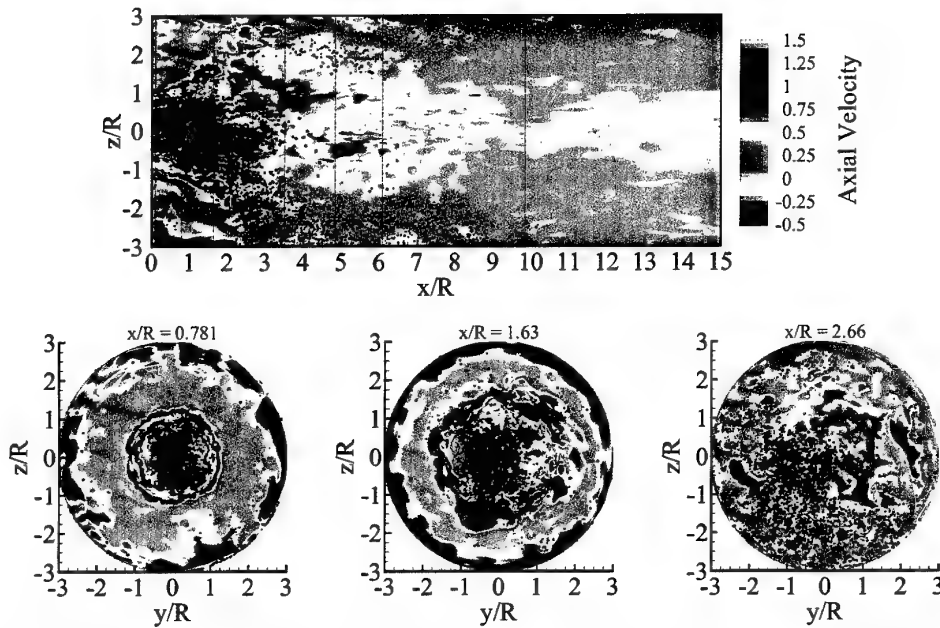
[b] 5 × Case 1.

14

Figure 15: One millimeter cross-sections of the instantaneous particle distribution for Case 2 superimposed on the corresponding turbulent velocity field ($R_{ref} = 32\,mm$, $U_{ref} = 12.9\,m/s$).

Tracking this number of particles is significant since it verifies the feasibility of employing large numbers of physical particles and eliminates the need to implement classical "parcel" approximations.

The mean flow characteristics for Cases 1 and 2 are shown in Fig. 16. This figure shows the time-averaged, azimuthally-averaged gas-phase velocity field. Key features of the flow include primary and secondary recirculation zones, a stagnation point in the core region and a reattachment point on the outer wall. The location of these points coincide with measured results to within 5 % for both cases. Figure 17 shows representative comparisons of (a) the mean axial gas velocity, (b) the corresponding mean axial particle velocity, (c) the mean particle diameter, and (d) the mean particle momentum flux for Case 2 at respective axial stations. The agreement between the measured and calculated results is excellent and similar agreements have been obtained with respect to the entire experimental data set.

After validating the LES methodology with the Sommerfeld data subsequent calculations were performed within the same configuration to gain a more quantitative understanding of the relevant modeling issues. Here, the validated broadband characteristics inherent to the LES methodology were used to obtain additional data that could not be
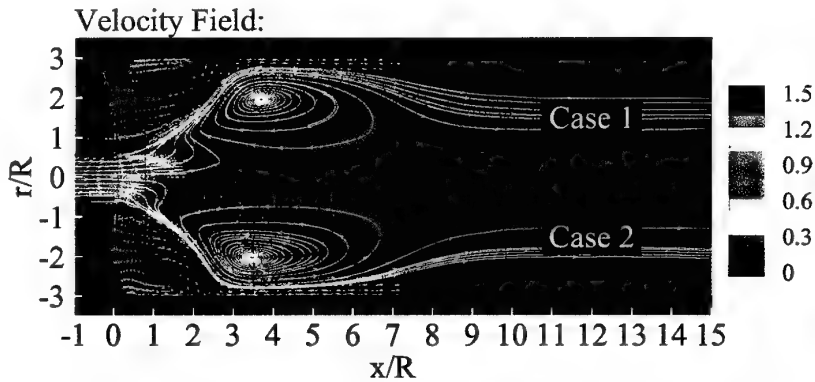

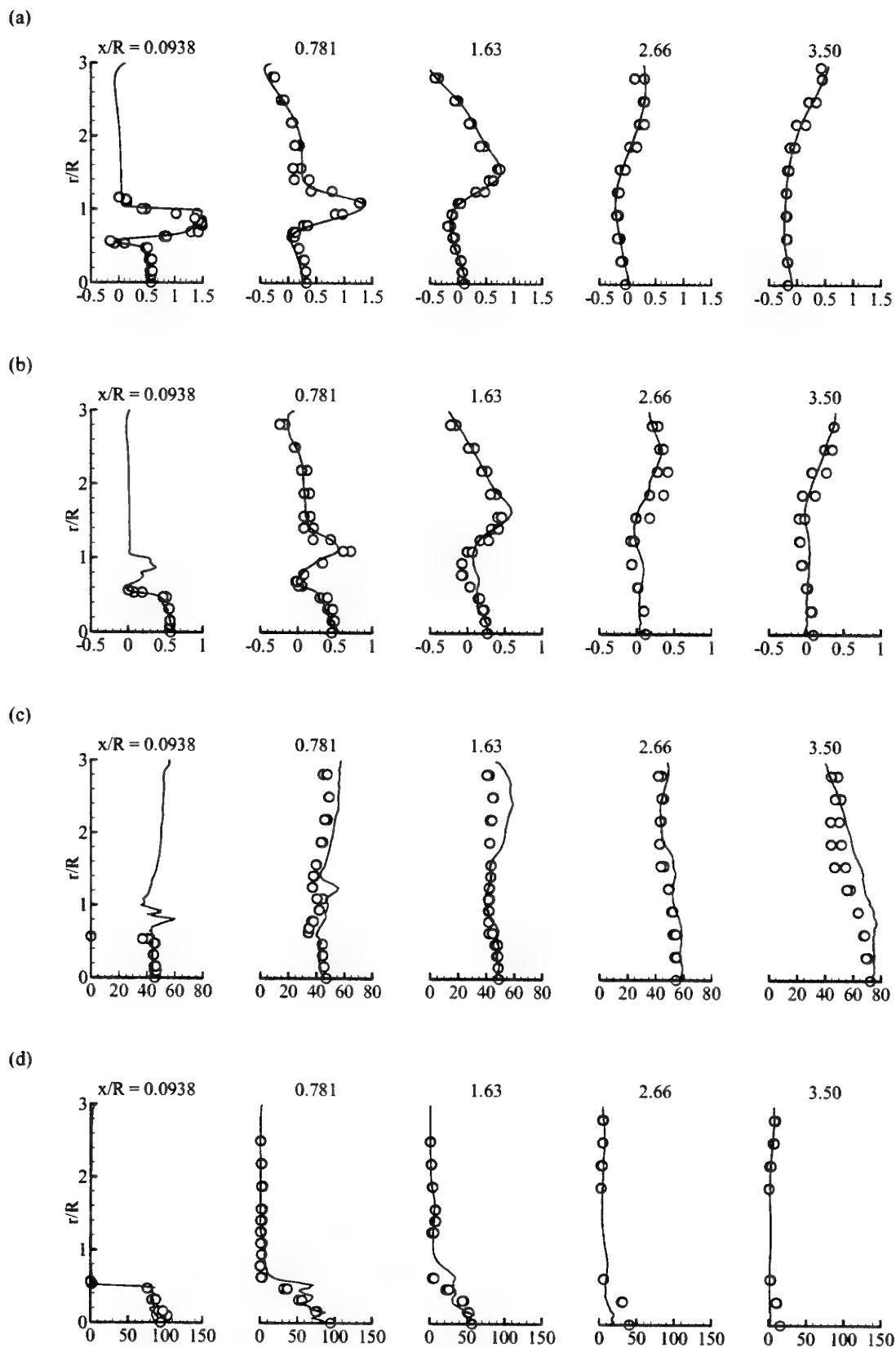Figure 16: Mean flow gas-phase stream function and velocity vectors.

15

Figure 17: Comparisons of measured (o) and calculated (—) time-averaged profiles of (a) the mean axial gas velocity, (b) the corresponding mean axial particle velocity, (c) the mean particle diameter, and (d) the mean particle momentum flux for Case 2.
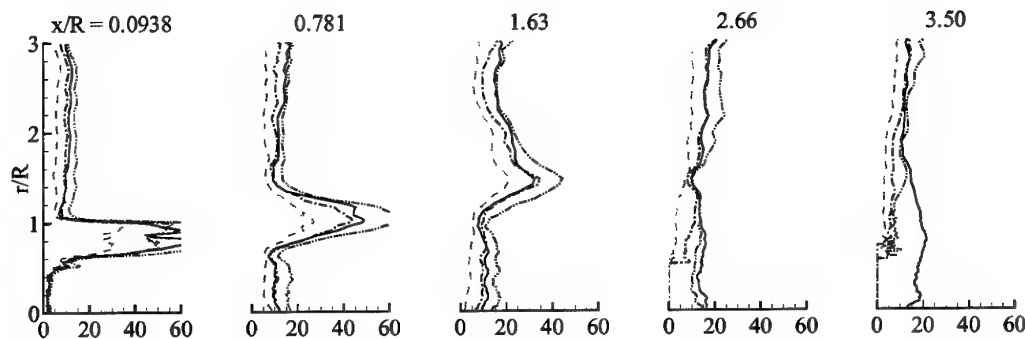
Figure 18: Mean particle Reynolds number corresponding to Case 2: $(-)$ all classes; $(\text{--}) \, d_p = 30 \pm 5 \, \mu m$; $(-)$ $d_p = 45 \pm 5 \, \mu m$; $(-) \, d_p = 60 \pm 5 \, \mu m$.

acquired from the experiment. In addition to the enhanced quantitative insight, this data was used to determine the envelope of conditions to be characterized by the model development effort. Figure 18 presents a representative set of results. Here profiles of the mean particle Reynolds number for Case 2 are given at respective axial stations for all size classes, $d = 30 \pm 5 \, \mu m$, $d = 45 \pm 5 \, \mu m$, and $d = 60 \pm 5 \, \mu m$. Other key scales and parameters obtained include 1) particle characteristics such as the particle number density, volume fraction, Sauter mean diameter etc., 2) flow characteristics such as the turbulence intensity, Kolmogorov microscales and Taylor microscales, and 3) time-scales such as the Stokes number and particle relaxation time.

Conclusions

Improvements in computer speed and capacity have made application of the large eddy simulation technique feasible for increasingly complex flows. The discussion and results presented have outlined the key phenomenological trends and have demonstrated model performance and accuracy requirements. Results have also highlighted various intricacies associated with transcritical and supercritical phenomena, highlighted the effect of pressure on near-critical mixing and combustion processes, and provided increased insights into the theoretical and numerical methodologies employed. Currently, coupled turbulent mixing and the treatment of thermodynamic and transport processes in laboratory-scale geometries can be handled quite accurately. The treatment of dilute spray dispersion and vaporization processes are also handled well. Accurate treatment of turbulent premixed and non-premixed flame phenomena, on the other hand, is still pending, as is the treatment of atomization processes and interface dynamics. The latter still lacks a strong theoretical basis. Current efforts are focused on model assessment and validation at realistic device-scale conditions and analysis of validated systems to systematically characterize the relevant time-scales, length-scales, and other key parameters which are of direct importance to sgs model development.

References

Bardina, J., Ferziger, J. H. and Reynolds, W. C. (1983). "Improved Subgrid Scale Models Based on Large Eddy Simulation of Homogeneous, Incompressible, Turbulent Flows," *Technical Report TF-19, Department of Mechanical Engineering*, Stanford University Stanford, California 94305.

Erlebacher, G., Hussaini, M. Y., Speziale, C. G. and Zang, T. A. (1992). "Toward the Large Eddy Simulation of Compressible Turbulent Flows," *Journal of Fluid Mechanics*, **238**: 155–185.

Germano, M., Piomelli, U., Moin, P. and Cabot, W. H. (1991). "A Dynamic Subgrid-Scale Eddy Viscosity Model," *Physics of Fluids*, **3**(7): 1760–1765.

Harlow, F. H. and Welch, J. E. (1965). "Numerical Calculation of Time-Dependent Viscous Incompressible Flow of Fluid with Free Surface," *Physics of Fluids*, **8**(12): 2182–2198.

Hinze, J. O. (1975). *Turbulence* second edn McGraw-Hill New York, New York.

Kulick, J. D., Fessler, J. R. and Eaton, J. K. (1994). "Particle Response and Turbulence Modification in Fully Developed Channel Flow," *Journal of Fluid Mechanics*, **277**: 109–134.

Lilly, D. K. (1992). "A Proposed Modification of the Germano Subgrid-Scale Closure Method," *Physics of Fluids*, **3**(11): 633–635.

Mayer, W. and Tamura, H. (1996). "Propellant Injection in a Liquid Oxygen/Gaseous Hydrogen Rocket Engine," *Journal of Propulsion and Power*, **12**(6): 1137–1147.

Moin, P., Squires, K., Cabot, W. and Lee, S. (1991). "A Dynamic Subgrid-Scale Model for Compressible Turbulence and Scalar Transport," *Physics of Fluids*, **3**(11): 2746–2757.

Oefelein, J. C. (1997). *Simulation and Analysis of Turbulent Multiphase Combustion Processes at High Pressures* PhD thesis The Pennsylvania State University University Park, Pennsylvania 16802.

Oefelein, J. C. (2001). "General Numerical Framework for Reacting Multiphase Flow with Complex Thermochemistry, Thermodynamics and Transport," Copyright 1992-2001 by J. C. Oefelein, All Rights Reserved.

Smagorinsky, J. (1963). "General Circulation Experiments with the Primitive Equations. I. The Basic Experiment," *Monthly Weather Review*, **91**: 99–164.

Sommerfeld, M. and Qiu, H. H. (1991). "Detailed Measurements in a Swirling Particulate Two-Phase Flow by a Phase-Doppler Anemometer," *International Journal of Heat and Fluid Flow*, **12**(1): 20–28.

Sommerfeld, M. and Qiu, H. H. (1993). "Characterization of Particle-Laden, Confined Swirling Flows by Phase-Doppler Anemometry and Numerical Calculation," *International Journal of Multiphase Flow*, **19**(6): 1093–1127.

Sommerfeld, M., Ando, A. and Wennerberg, D. (1992). "Swirling, Particle-Laden Flows through a Pipe Expansion," *Journal of Fluids Engineering*, **114**: 648–656.

Speziale, C. G. (1985). "Galilean Invariance of Subgrid-Scale Stress Models in the Large Eddy Simulation of Turbulence," *Journal of Fluid Mechanics*, **156**: 55–62.

Tennekes, H. and Lumley, J. L. (1972). *A First Course in Turbulence* The MIT Press Cambridge, Massachusetts.

Vargaftik, N. B. (1975). *Tables on the Thermophysical Properties of Liquids and Gases* second edn Wiley New York, New York.

Vreman, B., Geurts, B. and Kuerten, H. (1994). "On the Formulation of the Dynamic Mixed Subgrid-Scale Model," *Physics of Fluids*, **6**(12): 4057–4059.

Zang, Y., Street, R. L. and Koseff, J. R. (1993). "A Dynamic Mixed Subgrid-Scale Model and its Application to Turbulent Recirculating Flows," *Physics of Fluids*, **5**(12): 3186–3195.

2nd *International Workshop*

ROCKET COMBUSTION MODELING
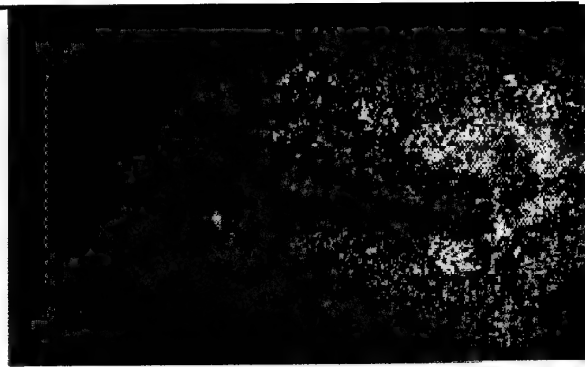
TEST CASE RCM-1
Cryogenic Injection

March 25 – 27, 2001
DLR, Lampoldshausen

French-German Research on Liquid Rocket Combustion

I- GENERAL PRESENTATION

The DLR Cryogenic Injector Facility M51 is used to study the jet break-up and mixing of cryogenic jets under high pressure conditions. The research is focused on the injection and mixing processes in cryogenic rocket engines with LOX (liquid oxygen) and GH2 (liquid hydrogen) as propellants (Ref. 1).

To study the fundamental processes of high pressure injection the propellants are replaced by non reacting simulation fluids (Ref 2 and 3). In the proposed test case LN2 (cold liquid nitrogen) is injected into a warm gaseous nitrogen environment. The LN2 jet is formed by a simple tube injector with an inner diameter of 2.2 mm.

The principal aim of the cold flow injection experiment is to understand the mixing process of a dense cryogenic jet in a light gas environment. The participant is free in the choice of the physical modeling. The idea is to have different approaches to finally find the most realistic simulation.

Shadow graph photography has been used for a preliminary flow field evaluation. Density profiles of the jet have been measured using two dimensional Raman scattering diagnostics.

II- GEOMETRY

a) Test chamber

The M51 test chamber consists of a cylindrical vessel with an inner diameter of 122 mm. The actual length of the vessel is 1000 mm (Figure 1). The test chamber has 4 windows for optical access. The injector is mounted in the center of the faceplate. The face plate has a ring slit of 5 mm.
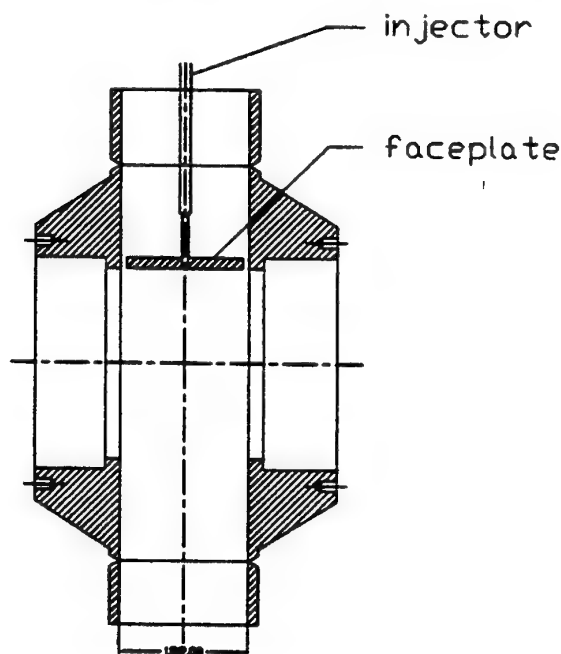

Figure 1: Test chamber with injector, faceplate and side walls (window section); the chamber inner diameter is 122 mm.

b) Injector

The tube injector is located in the center of the faceplate. The injector element's inner diameter is 2.2 mm. The tube length is 90.0 mm. As tube length to tube diameter ratio is more than 40 a fully developed turbulent velocity profile is to be expected at Position 2. The tube's inner walls are hydraulically smooth.

The injector manifold has an inner diameter of 6.0 mm.

Figure 2: Injector baseline dimensions
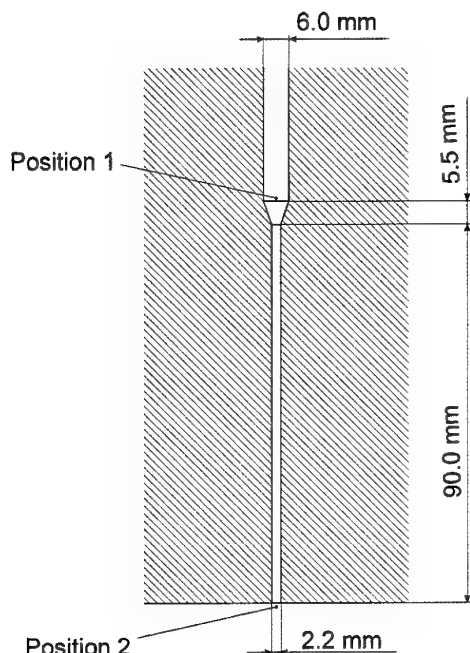
III- TEST OPERATING CONDITIONS

a) Operating points

The operating points chosen for RCM-1-A and RCM-1-B are actual test data and listed in the following table (P1 = Position 1, see Fig. 2):

Test case	RCM-1-A	RCM-1-B
Chamber Pressure	3.97 MPa	5.98 MPa
Temperature P1	126.9 K	128.7 K
Density P1	457.5 kg/m^3	514.0 kg/m^3

Mass flow P1	0.00995 Kg/s	0.01069 kg/s
Velocity P1	0.769 m/s	0.736 m/s
Viscosity P1	28.8×10^{-6} kg/m/s	35.8×10^{-6} kg/m/s

The mass flows and velocities are specified for the injector manifold at Position 1. The injector outlet velocity is then around 5.6 m/s in both cases (Position 2, see Fig. 2).

b) Fluid data

Liquid nitrogen (LN2) is injected. The physical properties of the LN2 for Position 1 (P 1, inlet boundary) are summarized in the table.

IV- GENERAL DATA FOR COMPUTATIONS

The list below describes the methods which should be used for this simulation.
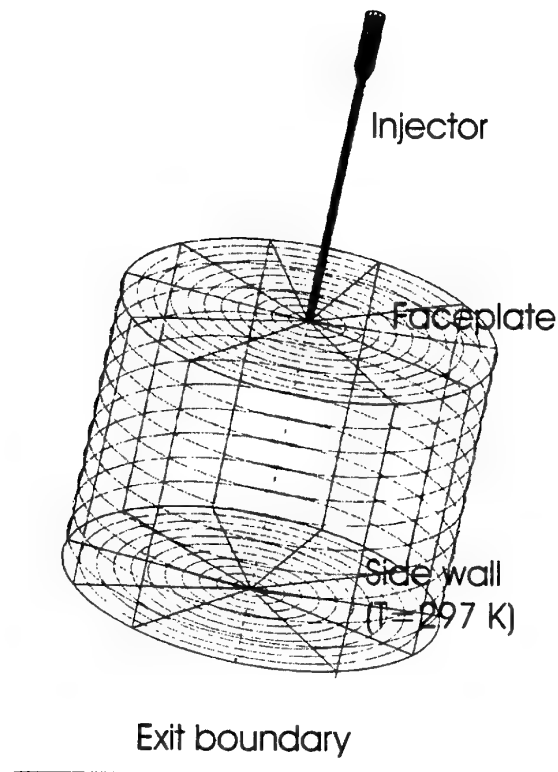
Computational Domain:

Figure 3: Principal sketch of computational domain (not in scale).

- The test chamber is a cylinder with an inner diameter of 122 mm.

- Computation of the entire chamber is preferred. The computed chamber length should be between 600 - 1000 mm. The length of the calculation regime may be less than the real length but should be long enough to ensure decoupling of the outflow boundary condition from the injector flow field.

- The ring slit should be neglected and wall boundary conditions should be set.

- The injector flow has to be simulated starting at Position 1 and using the data as specified in the table (fixed mass flow **inlet boundary**). This will result in an injector outlet mean velocity of around 5.6 m/s.

- All **wall boundary conditions** (injector inner walls, faceplate) are no slip and adiabatic except the chamber side wall. The chamber side wall has a constant temperature of 297 K.

- **Exit boundary** condition (chamber bottom): zero gradients in axial direction or extrapolated conditions exit at the specified chamber pressure (3.97 MPa or 5.98 MPa for RCM-1-A and RCM-1-B, respectively).

- **Initial condition:** The test chamber is filled with gaseous nitrogen at specified chamber pressure (3.97 MPa or 5.98 MPa for RCM-1-A and RCM-1-B, respectively) and at ambient temperature (297 K).

Physical Models

- Fluid: Nitrogen, pressure range 3.9 MPa - 6.2 MPa and temperature range 125 K - 300 K.

- Physical models for the turbulent flow calculation are not specified. Participants are free to choose these models. To study the influence of different models is one aim of this workshop. Therefore different solutions for the test cases may be presented.

- A real gas equation or appropriate fluid property data for nitrogen are necessary.

V- AVAILABLE DATA

- Two dimensional nitrogen density distribution in the chamber. The data have been measured using Raman scattering in a two dimensional laser light sheet set up. Instantaneous and averaged data are available. The time averaged data are used for reference of CFD simulations.

Figure 4: Typical flow field (shadow graph) of LN2 injection into gaseous nitrogen at 6.0 MPa chamber pressure.
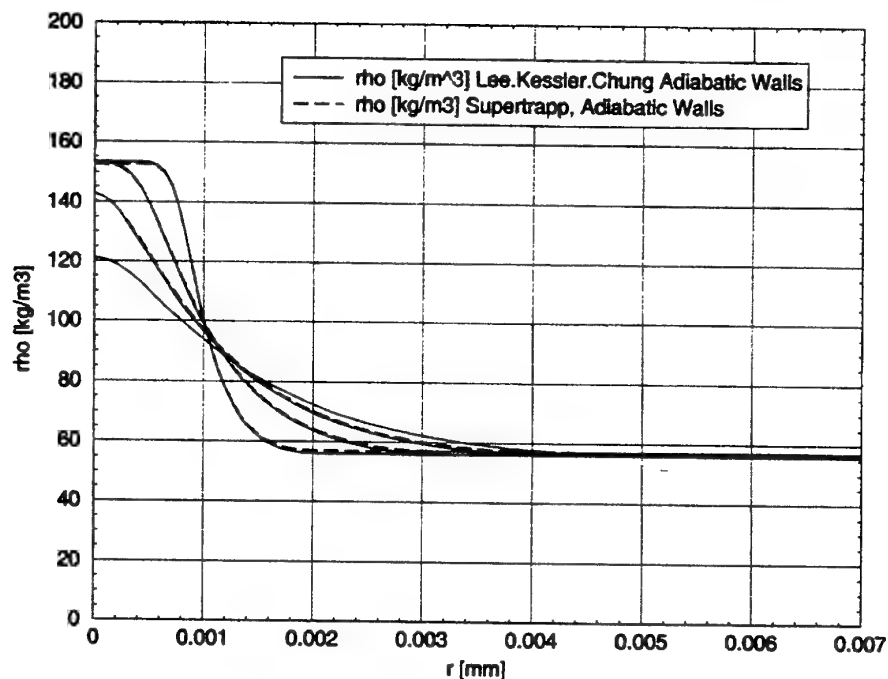
Figure 5:Typical time averaged density profiles of a LN2 Jet in gaseous nitrogen; parameter is the distance from the faceplate (principal tendency, data not for test case reference).

VI- REQUESTED RESULTS

- Injector exit condition (Position 2, see Fig. 2): velocity, density and turbulence profile.

- Radial density profiles for axial positions z = 5 mm, 15 mm, 25 mm, 35 mm, 45 mm, and 55mm downstream the faceplate (a sample is shown in Fig. 5, the data there are however from other injection conditions and therefore not for reference of this test case).

- Velocity field in chamber

II- REFERENCES

1. Mayer, W., Tamura, H., Propellant Injection in a Liquid Oxygen/Gaseous Hydrogen Rocket Engine, AIAA, Journal of Propulsion and Power, Vol. 12, No. 6, pp. 1137 - 1147, 1996

2. Oschwald, M., Schik, A., Klar, M., Mayer, W., Investigation of Coaxial LN2/GH2-Injection at Supercritical Pressure by Spontaneous Raman Scattering, 35th AIAA Joint Propulsion Conference, AIAA 99-2887, Los Angeles, CA, June 20-24, 1999

3. Mayer,W., Schik, A., Vielle B., Chaveau, C., Goekalp, I., Talley, D., Woodward, R., Atomization and Breakup of Cryogenic Propellants under High-Pressure Subcritical and Supercritical Conditions, Journal of Propulsion and Power, Vol. 14, No. 5, pp. 835-842, 1998

In case you need further information, you may contact: wolfgang.mayer@dlr.de

CFD SIMULATION OF LIQUID ROCKET ENGINE INJECTORS
Part 1. SIMULATIONS OF THE RCM-1 EXPERIMENTS

Richard Farmer & Gary Cheng
SECA, Inc.

Yen-Sen Chen
ESI, Inc.

In the course of developing a practical CFD model for simulating the many injector elements in a full-scale rocket engine, the wide variation in density and enthalpy was deemed to be of primary importance. The pressure based FDNS CFD code was modified to account for such variations. Very general thermal and caloric equations of state were developed for describing hydrogen, RP-1, and oxygen propellants over the range of pressures and temperatures expected. These thermodynamic equations, as well as the modifications needed to perform pressure iterations, are described in Part 3 of this paper. Such a CFD model would constitute a homogeneous simulation of a spray. While recognizing that this model does not account for thermal and velocity lag between drops and vapor, the model should represent supercritical jet flows very well.

The supericritical cryogenic injection experiments (RCM-1) are exactly the type needed to verify and tune the CFD model. The turbulence model used in the CFD code should be tuned to match appropriate test data. If the turbulence model alone is not adequate to match the data, a finite-rate equation could be used to delay vaporization by approximating inter-phase transport processes. The RCM-1 simulations discussed in the following are our first step in this tuning process.

The LN2 cases, RCM-1-A and -B, were simulated with the homogeneous spray model. The flow predicted resembles a dense fluid jet with strong density gradients in the shear layer. Such a flow has been observed in a similar super-critical nitrogen jet experiment reported by Chehroudi, et al[1]. These predictions should compare well to the DLR experimental data. If the comparisons are not good, adjustment of the parameters in the two-equation k-ε or the initial turbulence level parameters could be made for a better fit of the data. Such tuning has not previously been made since appropriate test data were not available. For a definitive analysis of the experiments, conjugate heat transfer to the injector hardware and consideration of the duration of the experiment should be made. The jet is discharging into a gaseous nitrogen environment; the recirculated gas should become slowly cooled until a steady state is reached. Since the temporal variation of the recirculating gas temperature was not reported, the time that the CFD simulation should be terminated can not be determined. Since the measurements were made very close to the injector exit, good simulation of the gas temperature might not be crucially important.

The injector configuration and flow conditions for the cryogenic nitrogen jet of the RCM-1 test cases are illustrated in Fig. 1. It can be seen that the chamber pressure for both cases is above the critical pressure of nitrogen. A 101x11-mesh system was used to discretize the injector section, while the chamber section was modeled by a 301x101-mesh system for Case RCM-1-A.. The same grid system was used to simulate both RCM-1-A and RCM-1-B test cases. The numerical result of RCM-1-A test case at the locations specified by IWRCM was plotted as shown in Figures 2-6.

1

Notice the temperature profiles in Figure 4. These two cold flow cases are not steady-state, although the simulations assumed this to be the situation. The simulations presented represent a time-slice at some arbitrary time. Figure 7 shows the flowfield near the injector tip. A finer grid system (101x15, and 301x141) was employed to simulate the RCM-1-B. The numerical results of RCM-1-B test case are plotted in Figures 8-12. The flowfield is presented in Fig. 13. Notice that only a small segment of the chamber is shown so that the gradients in the flowfield may be clearly seen.

REFERENCES

1. Chehroudi, B., et al, "Initial Growth Rate and Visual Characteristics of a Round Jet into a Sub- to Supercritical Environment of Relevance to Rocket, Gas Turbine, and Diesel Engines," AIAA 99-0206, 1999.
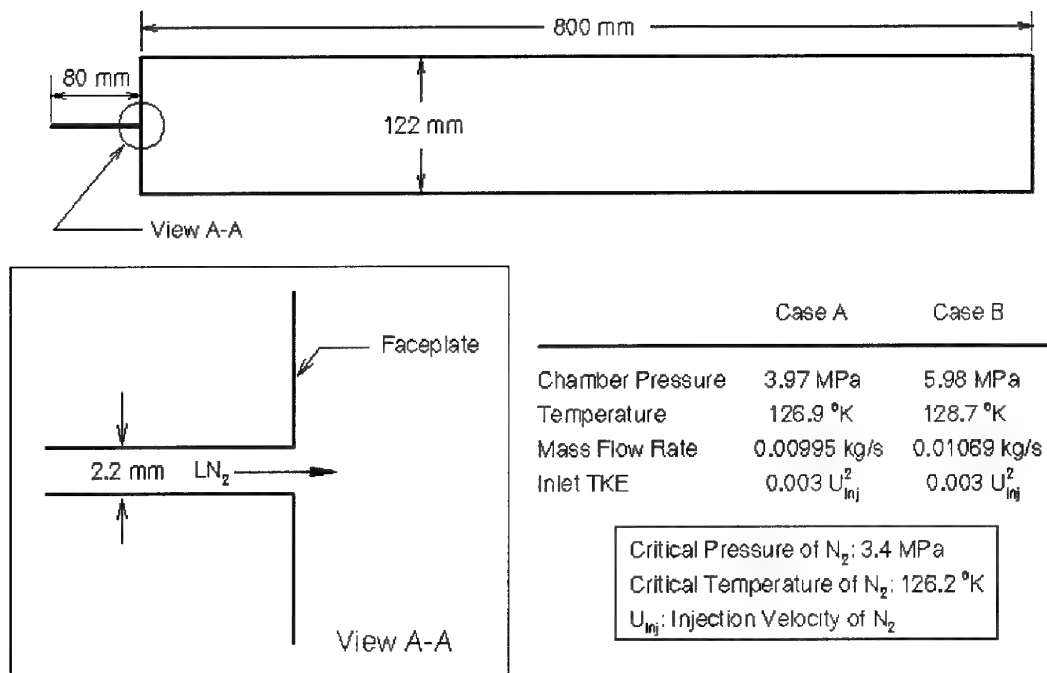
Figure 1. Configuration of RCM-1 Test Case.

Figure 2. Flow Properties at the Injector Exit of RCM-1-A.

Figure 3. Density Profiles at Various Streamwise Locations of RCM-1-A.

Figure 4. Temperature Profiles at Various Streamwise Locations of RCM-1-A.

4

Figure 5. Axial Velocity Profiles at Various Streamwise Locations of RCM-1-A.

Figure 6. Turbulent Kinetic Energy Profiles at Various Streamwise Locations of RCM-1-A.

5

Figure 7. Flow Properties Near the Injector of RCM-1-A.

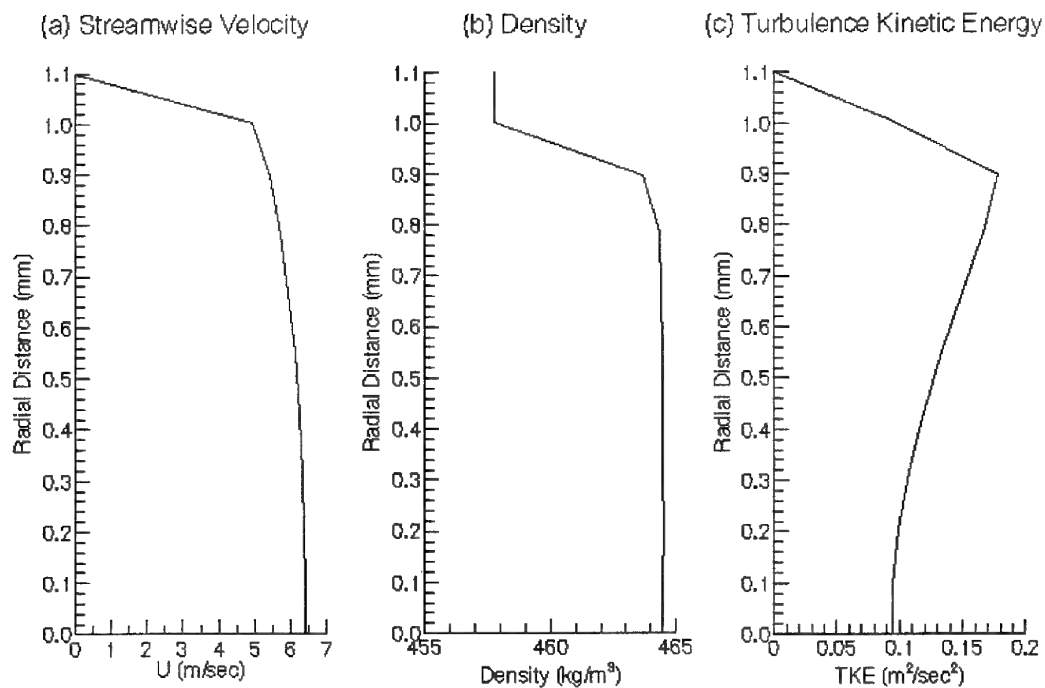(a) Streamwise Velocity   (b) Density   (c) Turbulence Kinetic Energy

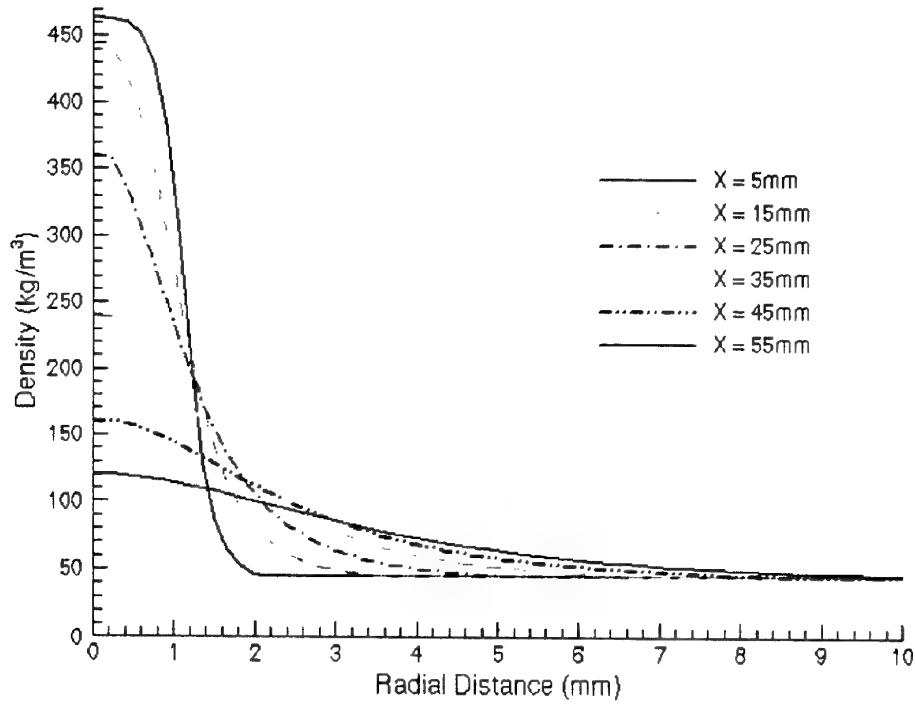Figure 8. Flow Properties at the Injector Exit of RCM-1-B.

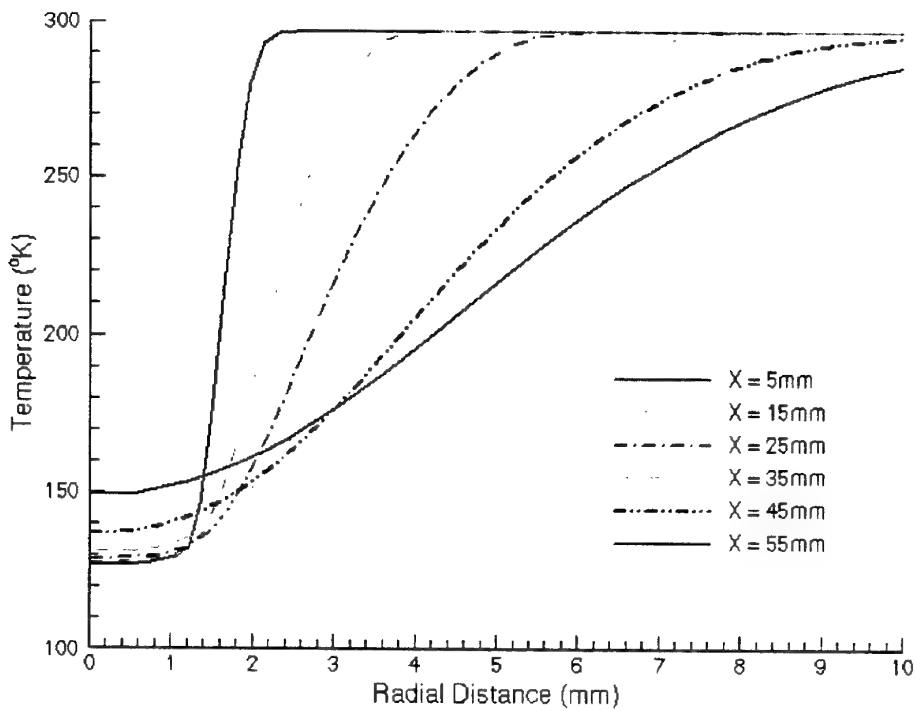Figure 9. Density Profiles at Various Streamwise Locations of RCM-1-B.

7

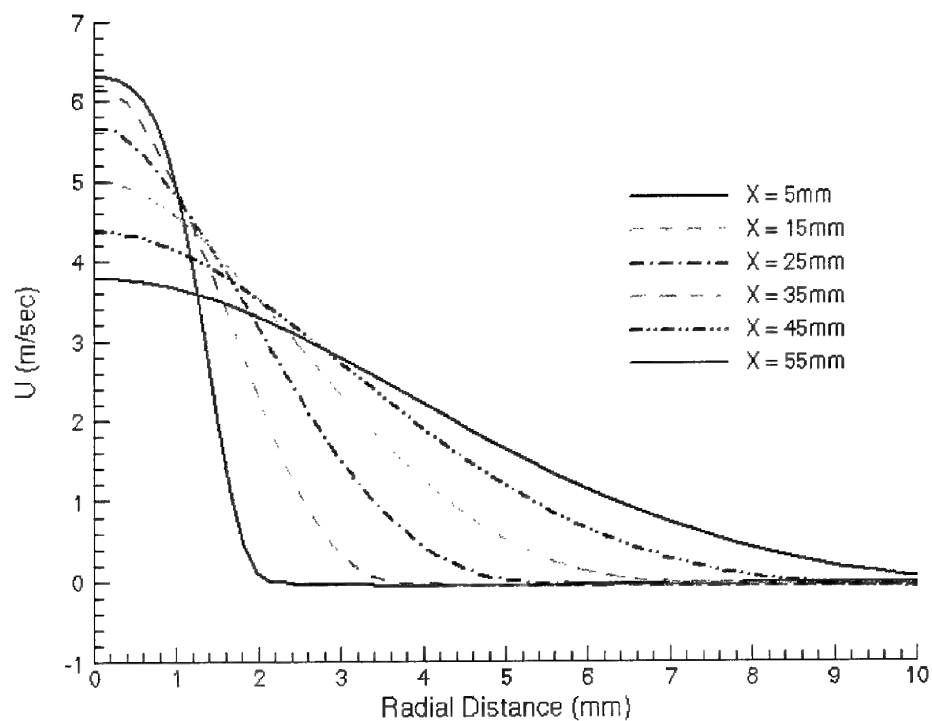Figure 10. Temperature Profiles at Various Streamwise Locations of RCM-1-B.

Figure 11. Axial Velocity Profiles at Various Streamwise Locations of RCM-1-B.
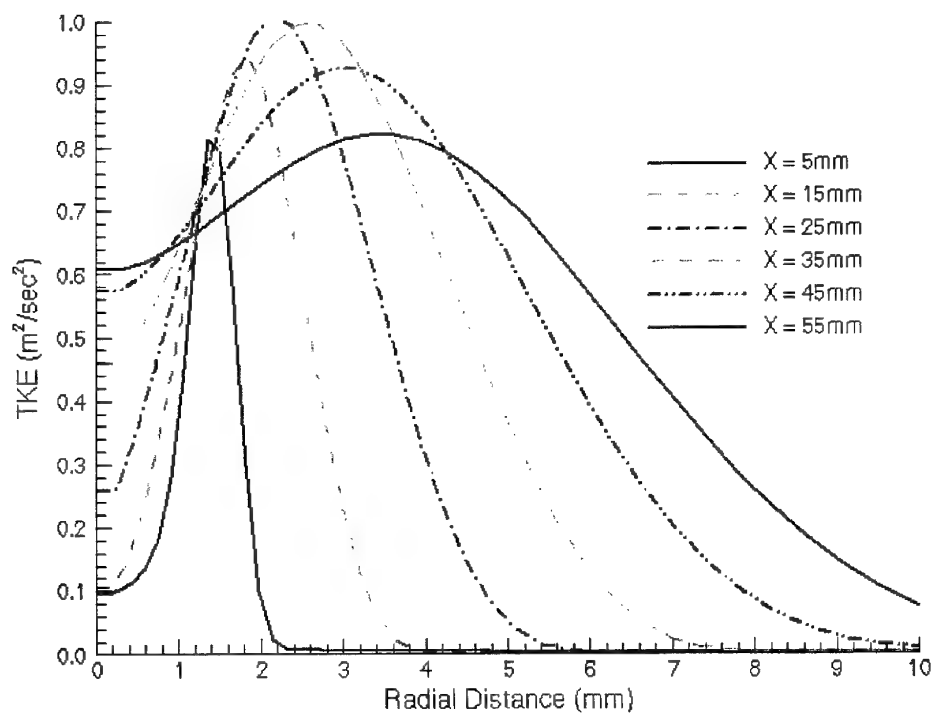
8

Figure 12. Turbulent Kinetic Energy Profiles at Various Streamwise Locations of RCM-1-B.
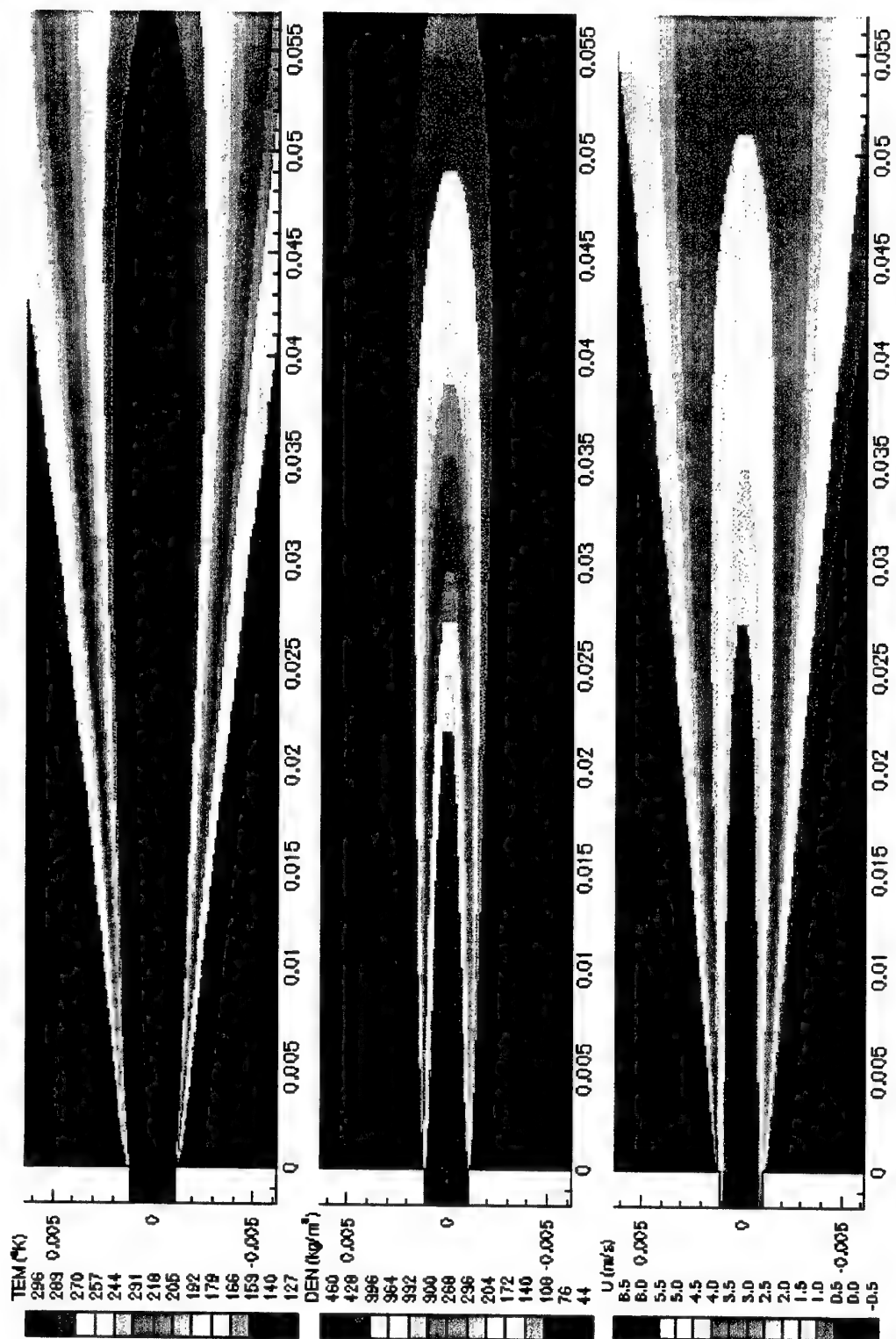
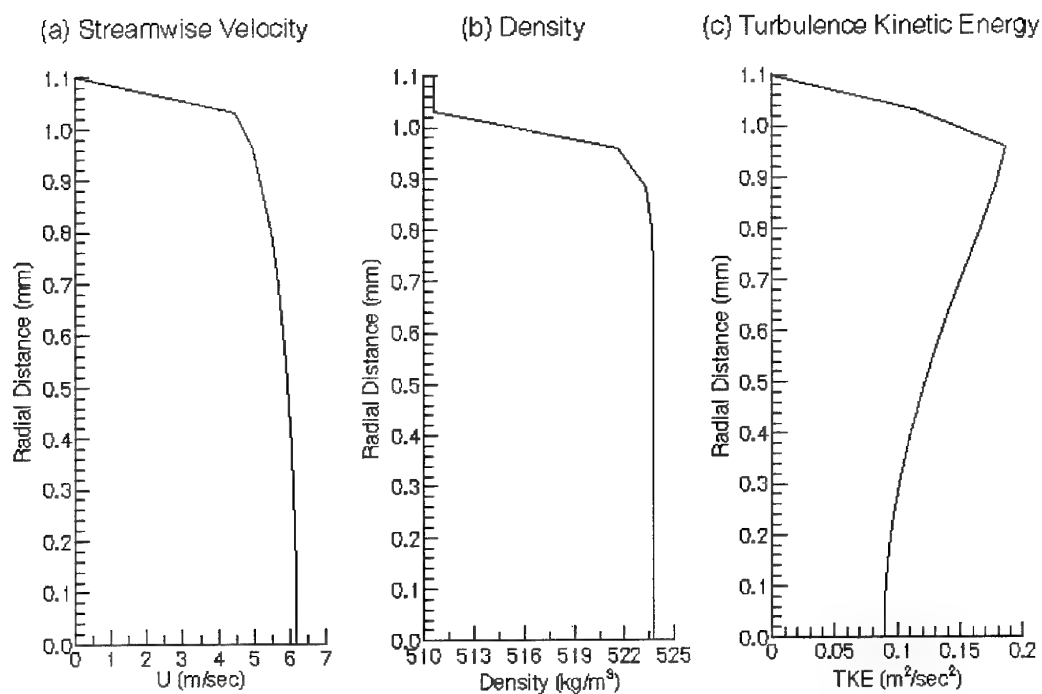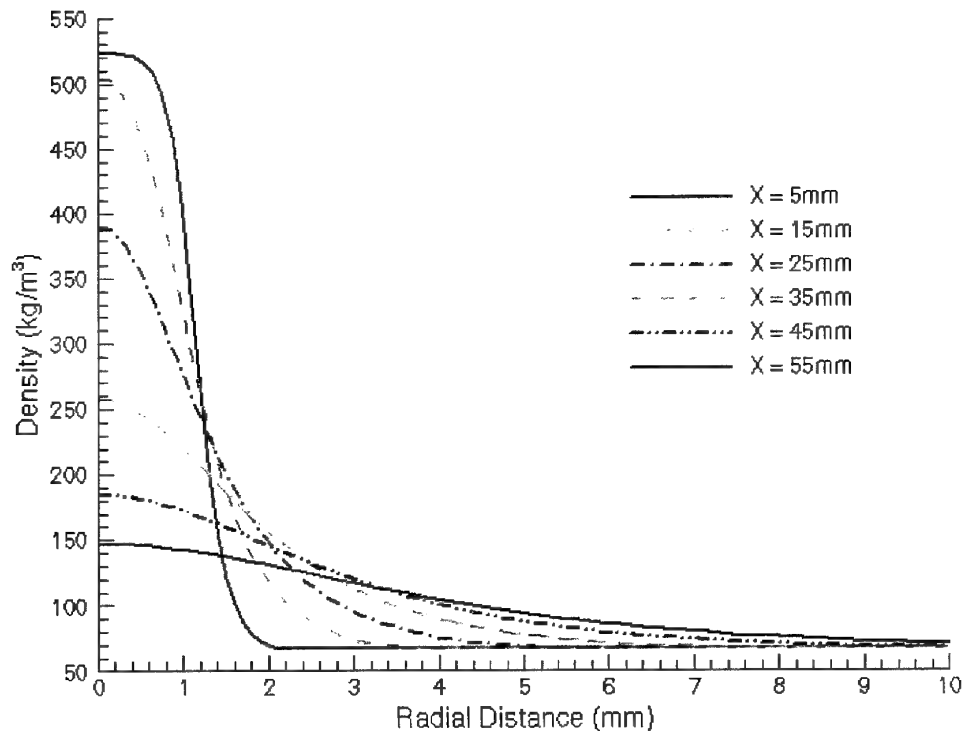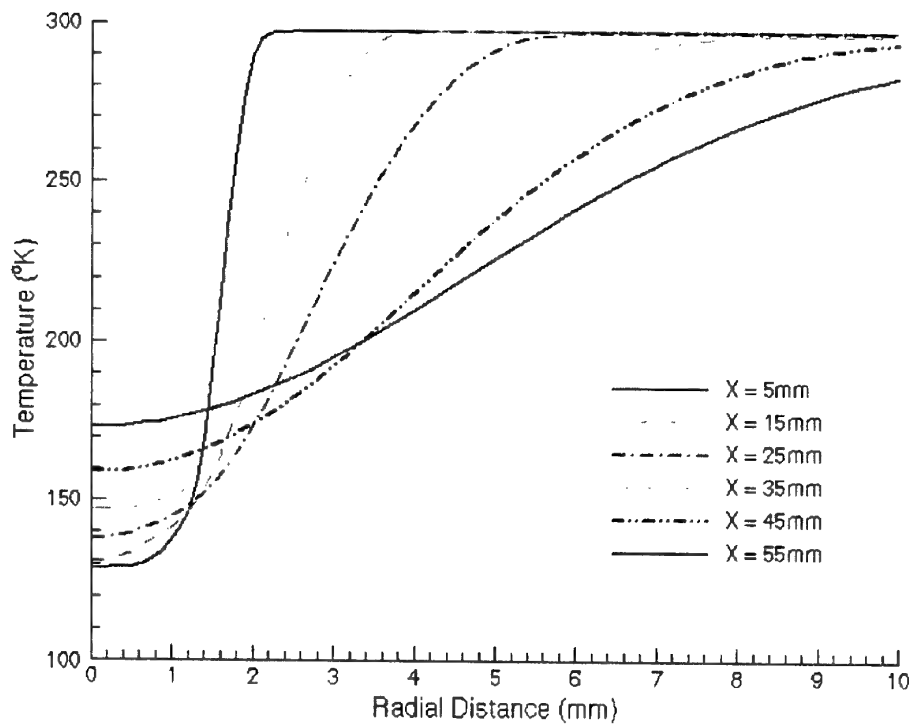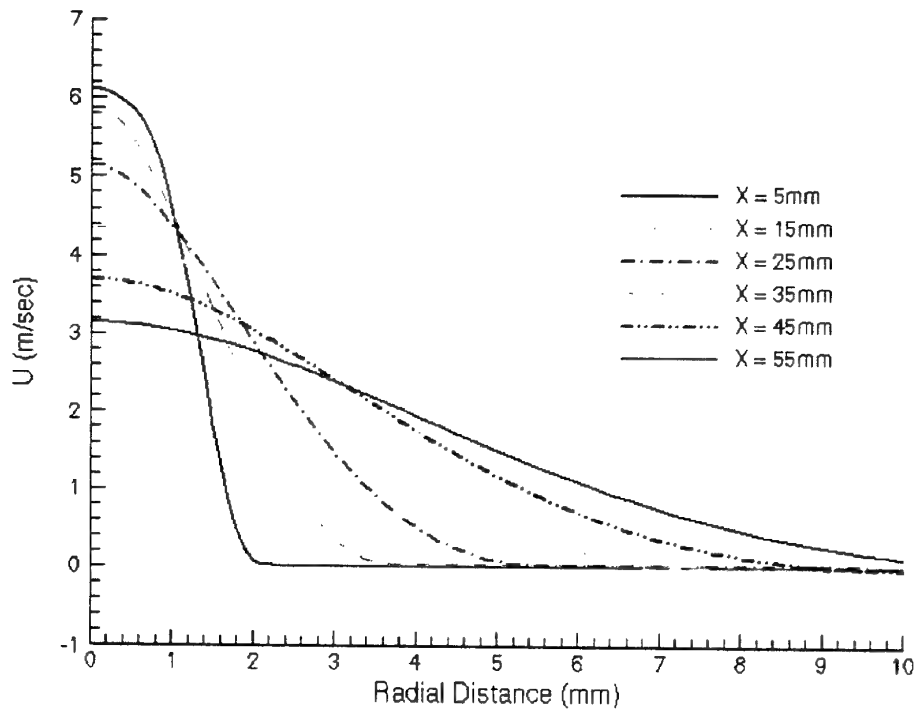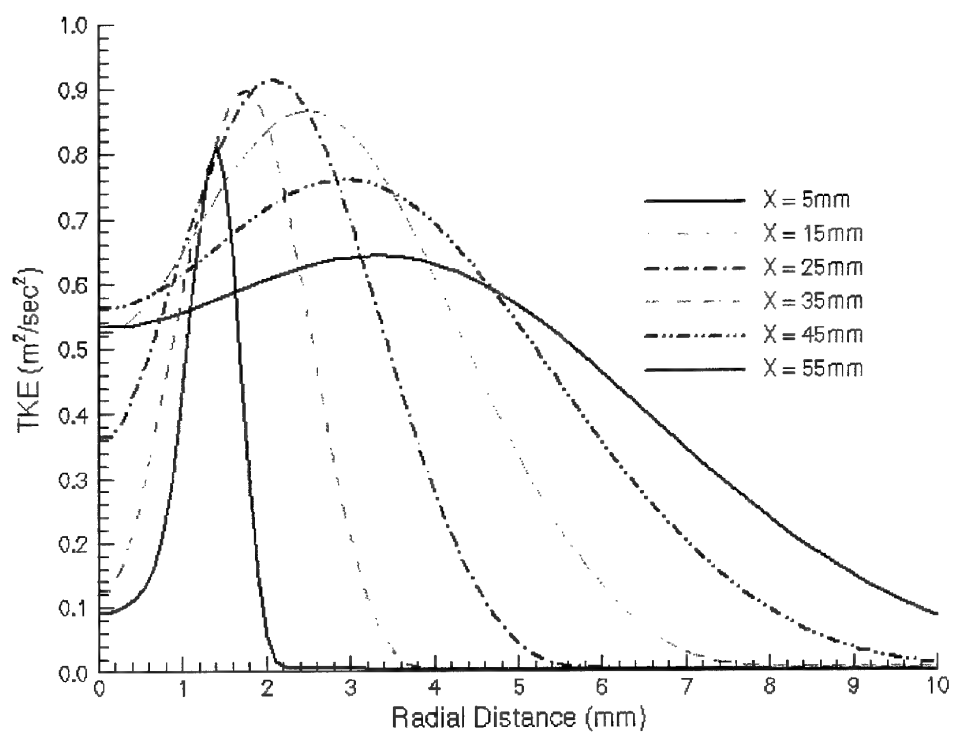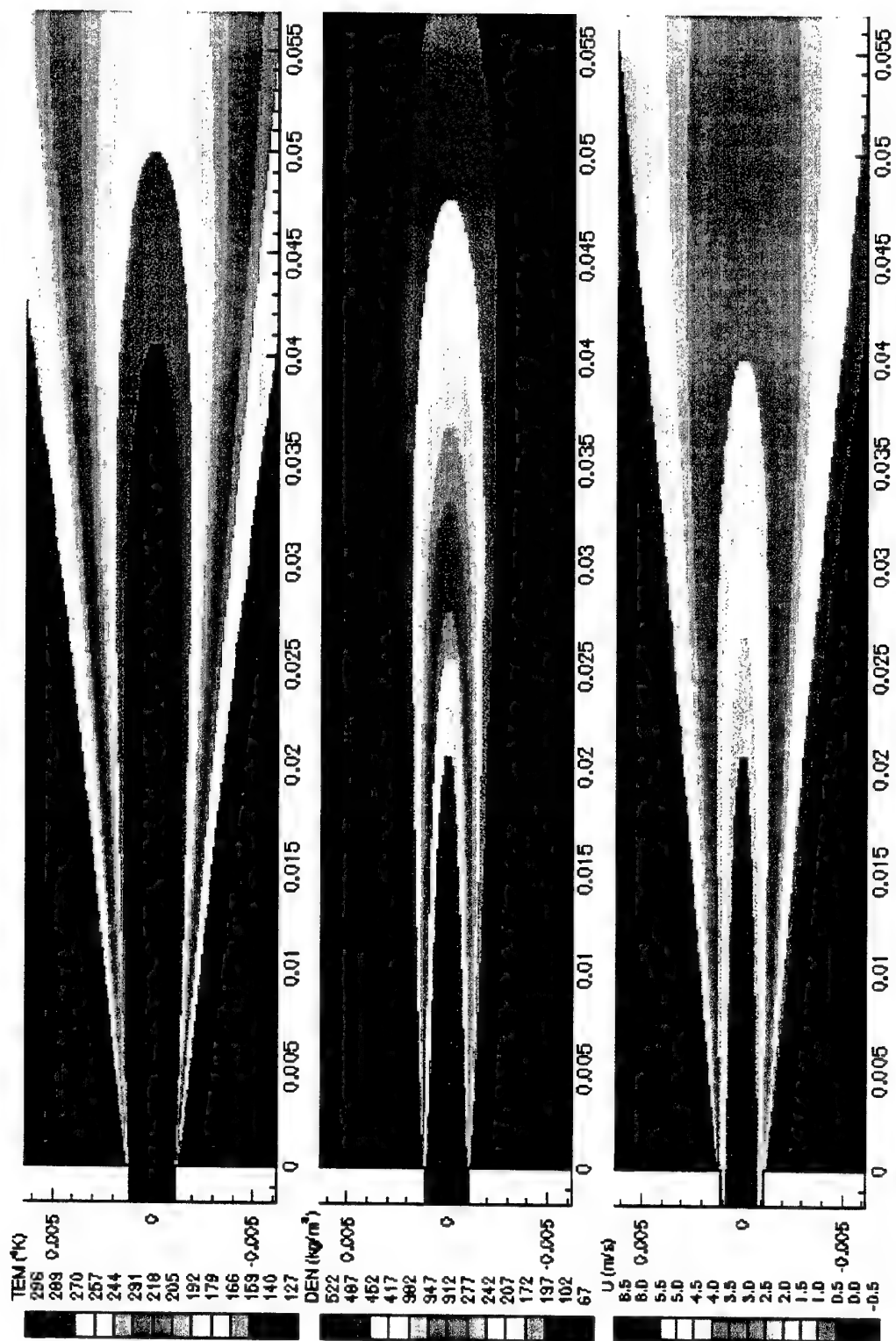Figure 13. Flow Properties Near the Injector of RCM-1-B.

Simulation of Cryogenic Jet Injection, RCM 1

R. Branam*, J. Telaar° and W. Mayer°

*Air Force Research Laboratory, Edwards AFB
German Aerospace Center (DLR), Space Propulsion Institute, Lampoldshausen

Abstract

Understanding the complex environment of the rocket chamber involves good knowledge of the injection phenomena. Understanding the injection phenomena allows the rocket designer to employ time and cost saving modeling tools to design a higher performance rocket engine. The rocket engine performance is highly dependent on the injection processes within the chamber. This project looked at injection processes in the supercritical régime of the injected fluid, cryogenic nitrogen, in order to better understand realistic conditions in the rocket engines of today. The investigation considered test conditions from 4.0 to 6.0 MPa at two different injection velocities and temperatures. For the RCM-1-A and RCM-1-B cases, the target test conditions are 5 m/s injection velocity and 120 K injection temperature. RCM-1-A is at 4 MPa and RCM-1-B is at 6 MPa. Experimental data taken by Raman imaging and Shadowgraphy were compared to computational models for these various test conditions. The test data allows comparisons of density, length scales and jet spreading angles. The results validate the computational models and agree with classical theory.

Introduction

There is much interest in high pressure combustion for the production of high power energy conversion and thrust. This is found in diesel engines, gas turbines, and, in particular, rocket engines. These high pressures often exceed the critical pressures of the injected fuel and/or oxidizer. Understanding the complex environment of the rocket chamber in order to get the most power out of it requires a good understanding of the injection phenomena. This understanding allows the rocket designer to employ time and cost saving modeling tools to better design a higher performing rocket engine. Much work has been accomplished in this area as can be seen in references [1, 2, 3] and [4], but a strong understanding of the injection process and the development of reliable modeling tools still requires much work. This work takes a step in this direction by looking at cryogenic injection at pressures above the critical pressure and modeling of this flow[5]. A more complete discussion of this effort including further testing conditions can be found in reference [6]. The comparison between measured and calculated values provides some insight as to the reliability of the modeling effort and behavior above critical pressures.

Problem

This investigation looks at the behavior and properties of a cryogenic, axisymmetric jet in a supercritical environment. The experiment injects liquid nitrogen above the critical point (3.39 MPa) through a single injector into a chamber filled with ambient temperature gaseous nitrogen. The experimental conditions look at the effects of pressure, temperature and injection speed of the liquid nitrogen into the chamber. The targeted testing conditions are injection values of 5 m/s and 120 K and RCM-1-A, 4 MPa; RCM-1-B, 6 MPa. Actual injection conditions are determined from previous experiments to determine temperature variation along the injector tube and calculated in the computational models based on these experiments. At these conditions, Raman and Shadowgraph images were taken encompassing the area from the injector to 60 mm (approximately 30 injector diameters) from the injector. The pictures were used to determine density distributions, jet spreading angles and length scales. These measured values were compared to computational models for each of the cases.

Cryogenic Jet

A jet flow has three distinct zones: potential core, development or transition region, and a similarity region as seen in Figure 1. The potential core contains some portion consisting of only injected fluid and reduces in thickness as the jet mixes with entrained fluid from the surrounding environment.
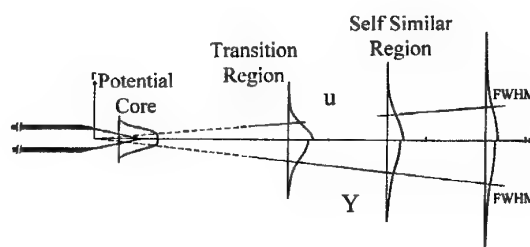
Figure 1: Jet mixing flow field

After the potential core region, the jet is in a transitional state which is considered the region of turbulent mixing for a jet. In this region, the energy dissipation and the jet behavior tend to be of the highest interest for mixing purposes. Researchers have indicated the most significant influences on jet development include the velocity ratio between initial jet velocity and the surrounding environment (u_o/u_∞) s and the density ratio (ρ_o/ρ_∞). These parameters show how the momentum and thermal energy dissipates from the jet into the flow field.

At some distance from the injection plane, the jet becomes self similar. This means a function of only one variable can express the flow field profiles as no longer varying in the axial direction. Schetz[7] stated this to occur at approximately $x/d \geq 40$, while others have indicated for

similar jets, velocity profiles exhibit self similar behavior as close as x/d ≥ 20 (Schlichting[8]). Other parameters such as turbulence intensities (u', v', w') may not show this behavior until well after x/d ≥ 200. Also, the particular variable employed to show self similar behavior varies between researchers.

Incompressible Jet

At pressures above the critical pressure and near critical temperatures, changes in the temperature can correspond to extreme density gradients. For this reason, real gas effects must be taken into account when determining flow properties. Since pressure is relatively constant, this density gradient is only dependent on temperature. The experiment considers the density to be incompressible or weakly compressible according to the classical definition of compressibility. By using a real gas relationship for density, coefficient of specific heat at constant pressure and viscosity, the computational model captures the effects of being weakly compressible when employing an incompressible solution technique. This relationship also defines a very strong relationship between temperature and density. The expected results for temperature and density in radial and axial profiles in the flow field are related but the relationship is not linear.

Turbulent Prandtl Number Considerations

Schetz[7] showed the value of the Prandtl number actually varies with radial location but on average is 0.7 for similar axisymmetric submerged jets. The evidence from Pabst[9] and Sakipov[10] calculated values ranging from 0.4 to 1.7 for various fluids and locations. Also, most modeling codes use values of 0.89 or 0.9 as the default value (Wilcox[11], CFD ACE manual[12]). Values less than one correspond to thermal energy dissipating in the flow quicker than momentum energy due to turbulent mixing. The resulting non-dimensional temperature profiles would then be wider in comparison to the non-dimensional velocity profiles. According to White[13], the value should be greater than 0.7 and suggests 0.9 or 1.0. Although this parameter varies over the radial profile of the flow, it is common to choose a constant value for the entire flow field. The solutions for RCM-1-A employed Prandtl number values of 1.0 (White) and 0.7 (Schetz) as defined by the following equation.

$$Pr_T = \frac{\nu_T}{\kappa_T / \rho c_p}$$

A constant value provided good results in these computational models. The results are further discussed later, but $Pr_T = 1.0$ proved to be more consistent with our experimental density data and was used. It also allows the results to show thermal influences due to the changes in the coefficient of thermal heat transfer under these temperature and pressure conditions without large influences caused by numerically induced turbulent energy transfer.

Property Value Comparisons

Non-dimensionalizing the flow properties for the radial profiles makes it possible to compare the data for the different testing conditions as follows.

$$\rho^* = \frac{\rho - \rho_c}{\rho_c - \rho_\infty} \qquad u^* = \frac{u}{u_c}$$

The c subscript refers to the centerline or maximum value for the profile and the infinity designates the environmental values. By this method, the profiles are 1.0 at the centerline and zero outside the jet itself. Non-dimensionalizing length measurements uses the jet diameter (d), Full Width Half Maximum (FWHM) values $(r_{1/2})$, and axial location as indicated.

The results compare the property profiles at axial locations of x/d = 0, 1.2, 5, 10, 15, 20, and 25. Measured values at x/d = 0 are not possible due to the reflection of laser light at these locations. The flow properties are also compared and investigated in the axial direction. Density and velocity are of particular interest. These employ similar relationships to the radial comparisons with one difference. The non-dimensionalization of these parameters uses the injection conditions (ρ_o, u_o) rather than the local centerline values as shown in the following equations.

$$\rho^+ = \frac{\rho - \rho_c}{\rho_o - \rho_\infty} \qquad u^+ = \frac{u}{u_o}$$

Jet Divergence Angle

The jet divergence angle seems to be one of the most highly considered parameters for jet flows. It lends itself to be easily measured and compared with other results. Chehroudi et. al.[14] provided a comparison of many different empirical models with available test data under various conditions. Of particular interest to this experiment were the models put forth by Dimotakis[15] and Papamoschou-Roshko[16]. Dimotakis investigated the entrainment of mass flow into the growing shear layer of a free jet. He proposed a vorticity growth rate equation seen below depending on velocity and density ratio between the fluid flows. For these testing conditions, the velocity ratio is zero, simplifying the following equation considerably.

$$\delta_\omega = 0.17 \left\{ \frac{\left(1 - \frac{u_\infty}{u_c}\right)}{\left[1 + \left(\frac{\rho_\infty}{\rho_o}\right)^{1/2}\left(\frac{u_\infty}{u_c}\right)\right]} \right\} \left\{ 1 + \left(\frac{\rho_\infty}{\rho_o}\right)^{1/2} - \frac{\left[1 - \left(\frac{\rho_\infty}{\rho_o}\right)^{1/2}\right]}{\left[1 + 2.9 \frac{(1 + u_\infty/u_c)}{(1 - u_\infty/u_c)}\right]} \right\}$$

Papamoschou and Roshko proposed a visual thickness equation for incompressible, variable-density mixing layers while studying the turbulence and compressibility effects in plane shear layers. This relationship uses a convective velocity definition to relate the difference in the flows. The experimentally determined constant (0.17) allows results to be compared with axisymmetric jet flows. Again, since the velocity ratio for this effort is zero, the relationship simplifies considerably.

$$\delta'_{vis} = 0.17 \left(1 - \frac{u_\infty}{u_o}\right) \frac{\left[1 + \left(\frac{\rho_\infty}{\rho_o}\right)^{1/2}\right]}{\left[1 + \left(\frac{u_\infty}{u_o}\right)\left(\frac{\rho_\infty}{\rho_o}\right)^{1/2}\right]}$$

Various methods could determine the spreading angle from the computational models. Direct evaluation of the edge of the shear layer using a 0.99 roll-off point for temperature, density, and velocity provides a simple

method to accomplish this task. This method can be compared with values determined using a FWHM approach. The edge of the shear layer is difficult to determine from Raman images, so the procedure determines the location of half the maximum value. The procedure is to multiply the value by two as suggested by Chehroudi et al.[14] to compare with visual techniques such as the results from the Shadowgraph images. A similar approach for the computational models also calculate FWHM values to use as a comparison for the Raman results. The Shadowgraph images allow direct determination of the angle. These pictures clearly show the edge of the shear layer.

Experimental Setup

Figure 2 shows the pressurized chamber with the injector used in the experiments presented in this paper along with the boundary conditions assumed for the model. The diameter of the injector is 2.2 mm and the length to diameter ratio is greater than 40 (Figure 3). The chamber can be pressurized up to 6 MPa and is equipped with an electronic heater to keep the wall temperature constant. Optical access to the chamber is provided by four windows. Cold nitrogen is injected into a warm nitrogen environment under different ambient and injection conditions. The temperature of the injected fluid can vary from 100 to 140 K, the injection velocity ranges from 1 to 10 m/s, and the ambient pressure can be as high as 6 MPa.

The temperature of the injected fluid is generally measured at position 1 (T1, Figure 3). Since the test setup includes no temperature regulation system, the injection temperature is varied by starting the injection at the ambient temperature of the injector and the piping. During injection, the piping and the injector cool down while the injected fluid heats up. When the temperature of the injected fluid reaches its targeted value, the experiment records the Shadowgraph or Raman images. Since the time required to take the images is small compared to the time the injector needs to cool down, the project assumes quasi steady state conditions.
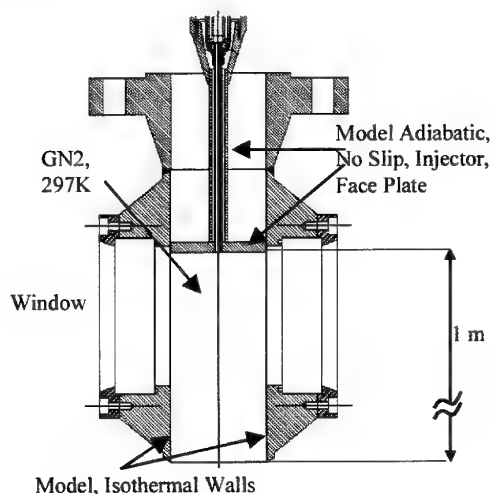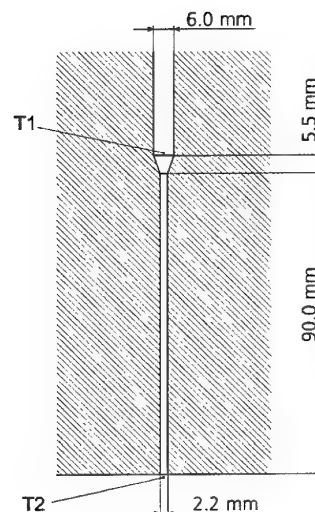

Figure 2: Test chamber

Figure 3: Injector

The Raman and Shadowgraph images taken were processed to produce density, length scales and spreading angles to compare to the modelled test conditions. This procedure is reported in reference 6.

Modeling

The model for this multi-physical problem bases itself on a straight forward computational approach. The flow field calculations employ directly the Navier-Stokes equations for incompressible flow. Since the test conditions are in the supercritical regime for nitrogen, real gas nitrogen properties are necessary. For this requirement, the model employs the Lee-Kessler[17] and Chung[18] model built into the CFD-ACE software. The model density results were compared to Younglove[19] to ensure accuracy of the input property data. Without high velocity and the use of real gas properties, it is possible to employ the incompressible solution scheme and still take into account the variable density. The model focuses on a steady state solution to determine average property distributions for this injection experiment. The orientation of the injector also allows the assumption of negligible body forces. A look at the calculated Grashof, Froud, and Reynolds numbers for this experimental range shows the inertial forces to be the most significant with buoyancy and viscous forces somewhat less reinforcing this assumption. Therefore, the classical flow equations for this problem are as follows:

Continuity

$$\frac{\partial}{\partial x_j}\left(\rho u_j\right) = 0$$

Momentum (Navier-Stokes)

$$\frac{\partial}{\partial x_j}\left(\rho u_i u_j\right) = -\frac{\partial P}{\partial x_i} + \frac{\partial}{\partial x_j}\left\{\mu \frac{\partial u_i}{\partial x_j} + \frac{\partial u_j}{\partial x_i} - \frac{2}{3}\mu\frac{\partial u_k}{\partial x_k}\delta_{ij}\right\}$$

Energy equation

$$\frac{\partial}{\partial x_j}\left(\rho u_j H\right) = \frac{\partial}{\partial x_j}\left(K\frac{\partial T}{\partial x_j}\right) + \frac{\partial u_i}{\partial x_i}\left(\tau_{ij}u_j\right) - \frac{\partial}{\partial x_j}\left(J_{ij}h_i\right)$$

Modeling these equations directly is very difficult and is only practical for simple flow situations. For this reason, the density averaging technique derives a time averaged solution by using an average value and fluctuation to replace actual flow parameter values. This relationship produces a workable equation set called Favre Averaged Navier-Stokes (FANS) and can be found in Cebec and Smith[20] as well as many other texts.

The FANS introduces the Reynolds stresses to account for turbulence in the flow. While several methods exist to estimate these values, the k-ε model seems to be the most appropriate. This method has shown much success in similar problems and reduces calculation times. The model calculations used this high Reynolds approximation in the flow and semi-empirical calculation techniques to determine flow parameters next to the wall. In the boundary layer the viscous forces are much greater than shear forces, Launder and Spalding[21]. The temperature calculation for the heat transfer is treated in a similar manner. The program discretized the governing equations using a third order accurate scheme to capture the large density gradients and damped with first order upwind discretization to maintain stable mathematical computations in the CFD-ACE software package[12].

The software package takes into account the contribution of heat and mass transfer from the turbulence by use of a turbulent Prandtl and Schmidt number. The heat transfer module solves the total enthalpy form of the energy equation as shown.

$$\nabla \bullet \left(\rho \vec{V} h_{,,}\right) = \nabla \bullet \left(k \nabla T\right) + \frac{\partial\left(u\, \tau_{,,}\right)}{\partial x_{,}}$$

The calculation of an effective conductivity (K_{eff}) value takes into account the turbulence effect. The following equation shows how the program uses a turbulent Prandtl number to accomplish this. By using the turbulent Schmidt number, the program handles the mass diffusion in a similar way to calculate an effective diffusion coefficient.

$$K_{eff} = K + \frac{v_{T}\rho c_{p}}{\mathrm{Pr}_{T}}$$

Grid

The computational grid used for this problem is a structured, 2-D, axisymmetric grid with just over 100,000 cells. The refinement in the injector region is critical and can be seen in Figure 4
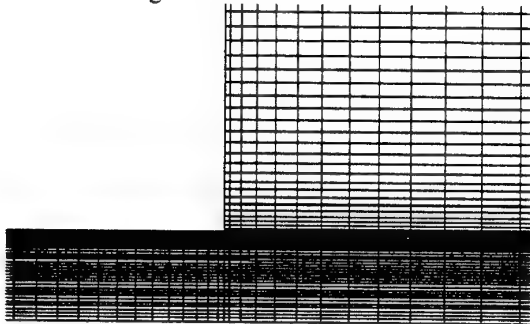

Figure 4: Grid

To show the solution is independent of this grid, the same conditions were calculated for Case 3 using several coarser grids. A grid with 85,000 cells compared well to the solution for the primary grid (100,000 cells). The agreement between the coarser grid and fine grid is very good. The axial density profile exemplifies this agreement (Figure 5). Therefore, the results are considered the same and the solution is independent of both grids. The finer grid was used for all the test conditions to ensure grid independence at the other testing conditions.
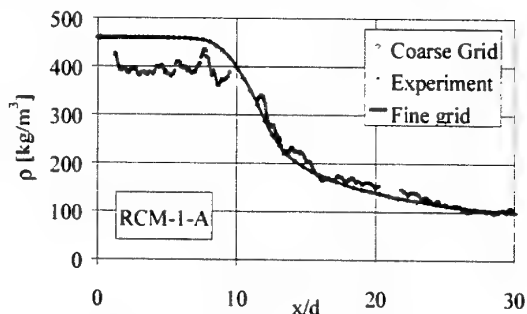

Figure 5: Density, 4 MPa, 5 m/s, 120 K

Boundary and Initial Conditions

The inlet and boundary conditions for this model are very important and extremely sensitive to temperature. The experiments include measurements to determine the influence of temperature on the actual temperature and pressure input values for the model. Measured mass flow, temperature and pressure determine the inlet conditions. From the measured values, initial inlet velocity, turbulent kinetic energy (k) and rate of dissipation (ε) are calculated and input to the model.

$$k = \frac{3}{2}\left(Iu\right)^{2} \qquad \varepsilon = \frac{C_{\mu}^{3/4} k^{3/2}}{0.014 l}, \quad C_{\mu} = 0.09$$

The Lee-Kessler-Chung real gas properties and measured mass flow for the test condition determine the inlet velocity from the density. For the inlet conditions, inlet velocity and an assumed turbulence intensity (for this model, 5%) determine k. The length scale (l) in the turbulent energy dissipation rate calculation is the inlet diameter (2.2 mm).

The outer wall of the chamber is isothermal to correspond to the character of the wall during testing. The actual test chamber has also shown some heat transfer to the nitrogen in the injector tube. To account for this in the model, the temperature determined at the chamber inlet is used as the injector tube inlet temperature. The boundary conditions used are then an adiabatic wall along the injector tube and the end of the chamber at the plane of injection into the chamber. This allows the temperature into the chamber to match experimentally measured values for these test cases. Also, to take into account turbulence contributions to thermal and momentum energy transfer, the turbulent Prandtl number is set to 1.0. This value corresponds to Reynolds contention of turbulent-momentum flux and heat flux being of the same order of magnitude (White[13]).

The model procedures calculate the outlet boundary condition based on total mass flow. The chamber is long

enough to consider the exit to be completely decoupled from the jet flow. Extrapolated calculations for the outlet did not take into account the mass flow being entrained in the jet from the chamber and therefore gave erroneous velocity. By establishing exit velocity as a fixed value, the calculations could account for this problem and smoothly resolve the jet flow realistically. The initial conditions for the calculations are simply set to the outlet boundary conditions, low velocity at ambient temperature and chamber pressure, Figure 2.

Convergence

The models went through between 20,000 to 30,000 iterations for the various test cases in order to ensure convergence of the solution. Several are similar to previously run test conditions and used these final solutions as the initial conditions therefore requiring fewer iterations to converge. A mass flow balance performed by the program provides final proof of convergence. The difference between mass inflow and mass outflow show values more than five orders of magnitude smaller than total mass flow into the chamber. During the iterations, the procedure required the models to stop and mass flow calculations were performed to ensure proper inlet velocity values were being used. The inlet velocity was adjusted as appropriate and the result was 0.00% to 0.12 % variance between model calculated mass flow and measured mass flow.

Results

The comparison of the various effects on the injection of liquid nitrogen includes density and velocity profile comparisons. Experimental data (Raman and Shadowgraph images) provide us with information on density profiles, divergence angles and length scales to compare to our model results as well.

Density Profiles

When looking at the progression of the calculated density profiles from x/d = 1.2 to x/d = 25, the graphs show the development of the flow as it moves toward a self similar solution. Figure 6 from RCM-1-A exhibits this trend seen at these testing conditions. The profiles closer to the injector show a flat region ($\rho^* = 1.0$) near the center line ($r/r_{1/2}= 0$) which eventually no longer exists at x/d ≥ 10. This corresponds to the potential core. Even though some of the testing cases show little potential core in the measured data, the models calculated core lengths for each testing condition. This results from the quality of the Raman images. The Shadowgraph images show a definite potential core in these regions and provide some validity to the model results.

The transition from a liquid-like jet behavior through the transition region to a fully gas-like jet behavior can be easily seen in the profile after $r/r_{1/2} = 1.0$. Following the progression of the jet using the density profiles from x/d = 1.2 to x/d = 10, the slope progressively increases. For the profile at x/d = 15, the slope has again dramatically decreased and the profiles after this axial location continue to decrease slightly and converge. The profiles for x/d = 20 and 25 very nearly share the same line. The experimental data has a considerable amount of variabil-

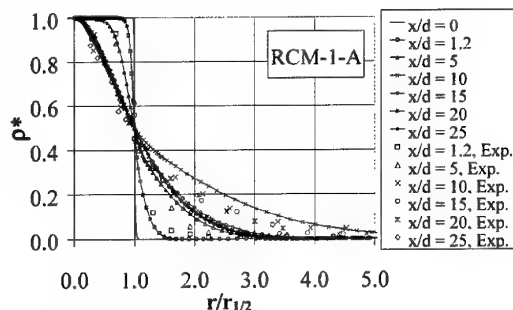ity (no error bars are shown for clarity) but follows the trend of the computational models.

Figure 6: Density; 4 MPa, 5 m/s, 120 K

Figure 7 shows another way to easily see the trend for the jet to move through the transition region and to the self similar region quickly. This figure presents density profiles (ρ^*) as a function of r/x, RCM-1-B.
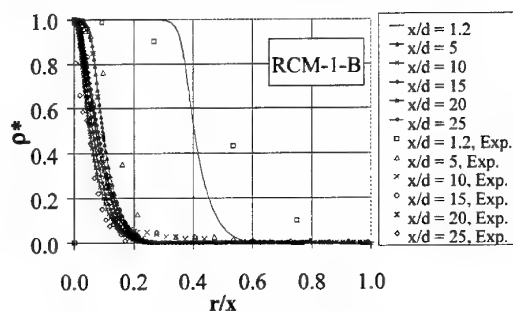

Figure 7: Density, 6 MPa, 5 m/s, 120 K

The effect of using axial position to normalize the profile radial position shifts the profiles very near the injector to the right and dramatically portrays the expected potential core (x/d = 1.2). As the profiles are plotted at intervals away from the injector, the density properties show similar behavior as seen in Figure 6. The slope for the entire profile increases until x/d = 10 and then begins to decrease again. This is opposite to the behavior in Figure 6 due to the method of presenting the data but corresponds to the same phenomena. The jet has a high density core to an axial position near x/d = 10, it then goes through a turbulent transition and then begins to develop into a self similar jet flow. Figure 7 also shows the profiles at x/d = 20 and 25 do not collapse to the same line, therefore the relationship suggests the flow has not yet reached self similarity. The experimental data corresponds with this trend again. At x/d = 1.2, the very sensitive nature of using axial position to present radial profiles at locations very near the injector causes the difference between the model and experimental data.

In looking at the agreement of the density determined from the Raman images and the calculated model, Figure 8 shows a representative sample of a profile at x/d = 20 for RCM-1-A. The experimental deviation was calculated from the values used to get an average density at each location. This difference is a product of the averaging technique and the variability of the data. This figure shows a good agreement with the experimental values.
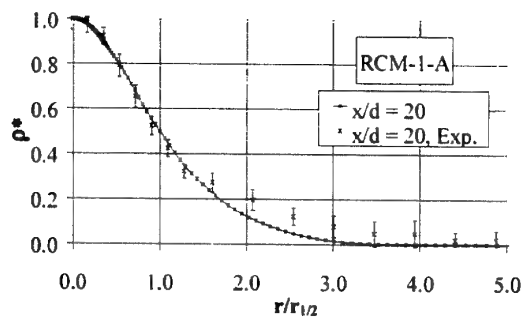
Figure 8: Density; 4 MPa, 5 m/s, 120 K

Velocity Profiles

The velocity profiles in the radial direction lend themselves to portraying jet development from the injection point to a fully developed condition better than density. With the flow inertially dominated, the expectation would be to see the velocity profiles developing rather quickly into self similar relationships. Figure 9, RCM-1-B shows the initial velocity to be a fully developed, turbulent pipe flow profile. It develops into a fairly self similar profile very quickly by x/d = 20 and 25. These profiles show the edge of the jet to be near $r/r_{1/2} \approx 2.5$.
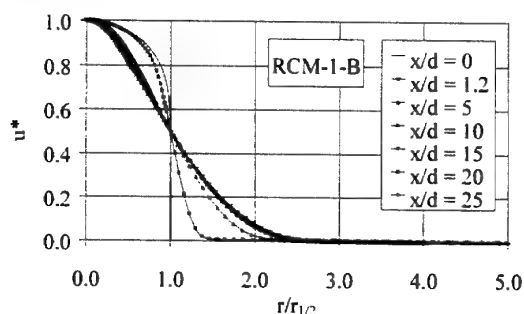

Figure 9: Velocity; 6 MPa, 5 m/s, 120 K

The velocity profiles of the flow develop much faster than temperature or density distributions for these modeled conditions. Figure 10 from RCM-1-A shows a typical representation of the velocity profiles as well. By x/d = 10, the jet appears to be nearly self similar although the jet is not fully developed as seen from the density profiles.
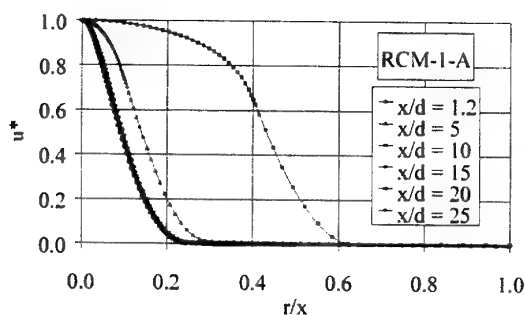

Figure 10: Velocity; 4 MPa, 5 m/s, 120 K

Centerline Density

The centerline density calculations prove to be useful in looking at several aspects of the jet. Primarily, this axial property relationship shows how the jet dissipates with distance from the injector. Observations of the axial density profile provide insight into the behavior of the jet as it moves through the various stages of a jet development. The experimental data also provides a means to compare the computational results with actual testing conditions. In Figure 11 Case 4, the computational results present a correlation with the experimental data, even though variability in experimental data makes it difficult to obtain exact agreement. If the temperature is below the peak in specific heat, the jet is very dense needing more energy to increase the temperature. Beyond this peak, the density ratio of ambient gas to injected fluid is higher than closer to the injector and the jet dissipates rapidly.
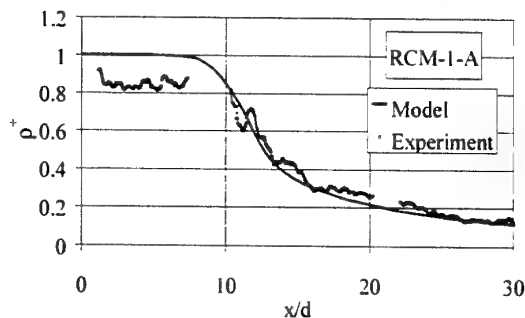
Figure 11: Density; 4 MPa, 5 m/s, 120 K

From Figure 11, the expected characteristics of the potential core are very obvious with the density ratio approximately constant until x/d ≈ 8. At this point, the density falls off fairly quickly but does not reach ambient values until much further downstream (x/d > 100). These profiles provide insight into the development of the jet through the various regions when viewed on a logarithmic scale as seen from Figure 12; the potential core, transition region and fully developed region.
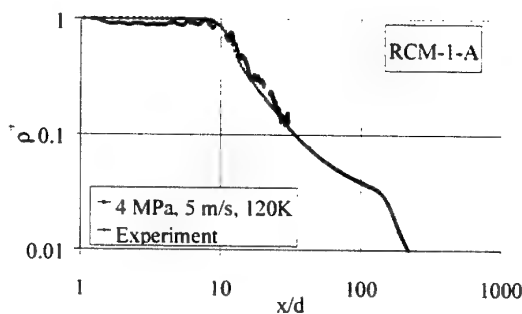
Figure 12: Density; 4 Mpa, 5 m/s, 120 K

Figure 12 shows the behavior of a jet (RCM-1-A) with a very dense core, the transition to a turbulent mixing zone and then into a fully developed region. The steep slope at x/d = 10 to approximately x/d = 30 shows the rapid transfer of both momentum and thermal energy. At this point in the jet flow, the density gradient is lower and the dissipation is also reduced suggesting a region of developed flow. At a point past x/d = 150, the density falls off quickly toward the chamber value suggesting the jet has almost completely dissipated. The model calculations show this location in the chamber to be the far edged of a recirculation zone established to transfer mass back to-

ward the injector. This mass is the mass entrained in the jet flow from the chamber.

Liquid Core Length

The centerline density is a power function of the axial distance from the injector. When plotted on a log-log scale, it is much easier to determine liquid core length and see the various regions of the jet. The location where the density begins to drop off rapidly determines the liquid core length (x_c/d). This location is easily seen in Figure 12. For these test campaigns, several other conditions were also tested and calculated. These testing conditions provide information at various density ratios. Figure 13 shows the comparison of these testing conditons for values of core length obtained from the calculated models against the Reynolds number relationship from Harsha and the relationship offered by Chehroudi. The two lines identify the range Chehroudi gave for the coefficient in his relationship. The calculated values agree better with the empirical gas relationship suggested by Harsha but tend to fall at or below the lower limit suggested by Chehroudi. The agreement of the core length calculations to a gas jet suggests the cryogenic jet under supercritical pressure behaves very similar to a gas jet.
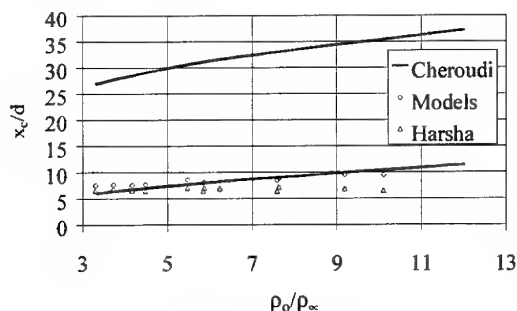

Figure 13: Core Length

Unfortunately, it is difficult to determine highly reliable values for the core length from the Raman and Shadowgraph images. Another observation of the relationship for the core length is the values appeared to be nearly linear over the range of Reynolds numbers and density ratios for these experiments.

Angle of Jet Divergence, α

The angle of jet divergence is determined from different methods. The computational models used two primary methods and applied each to velocity, temperature, and density. The first one uses the FWHM values and determines the spreading angle from these radial locations. As suggested by Chehroudi et al[14], the values are then multiplied by 2. The second one looks at the 99% roll-off point to determine the jet width. The computational models allow this point to be determined quite easily

The results show a considerable difference between the 50% method and the 99% values. When considering the possibility the FWHM location doesn't correspond to half of the jet width, another value for the 2x factor can be calculated. For velocity and temperature, this factor is approximately 2.5 which corresponds nicely with the radial profiles when using $r_{1/2}$ to normalize the radial

distance. In Figure 9, the profiles, beginning to show a self similar behavior, converge at $r/r_{1/2} \approx 2.5$ for the edge of the jet ($u^* \approx 0.0$). The relationship for the density is the same. In Figure 6, the profiles converge to an $r/r_{1/2} \approx 3.0$ and the value calculated from the model numbers is the same. This result can then be compared to the difference in the Raman and Shadowgraph methods since both techniques result from density relationships. The Raman images lend themselves to determining the FWHM values easier than finding the edge of the jet, while the Shadowgraphs show the edge of the jet fairly clearly.

From the Raman data, the FWHM difference between centerline and ambient density determines the jet spreading angle. Close to the injector exit, the centerline density is quite high and the jet is quite compact. Added to this, the temperature difference across the shear layer is small compared with the difference across the entire jet. The dense core of the jet therefore determines the FWHM instead of the shear layer. Therefore, the angle is small close to the injector when determined in the region $x/d \approx$ 0 to 10.

In the images for $x/d \approx$ 10 to 20 and 20 to 30, the jet warms up and dissipates. The centerline density is of the same order of magnitude as the density in the shear layer. Therefore, the FWHM location falls within the shear layer. Comparison with the computational results shows a fairly good agreement, Figure 14. For the coldest cases, the angles based on the FWHM are very small or even negative near the injector. For RCM-1-A, the minimum value for $r_{1/2}/d$ corresponds with the potential core length ($x_c/d = 9.52$). The conclusion then is the growth rate of the shear layer and the radial distance of the injected fluid moving away from the jet does not correspond to the angle measured from Raman data when the centerline density is significantly higher than the density in the shear layer and ambient gas (the region near the injector).
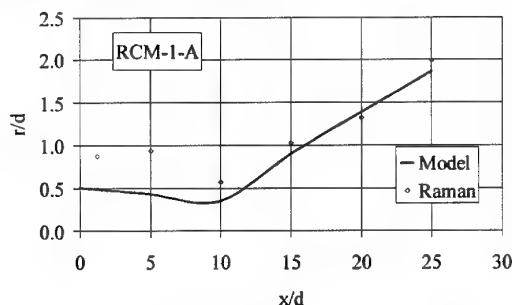
Figure 14: Density FWHM; 4 MPa, 5 m/s, 120 K

Looking at the computational model results and comparing them with the Shadowgraph values shows a slightly under-predicted trend. In the Shadowgraph images, regions are visible where the fluid is in turbulent motion causing local density gradients. The boundary of these regions at the quiescent ambient gas determines the jet spreading angle. A comparison to the angle from numerical calculations using the 99% roll-off point of the velocity shows good agreement.

Figure 15 shows how the models for various density ratios, Raman images and Shadowgraph images compare

with the relationships put forth by Dimotakis[15] and Papamoschou and Roshko[16]. Shadowgraph data was also added from testing conditions using an injector with l/d = 11.3 at sub- and supercritical conditions. The model calculations seem to agree fairly well with the Dimotakis relationship in this density ratio region. The variability of the averaged Raman data is fairly apparent in this figure. Even though there is also some variability in the Shadowgraph data, a relationship with the Dimotakis curve also seems apparent.

Data from earlier experiments is also included in Figure 15. The experiments at low density ratios (ρ_∞/ρ_0) show a significant influence of the Reynolds number. The Reynolds number depends on the increasing of the injection velocity. Correspondingly, the aerodynamic forces also and are sufficient to dissipate the jet. At increased density ratios, the jet dissipates even at low injection velocity and the Reynolds number has only a weak influence on the jet spreading angle.
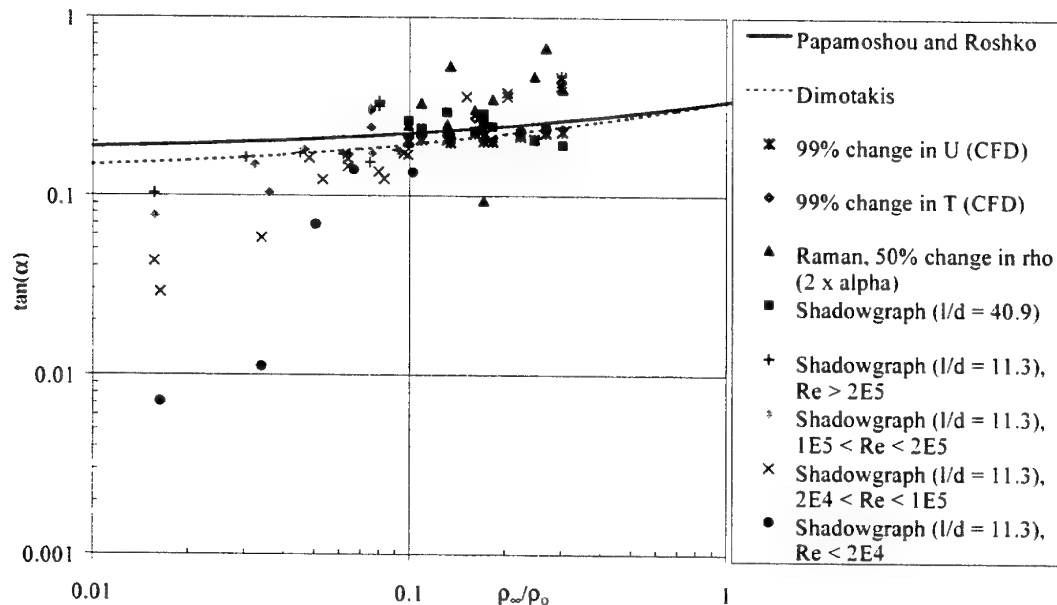

Figure 15: Jet Divergence Angle,

Length Scales

The Kolmogorov and Integral length scales are:

$$L_{kol} = \left[\frac{\nu^3}{\varepsilon}\right]^{1/4} \qquad L_{int} = \frac{k^{3/2}}{\varepsilon}$$

These values are highly dependent on the eddy viscosity method used for these calculations to model turbulence. The computational models calculated these values over the entire profile of the jet. At x/d = 5 (Figure 16, RCM-1-B), minimum values for the integral length scale (L_{int}) occur at the edge of the potential core flow and then again at the edge of the shear layer. The later location of r/d ≈ 1.4 corresponds to the edge of the jet based on 99% change for temperature and velocity.
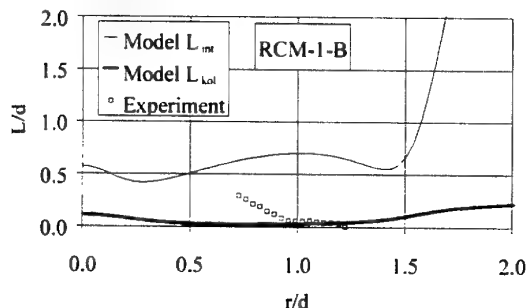

Figure 16: L_{int}, L_{kol} at x/d = 5; 6MPa, 5 m/s, 120 K

The Kolmogorov length scales tend to be slightly higher in the potential flow region and somewhat constant throughout the shear layer. Outside the shear layer, both length scales increase dramatically due to the chamber temperature but have little physical significance to the actual jet flow itself.

Figure 17 for RCM-1-B exemplifies a typical length scale comparison at x/d = 10. Since all cases show core lengths at approximately this location, the expectation would be no or little evidence of the first minimum in the integral length scale as seen in Figure 16. However, the graph shows some evidence of a potential core region. The reason is in this region the flow is in a high state of transition to a purely gas like jet flow. The second minimum at r/d ≈ 2.5 corresponds to the values calculated for the edge of the jet using temperature and velocity.

In both cases (Figure 16 and Figure 17), the geometric mean length scale determined from the Shadowgraphs shows a remarkably good comparison with the Kolmogorov length scale. Since these scales are the smallest expected eddies in the flow, these results are expected for a visual measuring technique. Measuring the integral length scales using this method is not possible since these structures also include all of the easier seen smaller length scales as well. The length scales closer to the center of the flow (r/d = 0) appear to increase slightly. For the colder flow fields (T = 120 K), the use of the Shadowgraph

images and the higher density gradients in this region cause the calculation technique to give larger values for the length scales near the centerline.
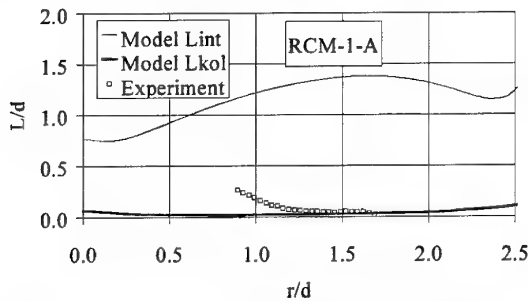

Figure 17: L_{int}, L_{kol} at x/d = 10; 4MPa, 5 m/s, 120 K

Turbulent Prandtl Number

The comparison of the results of two different turbulent Prandtl numbers for RCM-1-A, Figure 18 shows the better relationship for $Pr_T = 1.0$ when considering our experimental data for density. This data is comprised of three individual zones (x/d 0..10, 10..20, and 20..30 approximately). While the first region suggests a significant difference between the model and the measured data, the following two regions corresponded nicely with the model.

Since the relationship of the momentum and thermal energy dissipation defines the turbulent Prandtl number, a value of one would cause the velocity and temperature profiles to be very similar when non-dimensionalized. For values of turbulent Prandtl number less than one as in Figure 18, the similarity between the non-dimensional temperature and velocity would be less pronounced. Our experimental data compares better with an axial density profile when using $Pr_T = 1.0$. This suggests the turbulent momentum transfer is as important in explaining the state of the jet as turbulent thermal energy transfer as suggested by Reynolds (White[13]).
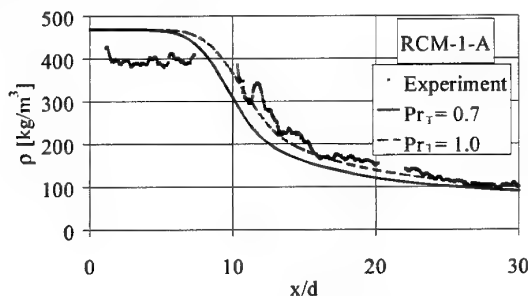

Figure 18: Density, 4 MPa, 5 m/s, 120 K

Pressure Influence

The different pressure conditions in the flow (4 and 6 MPa) show little impact on the behavior of the cryogenic jet since these pressure conditions are constant for the chamber and are all above the critical pressure of nitrogen (3.39 MPa). Figure 19 shows the axial density profile for Case 3 and Case 11, 120 K and 5 m/s. The Reynolds numbers and density ratios are very similar meaning the only significant difference is the pressure. The difference in temperature at the injector (T2) causes the slight variation between the two cases (Case 3, 126.9 and Case 11,

128.7K). At values so near the critical temperature of 126.2, this small variation influences the density significantly.
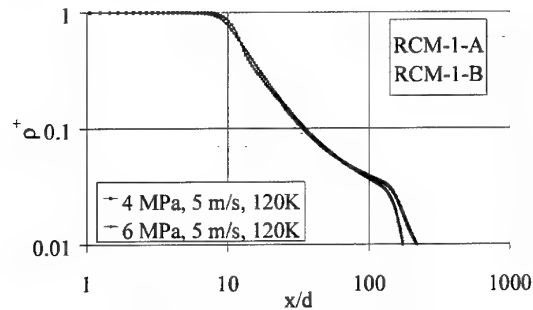

Figure 19: Density; 5 m/s, 120 K

The influence on the velocity field due to pressure differences also proves to be difficult to determine. Since the temperature and velocity values between the various test conditions vary somewhat (i.e. RCM-1-A, T = 126.9 K at u_{ave} = 5.72 m/s and RCM-1-B, T = 128.7 K at u_{ave} = 5.40 m/s), it is difficult to say the influence is only due to the pressure difference.

Conclusions

Understanding the complex phenomena of a supercritical injection flow field still requires a considerable amount of research, but this work provides some insights into several aspects of a rocket injector. This work accomplished this by examining a single injector using liquid nitrogen above the critical pressure. The various testing conditions considered pressures from 4 to 6 MPa at two target velocities (2 and 5 m/s) and a target injection temperatures of 120 K. The experimental data compares well with numerical results from these testing conditions. Agreement of the numerical results with density, length scales and jet spreading angles obtained from Raman and Shadowgraph images quantitatively validates them.

Under these testing conditions, the velocity and density profiles show a distinct trend toward a self similar jet flow as early as x/d = 25. The centerline density profiles in the axial direction provide considerable insight into the jet development from initial core length through to the dissipation of the jet. The core lengths determined from the computational models agree fairly well with the Harsha gas jet empirical approximation and appear to be fairly constant over this density ratio and Reynolds number range. Mass fraction profiles show the importance of the coefficient of specific heat, specifically in RCM-1-A. When injecting fluid below the critical temperature as well as above the critical pressure, as the jet warms up, it will reach the temperature at which c_p reaches a maximum value. The heat transfer from the surrounding gas to the colder jet at this temperature has a dramatically higher transfer rate at this location in the jet. The flow conditions and specifically density seem to be most affected by inlet temperature variations at temperatures so close to the critical point.

The various methods for determining the spreading angle proves useful for comparison, but values from the numerical models determined from a 99% roll off point for velocity agree best with the measured Shadowgraph val-

ues and the Dimotakis model. From the spreading rate analysis, a further conclusion reached is the growth rate of the shear layer and the radial distance injected fluid moves away from the jet has no significant influence on the angle measured from Raman data when the centerline density is significantly higher than the density in the shear layer and the ambient gas. This result is apparent from the FWHM method of determining the spreading angle from the Raman images. The resulting angles do not correspond with the Shadowgraph or the numerical results very well. The procedure of multiplying the FWHM values by a factor of 2 also does not prove to be very accurate when applied to the numerical results.

Acknowledgements

Nomenclature

C, C_μ	Constants
c_p	Coefficient of specific heat constant pressure
d	Injector diameter (2.2 mm)
g	Universal gas constant
h, H	Enthalpy
J	Momentum
k	Turbulent kinetic energy
k_T	Eddy conductivity
k_{eff}	Effective kinetic turbulent energy
K	Thermal conductivity
L_{int}	Integral length scale
L_{kol}	Kolmogorov length scale
Pr_T	Turbulent Prandlt number
r	Radial location
$r_{1/2}$	Radial location of half maximum value of a parameter
T	Temperature
u	Axial velocity
u', v', w'	Turbulence intensity values
x	Axial location
Y	Mass fraction
α	Jet divergence angle
δ_ω'	Vorticity growth rate (radians)
ε	Turbulent energy rate of dissipation, optical efficiency
κ	Thermal conductivity
ν	Kinematic viscosity
ν_T	Turbulent eddy viscosity
ρ	Density, number density
τ	Shear stress

Sub- and Super-scripts

ax	Axial direction
c	Centerline value at specified axial location
i, j, k	x, y and z, Cartesian directions
o	Centerline value at the injector
rad	Radial direction
T	Turbulent parameter
∞	Chamber property away from the jet
*, +	Dimensionless values
'	Fluctuation from the mean value

References

1. Mayer, W. and Tamura, H., "Propellant Injection in a Liquid Oxygen/Gaseous Hydrogen Rocket Engine," J. of Propulsion and Power, Vol. 12, No.6, pp. 1137 - 1147, 1996.

2. Ivancic, B.; Mayer, W.; Krülle, G.; Brüggemann, D., "Experimental and Numerical Investigation of Time and Length Scales in LOX/GH2-Rocket Combustors," 35th Joint Propulsion Conference, AIAA 99-2211, Los Angeles, June 20-24, 1999.

3. Mayer, W.; Schik, A.; Schäffler, M.; Tamura, H., "Injection and Mixing Processes in High-Pressure Liquid Oxygen/Gaseous Hydrogen Rocket Combustors," J. of Propulsion and Power, Vol. 16, No. 5, pp. 823-828, 2000

4. Mayer, W., "TEKAN - Research on Cryogenic Rocket Engines at DLR Lampoldshausen," 36th Joint Propulsion Conference, AIAA 2000-3219, Huntsville, July 16-19, 2000.

5. Mayer, W.; Schik, A.; Vieille, B.; Chaveau, C.; Goekalp, I.; Talley, D.; Woodward, R. "Atomization and Breakup of Cryogenic Propellants under High-Pressure Subcritical and Supercritical Conditions," J. of Propulsion and Power, Vol. 14, No. 5, pp. 835-842, 1998

6. Mayer, W.; Telaar, J.; Branam, R.; Schneider, G.; Hussong, J. "Characterization of Cryogenic Injection at Supercritical Pressure," 37th Joint Propulsion Conference, AIAA 2001-3275, Salt Lake City, July 9-11, 2001.

7. Schetz, J. A., Injection and Mixing in Turbulent Flow, Progress in Aeronautics and Astronautics, Vol 68, AIAA 1980, pp. 19-84.

8. Schlichting, H. Boundary-Layer Theory. McGraw Hill, New York, 1979, pp. 729-755.

9. Pabst, O., "Die Ausbreitung heisser Gasstrahlen in bewegter Luft, I Teil-Versuche in Kerngebiet," Deutsche Luftfahrtforschung, Aug. 1944.

10. Sakipov, Y.B. and Temirbaev, D.J., "On the Ratio of the Coefficients of Turbulent Exchange of Mass and Heat in a Free Turbulent Jet," Tepli i Massoperenos, Vol. 2, 1965, pp. 407-413.

11 Wilcox, D.C., Turbulence Modeling for CFD, DCW Industries, La Canada, CA, 1994, pps.181-2.

12. CFD-GUI5TM User manuals. CFD Research Corporation; Huntsville, AL, October 1998, pg. 3-13.

13. White, F.M. Viscous Fluid Flow. McGraw Hill, Inc. New York, 2nd Edition, 1991, pg. 482.

14. Chehroudi B.; Cohn, R.; Talley, D.; and Badakhshan A., "Raman Scattering Measurements in the Initial Region of Sub- and Supercritical Jets," 36th Joint Propulsion Conference, AIAA 2000-3392, Huntsville, July 14-19, 2000.

15. Dimotakis, P.E., "Two-dimensional Shear-layer Entrainment," AIAA Journal, vol. 24, no. 11, Nov. 1986, pp. 1791-1796.

16. Papamoschou, D. and Roshko, A. "The Compressible Turbulent Shear Layer: an Experimental Study," J. Fluid Mech., vol. 197, 1988, pp. 453-477.

17. Lee, B.I. and Kesler, M.G.,"A Generalized Thermodynamic Correlation Based on Three-Parameter Corresponding States," AIChE J., Vol. 21, p. 510, May 1975.

18. Chung et al., "Generalized Multiparameter Correlation for Nonpolar and Polar Fluid Transport Properties," Ind. Eng. Chem. Res., Vol. 27, p. 671, 1988.

19. Younglove, B.A. Thermophysical Properties of Fluids. Journal of Physical Chemistry, Reference Data 11: Supplement 1.

20. Cebec, T. and Smith A.M.O. Analysis of Turbulent Boundary Layers. Academic Press, New York, 1974.

21. Launder, B.E. and Spalding, D.B., "Computational Methods Applied Mechanical Engineering", vol. 3, 1974.

The RCM1_A test case

A first attempt to model a supercritical cryogenic injection using the CPS code

2nd International Workshop on Rocket Combustion Modelling

Lampoldshausen March 25-27, 2001

Presented by Laurent Lequette form Bertin Technologies

Bertin technologies

2nd RCM Workshop : RCM1_A test case

1. **The introduction**

2. **The objectives and the approach**

3. **The main results**

4. **The numerical and the physical models**

5. **The results presentation**

6. **The conclusion**

bertin technologies

2nd RCM Workshop : RCM1_A test case
The introduction

- ❑ Bertin Technologies
  - ❑ technological services provider and consultancy
  - ❑ French private company
  - ❑ staff : 250 employees

- ❑ The SIMA team
  - ❑ working in Information Systems and Advanced Modelling
  - ❑ has been involved in CFD modelling for more than 15 years and has developed several CFD tools like CALIFE, THESEE and now CPS

- ❑ This work has been founded by CNES

bertin technologies

2nd RCM Workshop : RCM1_A test case
The introduction

The CPS code

☐ new generation CFD code

  ☐ unstructured meshes (3D)

  ☐ Roe and Toumi formulation for Euler fluxes

  ☐ explicit and implicit schemes (for steady and for unsteady flows)

  ☐ turbulence models (Jones-Launder, Coakley, RNG, subgrid, …)

  ☐ Eulerian two phases model

  ☐ Lagrangian two phases model (LASVEGAS)

    ☐ atomisation and coalescence

    ☐ arbitrary time step

    ☐ high volumic rates

  ☐ Combustion models (Arrhenius, TECK, flame surface)

☐ developed by Bertin Technologies and SNPE Group together

  ☐ benefits from earlier developments of both companies

☐ a commercial version is being launched

  ☐ we are looking for pilot customers

bertin technologies

- LL - 23/03/2001

2nd RCM Workshop : RCM1_A test case
The objectives and the approach

❑ The objectives

    ❑ To have a first attempt to use CPS for supercritical flows

    ❑ To retrieve guidelines for future developments of CPS

        ❑ numerical point of view

        ❑ physical models

❑ The approach

    ❑ Several numerical strategies have been explored

        ❑ two phases flow

        ❑ single phase flow using Roe-Toumi fluxes and real gas law

        ❑ single phase flow using a the ICED-ALE scheme and real gas law

            ❑ implicit pressure treatment

            ❑ transport of internal energy

    ❑ Equation of state

        ❑ large validity range Benedict-Weeb-Rubin (BWR) formulation

        ❑ sound speed derived from this formulation

bertin technologies

2nd RCM Workshop : RCM1_A test case
The objectives and the approach

☐ The BWR equation of state for Nitrogen

☐ 33 coefficients

$$P(T,\rho) = \frac{\rho RT}{M} + \left(A1.T + A2.\sqrt{T} + A3 + \frac{A4}{T} + \frac{A5}{T^2}\right)\rho^2 + \left(A6.T + A7 + \frac{A8}{T} + \frac{A9}{T^2}\right)\rho^3 +$$

$$+ \left(A10.T + A11 + \frac{A12}{T}\right)\rho^4 + A13.\rho^5 + \left(\frac{A14}{T} + \frac{A15}{T^2}\right)\rho^6 + \frac{A16}{T}.\rho^7 + \left(\frac{A17}{T} + \frac{A18}{T^2}\right).\rho^8 +$$

$$+ \frac{A19}{T^2}.\rho^9 + \exp(-\gamma.\rho^2)\left[\left(\frac{A20}{T^2} + \frac{A21}{T^3}\right)\rho^3 + \left(\frac{A22}{T^2} + \frac{A23}{T^4}\right)\rho^5 + \left(\frac{A24}{T^2} + \frac{A25}{T^3}\right).\rho^7 +\right.$$

$$\left. + \left(\frac{A26}{T^2} + \frac{A27}{T^4}\right).\rho^9 + \left(\frac{A28}{T^2} + \frac{A29}{T^3}\right).\rho^{11} + \left(\frac{A30}{T^2} + \frac{A31}{T^3} + \frac{A32}{T^4}\right).\rho^{13}\right]$$

☐ The BWR enthalpy for Nitrogen

$$H(p,T) = H_0 + \int_{T_0}^{T} C_{p,0}(T) dT + \frac{p}{\rho(p,T)} - \frac{R.T}{M} + \int_{0}^{\rho(p,T)} \left(\frac{p}{\rho^2} + \frac{T}{\rho^2}\left(\frac{\partial p(\rho,T)}{\partial T}\right)_\rho\right)_T d\rho$$

avec $H_0 = 0$

bertin technologies

2nd RCM Workshop : RCM1_A test case
The main results

- The two phases approach could be interesting but is not mature enough in CPS for such a case

- As it is the Roe-Toumi scheme doesn't allow to use real gas properties
  - simplified laws may allow easier derivation

- The "old" ICED-ALE scheme works well for this case, without noticeable numerical difficulty, but :
  - the current API for real gas equation doesn't cover all aspects and has to be extended
  - the polynomial approach for Cp and Cv has to be extended to be more flexible
  - simplified boundary conditions had to be used in order to avoid perfect gas formulation

- For multispecies application the state of law for the mixing has to be built

bertin technologies

2nd RCM Workshop : RCM1_A test case
The numerical and the physical models

□ Numerical models and parameters

  □ Second order ICED-ALE scheme with implicit pressure treatment

  □ CFL 5

  □ conjugate gradient with ILU preconditioning

  □ unsteady

□ Physical models and parameters

  □ BWR law of state

  □ constant Cp and Cv $Cp = 1200.$ $J.kg^{-1}.K^{-1}$ $Cv = 800.$ $J.kg^{-1}.K^{-1}$

  □ constant laminar viscosity

  □ Jones-Launder (k,ε) turbulence model

□ Mesh

  □ 3230 elements

  □ 154 elements in the axial direction

berlin technologies

2nd RCM Workshop : RCM1_A test case
The numerical and the physical models

❑ Inlet boundary conditions : fixed values

    ❑ $Ps = 39.7 \ 10^5$ Pa $Ts = 126.9$ K $v = 0.769$ m s^{-1}

    ❑ $k = 0.0024$ m^2.s^{-2} $\omega = 10.$ s^{-1}

❑ Outlet boundary conditions : fixed pressure

    ❑ $Ps = 39.7 \ 10^5$ Pa $Ts = 293.$ K (for reentrant flow only)

    ❑ $k = 0.1$ m^2.s^{-2} $\omega = 40.$ s^{-1} Free velocity

❑ Injector and pipe wall conditions

    ❑ Adiabatic   slip condition with friction

❑ Chamber back wall

    ❑ Adiabatic   Ordinary law of the wall

❑ Chamber lateral wall

    ❑ Fixed temperature Tw = 297 K   Ordinary law of the wall

❑ Initial conditions

    ❑ downstream values with zero velocity

bertin technologies

2nd RCM Workshop : RCM1_A test case
The results

- The results correspond to
  - 50 000 time steps with laminar first order scheme
  - then 100 000 time steps with turbulent second order scheme
  - total CPU time 26 h on a Linux Xeon 350 MHz

- The results are converged in the jet spreading
  - at least down to 80 mm after injector outlet

- All the presented results are drawn with a radial to axial scale ratio of 5

bertin technologies

2nd RCM Workshop : RCM1_A test case
The results

Mesh
RCM1
Overall view
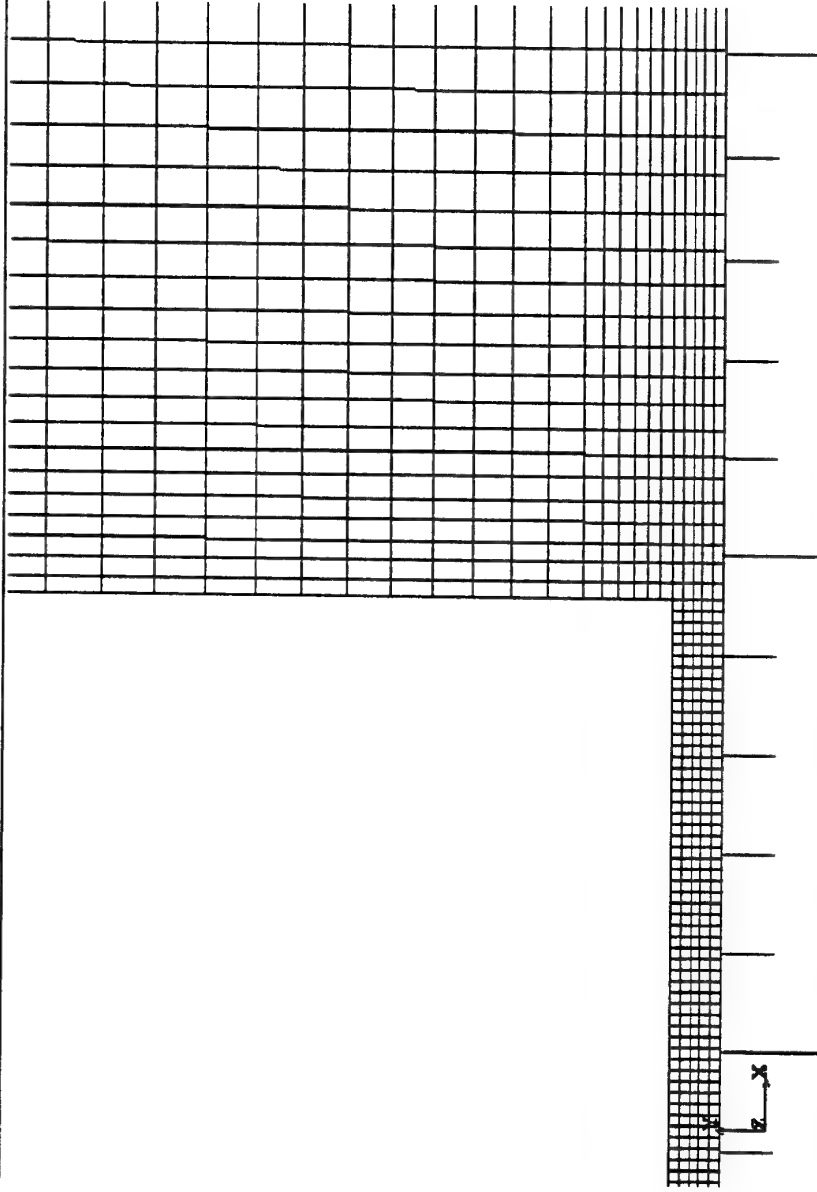
bertin technologies

- LL - 23/03/2001

2nd RCM Workshop : RCM1_A test case
The results

Mesh
RCM1
Zoom

bertin technologies

- LL - 23/03/2001

2nd RCM Workshop : RCM1_A test case
The results

Temperature
case RCM1-A
LN2 at 126.9 K and 39.7 MPa

t t   0.20106
n t   100000
mini: 126.84
maxi: 297.00

126.8
129.0
133.4
139.9
148.7
159.6
172.7
187.9
205.4
225.0
246.8
270.8
297.0

0.500E-01

0.1   0.15   0.2   0.25   0.3

bertin
technologies

bertin
technologies

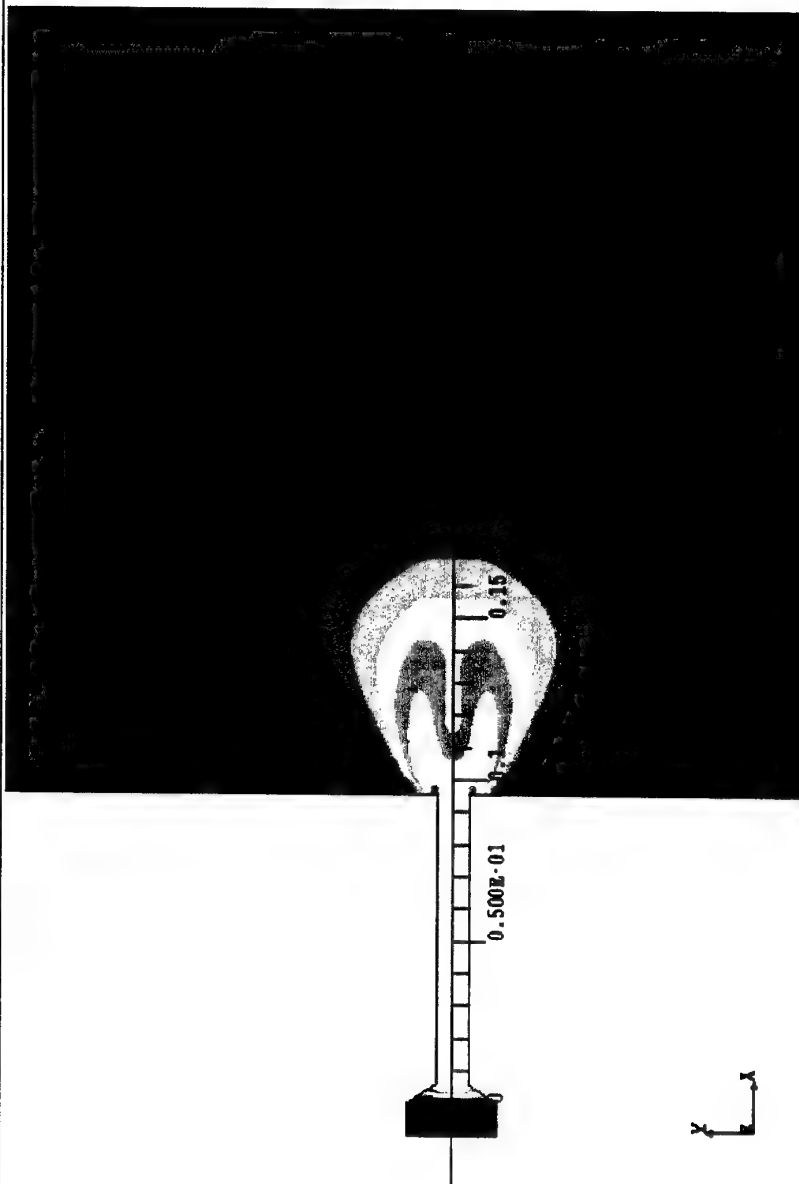- LL - 23/03/2001

Page : 13
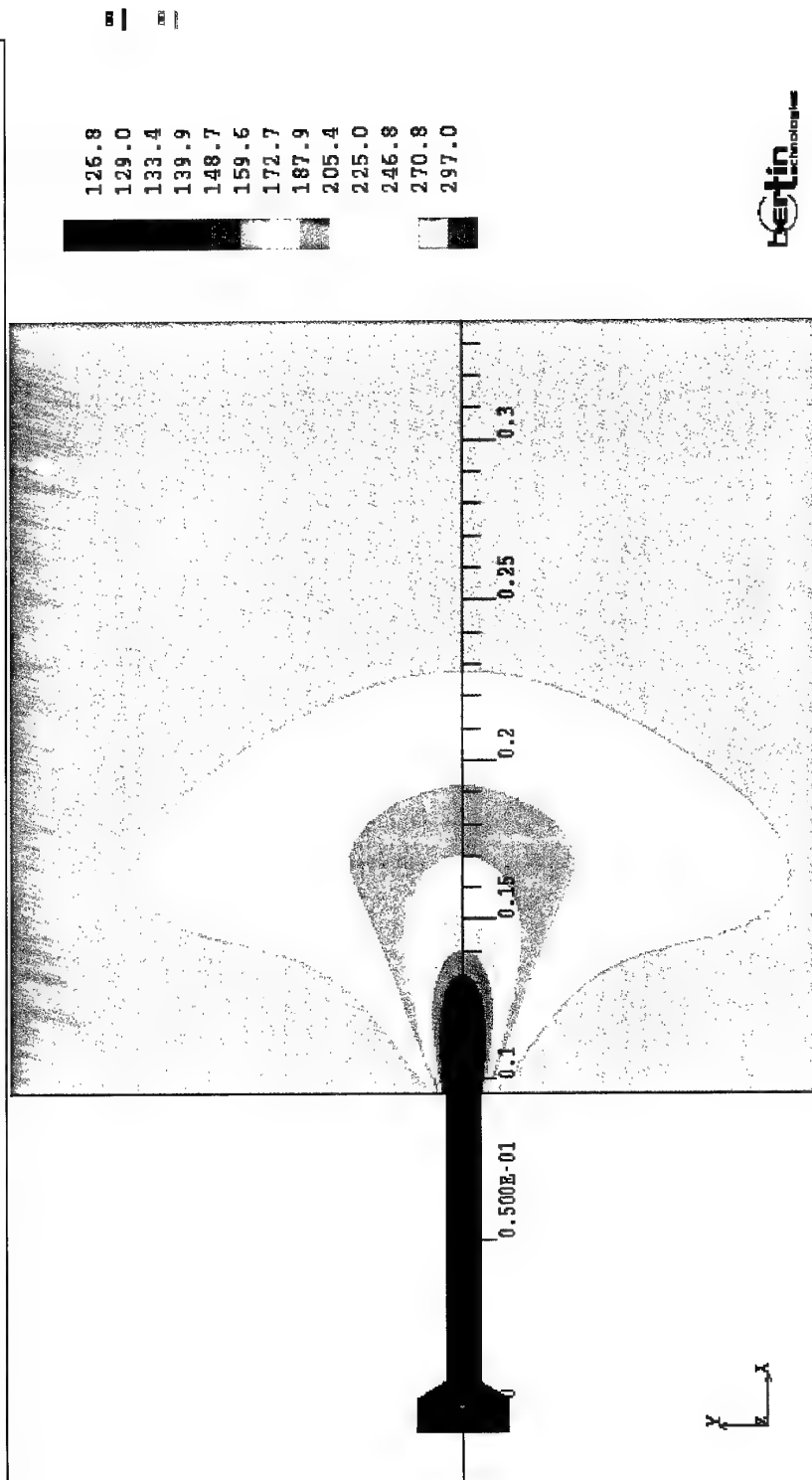
2nd RCM Workshop : RCM1_A test case
The results

Energie cinetique turbulente
case RCM1-A
LN2 at 126.9 K and 39.7 MPa

t :   0.20186
n :   100000
mini: 2.09170E-03
maxi: 4.0508

0.2092E-02
0.1461E-01
0.3340E-01
0.6157E-01
0.1038
0.1672
0.2623
0.4049
0.6189
0.9398
1.421
2.143
3.226

- LL - 23/03/2001

2nd RCM Workshop : RCM1_A test case
The results

```
Pression
case RCM1-A
LN2 at 126.9 K and 39.7 MPa
```

t : 0.20186
n t : 100000
mini: 3.96131E+06
maxi: 4.01469E+06

0.3961E+07
0.3966E+07
0.3970E+07
0.3975E+07
0.3979E+07
0.3984E+07
0.3988E+07
0.3992E+07
0.3997E+07
0.4001E+07
0.4005E+07
0.4010E+07
0.4015E+07

0.500E-01

bertin technologies

bertin technologies

- LL - 23/03/2001

2nd RCM Workshop : RCM1_A test case
The results

```
Masse volumique
case RCM1-A
LN2 at 126.9 K and 39.7 MPa
```

t :   0.20186
n t   100000
mini: 45.244
maxi: 459.95
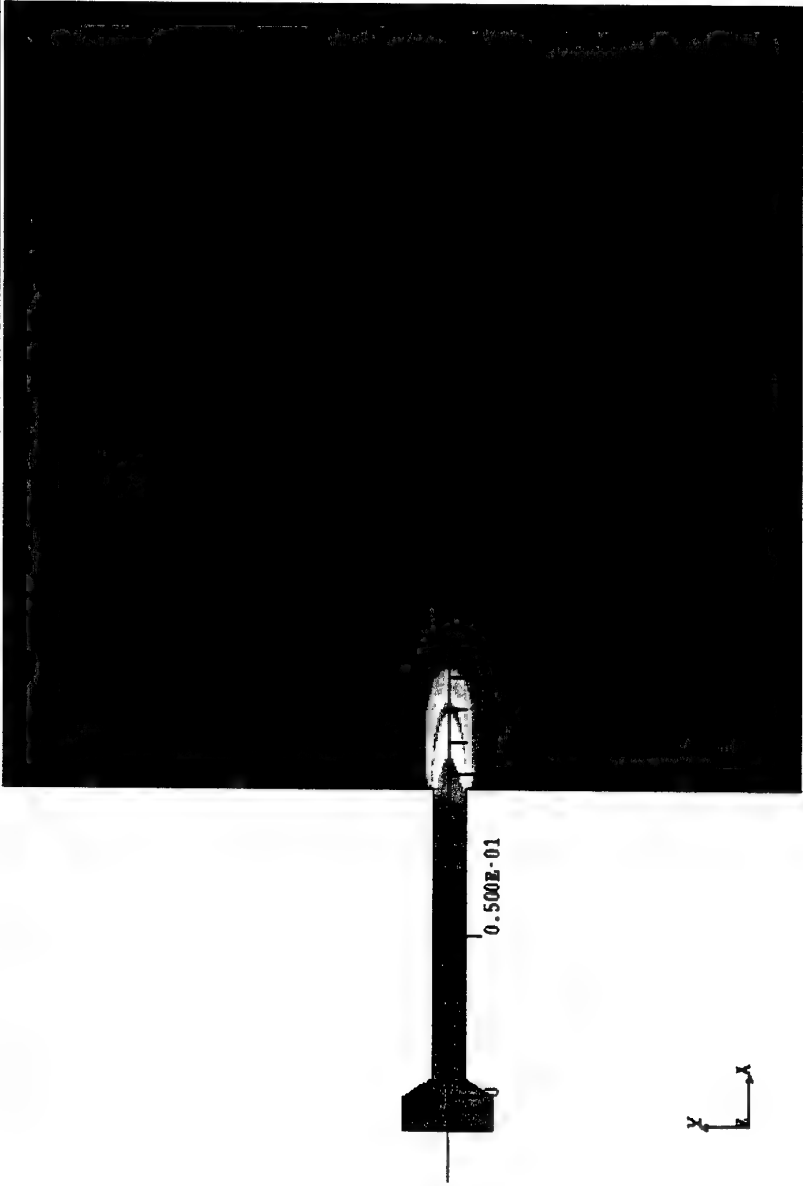
45.24
50.56
61.19
77.14
98.41
125.0
156.9
194.1
236.6
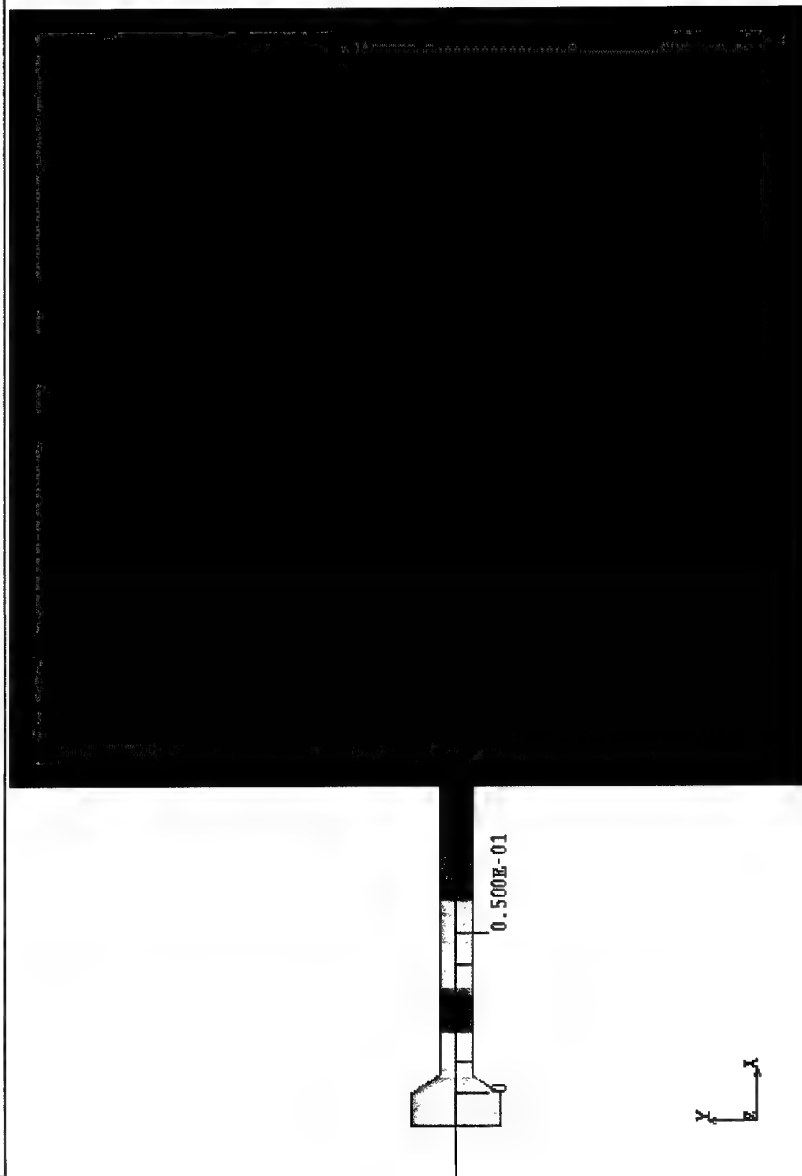284.5
337.7
396.1
459.9

0.500E-01

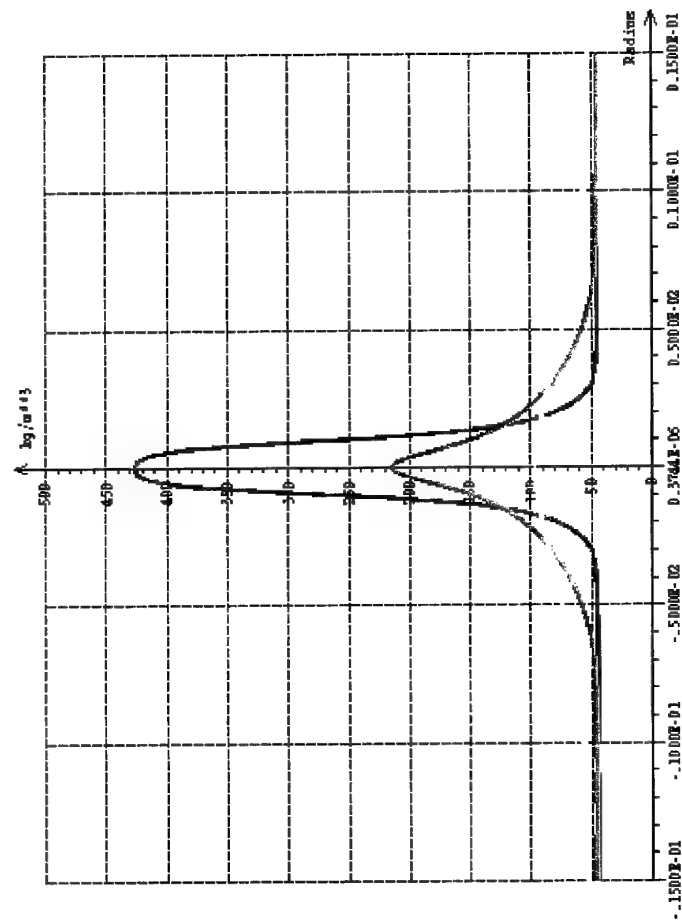bertin technologies

2nd RCM Workshop : RCM1_A test case
The results

Masse volumique
case RCM1-A
lN2 at 126.9 K and 39.7 MPa

t : 0.20186
n : 100000
mini: 45.244
maxi: 459.95

x = 5 mm

R = 25 mm

- LL - 23/03/2001

bertin
technologies

Page : 17

2nd RCM Workshop : RCM1_A test case
The conclusion

☐ This preliminary attempt to model a supercritical cryogenic injection with a general purpose code has shown that it is feasible

☐ Sophisticated thermodynamic laws :

   ☐ can be taken into account with simple numerical schemes

   ☐ require to adapt many features including boundary conditions

   ☐ cannot yet be taken into account easily for ordinary users

   ☐ induce a large CPU cost

☐ Further developments must be done to be able to use Roe-Toumi fluxes

☐ Simplified laws would help to implicit these schemes

bertin
echnologies

Turbulent Spray Combustion Modeling for Rocket Engine Applications

E. Gutheil

Interdisziplinäres Zentrum für Wissenschaftliches Rechnen
Universität Heidelberg, Im Neuenheimer Feld 368
69120 Heidelberg, Germany
Phone: +49-6221-546114, Fax: +49-6221-546111
e-mail: gutheil@iwr.uni-heidelberg.de

Abstract

The paper concerns the modeling of turbulent liquid oxygen/hydrogen spray combustion for elevated subcritical pressure and cryogenic inlet temperature conditions. Various approaches are outlined and discussed that concern current and future models for turbulent two-phase flows as well as models to include detailed chemical reactions. The presence of the liquid phase complicates the situation since the turbulence and the chemical reactions not only interact with each other but also with the spray processes. After the presentation and discussion of general approaches, the combustion in a single injector combustion chamber is modeled where experimental data are available for gas phase temperature and both droplet size and velocities. The model uses an Eulerian–Lagrangian formulation for the gas and the liquid phase, respectively. Detailed models for droplet heating and vaporization in a convective flow field are employed, and detailed gas phase reactions are accounted for through use of a flamelet model for turbulent spray combustion. The results show a very good agreement between experimental and computational spray characteristics. The computed gas phase temperature lies above the experimental values which is associated with CARS single shot measurements and incomplete data for the initial conditions of the combustion process.

1 Introduction

An improved understanding of the physical and chemical processes occurring in liquid rocket engines is required to ensure the stability, reliability, and efficiency of their performance. The gaseous hydrogen and the liquid oxygen (LOX) are injected at cryogenic inlet temperatures, and the turbulent combustion occurs in both the sub- and supercritical domain. Therefore, the models for the processes in systems such as the Ariane V or the Space Shuttle main engine are very complex. The paper concerns principal approaches to the modeling of these processes and discusses the state of the art as well as potential approaches in future.

Finally, the combustion process in a single injection combustion chamber is investigated for elevated pressure and cryogenic inlet temperatures. Experimental data are available for an elevated pressure situation of 5 bar, and the experimental data are published by Sender *et al.* [1]. The combustion in liquid rocket propulsion typically occurs in the flamelet regime of turbulent combustion [2] which enables the use of the flamelet model for turbulent spray diffusion flames [3, 4]. Structures of laminar hydrogen/oxygen flames are precalculated at 5 bar and for cryogenic inlet temperature of 100 K for hydrogen [5, 6]. They are incorporated into the turbulent spray combustion model which allows the computation of all chemical species

that are included in the detailed chemical reaction mechanism for the hydrogen/oxygen system that includes 8 reactive species and 38 chemical reactions [7].

2 Turbulence Modeling of Two-Phase Flows

Two-phase flows are characterized by the separation of the turbulent flow field and the strong interaction between the spray and the gas through processes such as turbulent mixing, droplet heating, vaporization, and motion as well as coupling with possible occurance of chemical reactions. In practical systems, most often the turbulent gas flow is modeled using a $k - \epsilon$ turbulence model where additional terms are added to account for the interaction with the liquid. This formulation is done within an Eulerian–Lagrangian formulation of governing equations for a dilute spray within either a discrete droplet or a continuous droplet model. c.f. Faeth [8]. An example of the mathematical equations within a discrete droplet model is given through [3]

$$L(\tilde{\Phi}) \equiv \frac{\partial(\bar{\rho}\tilde{u}\tilde{\Phi})}{\partial x} + \frac{1}{r}\frac{\partial(\bar{\rho}\tilde{v}\tilde{\Phi})}{\partial r} - \frac{\partial}{\partial x}\left(\frac{\mu_{\text{eff}}}{\sigma_\Phi}\frac{\partial\tilde{\Phi}}{\partial x}\right) - \frac{1}{r}\frac{\partial}{\partial r}\left(r\frac{\mu_{\text{eff}}}{\sigma_\phi}\frac{\partial\tilde{\Phi}}{\partial r}\right) = L_{\text{gas},\tilde{\Phi}} + L_{\text{spray},\tilde{\Phi}} \quad (1)$$

where the source terms are given in Tab. 1. Here a two dimensional axisymmetric configuration is considered where x and r denote the axial and radial directions, respectively. Favre averaged values are used.

Variable	Φ	$L_{\text{gas},\tilde{\Phi}}$	$L_{\text{spray},\tilde{\Phi}}$
Mass	1	0	$\sum_{k=1}^{N_p}(n\dot{m})_{\text{p,k}} \equiv \overline{L}_v$
Momentum in Axial Direction	$\tilde{u}$	$-\frac{\partial\bar{p}}{\partial x} - \frac{2}{3}\frac{\partial}{\partial x}\left[\mu_{\text{eff}}\left(\frac{\partial\tilde{u}}{\partial x} + \frac{1}{r}\frac{\partial(r\tilde{v})}{\partial r}\right)\right] + \bar{\rho}g$	$\sum_{k=1}^{N_p}(n\dot{m}u)_{\text{p,k}}$
Momentum in Radial Direction	$\tilde{v}$	$-\frac{\partial\bar{p}}{\partial r} - \frac{2}{3}\frac{\partial}{\partial r}\left[\mu_{\text{eff}}\left(\frac{\partial\tilde{u}}{\partial x} + \frac{1}{r}\frac{\partial(r\tilde{v})}{\partial r}\right)\right] - 2\frac{\mu_{\text{eff}}\tilde{v}}{r^2}$	$\sum_{k=1}^{N_p}(n\dot{m}v)_{\text{p,k}}$
Energy	$\tilde{h}$	0	$\sum_{k=1}^{N_p}(n\dot{m}h)_{\text{p,k}}$
Mixture Fraction	ξ	0	$\overline{L}_v$
Variance of the Mixture Fraction	$\widetilde{\xi''^2}$	$2\Gamma_{\widetilde{\xi''^2}_t}\text{div}^2\tilde{\xi} - 2\bar{\rho}\tilde{\epsilon}/\tilde{k}\widetilde{\xi''^2}$	$\overline{L}_v\tilde{\xi}''^2\left(1 - 2\tilde{\xi}\right)/\tilde{\xi}$
Turbulent Kinetic Energy	$\tilde{k}$	$G_{\text{k}} - \bar{\rho}\tilde{\epsilon}$	$\sum_{k=1}^{N_p}\overline{u''(n\dot{m}\tilde{v})}_{\text{p,k}}$
Dissipation Rate of the Turbulent Kinetic Energy	$\tilde{\epsilon}$	$(C_1G_{\text{k}} - C_2\bar{\rho}\tilde{\epsilon})\tilde{\epsilon}/k$ $G_{\text{k}} = -\overline{\rho u'' \otimes u''} : \text{grad}\tilde{\tilde{u}}$	$\epsilon/k\,L_{\text{spray},\tilde{k}}$

Table 1: Source terms for Eq. 1 [3].

	ϕ	$j_{\phi,k}$	$T_{\phi,k}$	S_ϕ	L_ϕ	
Continuity	1	0	0	0	L_v	
Momentum	v_i	0	τ_{ik}	$-\frac{\partial p}{\partial x_i} + \rho g_i$	$L_{m,i}$	$i = 1 \ldots 3$
Enthalpy	h	$-\frac{\lambda}{c_p}\frac{\partial h}{\partial x_k}$	0	0	L_e	
Mass Fractions	Y_α	$-\rho D\frac{\partial Y_\alpha}{\partial x_k}$	0	$\dot{\omega}_\alpha$	$L_{v,\alpha}$	$\alpha = 1 \ldots N$
Element Mass Fr.	Z_j	$-\rho D\frac{\partial Z_j}{\partial x_k}$	0	0	$\sum_{\alpha=1}^{N}\mu_{j,\alpha}L_{v,\alpha}$	$j = 1 \ldots M$

Table 2: Source terms for Eq. 2 [12].

Even though this model is used in most technical simulations, it has major drawbacks such as the well known problem of the $k - \epsilon$ model in strongly recirculating flows and its failure of modeling anisotropic turbulence which is common to all models using the turbulence energy k. Moreover, the model is based on a gradient diffusion assumption which is not appropriate to predict the effect of counter gradient diffusion which has been observed in turbulent gas flows.

More advanced models that are under investigation in gas phase flows are currently extended to two-phase flows. These are the LES – Large Eddy Simulation, the Reynolds stress models, and DNS – Direct Numerical Simulation. There is a special presentation [9] at the present meeting that deals with LES, and therefore this approach is not discussed within the frame of this presentation. The method of DNS is currently applied to small problems – small in the sense of physical dimensions of the system investigated [10] since the entire range of length scales needs to be resolved which restricts the dimension of the problem. However, the method is very interesting when well defined submodels are to be investigated.

The Reynolds stress models are typically used when non-isotropic turbulence occurs and if counter gradient diffusion is present. The model does not use the k equation but transport equations for the Reynolds stress terms $\widetilde{u_i''u_j''}$. Additional terms appear that describe the coupling between the velocity fluctuations and the spray source terms that stem from droplet heating, vaporization, and motion. The Reynolds stress equations yield

$$\frac{\partial(\bar{\rho}\widetilde{\psi''\phi''})}{\partial t} + \frac{\partial(\bar{\rho}\tilde{v}_k\widetilde{\psi''\phi''})}{\partial x_k} = \underbrace{-\bar{\rho}\widetilde{v_k''\psi''}\frac{\partial\tilde{\phi}}{\partial x_k} - \bar{\rho}\widetilde{v_k''\phi''}\frac{\partial\tilde{\psi}}{\partial x_k}}_{\text{I}} \underbrace{-\frac{\partial(\bar{\rho}\widetilde{v_k''\psi''\phi''})}{\partial x_k}}_{\text{II}} \tag{2}$$

$$\underbrace{-\overline{\phi''\frac{\partial}{\partial x_k}(j_{\psi,k} + T_{\psi,k})} - \overline{\psi''\frac{\partial}{\partial x_k}(j_{\phi,k} + T_{\phi,k})}}_{\text{III}} + \underbrace{\overline{\phi''S_\psi} + \overline{\psi''S_\phi}}_{\text{IV}}$$

$$\underbrace{-L_v\left(\widetilde{\phi''\psi''} + \tilde{\phi}\psi'' + \tilde{\psi}\phi''\right) + \overline{\phi''L_\psi} + \overline{\psi''L_\phi}}_{\text{V}},$$

and the source terms are given in Tab. 2:

For completeness and further use in the next section, the element mass fraction, Z_j, is also shown in the Tab. 2. The terms I to IV in Eq. 2 may be closed using the standard models for pure gas phase equations whereas ther terms V describe the interaction between the spray and the variable under consideration. These terms may be formulated according to the derivations in Ref. [3, 4], and they are currently under investigation.

Another approach is that of Burlaka and Borghi [11] that describes the spray surface, $\overline{\sum_i}$, with a transport equation

$$\frac{d}{dt}\left(\overline{\sum_i}\right) + \frac{d}{dx_k}\left(u_k\overline{\sum_i}\right) = \text{diffusion} + \text{production} + \text{destruction}. \qquad (3)$$

The destruction term includes the vaporization process. This model is motivated by the surface transport equation in turbulent premixed combustion, and the description of the vaporization process is still under development.

3   Models for Chemical Reactions in Turbulent Reactive Two-Phase Flows

The chemical reactions in a convective flow field may be described mathematically through the conservation equation of the mass fractions, Y_i, of chemical species i:

$$\frac{\partial(\rho Y_i)}{\partial t} = -\frac{\partial(\rho_i u_{ik})}{\partial x_k} + M_i\dot{w}_i + \delta_{iL}L_v, \qquad (4)$$

where $\dot{w}_i$ is the molar chemical reaction rate and L_v is the source therm due to liquid vaporization. δ_{iL} is the Dirac–Delta function where L denotes the species in liquid phase. The system of chemical reactions is written as

$$\sum_{i=1}^{M} \nu'_{ij}\mathcal{M}_i \rightleftharpoons \sum_{i=1}^{M} \nu''_{ij}\mathcal{M}_i, \qquad j = 1,\dots,N, \qquad (5)$$

and the consumption/production rate of a chemical species yields

$$\dot{w}_i = \sum_{j=1}^{N}(\nu''_{ij} - \nu'_{ij})w_j, \qquad i = 1,\dots,M, \qquad (6)$$

where w_j is the reaction rate of a reaction step, j, using the modified Arrhenius expression for the reaction constant

$$w_j = A_j T^{b_j} e^{E_j/(RT)} \prod_{i=1}^{M}[Y_i p\bar{M}/(RTM_i)], \qquad j = 1,\dots,N \qquad (7)$$

for N chemical reaction steps.

If the chemical reactions are to be modeled using a mixture fraction, the source term due to chemical reactions dissappears. The mixture fraction may be based on the elements, i, present in the system:

$$\xi(i) = \sum_{j=1}^{M} \mu_{ij}(Y_j - Y_{j\infty})/\sum_{j=1}^{M} \mu_{ij}(Y_{j-\infty} - Y_{j\infty}), \qquad (8)$$

4

where $i = $ N, O, H, and μ_{ij} is the mass of element i in molecule j. The mixture fraction may also be based on enthalpy [13]

$$\xi(h) = \sum_{i=1}^{M}(Y_i h_i - Y_{i\infty} h_{i\infty})/\sum_{j=1}^{M}(Y_{i-\infty} h_{i-\infty} - Y_{i\infty} h_{i\infty}). \qquad (9)$$

If the Lewis numbers of all species were unity, then there is no difference in the above definitions. However, for the hydrogen/oxygen system, this is not true, and some of the definitions show unreasonable values [13]. In the remainder of the paper, the mixture fractions is based on the element H which is the best choice in terms of monotonicity with physical space for the hydrogen/oxygen system.

Taking these definitions for the instantaneous values of the chemical reaction rate, there are various approaches to close the problem in turbulent reactive flows. The directest approach is the direct closure of the source term of chemical reactions through use of a joint probability density function (PDF), P, leading to the following averaged chemical reaction rate:

$$\overline{M_i \dot{w}_i} = M_i \int_0^1 \ldots \int_0^1 \int_0^\infty \int_0^\infty \dot{w}_i P(Y_1, \ldots, Y_N, p, T) dT dp dY_1 \ldots dY_N. \qquad (10)$$

Since the joint PDF is not known, most often it is factorized and beta functions are used to describe to single PDFs

$$\tilde{P}(\tilde{\Phi}) = \frac{\Gamma(\alpha + \beta)}{\Gamma(\alpha)\Gamma(\beta)} \tilde{\Phi}^{\alpha-1} (1 - \tilde{\Phi})^{\beta-1}. \qquad (11)$$

The α and β are linear functions of the variance of the variable Φ under consideration, and they are obtained through solution of their transport equations, c.f. Eq. 2.

Most often this approximation is not too bad in gas phase combustion. However, it apprears [10] that the beta-function is a poor approximation in regimes where the vaporization occurs. Therefore, new approaches need to be developed.

A promising approach seems to be the formulation through a PDF transport equation. This model has been developed by Pope [14] and Dopazo [15] for gas phase combustion. The PDF is modeled through a transport equation, and the chemical source terms may be used without the averaging procedure described above. The formulation of the PDF transport equation for the PDF of the mixture fraction, P_ξ, yields for turbulent two-phase flows

$$\frac{\partial(\rho P_\xi)}{\partial t} + \frac{\partial}{\partial x_i}(\rho U_i P_\xi) + \frac{\partial}{\partial x_i}(\langle \rho u_i' \mid \xi = \phi \rangle P_\xi) = \qquad (12)$$

$$\frac{\partial^2}{\partial \phi^2}\left[\rho D \langle \frac{\partial \xi}{\partial x_i}\frac{\partial \xi}{\partial x_i} \mid \xi = \phi \rangle P_\xi\right] + \frac{\partial}{\partial x_i}\left(\rho D \frac{\partial P_\xi}{\partial x_i}\right) - \frac{\partial}{\partial \phi}(L_v P_\xi)$$

where the third term on the LHS is usually modeled using

$$\langle \rho u_i' \mid \xi = \phi \rangle P_\xi = -\frac{\eta_t}{\sigma_\xi}\frac{\partial P_\xi}{\partial x_i}. \qquad (13)$$

This approach has not yet been investigated for turbulent two-phase flows to the author's knowledge, but it appears promising. The diffusion term needs to modeled using particle mixing models, and it is unclear if they can be used for two-phase flows without modification.

5

The major advantage of this approach is that the PDF transport equation needs no information on fluctuations of the droplet vaporization, and it enables the evaluation of a PDF that may possibly be approximated through an extension of well known standard PDFs. For reactive flows, the approach is beneficial because it does not require averaged chemical reaction terms – the instantaneous values are sufficent.

The chemistry itself may be included through use of detailed reaction schemes [7], reduced reaction mechanisms [16], or tabulated systems such as the ILDM approach [17]. There is a number of reduced chemcial reaction schemes for the hydrogen/oxygen system, and they range from 4-step to 2-step schemes [16]. The chemcial reactions in high pressure systems typically occur with small time scales so that the use of a lower number of reaction steps is more justified as pressure increases, and for very high pressure even a one-step mechanism performs well.

Another type of model to include detailed chemical reactions is the flamelet model for turbulent combustion [18, 19, 20] which has been extended for turbulent spray diffusion flames [3, 4]. The model considers the tubulent flame to consist of an ensemble of laminar flamelets that are stretched through the turbulence of the flow field, c.f. Fig. 1.
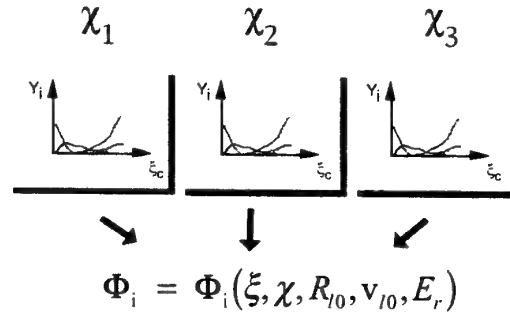

Figure 1: Schematic of the flamelet model for turbulent spray combustion.

The laminar flamelet depends on the mixture fraction, ξ, the scalar dissipation rate, χ, the initial droplet size and velocity, R_{l0} and v_{l0}, resp., and the equivalence ratio, E_r. The Favre averaged values of a variable, Φ, then yields [4]

$$\tilde{\Phi} = \int_0^\infty \int_0^\infty \int_0^\infty \int_0^\infty \int_0^1 \Phi(\xi, \chi, R_{l0}, v_0, E_r) \tilde{P}(\xi, \chi, R_{l0}, v_0, E_r) d\xi d\chi dR_{l0} dv_0 dE_r. \quad (14)$$

The joint probability density function is factorized, and the one-dimensional PDFs need to be determined [4]. Currently, there are libraries available for the liquid oxygen/hydrogen system [6] and for the methanol/air [21] and ethanol/air [22] systems.

In the following section, the flamelet model for turbulent spray diffusion flames is used together with the model described through the equations given in Tab. 1 to simulate the combustion process in the micro combustion chamber M3 of the DLR in Lampoldshausen [23].

6

4 Simulation of the Combustion Process in the Micro Combustion Chamber M3

4.1 Model

A dilute LOX spray is considered that is injected into a turbulent gaseous hydrogen stream where the inlet temperatures are cryogenic. The system pressure is 5 bar. The model includes an Eulerian description of the gas phase and Lagrangian equations for the dilute spray. The $k - \epsilon$ turbulence model is employed where additional terms account for the spray interaction [3], c.f. Tab. 1. The chemical reactions are described through a flamelet model for turbulent spray diffusion flames [3, 4] outlined in the previous section. The conservation equations for the mixture fraction and its variance also account for mass gain through vaporization of the liquid [3].

Convective heating and vaporization is described through a model developed by Abramzon and Sirignano [24]. The equation for droplet motion accounts for turbulence effects through a Gaussian distribution for turbulent fluctuations [25]. The spray distribution is described through the discrete droplet model [23].

For the computation of the gas phase characteristics in the cryogenic temperature regime, data from JSME tables [26] for pressures up to 200 bar and temperatures between 80 and 300 K are used. Moreover, the pressure (and temperature) dependence of the vaporization rate and of the binary equilibrium composition at the liquid/gas interface [27] is included. For the pressure considered here, the real gas effects in the gas phase are negligable [28].
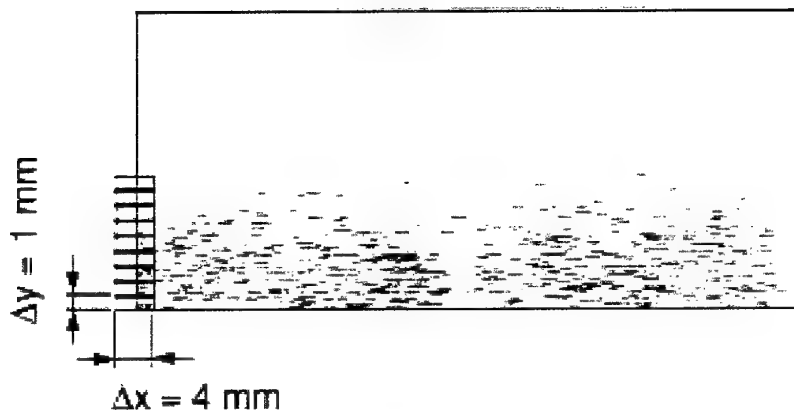
4.2 Results and Discussion

Figure 2: Measured droplet velocities in the range between 72 and 140 mm from their injector [1].

The experimental data [1, 23] include gas temperature as well as droplet velocites and size. Figure 2 displays the droplet velocities obtained from experiment using PIV. The area displayed ranges from 72 mm to 140 mm of the combustion chamber which is the second half of the entire single-injector micro combustion chamber M3 of the DLR in Lampoldshausen,
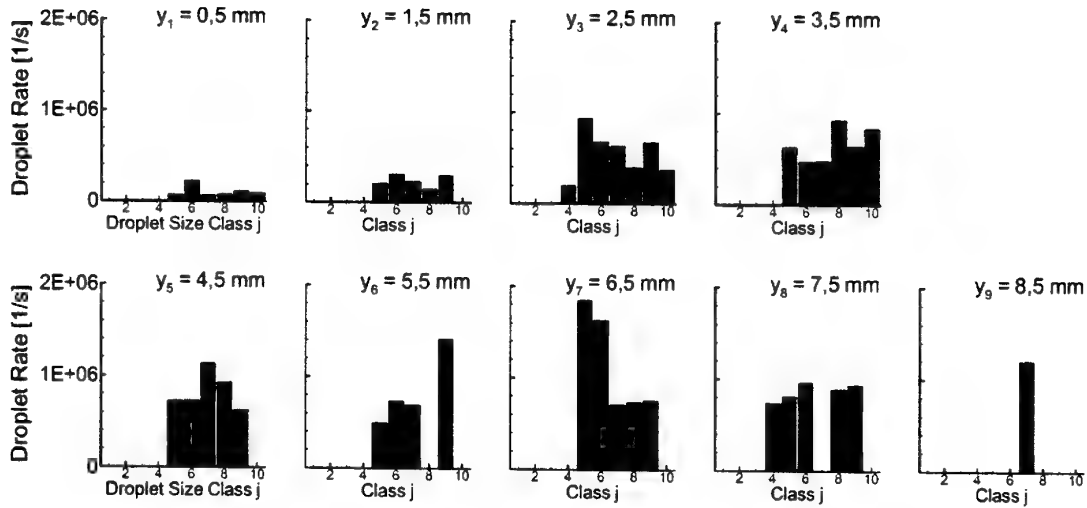
Figure 3: Initial droplet rate and distribution for 9 different size classes evaluated from experimental data [1] at $x = 72$ mm from the injector [23].
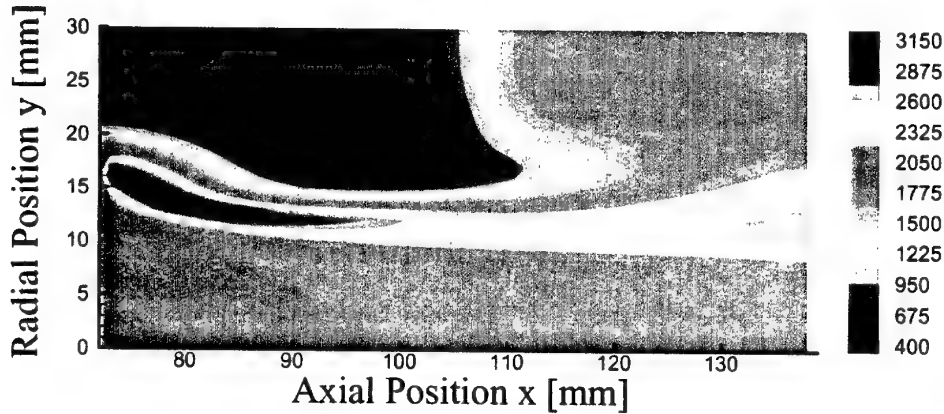

Figure 4: Contour plot of the gas temperature [23].

Germany. In the first part of the combustor, the spray is rather thick, and the model is not suitable. The experimental data are used to produce initial profiles for the simulation as well as for comparison further downstream in the combustion chamber.

Figure 3 shows the generated initial droplet rate at the axial position 72 mm. The depth of field in the experiment is 0.5 mm which has been used to calculate the droplet rate. The experiment typically does not comprise more than about 15 % of the entire liquid. Sometimes in the literature, this value is extrapolated to 100% and there are several methods to do so. However, we preferred to stick to the experimental data that we received since there is no reliable information about how much of the liquid flux exactly needs to be compensated for which causes a second ambiguity in the procedure.
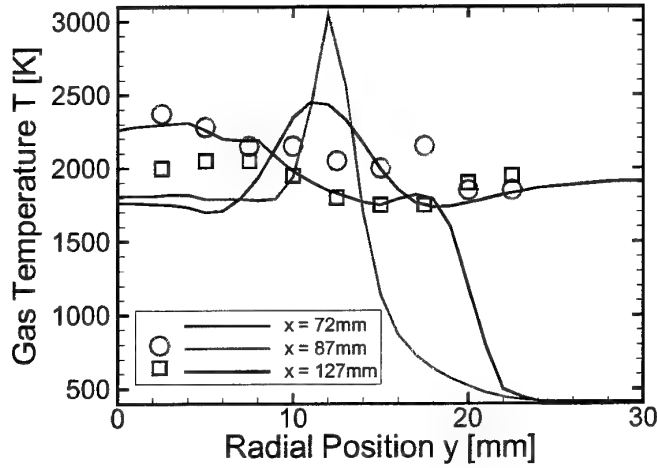
8

Figure 5: Radial profiles of the gas temperature for three different axial positions: Symbols present experimental data and lines show computational results [23].
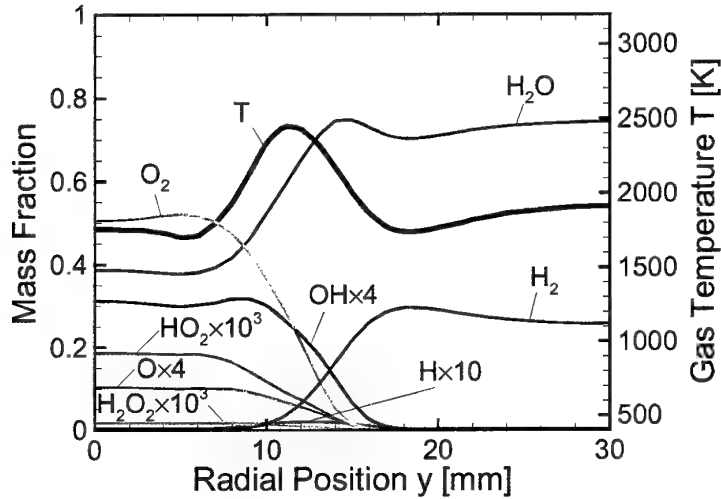

Figure 6: Radial profiles of the gas temperature and species mass fractions at $x = 127$ mm [23].

Also, there are no gas temperature measurements exactly at $x = 72$ mm, and the inlet conditions for the gas temperature have been obtained from interpolated experimental data at two surrounding axial positions. Moreover, the experimental data have been extrapolated into the outer regions where no experimental data are available.

There is no information on other gas phase characteristics such as species concentrations from the experiment. The initial gas velocity is taken from the experimental velocity of the smallest droplets, and the species profiles are estimated from the experimental gas temperature. The turbulence quantities k and ϵ are computed from the gas phase velocity.

Figure 4 shows the computed overall structure of the spray flame in terms of the computed
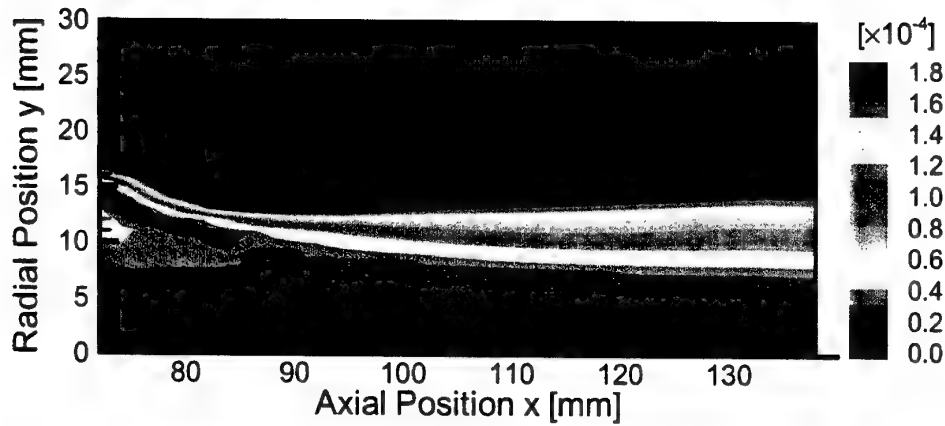
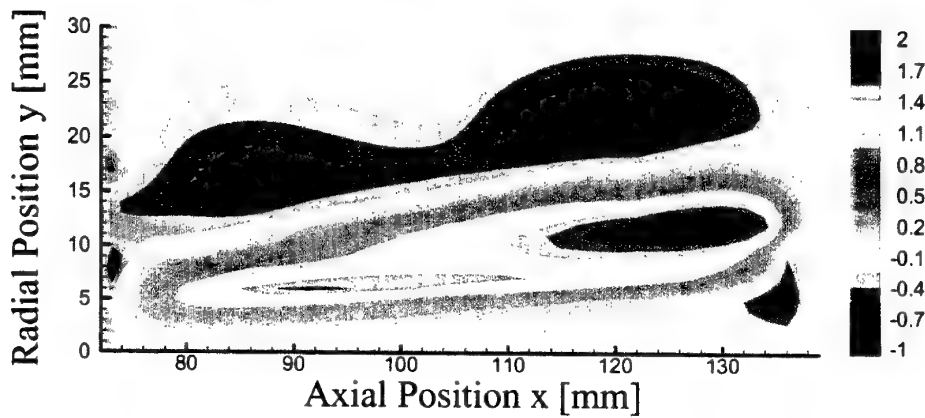Figure 7: Contour plot of the mass fraction of HO_2 [23].

Figure 8: Contour plot of the radial gas velocity [23].

gas phase temperature. The main chemical reaction zone is located at the boundary of the spray jet where vaporized oxidizer meets the surrounding hydrogen gas stream. The maximum flame temperature is about 3000 K which is typical for these high-pressure flames.

A more detailed investigation of flame temperature is shown in Fig. 5 where the calculated and experimental radial profiles of the gas temperature are shown for three different axial positions. Symbols show experimental data and lines are computational results.

Figure 5 shows that the gas temperature in the main reaction zone is overpredicted by the computations. This may be attributed to both experimental and computational uncertainties. First the experiments employed CARS single shot measurements, and the averaging procedure of these values typically leads to an underprediction of the measured gas temperatures. Moreover, the initial gas phase profiles needed for the computations is estimated from the gas temperature profile, and this procedure is somewhat arbitrary. Another reason is to be found in the incomplete liquid phase data as discussed earlier. The computations use the uncorrected data from measurements so that the vaporization of the
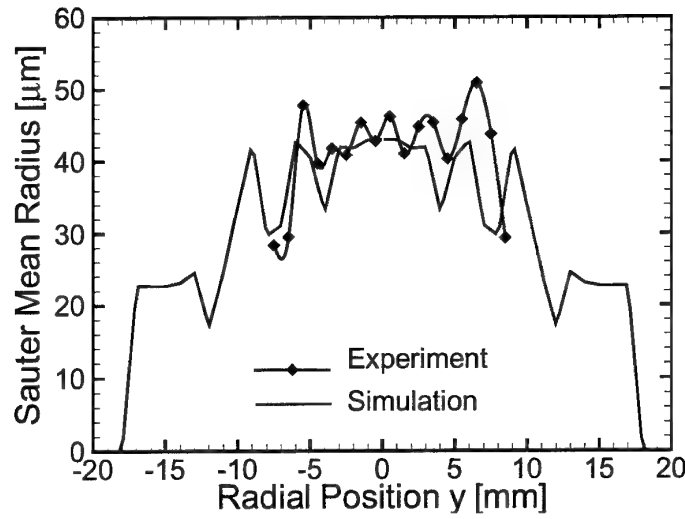
Figure 9: Experimental and computational results of the Sauter mean radius at $x = 104$ mm [23].
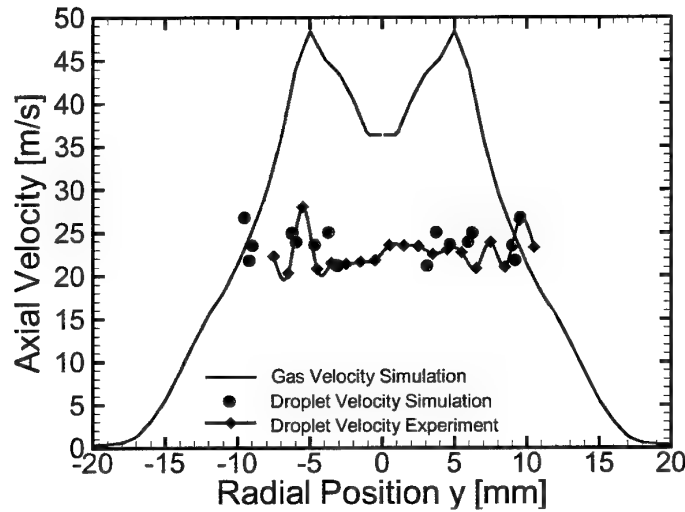

Figure 10: Experimental and computational results of the droplet velocities as well as calculated gas velocities at $x = 104$ mm [23].

neglected liquid would reduce the gas phase temperature. Therefore, the discrepancies of computed and measured temperature profiles in the gas phase is reasonable.

The flamelet model is suitable to predict all species profiles that are considered in the laminar flamelet library. Figure 6 shows radical profiles at $x = 127$ mm. The HO_2 and H_2O_2 are present in the colder flame region (due to their stability) near the axis of symmetry where molecular oxygen in the gas phase is present. The location of the H_2O peak is shifted to the fuel side which is typical for gas phase combustion. Figure 7 shows the contour plot of the HO_2 mass fraction, and the differences compared to the gas temperature contour plot are obvious. The HO_2 prevails into the colder regions of the combustion chamber favorably in regions where gaseous O_2 is present.

11

The gas phase velocities show that there is a region where recirculation occurs. This may be seen in Fig. 8 where the radial gas phase velocity is displayed. This finding is in agreement with experiment [1]. It is well known that the $k - \epsilon$ turbulence model that is used here is not the best choice if recirculation is present, and a future study will include a Reynolds stress model for turbulent spray flames.

Figures 9 and 10 show a comparison of liquid phase characteristics. Figure 9 displays the radial profile of the Sauter mean radius at $x = 104$ mm. Symbols mark experimental results, and the agreement between experiment and computation is excellent. The same is true for the profiles of axial velocities at the same axial position plotted in Fig. 10. Thus it is shown that the present model is suitable to correctly predict the liquid phase properties.

5 Summary and Future Research

The combustion process in the micro combustion chamber M3 has been studied by means of numerical computations. The Eulerian/Lagrangian model is suitable to predict the processes in the dilute spray regime of the combustion chamber. In particular, the prediction of the spray distribution and evolution is very good.

Calculated gas phase temperatures are higher than the experimental values which is explained by various reasons. First, the experimental data are probably underpredicted which is typical for CARS single shot measurements. Moreover, only a small portion of the total liquid flux was captured by the experimental techniques so that the energy consumed by droplet vaporization is underpredicted leading to too high values of gas temperature in the computation. Furthermore, there is no information of gas phase species profiles from experiment leading to uncertainties in evaluating the initial conditions for the computations.

Future studies should include the dense spray regime, and an extension of the present model into that region will be developed.

Moreover, the Reynolds stress model for turbulent spray flames will be employed to account for an improved simulation of the recirculation zone. Here the coupling terms of velocities and vaporization fluctuations need to be modeled.

In future, the pressure will also be increased into the high-pressure domain.

6 Acknowledgments

References

[1] Sender, J., Lecourt, R., Oschwald, M., Haidn, O. J.: *Application of Droplet-Tracking-Velocimetry to LOX/GH2 Coaxial-Spray Combustion with Varying Combustion Chamber Pressures*, Proceedings of the 13th Annual Conference on Liquid Atomization on Spray Systems, Florence, Italy, 145-154, 1997.

12

[2] Balakrishnan, G., *Studies of Hydrogen-Air Diffusion Flames and of Compressibility Effects Related to High-Speed Propulsion*, Ph.D. Thesis, University of California San Diego, CA, USA, 1993.

[3] Hollmann, C., Gutheil, E., *Proc. Comb. Inst. 26(1)*, 1731-1738, 1996.

[4] Hollmann, C., Gutheil, E., *Combust. Sci. and Tech.*, 135: 175-192, 1998.

[5] Schlotz, D., Gutheil, E., *15th Annual Conference on Liquid Atomization and Spray Systems*, July 5-7, 1999, Toulouse, France.

[6] Schlotz, D., Gutheil, E., *Combust. Sci. and Tech.*, 158: 195-210 (2000).

[7] Warnatz, J., Maas, U., Dibble, R. W., *Combustion*, Springer, Heidelberg, 1996.

[8] Faeth, G. M., *Evaporation and Combustion of Sprays, Prog. Energy Combust. Sci.*, 9, 1-76, 1983.

[9] Oefelein, J.: *A Perspective of Large Eddy Simulation and its Application to Liquid Combustion Systems*, Proc. 2nd Workshop on Rocket Combustion Modeling, Heilbronn, 2001.

[10] Miller, R. S., Bellan, J., *Proc. Combust. Inst.* **27**, 1611-1617, 1998.

[11] Burlaka, A., Borghi, R., *Simulation of Cryogenic Combustion with a new Engineering Model*, Proceedings of the Fourth Colloquium on Liquid Rocket Propulsion, Schntal, Oktober 1998.

[12] Brunner, M., Gutheil, E.: *A Reynolds Stress Model for Turbulent Two-Phase Flows*, Publication in Preparation, 2001.

[13] Gutheil, E., Williams, F. A.: *A Numerical and Asymptotic Investigation of Structures of Hydrogen-Air Diffusion Flames at Pressures and Temperatures of High-Speed Combustion*, Proc. Combust. Inst. 23, 513-521 (1991).

[14] Pope, S. B.: *PDF Methods for Turbulent Reactive Flows*, Prog. Energy Combust. Sci., Vol. 11, 119-129, 1985.

[15] Dopazo, C.: *Probability Density Function Approach of a Turbulent Axisymmetric Heated Jet. Centerline Evolution*, Phys. Fluids, Vol. 18, No. 4, 397-404, 1975.

[16] Peters, N., Rogg, B., *Reduced Kinetic Mechanisms for Applications in Combustion Systems*, Springer, Berlin (1993).

[17] Maas, U., Pope, S. B., *Combust. Flame*, 88, 239, 1992.

[18] Peters, N.: *Length Scales in Laminar and Turbulent Flames* in: Numerical Approaches to Combustion Modeling, (E. S. Oran, J. P. Boris, Eds.), Progress in Astronautics and Aeronautics, 155, 1991.

[19] Peters, N.: *Twenty-First Symposium (International) on Combustion*, The Combustion Institute, Pittsburgh, 1231-1250, 1986.

[20] Peters, N.: *Progr. Energy Combust. Sci.* 10: 319-339, 1984.

[21] Gutheil, E., Sirignano, W. A., *Combust. and Flame*, 113: 92-105, 1998.

[22] Gutheil, E.: *Structure and Extinction of Laminar Ethanol/Air Spray Flames.* Combustion Theory and Modeling **5**, 131-145 (2001).

[23] Schlotz, D., Brunner, M., Gutheil, E., Clauss, W., Sender, J.: *Modeling of Turbulent Spray Combustion under Cryogenic and Elevated Pressure Conditions.* Combust. Sci. and Tech., 2001, submitted.

[24] Abramzon, G., Sirignano, W. A., *Int. J. Heat Mass Transfer.* 9: 1605-1618. 1989.

[25] Amsden, A. A., O'Rourke, P. J., Butler, T. D.: *KIVA II, A Computer Program for Chemically Reactive Flows with Sprays.* Los Alamos National Laboratory Report LA-11560-MS, UC-96. 1989.

[26] *JSME Data Book, Thermophysical Properties of Fluids.* 1983.

[27] Yang, V., Lin N.N., Shueb, J.S., *Comb. Sci. and Tech.*, 97: 247-270, 1994.

[28] El-Gamal, M., Gutheil, E., Warnatz, J.: *The Structure of Laminar Premixed H_2-Air-Flames at Elevated Pressures*, Zeitschrift für Physikalische Chemie, 214. 4, 419-435 (2000).

STATISTICAL MODELING OF THE AIR-BLAST ATOMIZATION IN THE LAGRANGIAN COMPUTATION OF LIQUID SPRAY

M.GOROKHOVSKI

CORIA UMR/6614 CNRS University of Rouen, Mont Saint Aignan, France

I.   INTRODUCTION

When injection of liquid jet takes place into coflowing motion of high relative velocity gas, a wide range of turbulent eddies may impact on the liquid jet causing its breakup. This regime of atomization is often referred to as the air-blast atomization and is widely used in practical systems. The physics of air-blast atomization is very complex [1-5]. In addition to the gas turbulence-induced breakup, many other's random processes such as multiple droplets collision, turbulence in liquid, variations in the cavitating flow inside the injector, etc., contribute to the phenomenon of breakup. This implies that at each spray location, the spectra of size of produced droplets can be very large. Then the question of what are the probabilities of sizes that are involved into atomization, arises in the breakup modeling. Due to the complexity of phenomenon, it is too difficult to disclose clearly a dominant mechanism of air-blast breakup with expectation of a characteristic size of droplet. To this end, the basic idea behind the simulation undertaken in this paper, is as follows. The process of air-blast breakup is considered in the framework of cascade of uncorrelated breakage events in series , independently from the initial distribution of sizes. The stochastic modeling of droplets production under this hypotheses down to the critical (or maximum stable) size is the subject of this paper.

The cascade idea of breakup comes from the early work of Kolmogorov written in 1941 [6]. In this work, Kolmogorov described the breakup of solid particles as a discrete random process, where the probability to break each parent particle on a given number of parts is independent of the parent particle size. From Lyapunov's theorem, Kolmogorov has pointed out that such a general assumption leads to the log-normal distribution of particle size in the long-time limit. In this paper, the Kolmogorov's discrete model has been reproduced in the form of evolution equation for distribution function. The asymptotic solution of this equation has been applied to simulate the drop breakup alongside with Lagrangian model of spray dynamics. Performed computations of air-blast atomization are related to a spray close to the rocket engine configuration.

II.   KOLMOGOROV'S (1941) THEORY OF THE PARTICLE BREAKUP.

Let us consider an ensemble of breaking solid particles at discrete time moments $t=0,1,2,...$. These time moments are scaled by the breakup frequency v ($t=vt$). According to Komogorov[6], the number of particles $N(r,t)$ of size $\rho \le r$ was selected amongst all particles $N(t)$ at a given moment t. The expectations of total number of particles and of particles of size $\rho \le r$ were denoted as $\overline{N}(t)$ and $\overline{N}(r,t)$ correspondingly. Considering an outcome of breakup per unit time $[t, \ t+1]$ of a given parent particle of size r, the mean number $Q(\alpha)$ of secondary particles of size $\rho \le \alpha r$ ($0 \le \alpha \le 1$) was introduced. According to hypotheses of Kolmogorov, the probability to break each parent particle on a given number of parts is independent of the parent particle size. In other words, $Q(\alpha)$ does not depend of prehistory of breakup and is not influenced by others parent particles. By this assumption, Kolmogorov writes:

$$\overline{N}(r,t+1)=\int_0^1 \overline{N}\left(\frac{r}{\alpha},t\right)d\,Q(\alpha) \tag{1}$$

Introducing the logarithm of particle-size $x = \ln r$, Kolmogorov pointed out that

$$T(x,t)=\frac{\overline{N}(e^x,t)}{\overline{N}(t)}=\frac{N(e^x,t)}{N(t)} \tag{2}$$

Further, denoting $\xi = \ln \alpha$ and $Q(\alpha)= Q(1)\cdot S(\xi)$, equation (1) is rewritten by Kolmogorov in the following form:

$$T(x,t+1)= \int_{-\infty}^0 T(x-\xi,t)d\,S(\xi) \tag{3}$$

By Lyapunov's theorem, Kolmogorov stated that from discrete model (3), the long-time limit form of $T(x,t)$ tends to Gaussian function. Then the main result of Kolmogorov's work is that $N(r,t))$ is asymptotically governed by log-normal law.

III.   THE ASYMPTOTIC DIFFERENTIAL FORM OF THE DISCRETE KOLMOGOROV'S MODEL.

Here the discrete model (3) is represented by its differential approximation in the long time limit. Using parabolic scaling of variables $\tau = \varepsilon^2 t$, $y = \varepsilon x$, where ε is a scaling parameter and t is scaled by breakup frequency, the equation (3) can be written as

$$T(y,\tau+\varepsilon^2) = \int_{-\infty}^{0} T(y-\varepsilon\xi,\tau)s(\xi)d\xi \tag{4}$$

Expanding both the left-hand side and the expression under integral in (4), one gets

$$T(y,\tau+\varepsilon^2) = T(y,\tau) + \varepsilon^2 \frac{\partial T(y,\tau)}{\partial \tau} + O(\varepsilon^4)$$

$$T(y-\varepsilon\xi,\tau) = T(y,\tau) - \varepsilon\xi \frac{\partial T(y,\tau)}{\partial y} + \frac{1}{2!}(\varepsilon\xi)^2 \frac{\partial^2 T(y,\tau)}{\partial y^2} - \frac{1}{3!}(\varepsilon\xi)^3 \frac{\partial^3 T(y,\tau)}{\partial y^3} + O(\varepsilon^4)$$

Substituting these expansions in (4) and coming back to variables t and x, one yields:

$$\frac{\partial T(x,t)}{\partial t} + O(\varepsilon^4) = -\langle\xi\rangle \frac{\partial T(x,t)}{\partial x} + \frac{1}{2!}\langle\xi^2\rangle \frac{\partial^2 T(x,t)}{\partial x^2} - \frac{1}{3!}\frac{\partial^3 T(x,t)}{\partial x^3}\varepsilon^3 \int_{-\infty}^{0}\xi^3 s(\xi)d\xi + O(\varepsilon^4) \tag{5}$$

where $\langle\xi\rangle = \int_{-\infty}^{0}\xi\, s(\xi)d\xi$ and $\langle\xi^2\rangle = \int_{-\infty}^{0}\xi^2\, s(\xi)d\xi$ are two first moments of ξ. Assuming that the integral $\int_{0}^{1}|\ln\alpha|^3\, dQ(\alpha)$ is limited, the equation (5) can be written in the long-time limit $\varepsilon \to 0$ ($t \to \infty$), as

$$\frac{\partial T(x,t)}{\partial t} + v\langle\xi\rangle \frac{\partial T(x,t)}{\partial x} = \frac{1}{2!}v\langle\xi^2\rangle \frac{\partial^2 T(x,t)}{\partial x^2} \tag{6}$$

The dimensional time has been used in (6). The solution of (6) is Gaussian function. This repeats the main result of Kolmogorov[6]. At the same time, an influence of the initial distribution before breakup starts can be taken into account by using (6). The solution of (6) verifies to be:

$$T(x,t) = \int_{-\infty}^{0} \frac{1}{\sqrt{2\pi\langle\xi^2\rangle v t}} \exp\left[-\frac{(x-x_0)^2}{2\langle\xi^2\rangle v t}\right] T_0(x_0 - \langle\xi\rangle v t) dx_0 \tag{7}$$

where $T_0(x_0)$ is the initial distribution of the logarithm of droplet radius and x_0 is logarithm of radius of the parent drop. One can rewrite equation (6) for the normalized distribution of radius $f(r)$:

$$\frac{\partial f(r)}{\partial t} = -v\langle\xi\rangle \frac{\partial}{\partial r}(r f(r)) + \frac{1}{2} v\langle\xi^2\rangle \frac{\partial}{\partial r}\left(r\frac{\partial}{\partial r}(r f(r))\right) \tag{8}$$

The solution of this equation has the following form:

$$f(r,t) = \frac{1}{r} \int_0^\infty \frac{1}{\sqrt{2\pi\langle\xi^2\rangle v t}} \exp\left[-\frac{\left(\ln\frac{r_0}{r} + \langle\xi\rangle v t\right)^2}{2\langle\xi^2\rangle v t}\right] f_0(r_0) dr_0 \tag{9}$$

where $f_0(r_0)$ is the initial distribution of droplet radius before breakup starts.

IV.   IMPLEMENTATION INTO COMPUTATIONAL CODE KIVA II

IV.1   General procedure

The right hand side of equation (8) can be added to the transport spray equation[7] as a source term due to drop breakup. The modeling of the spray equation is often based on Lagrangian formulation[8]. The spray is considered to be composed of discrete parcels of particles, each of which represents a group of droplets of similar size, velocity and position. These groups of droplets are followed as they interact and exchange momentum and energy with surrounding gas. The basic ideas of this method, including the modeling of turbulent dispersion of

particles, are presented in [9]. Here, the Lagrangian tracking is coupled with stochastic computing of breakup. Two additional physical processes were included in the Monte Carlo procedure. Namely, the product droplet velocity has been modeled and the breakup has been considered down to the local magnitude of the critical (or maximum stable) radius, r_{cr}. The liquid fuel was injected in the axial nozzle direction in form of discrete parcels of drops with characteristic size equal to the exit nozzle radius. The injection velocity was determined from the known liquid injection rate.

Let us consider the motion of a given $j-th$ primary parcel that undergoes breakup. Before breakup starts, the distribution function associated with this parcel, is Dirac function at radius of the parent drop. After passage of time, which is inversely the breakup frequency, the new droplets arise due to breakup. In sequel, the droplet-radius distribution function changes. We suppose that the new distribution may be described according to solution (9) taken at $vt = 1$ with $\langle \xi \rangle$ and $\langle \xi^2 \rangle$ as parameters of the model. In order to alleviate computations, we can proceed the following way. Let us assume that once every breakup time scale, all outcomes of breakup in the given parent parcel are in mean (over many computations), recovered by one new parcel that replaces the parent one. The radius of droplet associated with produced parcel is sampled from (9). The new number of droplets is computed by mass conservation from the primary parcel to the secondary one. After the sampling procedure, the current time, t, prescribed for produced parcel is counted from zero and Lagrangian tracking is continued up to the moment ($vt = 1$) of the further breakup.

In computations, we used expressions obtained for the distribution of the logarithm of radius. The starting distribution for the logarithm of droplet radius in $j-th$ primary parcel is

$$T_{0j}(x_0) = \delta(x_0 - x_j) \tag{10}$$

Using this distribution function in (7) at $vt = 1$, one can express the solution by the error function erf :

$$T_j(x,t) = \frac{1}{2}\left[1 + erf\left(\frac{x - x_j - \langle \xi \rangle}{\sqrt{2\langle \xi^2 \rangle}}\right)\right] \tag{11}$$

The product droplet velocity is computed by adding to the primary parcel velocity a velocity $\mathbf{w}_{bu}$, which is randomly distributed in a plane normal to the relative velocity vector between the parent droplet and gas. The quantity of $\left|\mathbf{w}_{bu}\right|$ is determined by the mean local Sauter radius of parent drops, r_{32}, and the breakup frequency, V:

$$\left|\mathbf{w}_{bu}\right| = r_{32} V \tag{12}$$

IV.2 Critical radius, breakup frequency

The critical (or maximum stable) radius is determined when disruptive hydrodynamic forces are balanced by capillary forces:

$$r_{cr} = We_{cr}\delta / \rho_g u_r^2 \tag{13}$$

where u_r is the relative between liquid and gas velocity, δ is the surface tension coefficient, We_{cr} is the critical Weber number, which can be taken of order one over a large interval of Ohnesorge numbers [10,11]. In the paper, written in 1949 [12], Kolmogorov considered the stretched drop of insoluble liquid that was submerged in a turbulent flow. Using the Obuchov-Kolmogorov's scaling law for the velocity difference across a size when the surface tension force becomes significant, Kolmogorov introduced a critical size of produced droplets as:

$$r_{cr} = \frac{1}{2}\left(\frac{We_{cr}\delta}{\varepsilon^{2/3}\rho_g}\right)^{3/5} \quad \text{if } 2\,r \gg \eta \tag{14}$$

$$r_{cr} = \frac{1}{2}\left(\frac{We_{cr}\delta v}{\varepsilon\rho_g}\right)^{1/3} \quad \text{if } 2\,r \ll \eta \tag{15}$$

where ε is the mean viscous dissipation rate and ρ_g is density in the gas.

An estimation of r_{cr} by using experimental data from [4] gives an enhanced magnitude of r_{cr} comparing to the measurements. In order to account for the inertia of liquid, namely for the density of the liquid ρ_l, the expression (14) can be modified. Estimating the mean square of relative droplet-to-gas velocity by mean viscous dissipation and Stokes time scale[13,14],

$$\left\langle u_r^2 \right\rangle \approx \varepsilon \tau_{st} \qquad (16)$$

one yields a new expression for critical radius:

$$r_{cr} = \frac{36^{1/3}}{2} \left(\frac{We_{cr} \delta v}{\varepsilon \rho_l} \right)^{1/3} \qquad (17)$$

Using the experimental data from [4]: water density, 1000 kg/m³; gas viscosity, 1.5×10^{-5} m²/s; gas orifice size, 2.1 mm; surface tension, 0.07 kg/s²; gas injection velocity, 140 m/s and by setting the turbulent gas velocity at one tenth of the gas injection velocity, one gives for critical radius 3×10^{-5} m, which is of the same order that was measured in [4]. At the same time, expressions (17) requires a reliable knowledge of viscous dissipation rate, which is a problem in the turbulence computation. For these reasons, the critical radius is calculated in this work by the standard expression (13), where $u_r = \mathbf{v}_g - \mathbf{v}_P$ is calculated by the mean relative velocity between gas and liquid particle, computed by the model of turbulent dispersion of particles [13]. Note that introducing the turbulent Weber number, $We_{tur} = \dfrac{\rho_g l_{tur} u_{tur}^2}{\delta}$, and using (16), one may write for the critical Weber number:

$$We_{cr} = \frac{1}{36} \frac{\rho_l}{\rho_g} Re_{tur} We_{tur} \left(\frac{2 r_{cr}}{l_{tur}} \right)^3 \qquad (18)$$

Assuming that at scales where breakup takes place Re_{tur} is of order of unity and $l_{tur} \approx \eta$, one may propose:

$$\frac{2 r_{cr}}{\eta} = 3.3 \left(\frac{We_\eta}{We_{cr}} \right)^{-\frac{1}{3}} \left(\frac{\rho_g}{\rho_l} \right)^{\frac{1}{3}} \qquad (19)$$

The choice of the breakup frequency has to be stated from the physics of atomization. In this paper, the breakup time scale is taken from [15-17]:

$$v = B \frac{\left| \mathbf{v}_g - \mathbf{v}_P \right|}{r_{32}} \sqrt{\frac{\rho_g}{\rho_l}} \qquad (20)$$

where r_{32} is the local Sauter mean radius of parent drops and $B = 1/\sqrt{3}$ is taken from TAB model [18].

IV.3   Choice of parameters $\langle \xi \rangle$ and $\langle \xi^2 \rangle$

Multiplying (8) by r and integrating over the entire r – range give us an expression for the first moment

$$\langle r \rangle = \langle r \rangle_{t=0} \exp\left[\nu \left(\langle \xi \rangle + 0.5\langle \xi^2 \rangle \right) t \right] \tag{21}$$

The condition

$$\langle \xi \rangle < -\frac{1}{2}\langle \xi^2 \rangle \tag{22}$$

provides for $\dfrac{\langle r \rangle}{\langle r \rangle_{t=0}} < 0$. In this paper, the magnitude for $\langle \xi^2 \rangle$ is supposed to be proportional to

the maximal dispersion of radius $\langle \xi^2 \rangle \propto \ln 1 - \ln \dfrac{r_{cr}}{r_{32}}$. Replacing in (19) η by the local Sauter

mean diameter of parent drops, one may assume that

$$\langle \xi^2 \rangle \approx -\ln \frac{r_{cr}}{r_{32}} \approx const \cdot \ln\left(\frac{We_{r_{32}}}{We_{cr}} \right)^{1/3} \tag{23}$$

and $\langle \xi \rangle$ is an arbitrary parameter to be taken according to (22) and (23).

V.   EXAMPLE OF LAGRANGIAN COMPUTATION OF THE ATOMIZING SPRAY

The configuration and inlet parameters from the CORIA's injector[19] are used in the computation. In this experiment, the round jet of water issues from the central tube ($D_l = 1.8mm$) at low velocity and atomizes by a parallel coflow of air issuing at high velocity from an annular duct ($D_g = 3.4mm$). An example of spatial distributions of drops in the spray, the schematic of the injector and the evolution in time of distributions of droplet-size probability density function (pdf) at two cross sections in the near-nozzle region are given in Fig.1. The pdf distributions are scaled on the total drops number crossing the given section at the given time moment. The statistics of radius at (3-5) mm shows mostly the large unbroken drops of size of the injector orifice that are accompanied by small striped droplets. From pdf's

at (7-9) mm, it is seen that the probability to find drops of size of the injector orifice is essentially decreased while new droplets are produced with radius from 50 μm to 250 μm. These figures and zooming given in Fig.2 show that a broad spectra of droplet size is presented by computations with a co-existence of large drops and small droplets. Computations are performed for different inlet air and water velocities represented in [19] providing for the different magnitudes of the parameter $J = \dfrac{\rho_g u_g^2}{\rho_l u_l^2}$ and the inlet Weber number. The qualitative agreement have been obtained between measured impact liquid core and the estimated length of the zone presented by computed blobs of size of the injector orifice. The modified numerical code with the stochastic model of breakup is specifically target on the computation of the spray combustion in the configuration likely to rocket engine.

VI.   CONCLUSION

A new sub-grid-scale stochastic model of drops air-blast breakup is presented in this paper. The stochastic process is considered in the framework of cascade of uncorrelated breakage events in series down to the critical size, independently from the initial distribution of sizes. To this end, the Kolmogorov's discrete model of particle breakup has been reproduced in the form of evolution equation for distribution function. The asymptotic solution of this equation has been applied to simulate the drop breakup alongside with Lagrangian model of spray dynamics. Performed computations of air-blast atomization are related to a spray close to the rocket engine configuration. A broad spectra of droplet size is simulated at each spray location with a co-existence of large drops and small droplets. The evolution of shape of the droplet-size pdf's is shown at different sections in downstream direction.

REFERENCES

[1]Lefebvre A.H. Atomization and Sprays. New York: Hemisphere (1989)

[2]Liu A.B., Reitz R.D. "Mechanism of Air-Assisted Liquid Atomization," J. Atom. Sprays, 3, 55-75 (1993)

[3]Chigier N., Reitz R.D, "Regimes of jet breakup mechanisms (physical aspects). In Recent Advances in Spray Combustion: Spray Atomization Drop Burning Phenomena", ed. K.K.Kuo, 1:109-135, Reston, AIAA (1996)

[4]Lasheras J.C., Villermaux E., Hopfinger E.J., "Break-up and atomization of round water jet by a high-speed annular air jet" J. Fluid Mech., 357, 351-379, 1998

[5]Hopfinger E.J., "Atomization of a Liquid Jet by a Coaxial Gas Jet: A Critical Review", in *"Combustion dans les moteurs fusées "*, Cépaduès Editions, 2001

[6]Kolmogorov A.N., "On the Log-Normal Distribution of Particles Sizes During Break-Up Process," Dokl. Akad. Nauk. SSSR , XXXI, 2, 99-101 (1941)

[7]Williams F.A., "Spray combustion and atomization" Phys. Fluids, 1, 541, 1958.

[8]Dukowicz J.K., "A particle-fluid numerical model for liquid sprays," J. Comput. Phys., 35, 229 (1980)

[9]Amsden A.A., O'Rourke P.J., Butler T.D., The KIVA-II: A Computer Program for Chemically Reactive Flows with Sprays, LA-11560-MS (1989)

[10]Gel'fand B.E., Gubin S.A., Kogarko S.M., Komar S.P., Singularities of the Breakup of Viscous Liquid Droplets in Shoc Waves, *J. Engng Phys.*, vol. 25, pp.1140-1142. 1975.

[11]Pilch M., Erdman C.A., Use of Breakup Time Data and Velocity History Data to Predict the Maximum Size of Stable Fragments for Acceleration-Induced Breakup of a Liquid Drop, *Int. J. Multiphase Flow*, vol. 13, 6, pp. 741-757, 1987

[12]Kolmogorov A.N., On the Drops Breakup in the Turbulent Flow, *Gidromekanika*, DAN, vol. LXVI, NS, pp. 825-828, 1949.

[13]Sabel'nikov V.A., private communication.

[14]Kuznezov V.R., Sabel'nikov V.A. *Turbulence and Combustion, Hemisphere Publishing Corporation*, 362 p., 1990.

[15]O'Rourke P.J., Collective Drop Effects on Vaporizing Liquid Sprays, *Ph. D Thesis 1532-T, Princeton University*, 1981.

[16]Faeth G.M., Hsiang L.P., Wu P.K., Structure and Breakup Properties of Sprays, *Int. J. Multiphase Flow*, vol. 21, pp.99-127, 1995.

[17]Chigier N.A., *The Physics of Atomization. Plenary Lecture. ICLASS 91, Gaithersburg, MD, USA, July 1991.*

[18]O'Rourke P.J., Amsden A.A., The TAB Method for *Numerical* Calculations of Spray Droplet Breakup, *SAE Tech. Pap.*, 872089, 1987.

[19]Stepowski D., Werquin O. Rapport du CORIA, au GDR Moteur Fusée, Janvier 1999, SEP, R13.35, 27 p.

t=0.6 sec   t=2 sec   t=3 sec

spatial distribution of blobs, cm

3.4mm

2.3mm

1.8mm

air (180m/s)

water (4.07m/s)
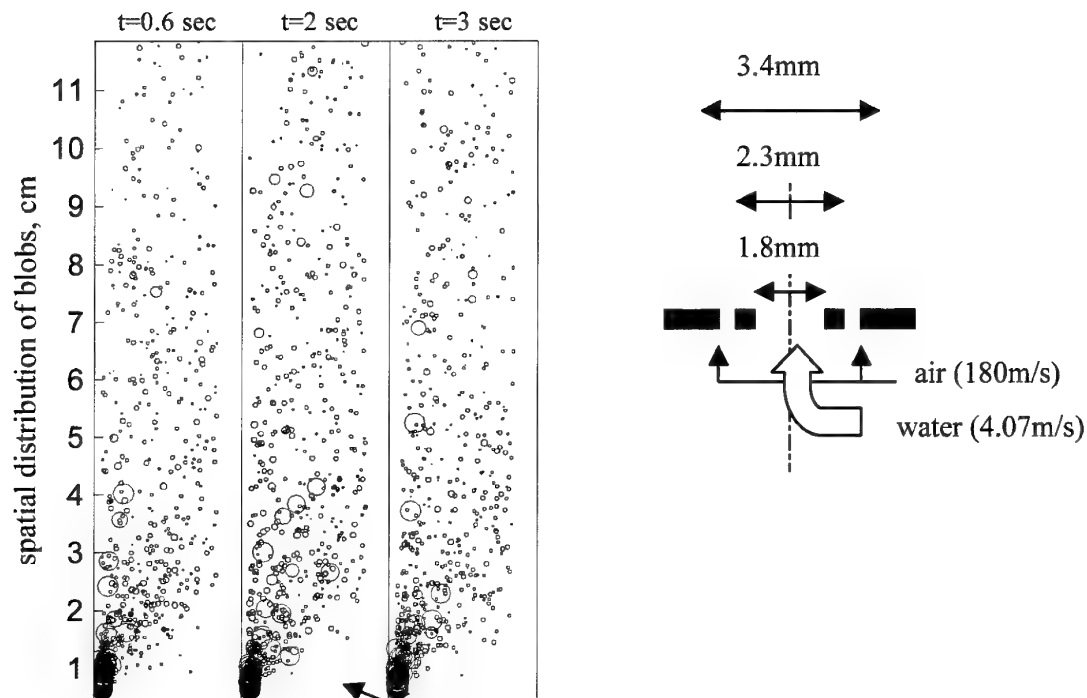
PDF's of liquid size at [3-5]mm and at [7-9]mm from injector orifice

PDF

time (s)

droplet radius, μm
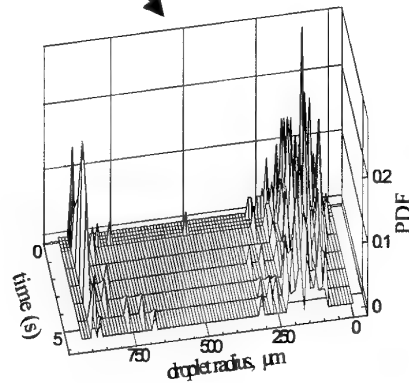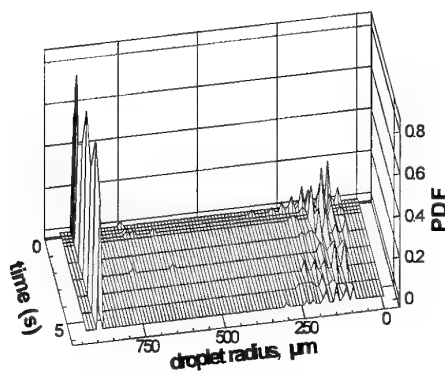
PDF

time (s)

droplet radius, μm

Fig.1 Computed one-side spatial distributions of drops and PDF's of size at different sections. CORIA GDR injector.

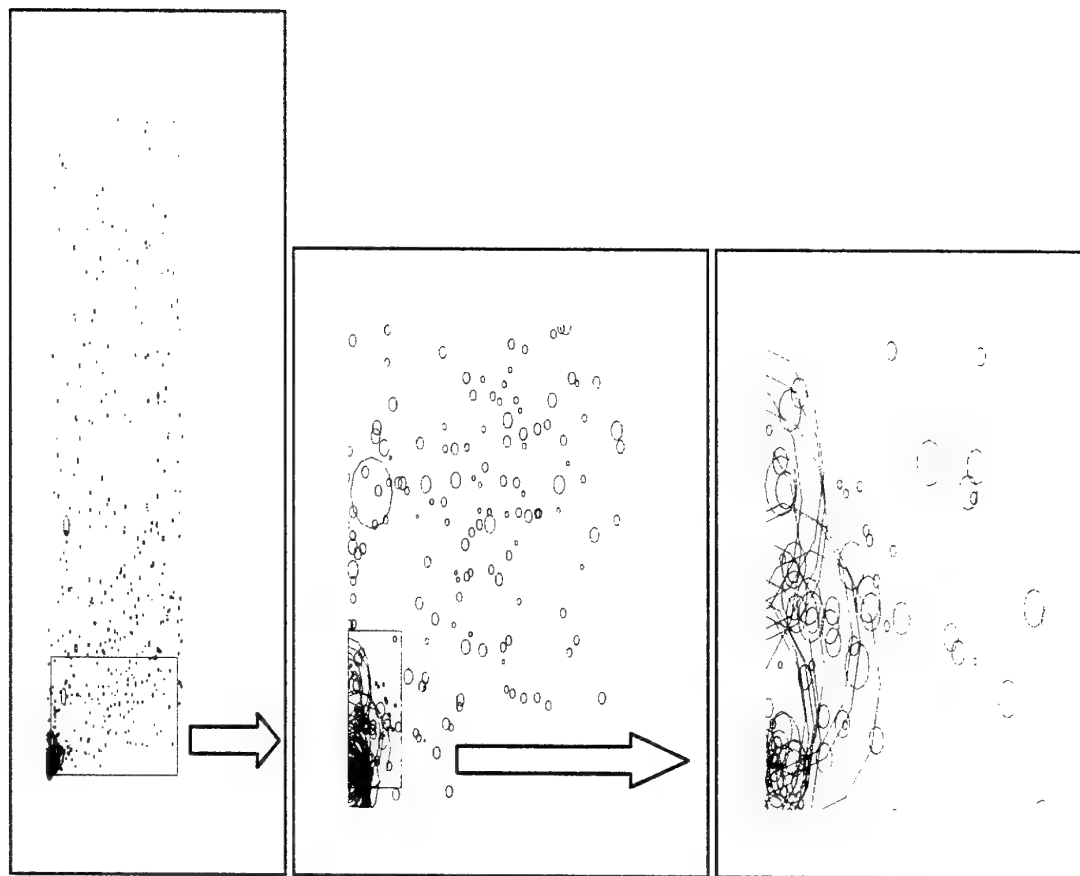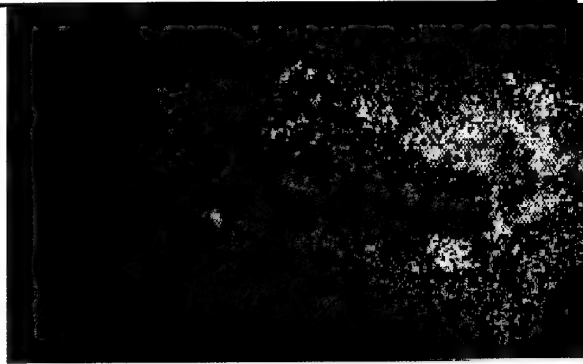**Fig.2** Zooming of spatial distributions of blobs computed in the near-injector region.

2nd International Workshop

ROCKET COMBUSTION MODELING

TEST CASE RCM-2

Mascotte single injector
- 10 bar -

March 25 – 27, 2001
DLR, Lampoldshausen

French-German Research on Liquid Rocket Combustion

I- GENERAL PRESENTATION

The MASCOTTE cryogenic combustion test facility was developed by ONERA to study fundamental processes which are involved in the combustion of cryogenic propellants, namely liquid oxygen (LOX) and gaseous hydrogen (GH2). Three versions of this test facility have been built since the project was started in 1991. The first tests at atmospheric pressure were performed in January 1994, while pressures up to 10 bar were achieved in fall 1995. Test case RCM2 will consist of modeling the MASCOTTE combustor at a chamber pressure of 10 bar. The details for both the test facility geometry and the operating conditions required for the numerical simulations are listed below.

II- GEOMETRY

a) Test combustor

The MASCOTTE test combustor has a square section of 50 mm x 50 mm (Figure 1).

The injector head consists of a single coaxial injector element.

Combustion is initiated by using an H2/O2 igniter (O/F = 4) for roughly 2 seconds.

Figure 2 summarizes the geometry of the combustion chamber used for tests at 10 bar . The black dots indicate the locations of wall temperature transducers.

b) Injector

The MASCOTTE injector is a shear-coaxial element consisting of a core of liquid oxygen surrounded by a high speed flow of gaseous hydrogen to provide good atomization properties.
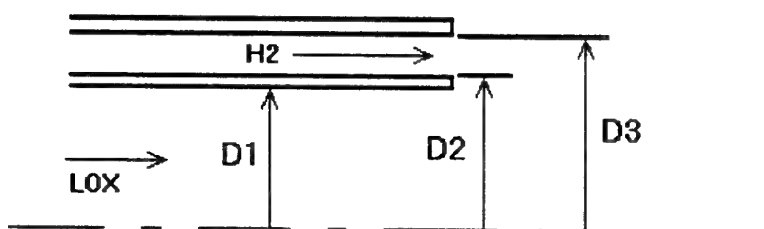
The dimensions of the injector are listed below.

	D1	**D2**	**D3**
DIAMETER	5.0 mm	5.6 mm	12.0 mm

Figure 3 shows the actual injector head geometry. However, computations may be performed with the above simplified geometry.

III- TEST OPERATING CONDITIONS

a) Operating point

The operating point chosen for this test case is a 10 bar case which has been extensively investigated experimentally. The operating conditions are defined in the following table:

PRESSURE	O/F	$\dot{m}$ (LOX)	$\dot{m}$ (H2)
10 bar	2.11	50 g/s	23.7 g/s

b) Propellants

Oxygen is injected under liquid conditions at 85 K, while hydrogen is injected under gaseous conditions at a temperature of approximately 287 K.

The physical properties of the propellants are summarized below:

Conditions	H2	O2
Pressure	1 MPa	1 MPa
Massflow	23.7 g/s	50 g/s
Temperature	287 K	85 K
Density	$0.84\ kg/m^3$	$1170\ kg/m^3$
C_p	14300 J/kg/K	1690 J/kg/K
Velocity	319 m/s	2.18 m/s
Viscosity	8.6×10^{-6} kg/m/s	1.94×10^{-4} kg/m/s
Surface tension	-	1.44×10^{-2} N/m

c) Turbulence

No data are yet available regarding the turbulence level at the injector exit. However, in order to make the comparison between various computations easier, we propose fixing the kinetic energy level at $\tau = 5\ \%$ ($\tau^2 = 2/3\ k\ /\ U^2_{inj}$), where U_{inj} is the hydrogen injection velocity. In addition, we recommend deriving the value of turbulence dissipation ε at the inlet using a turbulence length of 4 mm as a representative scale of the GH2 injection ring.

IV- GENERAL DATA FOR COMPUTATIONS

The list below describes the methods which should be used for this simulation.

- Although the chamber has a square cross section, computations may be performed in an axisymmetrical cylindrical geometry with the same cross section as the actual chamber.

- Computational Domain

  - A computation of the entire chamber (i.e., including the nozzle) is preferred.

  - If there are problems, computations may be performed for a shorter chamber (without the nozzle) with the following characteristics:

    - Chamber length = 400 mm

    - Exit boundary condition: Constant pressure, p = 10 bar.

    - An adiabatic wall boundary condition may be used.

- Droplet Injection

  - Injection on conical solid boundary representing the liquid core: length of core - 7.8 mm (if not possible, droplets may be injected at the injector exit).

Injection boundary

7.8 mm
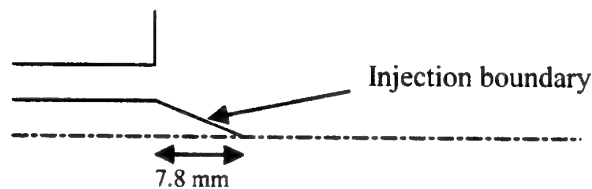
Flow visualizations and optical particle sizing have been achieved at 10 bar, which show that the atomization process is very complex and far from being complete (presence of ligaments). Nevertheless, some data could be obtained by means of a one-component PDPA (Phase Doppler Particle Analyzer) at 30 mm from the injector with an acceptable validation rate (47%). These measurements represent the droplet data at the closest location from the injector exit and can be used as inlet boundary condition. In order to fit these data with a Rosin-Rammler distribution, the PDPA distribution has been truncated at 250 µm by removing a small number of big droplets. This leads to the following distribution :

Rosin-Rammler distribution : $1 - v_c(D) = \exp[-(D/D_{RR})^N]$, where $v_c(D)$ is the cumulative volume undersize distribution, with $D_{RR} = 130$ micron, N = 2.25

Participants may choose from the following :

- the above distribution with the initial axial velocity of drops, Vinj = 10 m/s for all drops

- one single droplet size of D32 = 82 micron (which is the Sauter Mean Diameter of the above distribution), initial axial velocity of drops, Vinj = 10 m/s

- For the angle of injection, the following function derived from experimental results (Ref. 6) can be used: $\theta(x) = \arctan[R_i(1-x/L_c)/(x+R_i/\tan\theta_i)]$

  where $\theta_i = \theta(0)$, $\tan\theta_i = 0.68(U_{gas}/U_{liq}-1)\sqrt{\rho_{gas}/\rho_{liq}}$,

$R_i = D_1/2$ (see section II-b), L_c is the length of the core, and x is the axial distance from the injector exit to the point of injection.

- Physical Models

  - Combustion, turbulence, and evaporation models are not specified. Participants are free to choose these models as they see fit.

V- EXAMPLES OF AVAILABLE DATA

Each test run performed on MASCOTTE provides a set of standard temporal data, such as propellant mass flow rate, pressures, wall temperatures, and propellant temperature at the inlet.

In addition to classical measurements, several test campaigns have been carried out on MASCOTTE using non-intrusive or intrusive combustion diagnostics: laser-induced fluorescence of OH, fluorescence of gaseous oxygen, laser tomography, Phase Doppler Particle Analysis, measurement of liquid/gas mass fraction by a fiber optic device.

Figure 4 summarizes the locations where these various diagnostics have been applied.

Much of the test data obtained in the MASCOTTE test facility has been reported in the literature (see references). Figures 5-9 show some typical results (reference [5]).

An instantaneous OH emission image is presented in Figure 5, whereas Figure 6 presents the probability distribution of the flame location based on O2 LIF results.

Figure 7 shows typical OH images. Figure 8 shows the radial distribution of mean temperature, as well as the standard deviation, near the injector exit. Figure 9 displays the axial evolution of temperature at a fixed radial position for both 1 and 10 bar.

VI- REQUESTED RESULTS

The results of numerical computations must be presented in such a way that they can be compared to experimental data. For this reason, the participants are requested to provide the following information (to the extent possible depending on the output of the numerical code):

- Radial profiles of mean temperature and standard deviation at CARS measurement locations (x/D1 = 2; 10; 16; 20; 36; 40; 43; 50; 60) (Figures 4 and 8). x represents the axial distance from the injector exit (see Figure 2), D1 = 5 mm.

- Mean temperature as a function of distance from the injector exit at four radial locations (y/D1 = 1; 2; 3; 4) (see Fig. 9).

- OH mass fraction contours in the near field of the injector (up to 150 mm downstream); see Fig. 7.

- Gaseous oxygen contours in the near field of the injector (up to 150 mm downstream). An example of the probability distribution of flame location is given for an 8 bar case in Figure 6.

- Axial profile of mean wall temperature (adiabatic wall temperature).

VII- REFERENCES

[1]   Habiballah. M, Vingert. L, Traineau. JC, Vuillermoz. P, "MASCOTTE : a test bench for cryogenic combustion research", IAF-96-S.2.03, *47th International Astronautical Congress*, (Beijing, China), October 7-10, 1996.

[2]   Bazile. R, Guerre. S and Stepowski. D, "Planar Laser Induced Fluorescence of Hot O2 in MASCOTTE", *Second French-German Colloquium on Research on Liquid Rocket Propulsion*, (Aachen, Germany), 1996.

[3]   Herding. G, Snyder. R, Scouflaire. P, Rolon. C and Candel. S, "Emission and Laser Induced Fluorescence Imaging of Cryogenic Propellant Combustion", *Conference on Propulsive Flows in Space Transportation Systems"*, (Bordeaux, France), pp 1-14, 1995.

[4]   Brummund. U et al, Péalat. M et al and Candel. S et al "Laser Diagnostics for Cryogenic Propellant Combustion Studies", *Proceeding of the 2nd International Symposium on Liquid Rocket Propulsion"* (Châtillon, France), 1995, pp. 19.1-19.22.

[5]   Candel. S, Herding. G, Snyder. R, Scoufflaire. P, Rolon. C, Vingert. L, Habiballah. M, Grish. F, Péalat. M, Bouchardy. P, Stepowski. D, Cessou. A, Colin. P, "Experimental investigation of shear-coaxial cryogenic jet flame", *Third International Symposium on Space Propulsion*, (Beijing, China), August 11-13, 1997.

[6]   Caré, I. Etude d'un injecteur coaxial assisté. Thèse de doctorat. Université de Rouen, 1990.

In case of further information, you may contact:

mohammed.habiballah@onera.fr
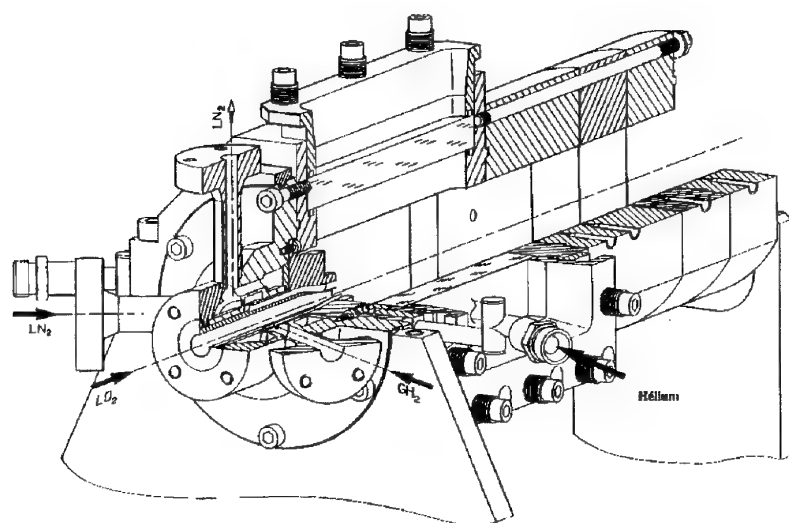
Figure 1: MASCOTTE Combustor
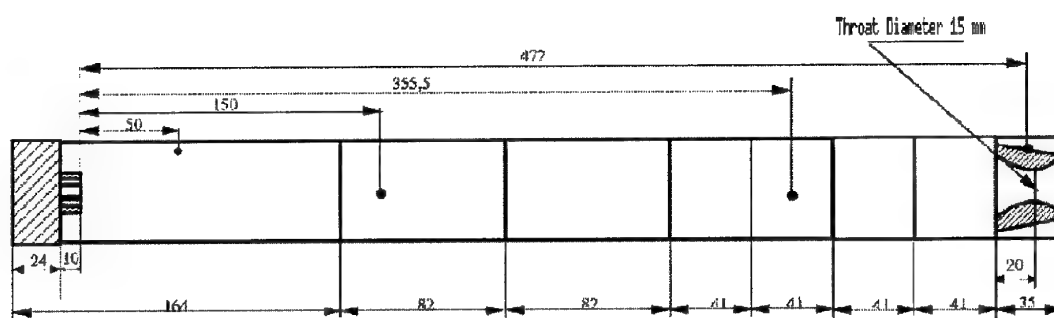
Figure 2: Combustor geometry (in mm) for the 10 bar case
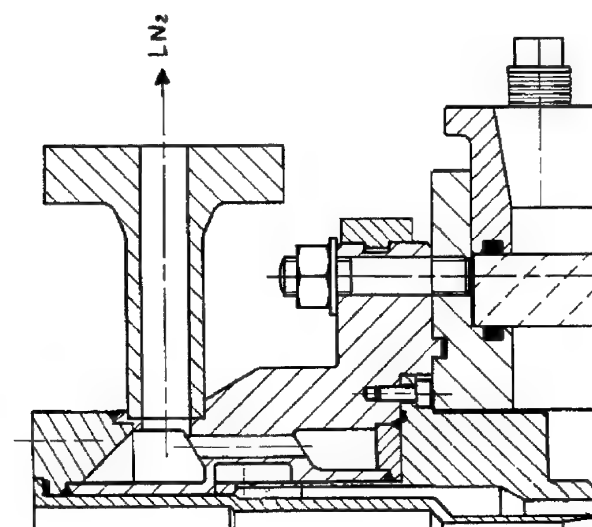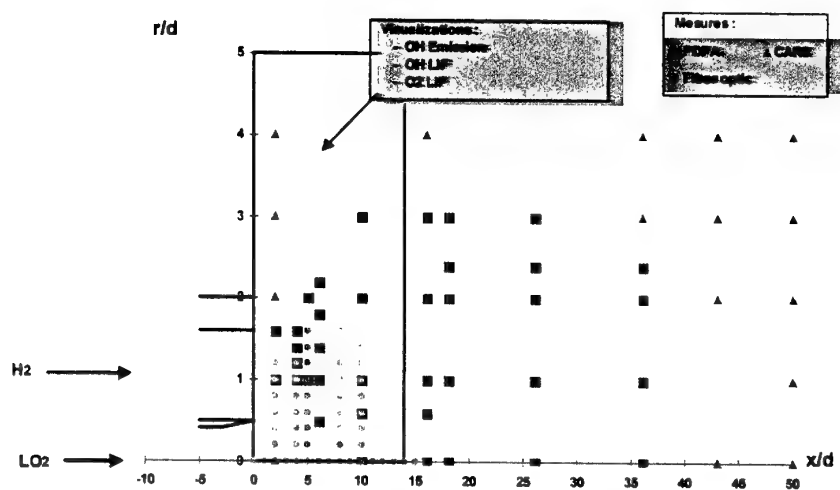

Figure 3: Injector head

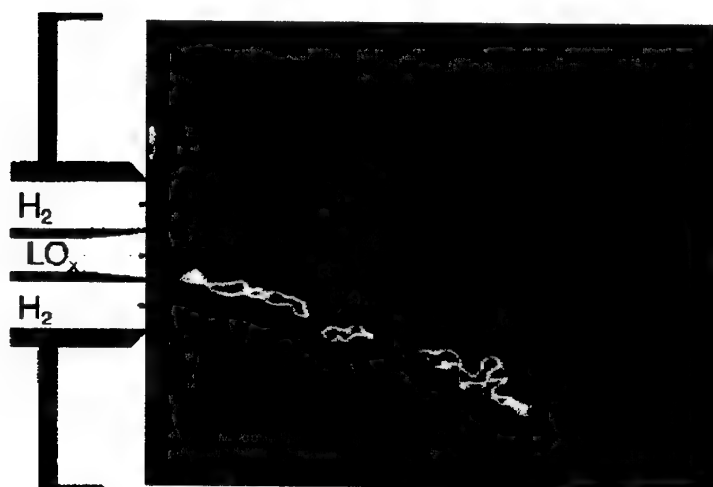Figure 4: CARS, PDPA, and fiber optic measurement locations

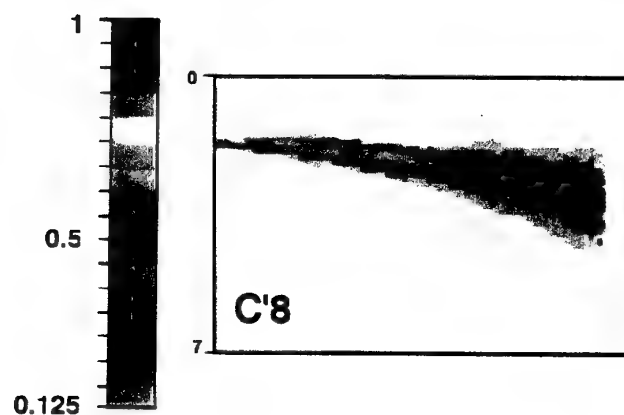Figure 5: Instantaneous LIF image of OH emission

Figure 6: Probability distribution of flame location based on O2 LIF results (8 bar)
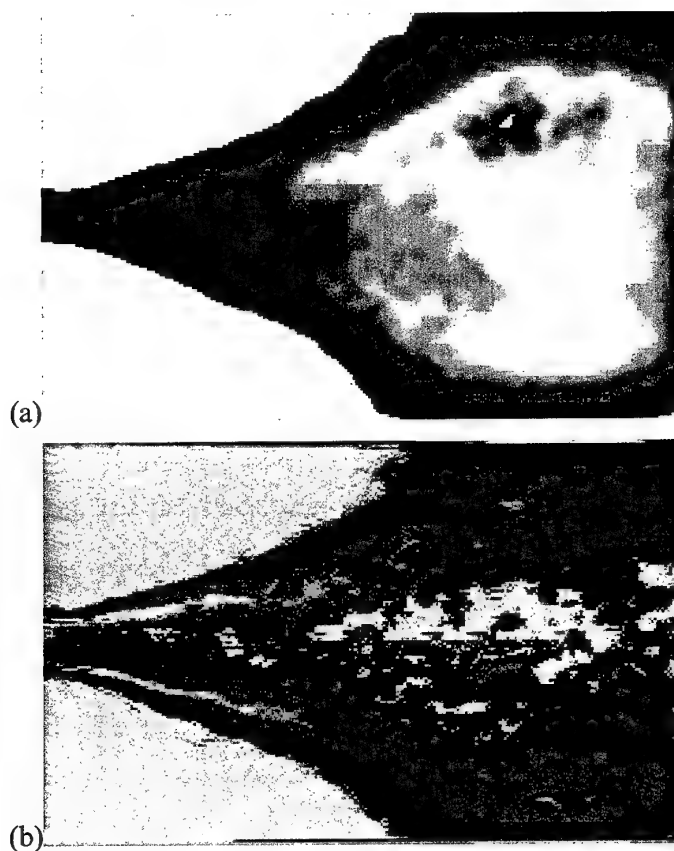
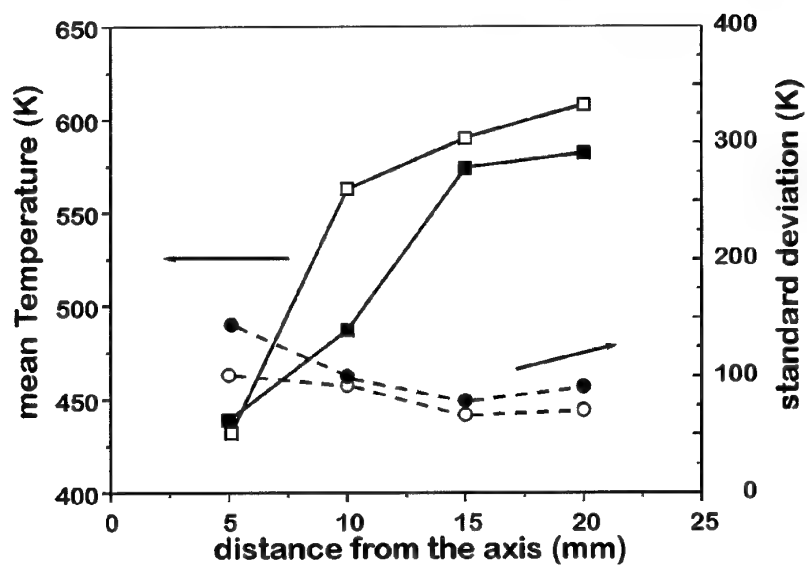Fig. 7: Average emission image a) and Abel-transformed emission image b) for operating point A-10, p = 10 bar.

Fig 8: Mean temperature (squares) and standard deviation of temperature (circles) recorded as a function of distance from axis. The black symbols correspond to the operating conditions specified for this test case.
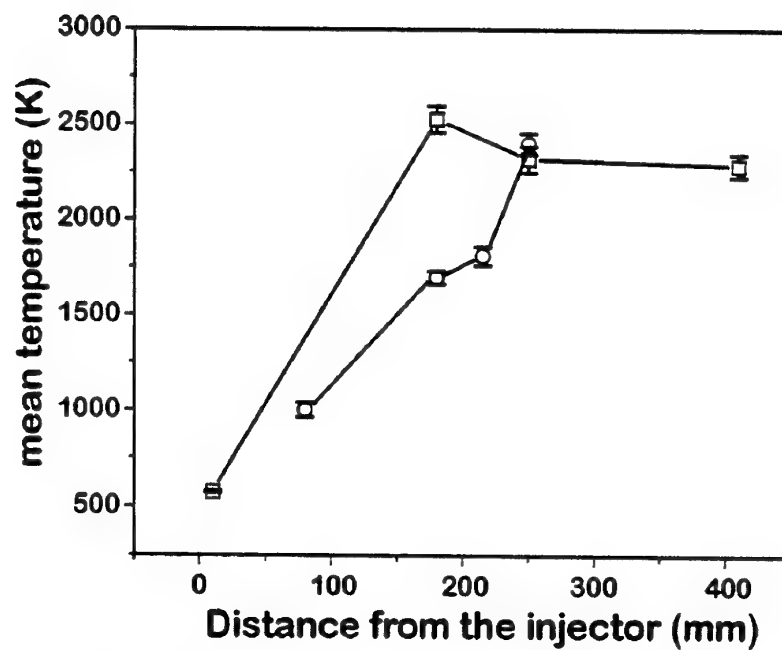
Fig 9: Mean temperature profiles recorded as a function of distance from the injector. The circles correspond to $p = 1$ bar and squares to $p = 10$ bar

MODELING OF MASCOTTE 10 BAR CASE WITH THESEE CODE WITH AND WITHOUT A SECONDARY ATOMIZATION MODEL

Emmanuel Bodèle, Iskender Gökalp
Centre National de la Recherche Scientifique
Laboratoire de Combustion et Systèmes Réactifs
1c Avenue de la Recherche Scientifique
45071 Orléans Cedex 2 France

Stephan Zurbach, Didier Saucereau
SNECMA Moteurs
Groupe SNECMA
BP 802 Forêt de Vernon
27208 Vernon France

Introduction

This paper presents the results of numerical simulations corresponding to the MASCOTTE 10 bar case, done by LCSR and SNECMA. These computation concern mainly the comparison between two cases : one case with a secondary atomization model developed at LCSR and one case without secondary atomization. In this paper we will describe shortly the secondary atomization model (other details are available in ref. [1,2]), the operating point (condition of injection, computational domain, …), and finally we will discussed briefly the main results issuing of these computations.

The secondary atomization model

The secondary atomization model is based on an experimental study which concerns the characterisation of the secondary break-up process in terms of break-up regimes, characteristic times and secondary distributions (for mores details see ref. [3]).
The break-up regime is determine with the following correlation:

$$\frac{We}{\sqrt{Re}} = C.DR^{0.25}.VR^{-0.5}$$

Where DR and VR represent respectively the density en viscosity ratios between the gaseous and liquid phases. The value of the constant C determine the transition between the 3 break-up regimes considered in this study: 0.25 for bag break-up, 0.7 for transitional break-up and 0.9 for shear break-up.

When a droplet is in one of these 3 break-up regimes, i.e. C greater than 0.25, an evaluation of the duration for the break-up time called initiation time T_{ini} is done with the relation:

$$T_{ini} = 0.75\ T\ We^{-0.06} \quad where \quad T = \frac{D_0}{V}\sqrt{\frac{\rho_l}{\rho_g}}$$

Finally, after a duration equal to Tini, the break-up occurs, and the initial droplet is decomposed in secondary fragments following a distribution in size and number, as shown in the table below:

Break-up regime	Size of secondary fragments (fraction of initial droplet diameter)			
	10%	30%	50%	Residual
Bag break-up	2	2	1	93,60%
Transitional Break-up	3	1	1	94,50%
Shear Break-up	2	4	2	86,20%

Operating point

The specification for the MASCOTTE 10 bar case are respectively 10 bar, 2.11, 50g/s and 23.7g/s for pressure, mixture ratio, mass flow rate of liquid oxygen and mass flow rate of gaseous hydrogen. Liquid oxygen is introduce in the computational domain with a Rosin Rammler distribution with $D_{32}=82\mu m$ at the surface of a liquid core as shown in figures 1 and 2 .

Computational domain and liquid oxygen injection

The computational domain consists in a 2D axisymetric geometry (fig. 1). The domain is 400 mm long and 28 mm for radius. The nozzle is not modelled. Droplets are introduced in the computational domain with a constant normal velocity (fig.2).

Overview of the THESEE code and condition of simulation

The code used for these computations is the THESEE code operated by SNECMA. This solver can operate with 2D or 3D configurations, multiphase, multispecies turbulent reactive flows.

The computations are performed with the following properties:
- Compressible reactive flow
- K-e turbulence model
- EBU combustion model
- Sirignano-Delplanque vaporization model
- Variable thermodynamic properties for the liquid oxygen
- Ideal gas law and variable thermodynamic for hydrogen

In the computational domain, four species (3 gaseous and 1 liquid) are considered : gaseous hydrogen (GH_2), gaseous oxygen (GO_2) obtain by vaporization of liquid oxygen (LOX) and gaseous water (H_2O). A single chemical reaction is used to obtain H_2O from gaseous hydrogen and gaseous oxygen:

$$H_2 + \frac{1}{2}O_2 \rightarrow Pr\,oducts(H_2O + Dissociation)$$

The Cv for H_2O is corrected to take into account the dissociation processes of water at high temperature. All the properties for liquid and gaseous phases are function of temperature.

Numerical results

The results presented in this part are essentially a comparison between the case with the secondary atomization model activated and the case without the secondary atomization model. The total CPU time to obtain all these results is about 300 hours

Mass fraction contours

On figures 3 and 4 are represented the mass fraction for the 3 gaseous species present in the computational domain. With these figures is it easy to see the apparition of gaseous oxygen near of the liquid injection zone due to the vaporization and the rapid disappearing of the gaseous oxygen and appearing of gaseous water due to the combustion process.

The reaction rate

On figures 5 and 6 the reaction rate is represented for the two cases of computation. In these figures it is clear that the flame form is directly influenced by the secondary atomization process. The thickness of the flame is higher in the case of computation without secondary atomization model because of the bigger droplet and therefore because of the difference of the

vaporization times in these two cases of computation. The flame is positioning nearer of the liquid injection zone in the case of computation with the secondary atomization model activated.

Radial profiles of mean temperature

On figures 7 and 8 radial profiles of mean temperature are represented for several axial locations. For the two cases of computation, the maximal temperature is obtain for the X/D1=10 location, with a maximal temperature of about 3000K.

Axial profiles of mean temperature

On figure 9 and 10, axial profiles of mean temperature are represented for 4 radial locations. The maximal temperature is obtain for the Y/D1=2 location, with a maximal temperature of about 3200K. the oscillation of mean temperature for computation with the secondary atomization model at the X/d1=3 and X/D1=4 locations are due to a divergence of computation during the simulation.

The field of temperature

The figures 11 and 12 are representation of the field of temperature for the two cases of computation. With these two figures it is not easy to characterise the difference between the two cases of computation.

Droplet location

The figures 13 and 14 are representation of superimposition of mean velocity field and droplets in the two cases of computation. The first remark with these two figure is the difference of size for the droplets in the two cases of computation and the efficiency of the secondary atomization process. Secondly, the length of the "spray" is higher in the case of computation without the secondary atomization model because of the slower vaporization of big droplets.

Conclusion

A secondary atomization model has been developed and used to simulate the MASCOTTE 10 bar case. Results presented here show the difference between two cases of computation which correspond to a calculation with the break-up model activated and a case without the break-up model.

The main difference between these computations appears on the flame structure : location, length and thickness. Another difference is the liquid location in the computational domain : there is no more droplets in the computational domain after a distance of about 4 cm from the injection when the secondary atomization model is activated whereas in the other case, droplets already exist up to 10 cm.

References
[1]   Gökalp, I, Cousty, R., Vieille, B., Bodèle, E., Fedioun, I., Saucereau, D. and Zurbach, S., *AIAA paper n°2000-3946*, (2000).
[2]   Gökalp, I, Bodèle, E., Cousty, R., Vieille, B., Fedioun, I., Saucereau, D. and Zurbach, *Proceedings of the 6th French-German Colloquium on Research in Liquid Rocket Propulsion*, (2000).
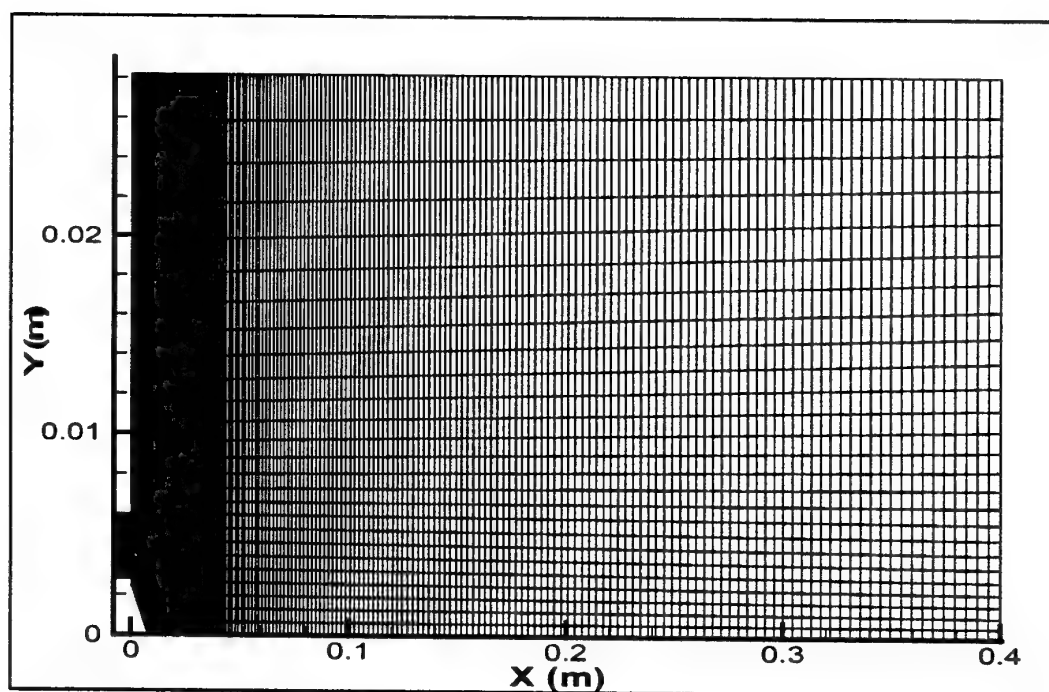[3]   Vieille, B., *PhD Thesis, University of Orléans*, France, (1998).
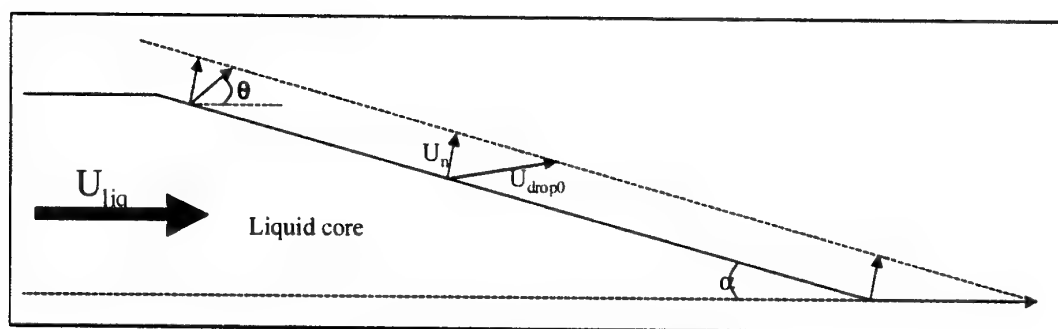
Figure 1. The computational domain
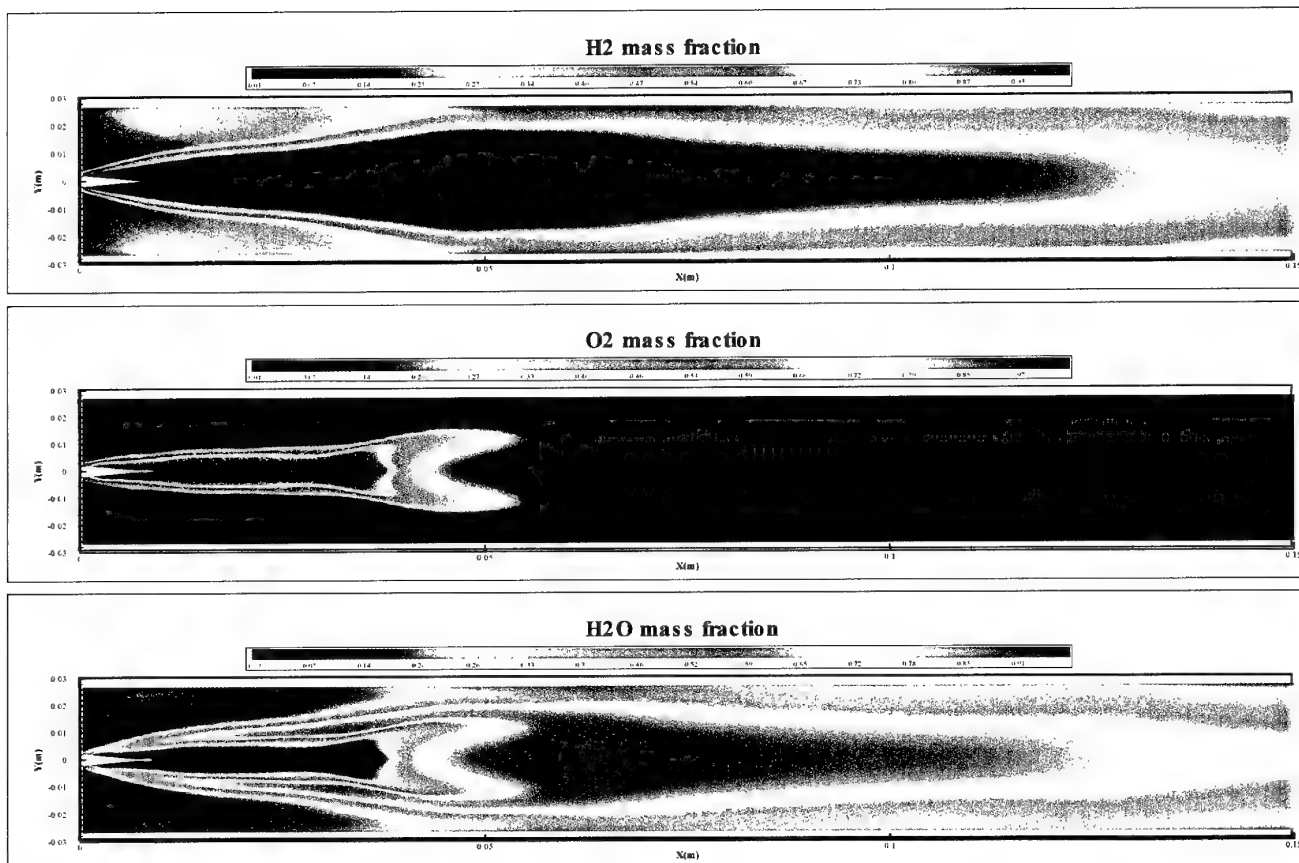

Figure 2. Injection of droplets

Figure 3. Mass fraction for computation with secondary atomization
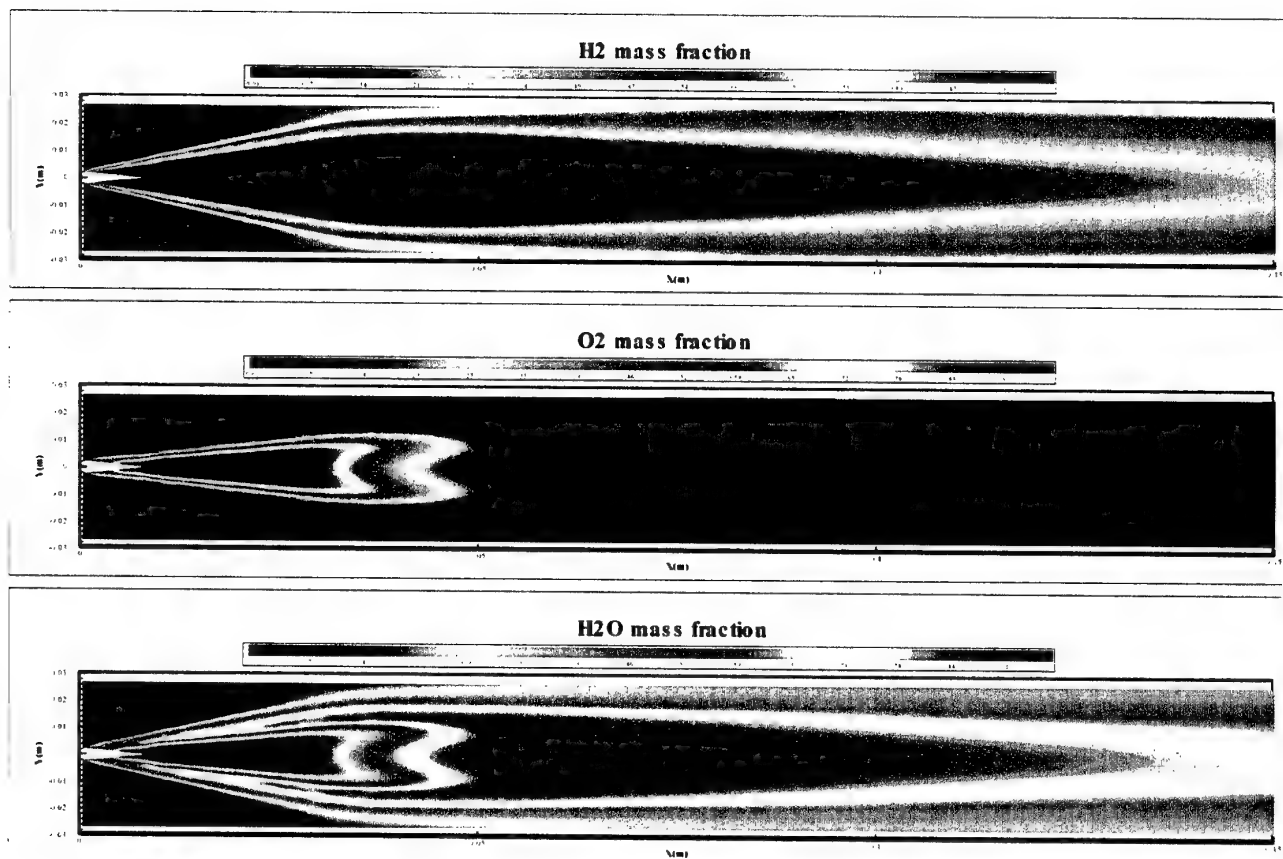
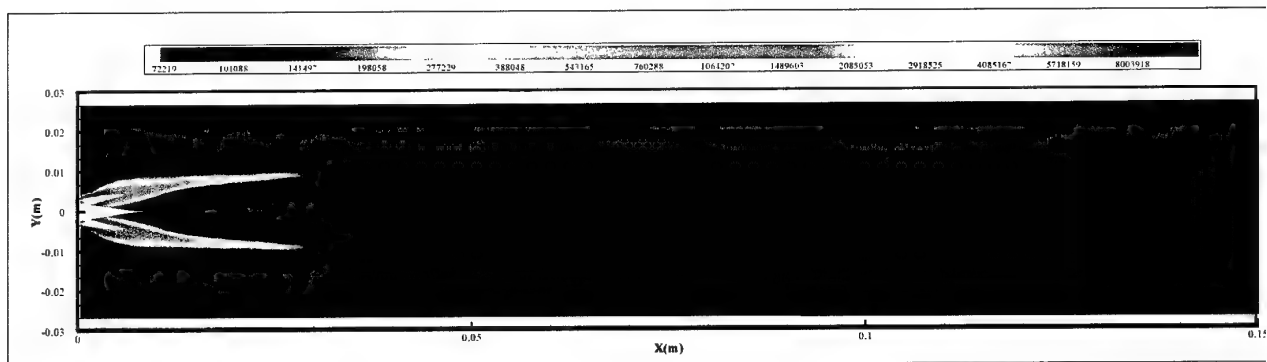*Figure 4.* Mass fraction for computation without secondary atomization

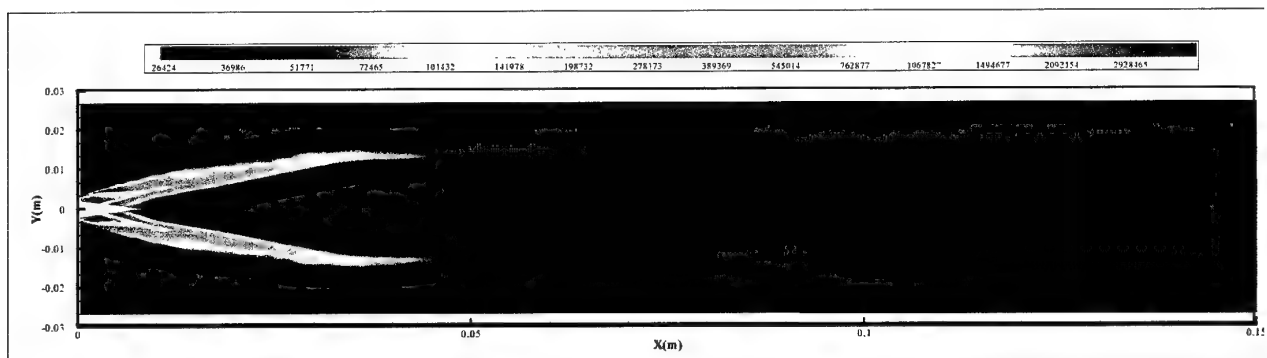*Figure 5.* Reaction rate for computation with secondary atomization

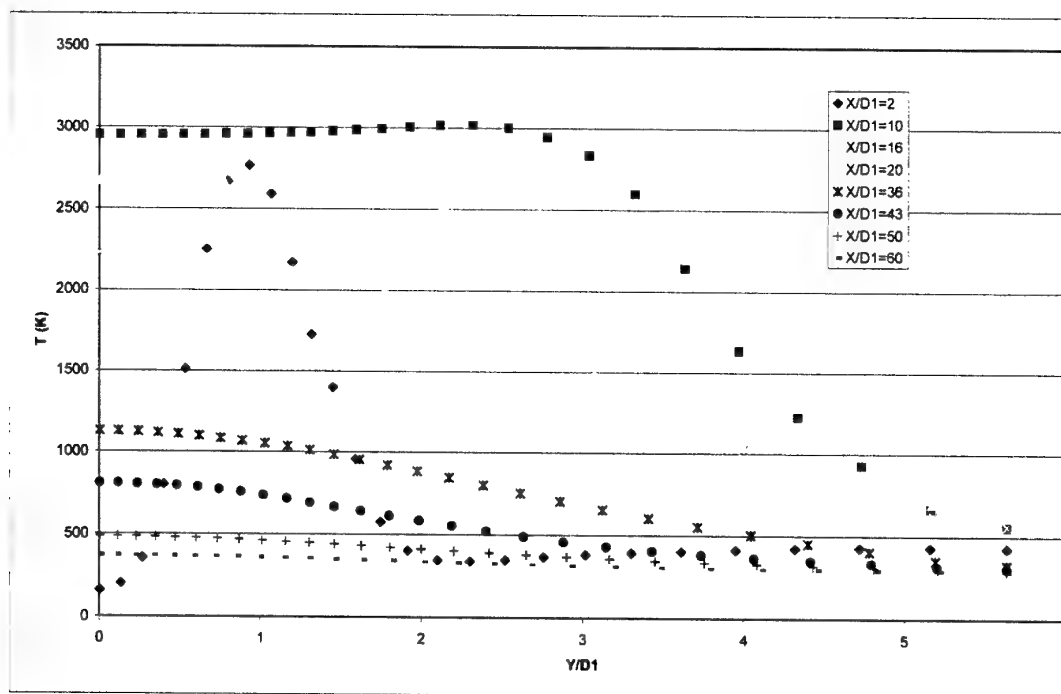*Figure 6.* Reaction rate for computation without secondary atomization

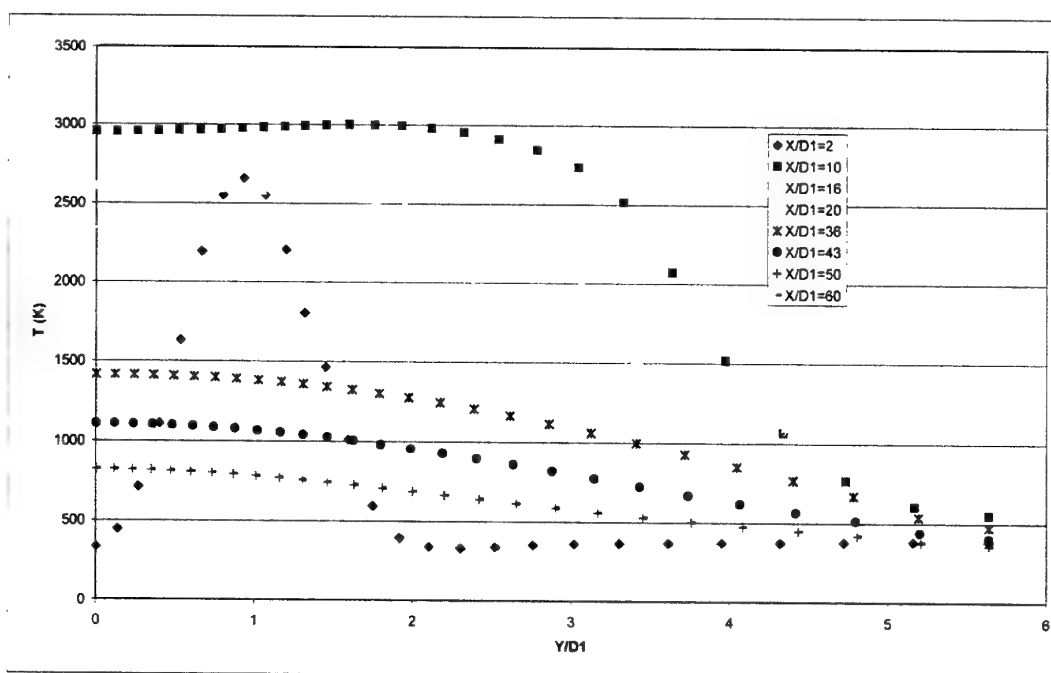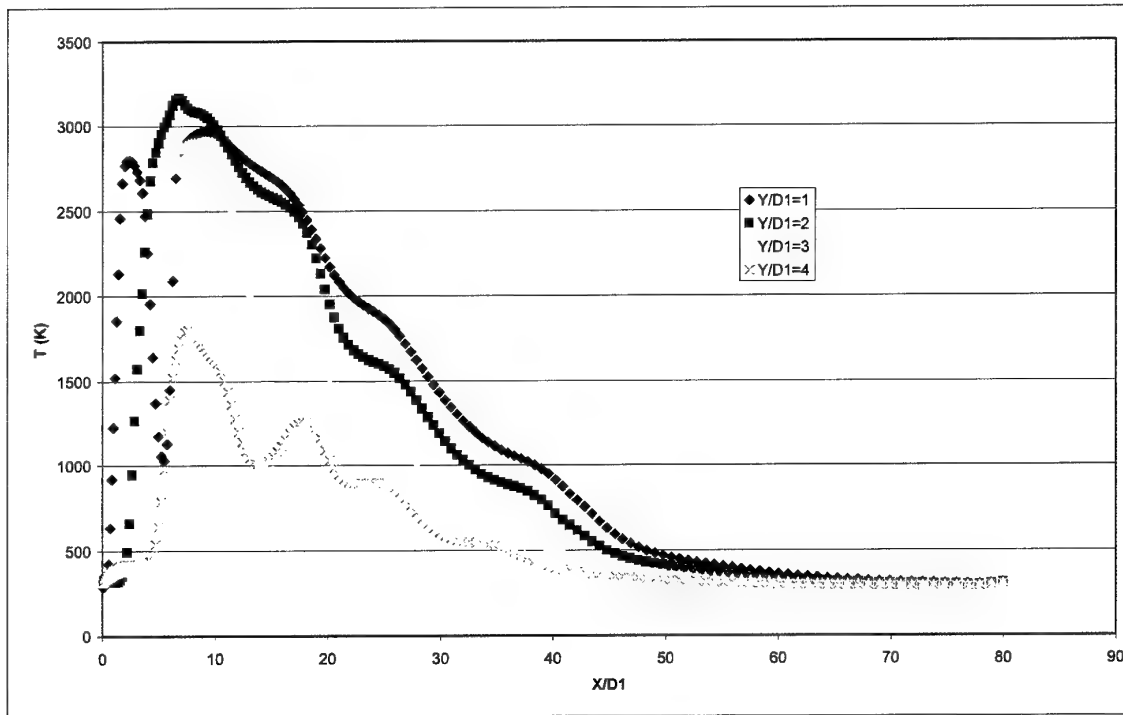*Figure 7.* Radial profiles of mean temperature for computation with secondary atomization

Figure 8. Radial profiles of mean temperature for computation without secondary atomization

Figure 9. Axial profiles of mean temperature for computation with secondary atomization
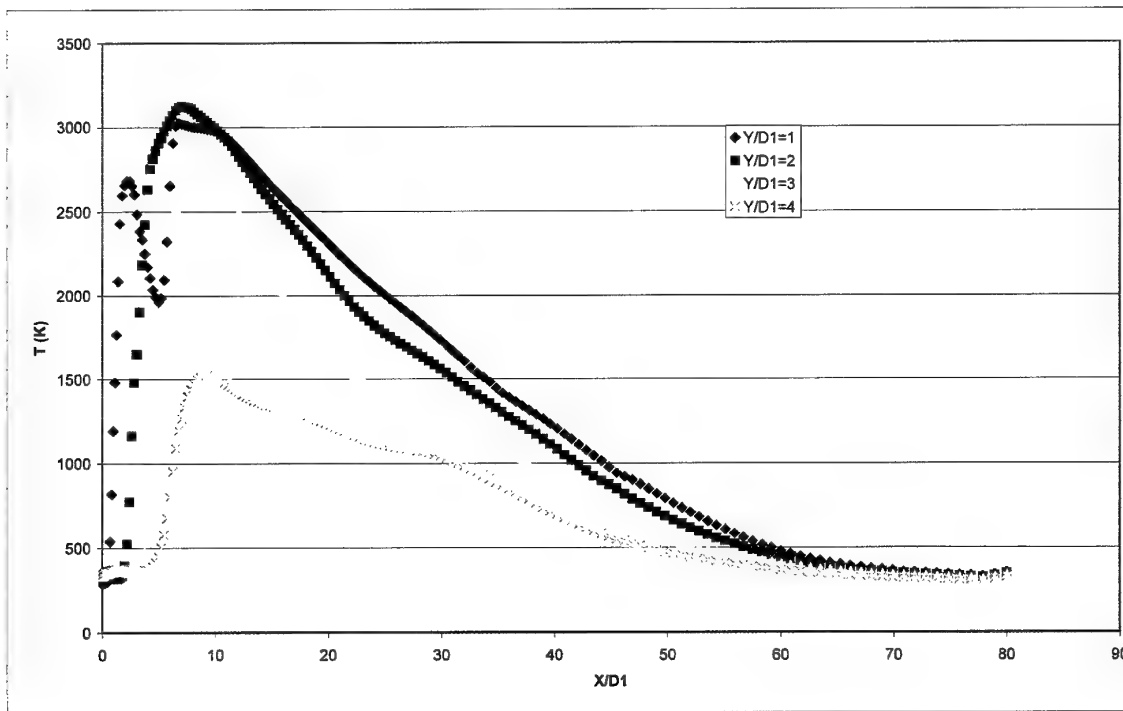

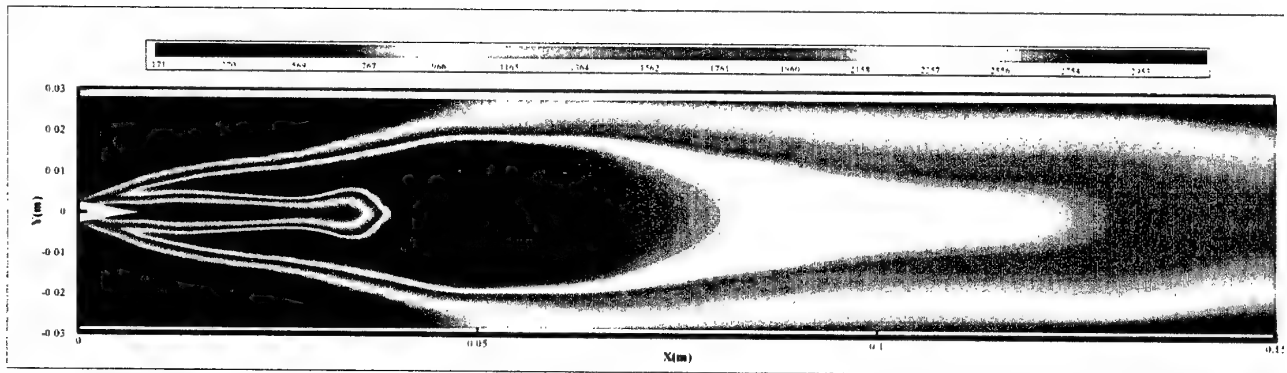*Figure 10.* Axial profiles of mean temperature for computation without secondary atomization

Figure 11. Field of mean temperature for computation with secondary atomization
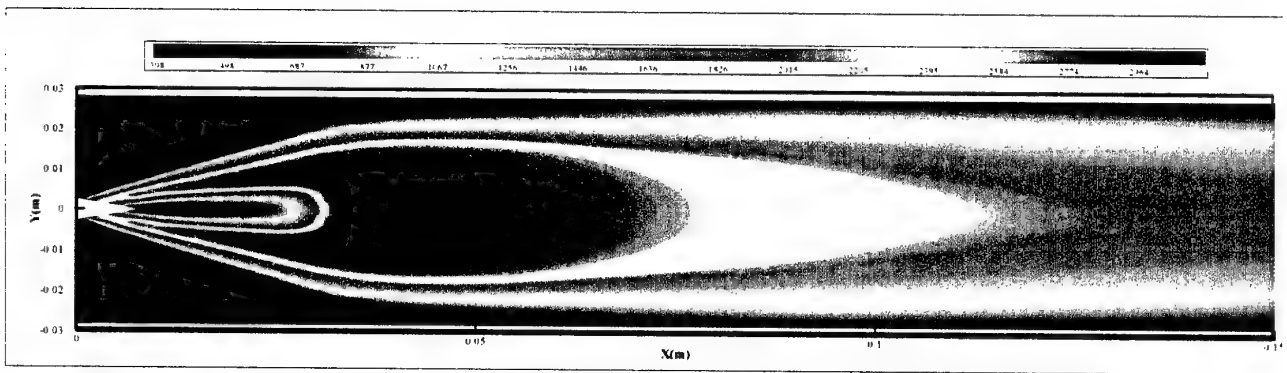

Figure 12. Field of mean temperature for computation without secondary atomization
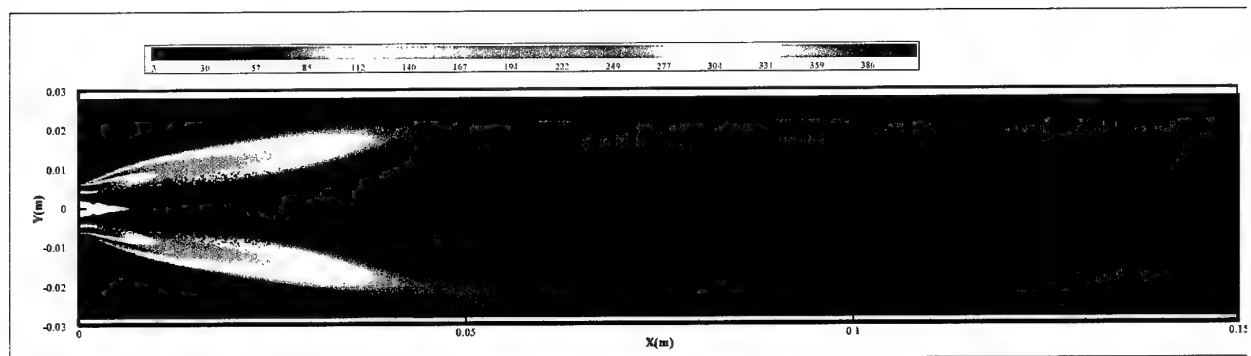
Figure 13. Superimposition of mean velocity field and droplets for computation with secondary atomization
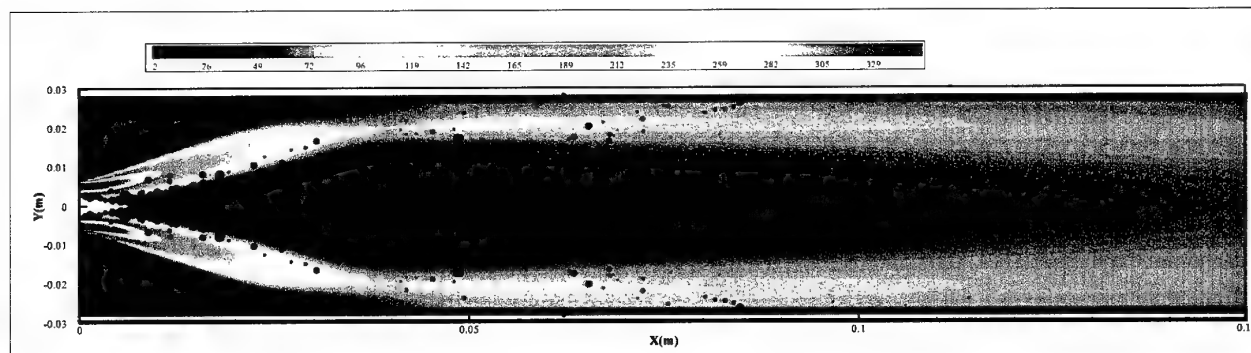

Figure 14. Superimposition of mean velocity field and droplets for computation without secondary atomization

CFD SIMULATION OF LIQUID ROCKET ENGINE INJECTORS
Part 2. SIMULATIONS OF THE RCM-2 EXPERIMENT

Richard Farmer & Gary Cheng
SECA, Inc.

Yen-Sen Chen
ESI, Inc.

The sub-critical combustion case, RCM-2, was simulated with both heterogeneous and homogeneous spray combustion models. The MASCOTTE test data should be better than any which have been previously used to tune the several parameters in these models. It is unreasonable to expect that spray flames, even of hydrogen and oxygen, can be accurately predicted without extensive model validation with test data representative of the conditions which exists in rocket engine combustion chambers. Even global data such as chamber pressure and thrust have not been obtained for single coaxial element combustor flows. The IWRCM data provide a good starting point, but no CFD model tuning has yet been attempted for such experiments. Direct comparisons of predictions to test data at this point will not establish which of several modeling techniques is best.

Heterogeneous Spray Combustion Model

Simulations of shear coaxial injector combustion may include models that characterize the breakup or atomization of the round liquid jet, subsequent droplet secondary breakup, turbulence dispersion, droplet evaporation and gas-phase mixing and combustion. The primary atomization rate of the liquid jet is modeled following the work of Reitz and Diwakar[1]. Applications of this model to shear coaxial injector test cases, with a volume-of-fluid equation to model the liquid fuel/oxidizer jets, were presented by Chen, et al.[2]. For the present application, since the liquid core length and the initial droplet size are specified, the primary atomization model is therefore ignored.

Particulate Two-Phase Flow Model
The two-phase interactions are important throughout the life history of the droplets. In the initial phase of injection, momentum and energy exchanges through the drag forces and heat transfer are dominating. These inter-phase transfer terms appear in the Navier-Stokes equations that are solved using the present CFD flow solver. Mass transfer occurs as the particles are heated through the surrounding hot gas. Mean gas-phase properties and turbulence eddy properties are used for the statistical droplet tracking calculations.

Droplet Secondary Breakup Model
The TAB (Taylor Analogy Breakup) model of O'Rouke and Amsden[3] is based on an analogy between an oscillating and distorting droplet and a spring-mass system. The restoring force of the spring is analogous to the surface tension forces on the droplet surface. The external force on the mass is analogous to the gas aerodynamic force. The damping forces due to liquid viscosity are introduced also based on this model.

Droplet-Turbulence Interaction

A two-equation turbulence model is used to characterize the flowfield turbulence quantities, such as turbulence fluctuations, eddy life time and length scale. Turbulent effects on particles are modeled by assuming the influence of velocity fluctuations on the particles creates statistical dispersion of the particles. The velocity fluctuations, which are calculated from the solutions of the turbulence kinetic energy, are assumed to follow a Gaussian distribution with standard deviation proportional to the square root of turbulence kinetic energy. This magnitude of this statistical particle dispersion is then transported following the trajectory of the particles with their radii of influence within which coupling effects (also follow the Gaussian distribution) between two phases occur. This method is classified as the parcel PDF (cloud) model, by Shang[4], for turbulent particle dispersion. As oppose to the stochastic separated flow (SSF) model, the number of computational particles required is drastically reduced for the same statistical representation of the spray. This provides great savings in computational effort in performing the spray combustion computations.

Droplet Evaporation Model

The droplet evaporation rates and the droplet heat-up rates are determined using the general evaporation model of Schuman[5], which is continuously valid from subcritical to supercritical conditions. This vaporization model was extended from the classical approach[6], by neglecting the effects of solubility of the surrounding gas into the droplet. However, this approach satisfies the global transient film continuity equation for the drop vapor and the ambient gas to obtain the expressions consistent for the molar flow rates.

Chemical Reaction Model

A finite-rate chemistry model with point-implicit integration method is employed in the present study. A 9-reaction kinetics model of Anon[7] is used for modeling the H_2-O_2 combustion. The initiation reaction used produced OH. This chemistry model is listed in Table 1 of Part 3 of this paper.

Results

The MASCOTTE single injector test chamber was used in a series of experimental programs for subcritical and/or supercritical H_2-O_2 combustion. In the subcritical spray combustion test case (RCM-2), the designed chamber pressure is 10 bar (or 9.87 atm). The injector orifice diameter for the liquid oxygen (LOX) injection is 5 mm surrounded by an annular gaseous hydrogen jet with channel width of 6.4 mm. The overall O/F ratio for this case is 2.11 (see the test conditions given in Table 1).

Table 1. RCM-2 Test Case Operating Conditions

Conditions	H_2	O_2
Pressure	1 MPa	1 MPa
Mass flow rate	23.7 g/s	50 g/s
Temperature	287 K	85 K
Density	0.84 kg/m3	1170 kg/m^3
Cp	14300 J/kg/K	1690 J/kg/K
Velocity	319 m/s	2.18 m/s
Viscosity	8.6E-6 kg/m/s	1.94E-4 kg/m/s
Surface Tension	-	1.44E-2 N/m

The computational model includes the injector geometry, the combustion chamber and the nozzle section. A 10-block structured mesh is generated (the total number of grid points equals 14,444) for the two-phase flow computation. Relative high grid density (about 10 micron spacing)is packed in the injector lip region for the purpose of better flow resolution and flame holding in the expected area. The LOX core length of 7.8 mm is assumed, which serves as the particle injection boundary with the fixed particle size (82 microns), velocity (10 m/s) and angle distributions given in the problem specification. Fixed mass-flow boundary conditions are used at the inlet while all flow properties are extrapolated at the nozzle exit. Supersonic exit flow develops as part of the solution.

The computation starts with a cold flow with inlet and chamber pressure specified. The two-phase flow particle breakup and evaporation model models are activated from the beginning. The time step size of the time-marching solution method is 1 μsec. After 1000 time steps of cold flow run, a heat source is introduced in the lip region between and oxygen and hydrogen streams where a recirculation zone is established. At the same time, the finite-rate chemistry model is turned on to start the flame spreading throughout the chamber. The chamber pressure drops at the beginning until the flame fills up the entire chamber. Then, the pressure started to build up to the expected level when the inlet and exit flows show satisfactory mass conservation condition. The calculated averaged chamber pressure is around 9.96 atm. The majority of the LOX particles do not survive very far downstream of the injector exit. Some particles along the chamber axis do survive up to 70 mm downstream of the injector.

The time-averaged temperature, temperature standard deviation, species mass-fraction contours and temperature profiles at specified locations are plotted in the following figures. These data are prepared as requested for data comparison purpose.

Figure 1 shows the mean temperature and standard deviation through the entire length of the combustion chamber. A close up view of the nozzle tip region is also shown in this figure. Figure 2 shows the OH and O_2 and Figure 3 the H_2 and H_2O concentration profiles, respectively, in this same region. Figure 4 shows the predicted radial temperature profiles at various axial locations. Figure 5 shows the predicted axial temperature profiles at various radial locations. The flame predicted using this model does not expand as indicated in the experiment. The recirculation zone is relatively long.

Homogeneous Spray Combustion Model

The RCM-2 experiment was also simulated with the homogeneous spray combustion model. Details of this model are presented in Part 3 of this paper. The volume upstream of the injector element tip was neglected for this simulation. The grid use for the internal element flow was 61x43; for the chamber it was 301x101. The nozzle was not simulated. This grid system had a minimum grid spacing of 60 microns in the wake behind the lip separating the LOX and hydrogen streams. The boundary conditions used are shown in Figure 6. An equilibrium and several finite rate solutions were obtained for this configuration. An initial finite-rate simulation was run by setting the rate of the global initiation reaction fast enough to stabilize the flame near the start of the shear layer. This rate also essentially eliminated the waviness in the shear layer separating the LOX and hydrogen streams, without averaging the solution. The stoichiometric coefficients in the global rate expression were determined by an equilibrium calculation for a stoichiometric flame at the expected chamber pressure.

3

Such a practice produces temperatures with one rate expression, which are very close to those resulting from using a more detailed reaction mechanism. However, predicted OH concentrations are apparently too high. The procedure used in the case 3 simulation is believed to be much better. This modified procedure uses nine elementary rate equations and switches to an equilibrium solution when the local temperature exceeds a specified value. Temperatures and OH concentrations are believed to be accurately simulated by this method.

The equilibrium solution at the interface between the internal element flow and the flow at the nozzle tip are shown in Figure 7. The temperature profiles in the radial and axial directions are shown in Figures 8 and 9, respectively. The temperature and oxygen and OH concentration profiles are shown in Figure 10. The wall temperature profile is shown in Figure 11. All of these figures are for the equilibrium solution. The modified finite rate solution for the equilibrium/finite-rate combustion model yielded solutions very similar to the equilibrium only model. This modified finite-rate model is believed to be the most accurate and useful model tested.

Comparing the heterogeneous and homogeneous solutions, the former produced a longer, thinner flame than the latter. Parameters in the spray combustion model could have been set such that the solutions matched very closely, or so that both could match test data. Such a step cannot be made until the RCM test data are made available and the CFD models tuned. An optimum rocket engine spray combustion model cannot be determined until this next validation step is undertaken.

REFERENCES

1. Reitz, R. D., and Diwakar, R., "Structure of High-Pressure Fuel Sprays," SAE Paper 860469, 1986.

2. Chen, Y. S., Shang, H. M., and Liaw, P., "A Fast Algorithm for Transient All-Speed Flows and Finite-Rate Chemistry," AIAA Paper 96-4445, 1996 AIAA Space Programs and Technologies Conference, September 24-26, 1996, Huntsville, AL.

3. O'Rourke, P. J., and Amsden, A. A., "The TAB Method for Numerical Calculation of Spray Droplet Breakup," SAE Paper 872089, 1987.

4. Shang, H. M., "Numerical Studies of Spray Combustion in Liquid-Fueled Engines," Ph.D. Thesis, University of Alabama in Huntsville, 1992.

5. Schuman, M. D., "General Evaporation Model," CDR-88-054, Rockwell International Corp., Feb. 1988.

6. Abramzon, B., and Sirignano, W. A., "Droplet Vaporization Model for Spray Combustion Calculations," AIAA Paper 88-0636, 1988.

7. Anon, "Spray Combustion of Synthetic Fuels, Phase II – Spray Combustion Phenomena," DOE/PC40276-5, SAI, Inc., Chatsworth, CA, May 1983.
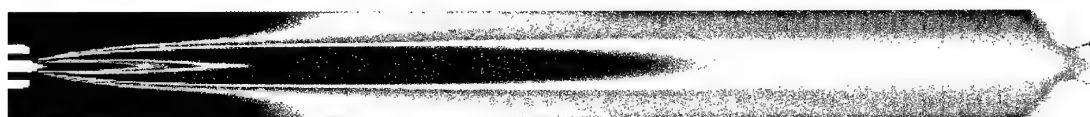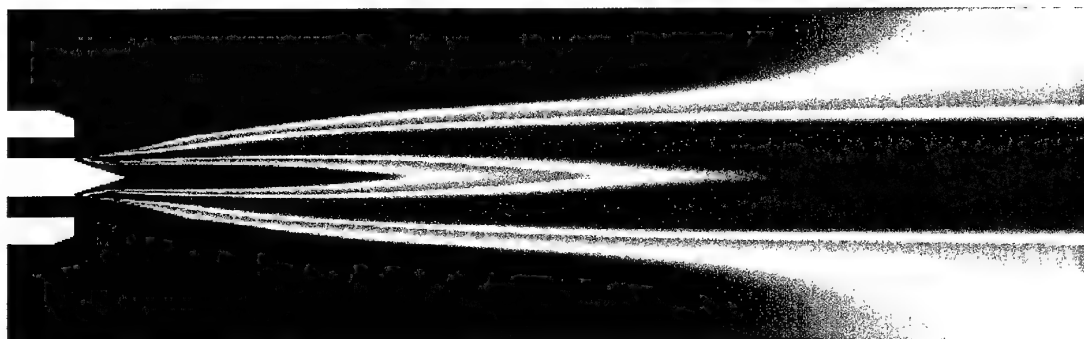
DATA #1
3.2619e+03
2.4676e+03
1.6734e+03
8.7921e+02
8.4995e+01

(a) Time-Averaged Temperature (K)

DATA #2
9.9013e+02
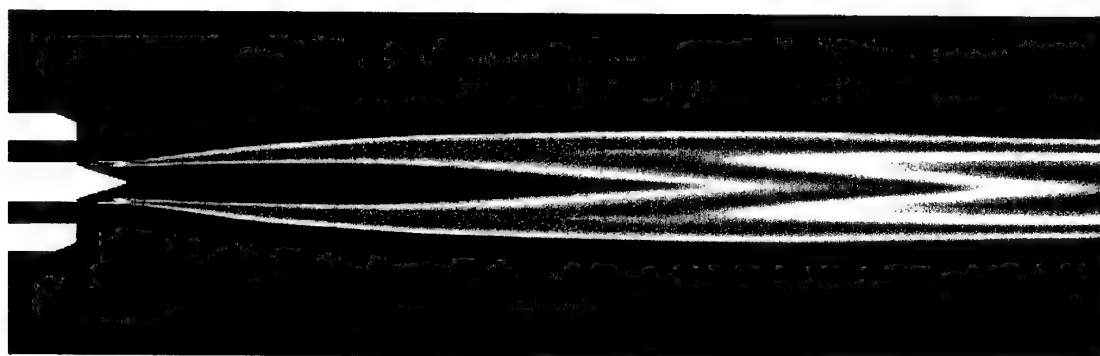7.4255e+02
4.9506e+02
2.4753e+02
1.0000e-15

(b) Temperature Standard Deviation (K)

DATA #1
3.2619e+03
2.4676e+03
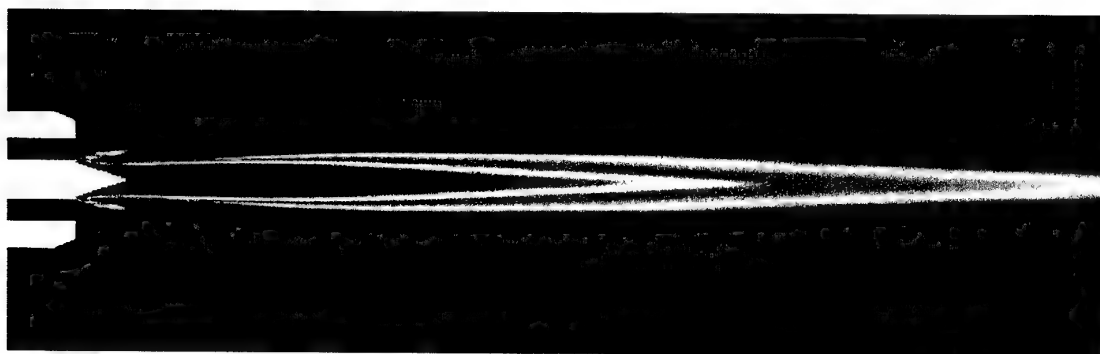1.6734e-03
8.7921e+02
8.4995e-01

(c) Time-Averaged Temperature (K) for X up to 150 mm

Figure 1. Time-Averaged Temperature and Temperature Standard Deviation of RCM-2.

5

DATA #5
1.0810e-01
8.1076e-02
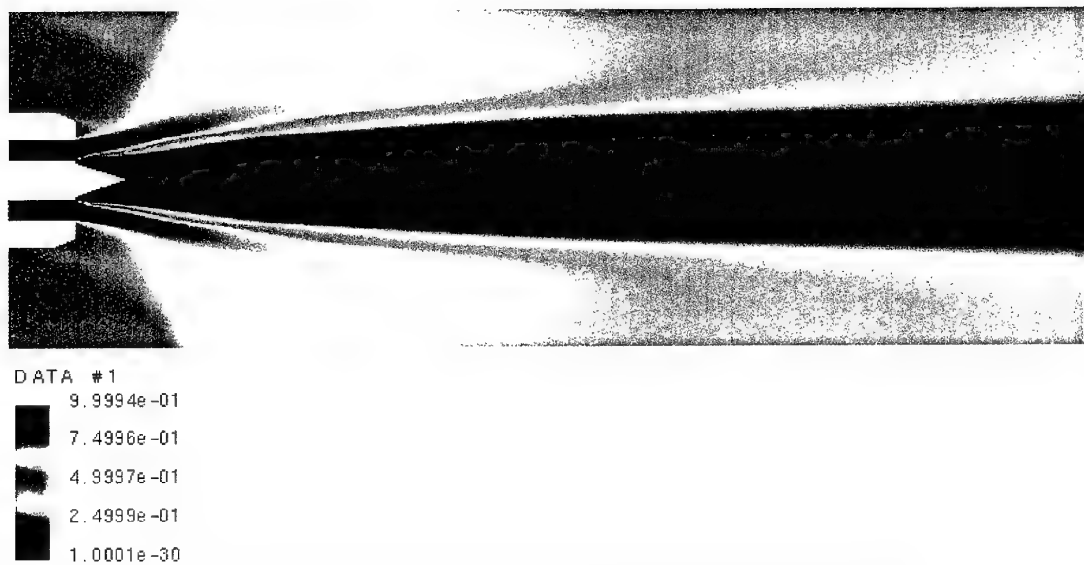5.4051e-02
2.7025e-02
1.0001e-30

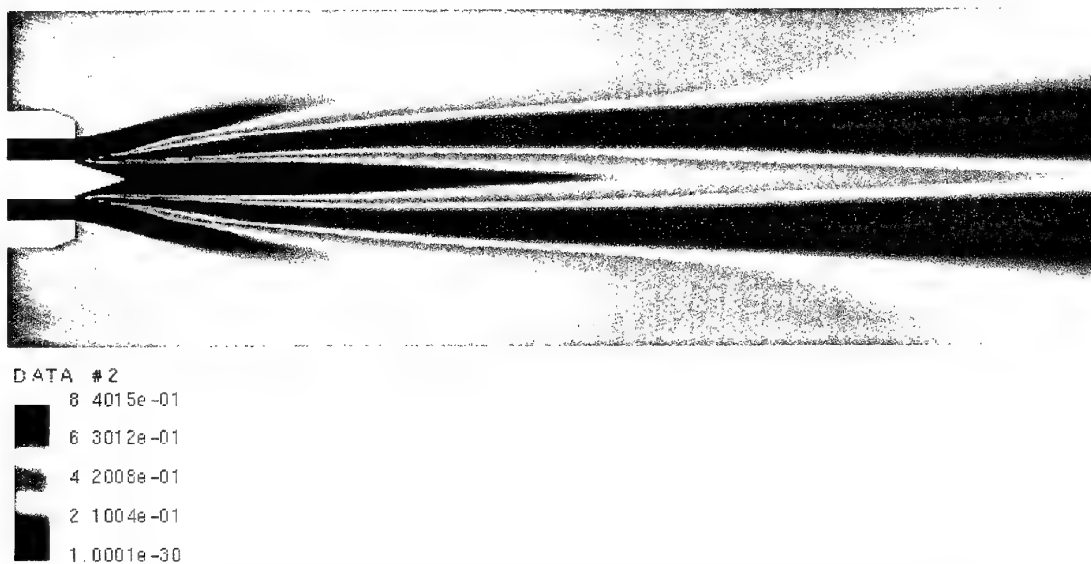(a) Time-Averaged OH Mass-Fraction Contours for X up to 150 mm

DATA #5
9.9994e-01
7.4996e-01
4.9997e-01
2.4999e-01
2.1287e-22

(b) Time-Averaged O2 Mass-Fraction Contours for X up to 150 mm

Figure 2. Time-Averaged OH and O_2 Mass Fractions of RCM-2.

DATA #1
- 9.9994e-01
- 7.4996e-01
- 4.9997e-01
- 2.4999e-01
- 1.0001e-30

(a) Time-Averaged H_2 Mass-Fraction Contours for X up to 150 mm

DATA #2
- 8.4015e-01
- 6.3012e-01
- 4.2008e-01
- 2.1004e-01
- 1.0001e-30

(b) Time-Averaged H_2O Mass-Fraction Contours for X up to 150 mm

Figure 3. Time-Averaged H_2 and H_2O Mass Fractions of RCM-2.
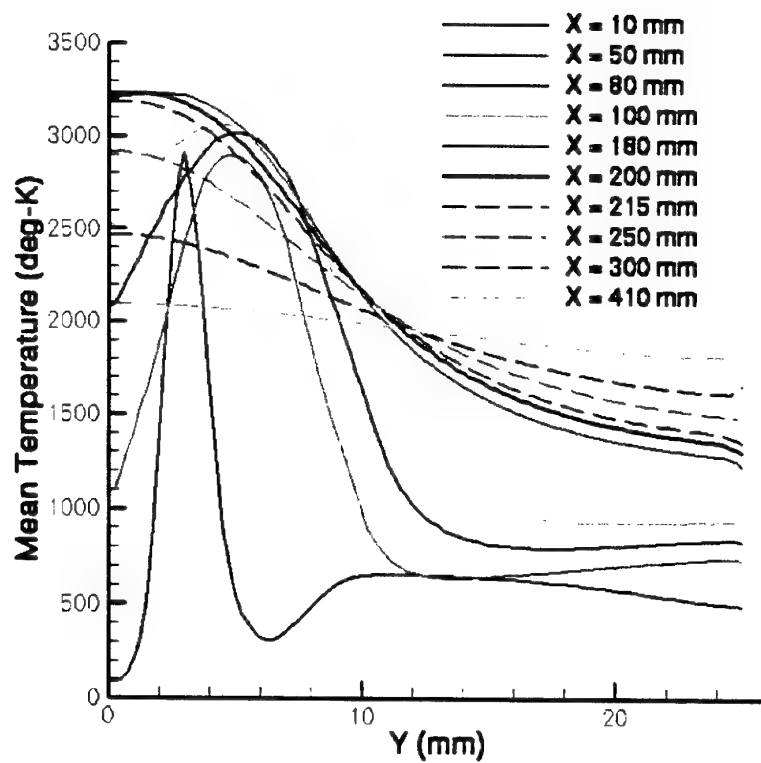
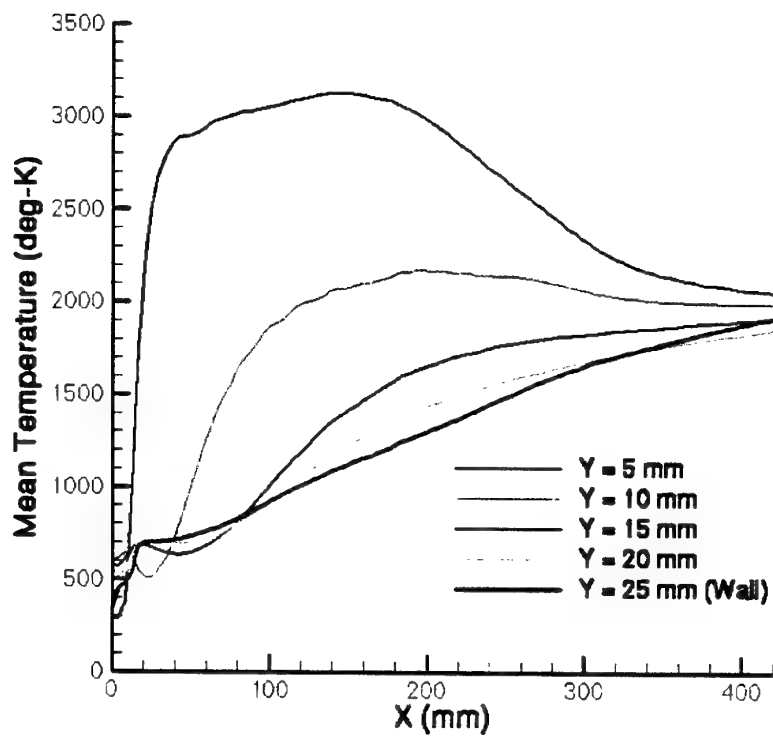Figure 4. Predicted radial profiles of mean temperature of RCM-2.

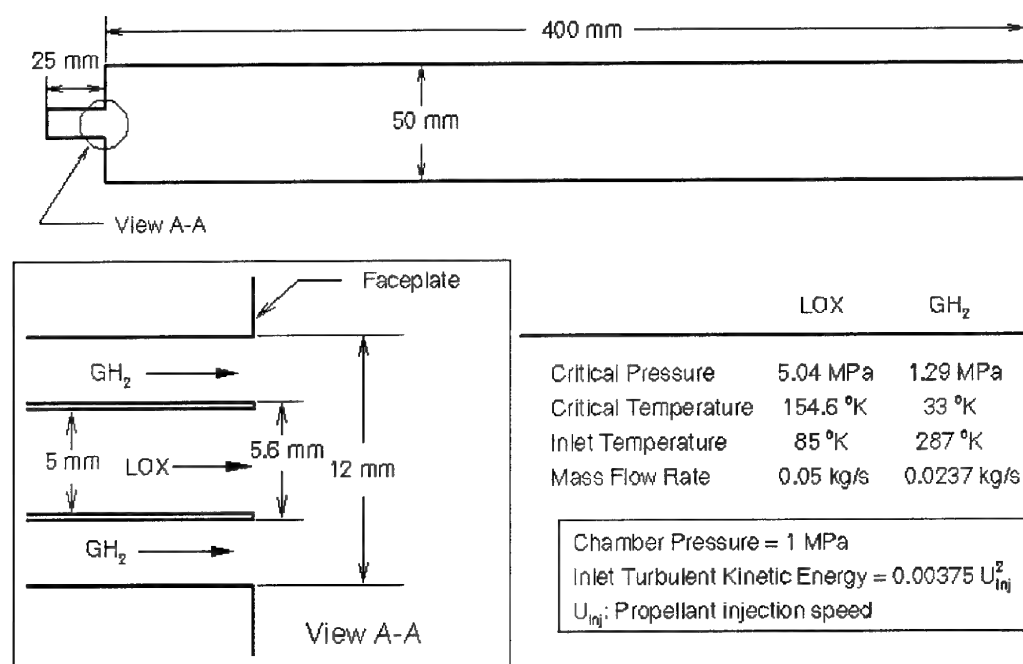Figure 5. Predicted axial profiles of the mean temperature of RCM-2.

8

Figure 6. Configuration of the RCM-2 Case (Homogeneous Spray Model).

The figure contains the following labeled data:

	LOX	GH$_2$
Critical Pressure	5.04 MPa	1.29 MPa
Critical Temperature	154.6 °K	33 °K
Inlet Temperature	85 °K	287 °K
Mass Flow Rate	0.05 kg/s	0.0237 kg/s

Chamber Pressure = 1 MPa
Inlet Turbulent Kinetic Energy = 0.00375 U_{Inj}^2
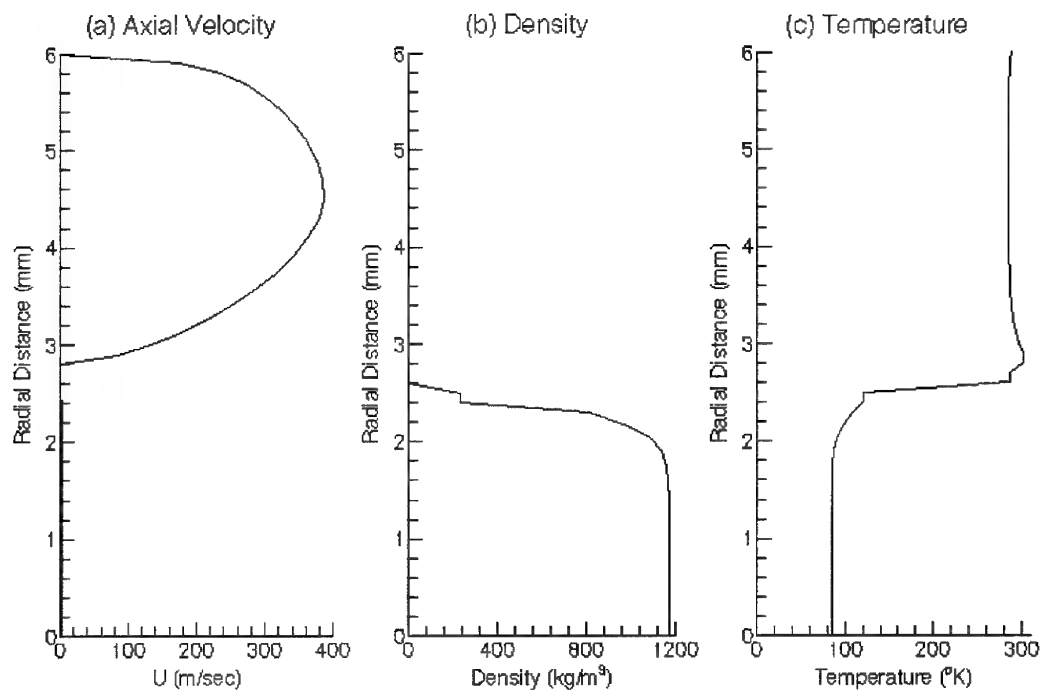U_{Inj}: Propellant injection speed

Figure 7. Flow Properties at the Injector Exit of RCM-2 (Homogeneous Spray Model)
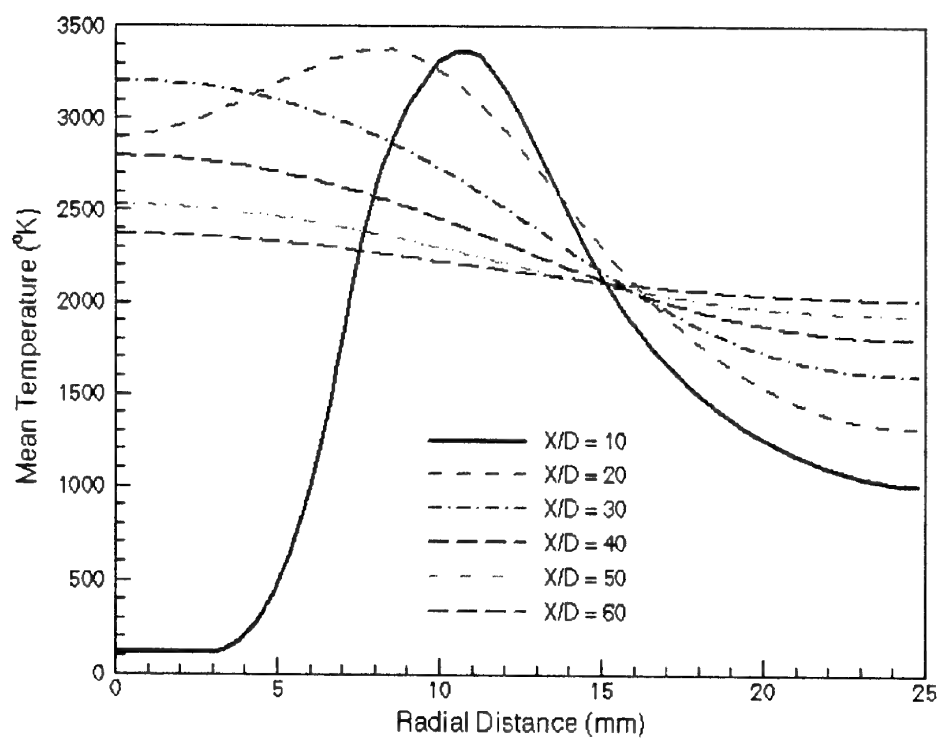
9

Figure 8. Radial Profiles of the Mean Temperature at Various Axial Locations of RCM-2.
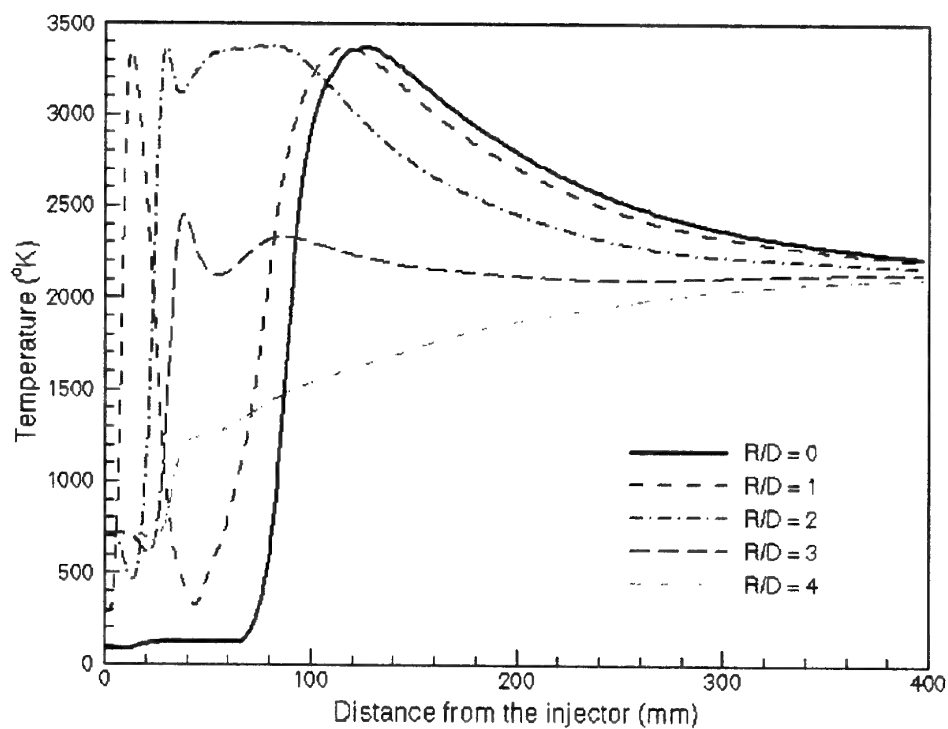

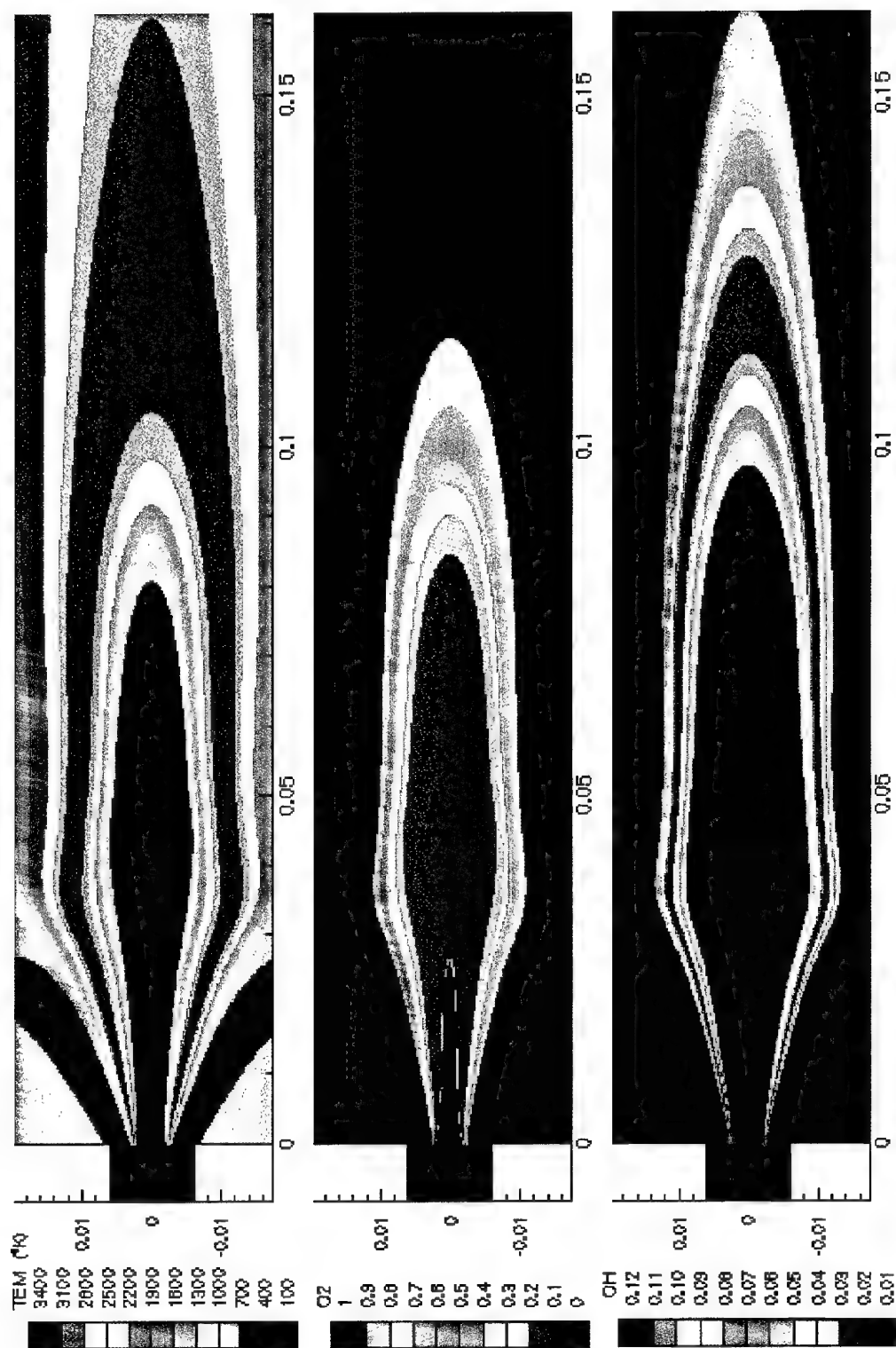Figure 9. Axial Profiles of the Mean Temperature at Various Radial Locations of RCM-2.

10

Figure 10. Temperature and Species Concentrations Near the Injector of RCM-2.
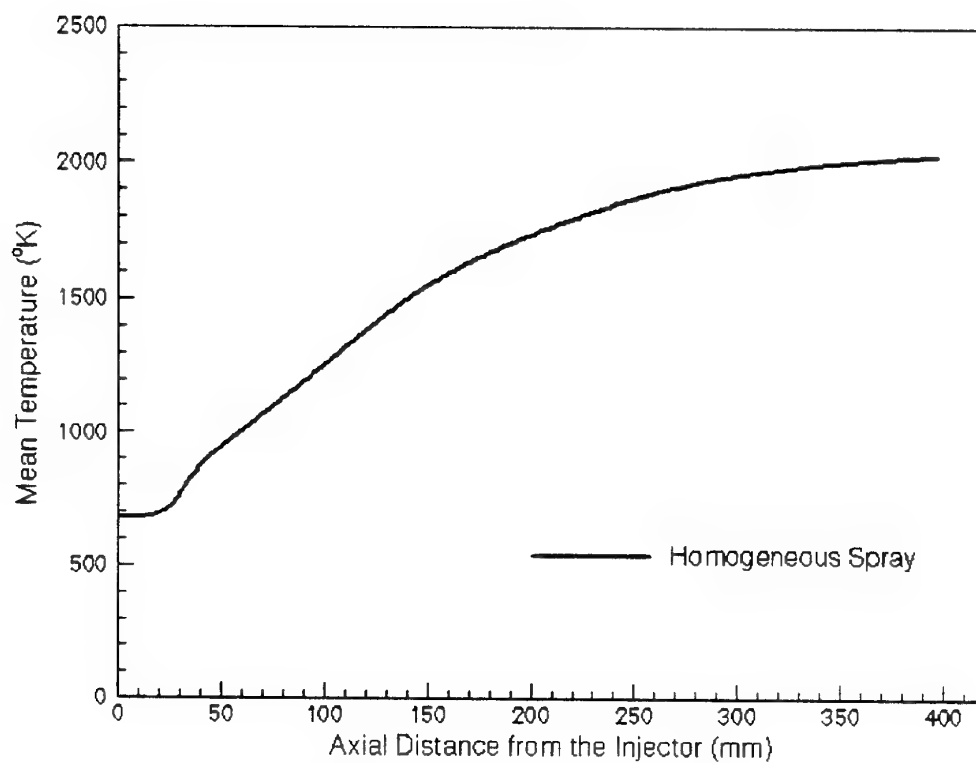
Figure 11. Near Wall Temperature Distributions for Various Chemistry Models of RCM-2.

The RCM2 10 bars test case

Combustion
of cryogenic propellant at 10 bars
using the
CPS code

2nd International Workshop on Rocket Combustion Modelling

Lampoldshausen March 25-27, 2001

Presented by Laurent Lequette form Bertin Technologies

bertin
technologies

2nd RCM Workshop : RCM2 10 bars test case

1   The introduction

2   The objectives and the approach

3   The main results

4   The numerical and the physical models

5   The results presentation

6   The conclusion

bertin technologies

2nd RCM Workshop : RCM2 10 bars test case
The introduction

□ Bertin Technologies

    □ technological services provider and consultancy

    □ French private company

    □ staff : 250 employees

□ The SIMA team

    □ working in Information Systems and Advanced Modelling

    □ has been involved in CFD modelling for more than 15 years and has developed several CFD tools like CALIFE, THESEE and now CPS

□ This work has been founded by CNES

bertin technologies

2nd RCM Workshop : RCM2 10 bars test case
The introduction

The CPS code

❑ new generation CFD code
  ❑ unstructured meshes (3D)
  ❑ Roe and Toumi formulation for Euler fluxes
  ❑ explicit and implicit schemes (for steady and for unsteady flows)
  ❑ turbulence models (Jones-Launder, Coakley, RNG, subgrid, ...)
  ❑ Eulerian two phases model
  ❑ Lagrangian two phases model (LASVEGAS)
    ❑ atomisation and coalescence
    ❑ arbitrary time step
    ❑ high volumic rates
  ❑ Combustion models (Arrhenius, TECK, flame surface)

❑ developed by Bertin Technologies and SNPE Group together
  ❑ benefits from earlier developments of both companies

❑ a commercial version is being launched
  ❑ we are looking for pilot customers

bertin technologies

2nd RCM Workshop : RCM2 10 bars test case
The objectives and the approach

❑ The objectives

    ❑ To asses the most recent developments of CPS for cryogenic applications

    ❑ To retrieve guidelines for future developments of CPS

        ❑ numerical point of view

        ❑ physical models

❑ The approach

    ❑ Lagrangian two phases models (LASVEGAS model)

    ❑ Use of CPS from an engineer point of view

        ❑ Use of standard options only

        ❑ No special treatment for the injection area

        ❑ No parameters tuning

        ❑ Start from zero with all the models activated

    ❑ Comparison of normal Lox injection (3 m/s) and accelerated (10 m/s) as recommended for the WS

bertin technologies

2nd RCM Workshop : RCM2 10 bars test case
The main results

- No major numerical difficulty using the explicit Roe-Toumi scheme, but
  - it has not been possible to inject inside the Lox injector
  - the implicit scheme is not robust enough for such an application

- The results are sensitive to the laminar binary diffusion coefficients values

- The results are not very sensitive to the use of the Rosin-Ramler distribution instead of constant diameters

- Some improvements of the injection area have to be done
  - it is not clear where the added Lox quantity of movements comes from, for the 10 m/s injection case

- The maximum temperature is around 2500 K and the pressure close to 10 bars
  - it seems to be close from experimental values

bertin technologies

2nd RCM Workshop : RCM2 10 bars test case
The numerical and the physical models

❑ Numerical models and parameters

    ❑ second order Roe-Toumi explit scheme

    ❑ CFL 0.5

    ❑ steady state optimisation (local time steps for gas)

    ❑ unsteady approach for droplets

❑ Physical models and parameters

    ❑ Mixing of perfect gas (H2, O2 and H2O)

    ❑ varying Cp and Cv

    ❑ laminar viscosities function of the temperature

    ❑ Coakley (q, ω) turbulence model

    ❑ LASVEGAS Lagrangian two phases model

    ❑ TECK combustion model (improved EBU-Arrhenius model)

❑ Mesh

    ❑ 3880 elements

    ❑ Whole domain including the nozzle

berlin technologies

2nd RCM Workshop : RCM2 10 bars test case
The numerical and the physical models

□ GH2 Inlet boundary conditions : mass flow rate and total temperature fixed

   □ Q = 267.96 kg m^{-2} s^{-1} Tt = 290.56 K

   □ k = 380 m^2 s^{-2} ω = 800 s^{-1}

□ Outlet boundary conditions : fixed pressure

   □ Ps = 39.7 10^5 Pa   Ts = 293. K (for reentrant flow only)

   □ k = 10 m^2 s^{-2} ω = 100 s^{-1} (for reentrant flow only)

□ Lox Injector

   □ T = 85 K   Q = 2546.5 kg m^{-2} s^{-1} v = 2.18 m/s or 10 m/s

   □ Rosin-Ramler diameters distribution

   □ equivalent to a wall for the gas

□ Walls

   □ adiabatic

   □ turbulent law of the wall

   □ tangential film for impacting droplets

berlin technologies

2nd RCM Workshop : RCM2 10 bars test case
The numerical and the physical models

- ❏ Chemistry parameters for TECK model
  - ❏ Activation temperature 2000 K
  - ❏ Pre-exponential coefficient 10^{12}
  - ❏ H2 and O2 partial orders 1.
  - ❏ Threshold temperature 300 K

- ❏ Binary diffusion coefficients
  - ❏ $D_{A,B} = 1.013 \ 10^{-7} \ T^{-1.75} \ (1/M_A + 1/M_B)^{1/2} \ / \ P \ / \ (V_A^{1/3} + V_B^{1/3})$
    - ❏ with P defined in bars, M in g/mole
    - ❏ $V_{O2} = 16.6$ $V_{H2} = 7.07$ $V_{H2O} = 12.7$

- ❏ Thermal conductivities
  - ❏ function of temperature

- ❏ Initial conditions
  - ❏ $Ps = 10^5$ Pa $Ts = 300$ K $v = 100$ m s^{-1}
  - ❏ YH2=1. $K = 200$ m^2 s^{-2} $\omega = 100$ ms-1

bertin technologies
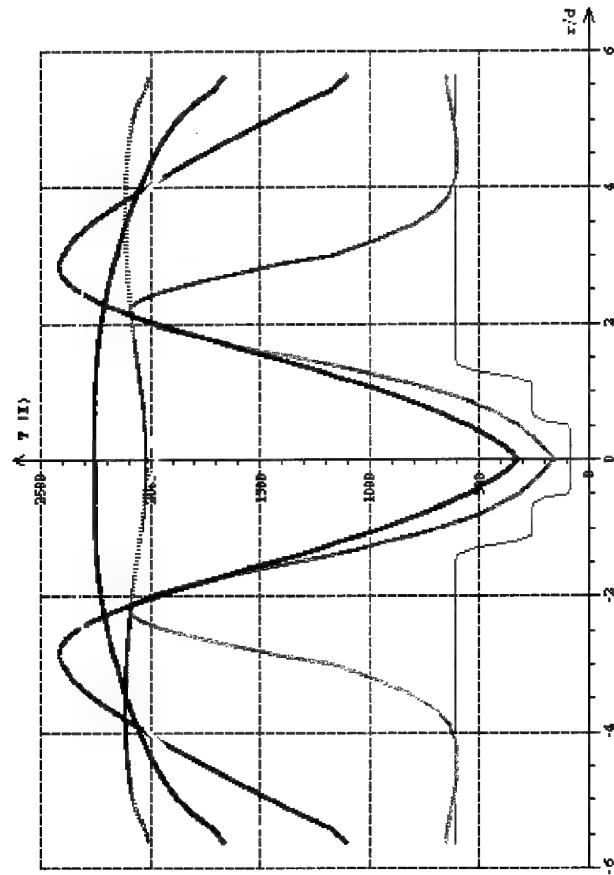
2nd RCM Workshop : RCM2 10 bars test case
The results

- Some results may not be thoroughly converged but all of them are converged in the combustion area

- As a single reaction model was used, OH fractions cannot be presented, but the production rate for temperature can be used to visualise the flame location

bertin technologies

2nd RCM Workshop : RCM2 10 bars test case
The results

Temperature
RCM2 2D : monodisperse case
droplet diametre = 110 microns

n : 270993
mini: 85.371
maxi: 2418.7

Temperature a x = 0 mm

Temperature a x = 3 mm

Temperature a x = 6 mm

Temperature a x = 12 mm

Temperature a x = 15 mm

Page : 11

- LL - 23/03/2001

2nd RCM Workshop : RCM2 10 bars test case
The results

Volumic rate for the polydispersed phase
RCM2 2D : monodisperse case
droplet diametre = 110 microns

```
n t     270991
mini:   0.0000
maxi:   4.7030
```

```
0.000
0.1808E-02
0.5062E-02
0.1092E-01
0.2146E-01
0.4044E-01
0.7460E-01
0.1361
0.2468
0.4460
0.8045
1.450
2.612
```

.300E-01

bertin technologies

- LL - 23/03/2001

2nd RCM Workshop : RCM2 10 bars test case
The results

Reactive rate (mole/kg/s)
RCM2 2D : monodisperse case
droplet diametre = 110 microns
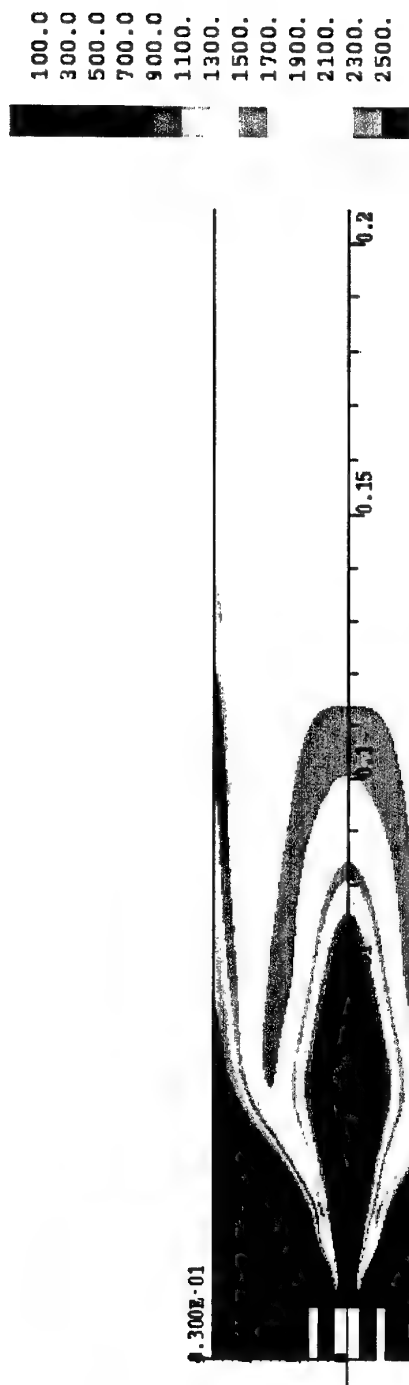
n t 270991
mini: 8.02469E-09
maxi: 1.75812E+06

0.1000E-07
675.8
1892.
4082.
8023.
0.1512E+05
0.2789E+05
0.5087E+05
0.9224E+05
0.1667E+06
0.3008E+06
0.5420E+06
0.9764E+06

0.300E-01

Page : 13

- LL - 23/03/2001

2nd RCM Workshop : RCM2 10 bars test case
The results

Temperature
RCM2 2D : monodisperse case
droplet diametre = 110 microns

n t   270993
mini   85.371
maxi   2418.7

100.0
300.0
500.0
700.0
900.0
1100.
1300.
1500.
1700.
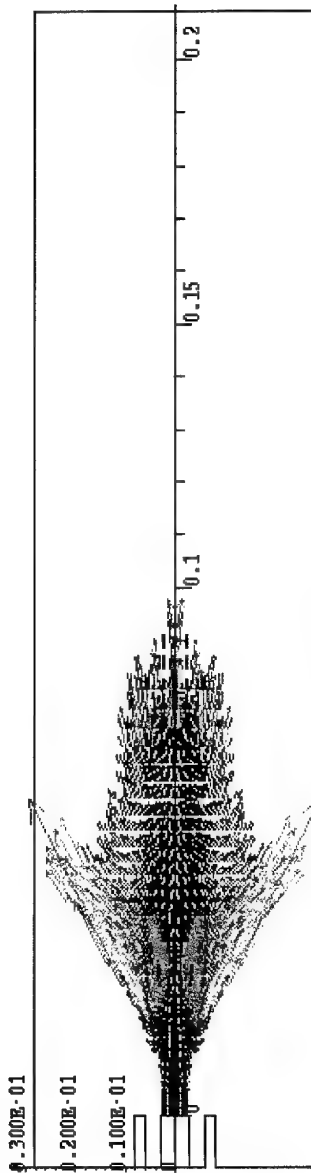1900.
2100.
2300.
2500.

2nd RCM Workshop : RCM2 10 bars test case
The results

Velocity vectors of the dispersed phase
RCM2 2D : monodisperse case
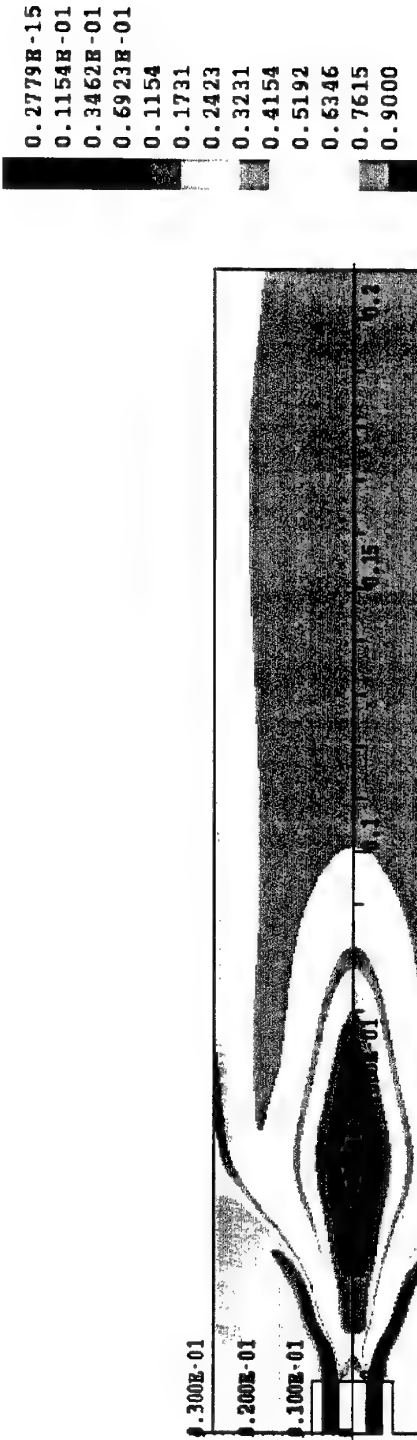droplet diametre = 110 microns

n t   270991
minit 0.0000
maxi: 41.61

0.000
0.5335
1.600
3.201
5.335
8.002
11.20
14.94
19.21
24.01
29.34
35.21
41.61

0.300E-01
0.200E-01
0.100E-01

2nd RCM Workshop : RCM2 10 bars test case
The results

Massic fraction of H2O
RCM2 2D : monodisperse case
droplet diametre = 110 microns

n : 270993
mini: 2.77865E-16
maxi: 0.87504

0.2779E-15
0.1154E-01
0.3462E-01
0.6923E-01
0.1154
0.1731
0.2423
0.3231
0.4154
0.5192
0.6346
0.7615
0.9000

bertin
technologies

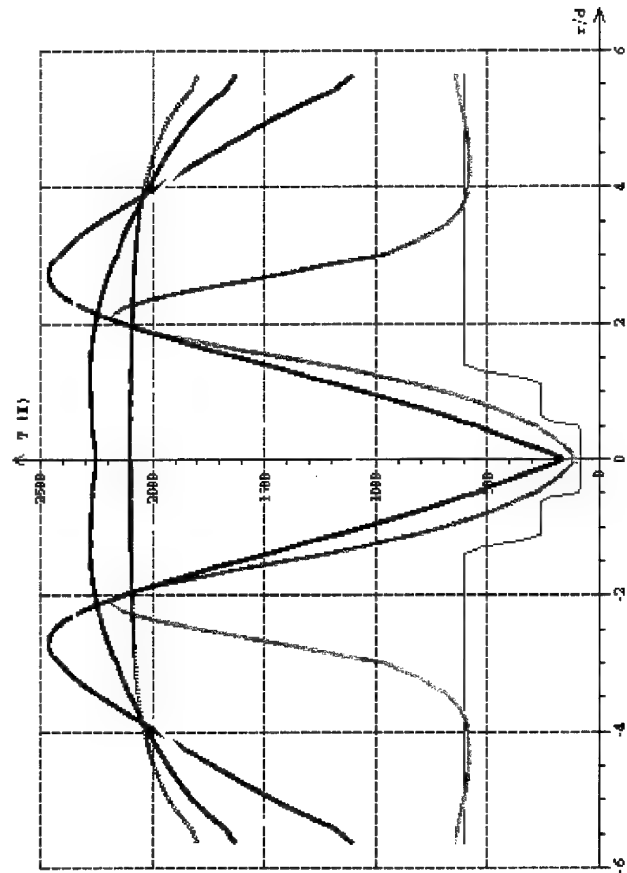- LL - 23/03/2001

Page : 16

2nd RCM Workshop : RCM2 10 bars test case
The results

Temperature
RCM2 2D : polydisperse case
Rosin-Rammler droplet distribution

n t   134004
mini: 81.648
maxi: 2481.5

Temperature a x = 0 mm

Temperature a x = 3 mm

Temperature a x = 6 mm

Temperature a x = 12 mm

Temperature a x = 15 mm
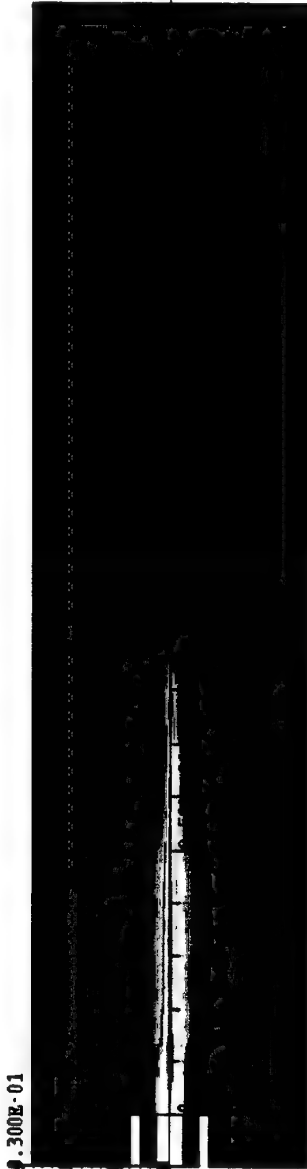

- LL - 23/03/2001

Page : 17

2nd RCM Workshop : RCM2 10 bars test case
The results

Volumic rate for the polydispersed phase
RCM2 2D : polydisperse case
Rosin-Rammler droplet distribution

n : 134004
mini: 0.0000
maxi: 4.3172

0.000
0.1808E-02
0.5062E-02
0.1092E-01
0.2146E-01
0.4044E-01
0.7460E-01
0.1361
0.2468
0.4460
0.8045
1.450
2.612

0.300E-01

bertin
echnologies

Page : 18

- LL - 23/03/2001

2nd RCM Workshop : RCM2 10 bars test case
The results

```
Reactive rate (mole/kg/s)
RCM2 2D : polydisperse case
Rosin-Rammler droplet distribution
```
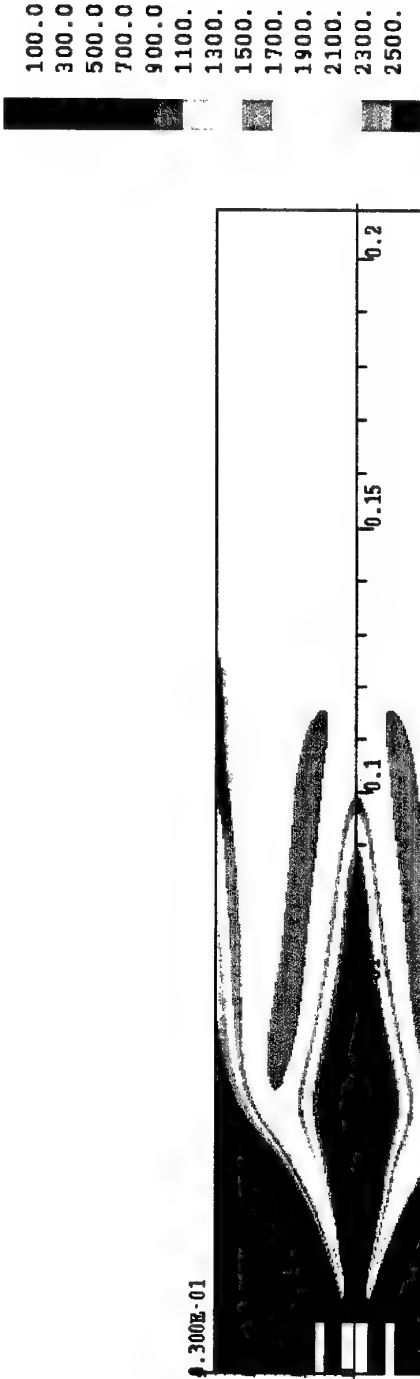
n t   134004
minit 8.02469E-09
maxit 2.69424E+06

0.1000E-07
675.8
1892.
4082.
8023.
0.1512E+05
0.2789E+05
0.5087E+05
0.9224E+05
0.1667E+06
0.3008E+06
0.5420E+06
0.9764E+06

0.300E-01

0.1

bertin
echnologies

- LL - 23/03/2001

Page : 19

2nd RCM Workshop : RCM2 10 bars test case
The results

Temperature
RCM2 2D : polydisperse case
Rosin-Rammler droplet distribution

n : 134004
mini: 83.648
maxi: 2483.5

100.0
300.0
500.0
700.0
900.0
1100.
1300.
1500.
1700.
1900.
2100.
2300.
2500.

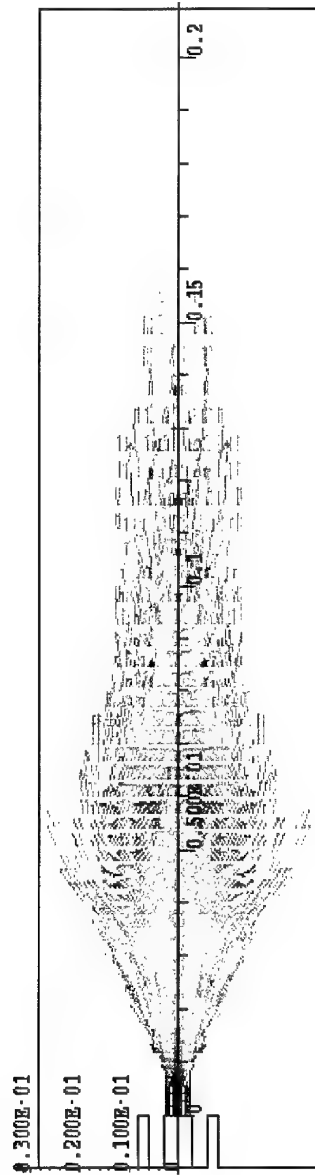- LL - 23/03/2001

bertin
echnologies

Page : 20

2nd RCM Workshop : RCM2 10 bars test case
The results

Velocity vectors of the dispersed phase

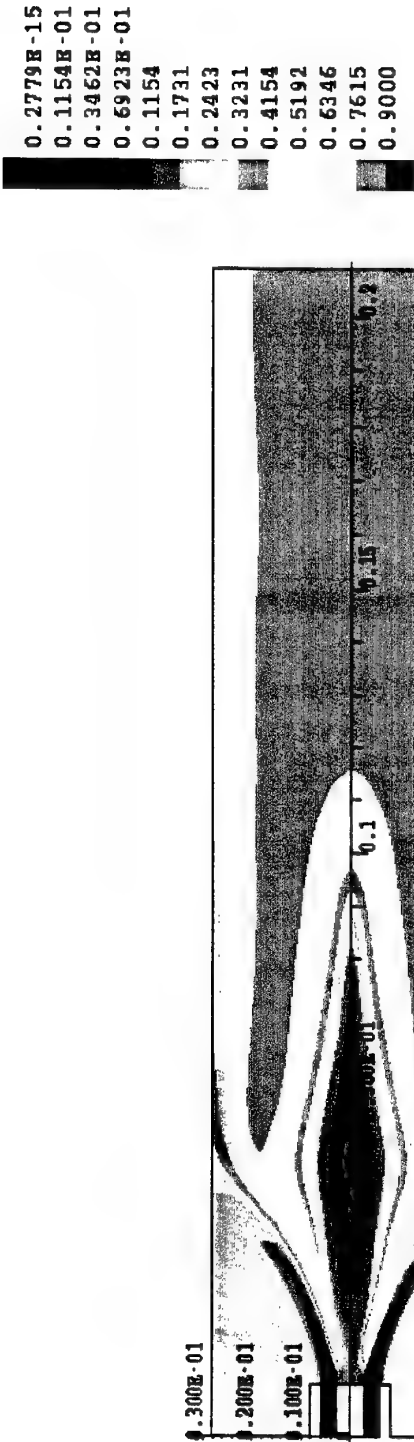RCM2 2D : polydisperse case

Rosin-Rammler droplet distribution

n t   134004
mini: 0.0000
maxi: 15.247

0.000
0.1955
0.5864
1.173
1.955
2.932
4.105
5.473
7.037
8.796
10.75
12.90
15.25

- LL - 23/03/2001

Page : 21

2nd RCM Workshop : RCM2 10 bars test case
The results

Massic fraction of H20
RCM2 2D : polydisperse case
Rosin-Rammler droplet distribution

n : 114004
mini: 2.10579E-16
maxi: 0.07382

0.2779E-15
0.1154E-01
0.3462E-01
0.6923E-01
0.1154
0.1731
0.2423
0.3231
0.4154
0.5192
0.6346
0.7615
0.9000

bertin technologies

Page : 22

- LL - 23/03/2001

2nd RCM Workshop : RCM2 10 bars test case
The results

Volumic rate for the polydispersed phase

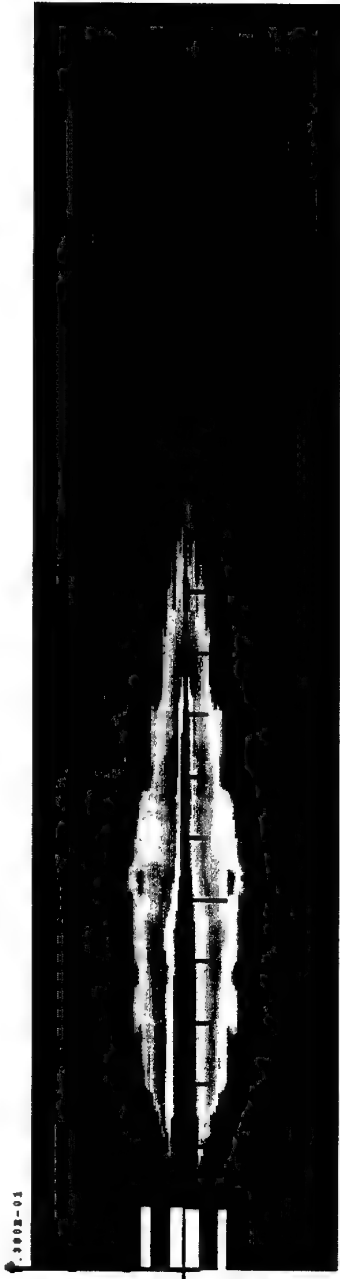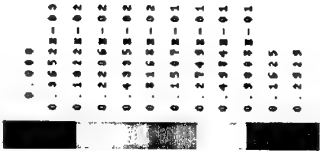Test case   Rosin Ramler v=10 m/s

t :   0.0000

mini: 0.0000
maxi: 0.41059

```
0.000
0.9652E-09
0.1022E-02
0.2206E-02
0.4395E-02
0.8168E-02
0.1507E-01
0.2749E-01
0.4984E-01
0.9008E-01
0.1625
0.2929
```

.300E-01

bertin
technologies

- LL - 23/03/2001

Page : 23

5

2nd RCM Workshop : RCM2 10 bars test case
The results

Volumic rate for the polydispersed phase
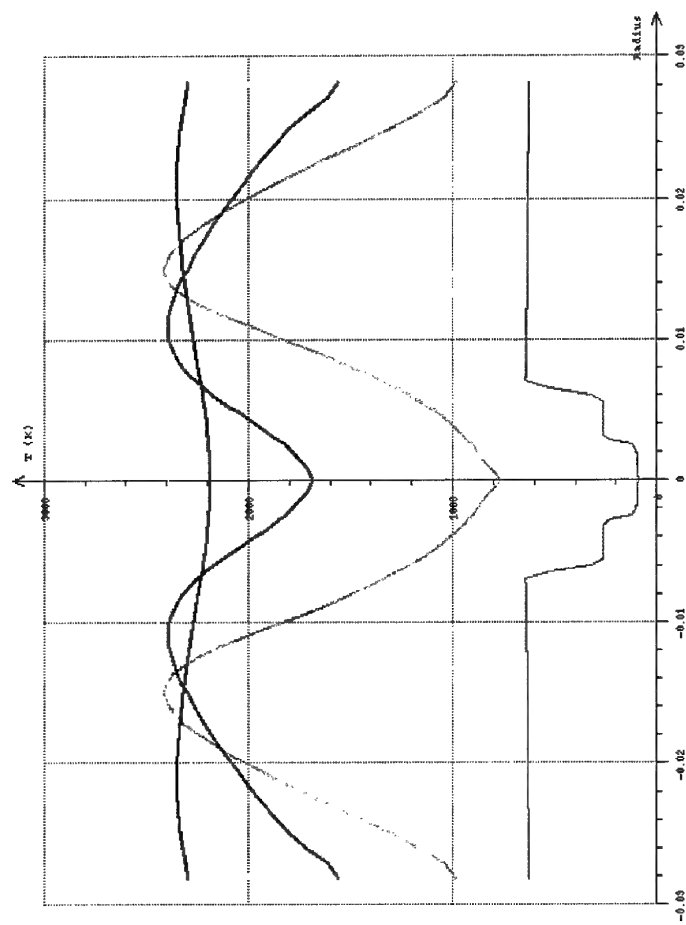
Test case   Rosin Ramler v=3 m/s

2nd RCM Workshop : RCM2 10 bars test case
The results

Temperature

Test case   Rosin Ramler V=10 m/s

t :   0.0000

mini. 91.925
maxi. 2459.5

x = 0 cm

x = 5 cm

x = 10 cm

x = 20 cm
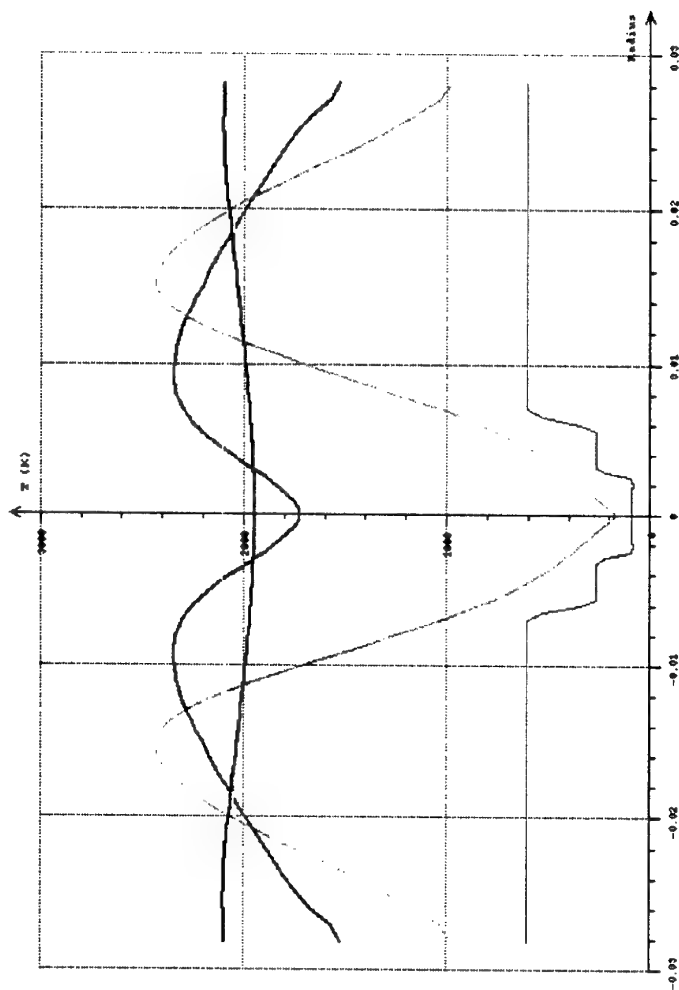
- LL - 23/03/2001

Page : 25

2nd RCM Workshop : RCM2 10 bars test case
The results

Temperature

Test case   Rosin Ramler V=3 m/s
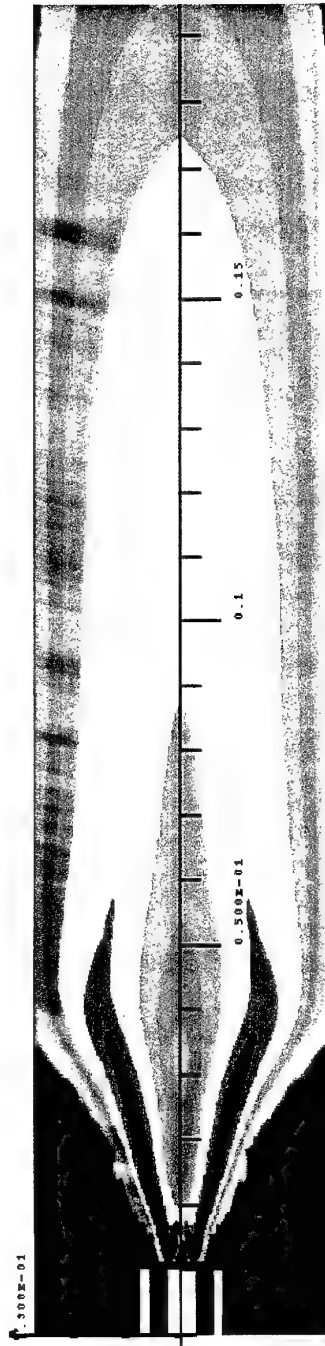
2nd RCM Workshop : RCM2 10 bars test case
The results

Production rate Te

Test case   Rosin Ramler v=10 m/s

t :   0.0000

mini:-1.6191E-06
maxi: 1.8004E+08

0.000
125.4
501.8
1631.
5018.
0.1518E+05
0.4566E+05
0.1371E+06
0.4115E+06
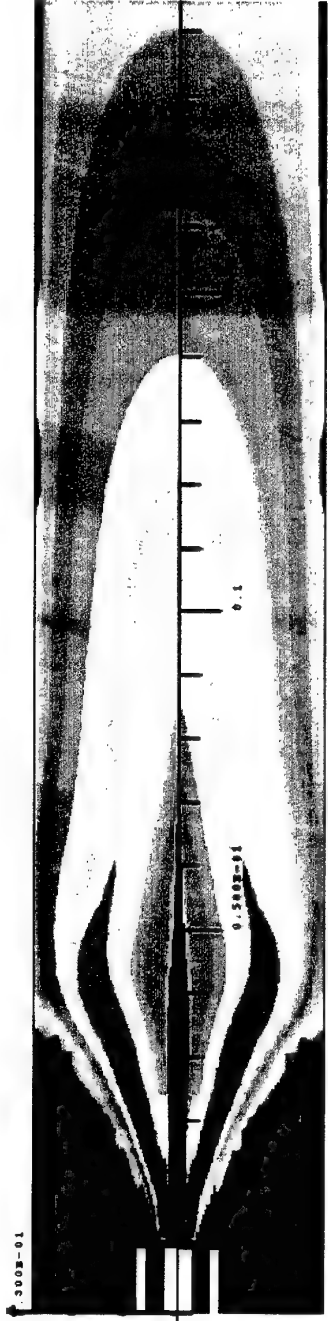0.1295E+07
0.3704E+07
0.1111E+08
0.3333E+08

0.15
0.1
0.500E-01

.300E-01

bertin
technologies

2nd RCM Workshop : RCM2 10 bars test case
The results

Production rate Te

Test case   Rosin Ramler v=3 m/s
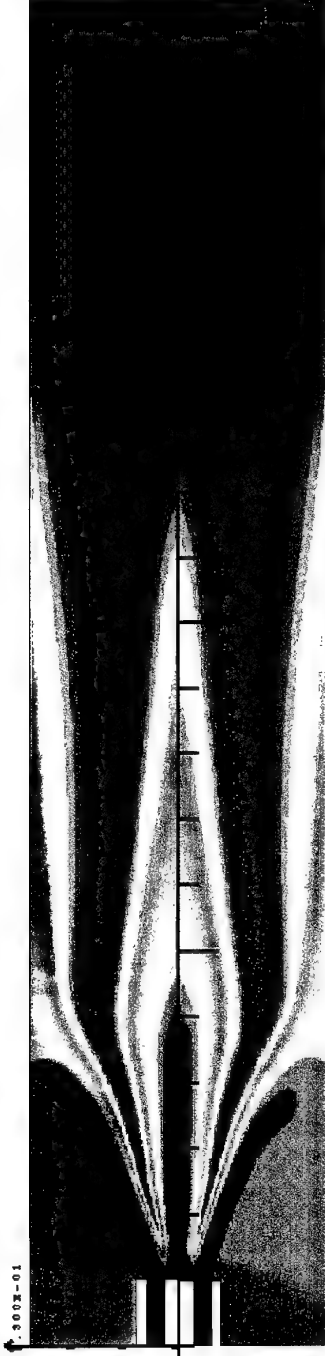

- LL - 23/03/2001

Page : 28

2nd RCM Workshop : RCM2 10 bars test case
The results

Temperature

Test case   Rosin Ramler V=10 m/s

t :   0.0000

mini: 91.325
maxi: 2459.5

```
100.0
200.0
300.0
400.0
500.0
600.0
700.0
800.0
900.0
1000.
1100.
1200.
1300.
1400.
1500.
1600.
1700.
1800.
1900.
2000.
2100.
2200.
2300.
```
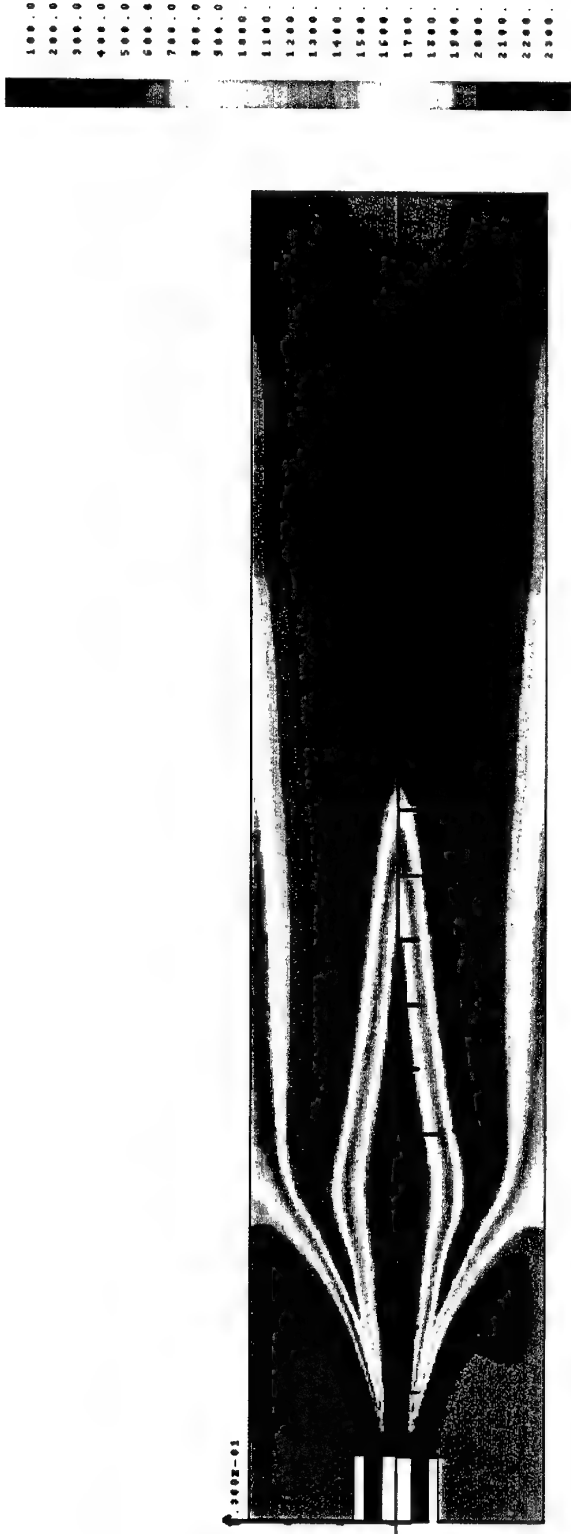
- LL - 23/03/2001

Page : 29

2nd RCM Workshop : RCM2 10 bars test case
The results

Temperature

Test case   Rosin Ramler V = 3 m/s

t :   0.0000

mini: 89.648
maxi: 2489.5

bertin
technologies

- LL - 23/03/2001

2nd RCM Workshop : RCM2 10 bars test case
The conclusion

☐ The use of the most recent version of CPS has been quite straightforward

 ☐ the recent developments to deal with high volumic rates areas appear to be quite robust and can still be enhanced with respect to evaporation

 ☐ it would be be very easy to introduce some very large "droplets" as it seems it appears during experiments

☐ Further developments must be done to be able to use the implicit solver

 ☐ this mandatory to decrease the CPU cost which is very high

☐ The comparison with experimental results will allow to asses the quite "rough" injection strategy

 ☐ at least it is conservative

☐ Good thermodynamic properties is essential for a good evaporation model

bertin technologies

NUMERICAL ANALYSIS OF THE 10 BAR MASCOTTE FLOW FIELD

Mani POUROUCHOTTAMANE[*], Francis DUPOIRIEUX[*],
Lucien VINGERT[*], Mohammed HABIBALLAH[*], and
Victor BURNLEY[§]
[*]ONERA - B.P. 72 – 92322 CHATILLON CEDEX – France
[§]Air Force Research Laboratory, visiting scientist at ONERA

1. Introduction

In liquid propulsion area, as in many other fields, aspects like reliability, delays and cost reduction become a priority. The use of calibrated design tools (CFD codes) may help to make the primary design choice associated to reliable and reduced cost technologies. As far as delays are concerned, they can be reduced by using improved and calibrated predicting tools since the latter will allow to limit the total number of qualifying tests and to focus on the identified critical operational range of a combustion device for instance. CFD analysis may be also used to help directing development tests, analyzing test results and consequently helps to reduce costs and delays.

As far as the propulsion system is concerned, Oxygen/Hydrogen engines are usually the most preferred, due to their high performance. Although the technology of such engines is well known, physical-chemical processes involved in their operation are not all well described yet. In particular, the combustion chamber flow dynamics still arises many questions, in the scientific community. In order to get insight into the complex phenomena involved in the operation of such engines, a research programme has been carried out for several years, in the framework of the GDR research group, involving CNRS, ONERA, SNECMA Moteurs and CNES. The objective of this programme is to step forward in the understanding of the physical-chemical processes taking place in cryogenic (LOX/GH$_2$) rocket engine combustion chambers, and to build up appropriate modelling of such processes. The ultimate goal of such an approach is to provide calibrated predictive CFD tools that can be used during the development programme of launcher propulsion systems.

In the framework of the GDR, ONERA has developed a cryogenic test facility, called Mascotte[1-3], to improve the understanding and modelling of the elementary processes involved in LOX/GH$_2$ combustion. The facility was designed and built up from 1991 to 1993, in the ONERA Palaiseau center, and has been operating since 1994. A large database is now available for model and code validation.

In parallel to the research programme, workshops on Rocket Combustion Modelling (RCM) are organized in cooperation with Germany in the framework of the French-German Memorandum of Understanding on high pressure combustion. The objectives of such workshops is to assess the capabilities of CFD codes to predict liquid rocket engine like flows. To this end, documented test cases are proposed to the contributors.

The first workshop was held in Toulouse (France) in 1998 and the second one in Heilbronn (Germany) in 2001. This paper is a contribution to this second workshop. It deals with the test case RCM2 which consists in the numerical simulation of the 10 bar Mascotte flow field. The test case was computed using the ONERA MSD code. In the following sections, characteristics of the MSD code, computational geometry, injection conditions and models used are first described. Then, results are compared with experimental data and discussed.

2. The MSD code

The MSD code solves the unsteady, three-dimensional, Reynolds-Averaged, Navier-Stokes equations, for a mixture of perfect gases. Discretization is based on finite volume techniques on curvilinear structured grids. The time integration can be either explicit, then a predictor-corrector scheme is used, or implicit with first or second-order accuracy. The implicit algorithm uses a classical ADI factorisation. The spatial discretization scheme is second-order accurate. The Euler fluxes are evaluated through a "Flux Difference Splitting" TVD scheme. The viscous fluxes are calculated at the center of cells and then interpolated on the cell interfaces.

The code presents many features like multi-domain integration; fast convergence towards steady-state solutions can be achieved through multigrid cycles. $k - \varepsilon$ type two-equation models, with Boussinesq closure or ASM closure, are available for the treatment of turbulence and several combustion models are implemented in this code (purely kinetic models and turbulent combustion models).

A Lagrangian solver, named DLS, is also available for particle tracking with one-way or two-way coupling with the gas phase.

3. The Mascotte combustor and computational geometry

The Mascotte combustor and geometry are those specified for the test case RCM2. There are depicted in figures 1 and 2.
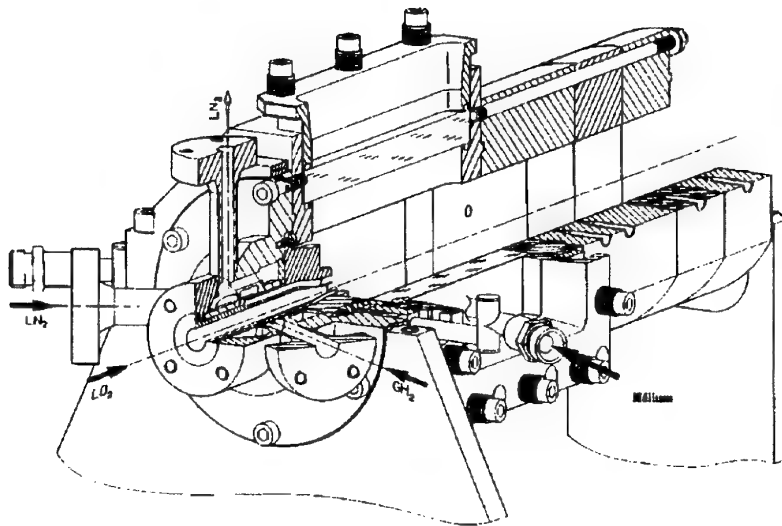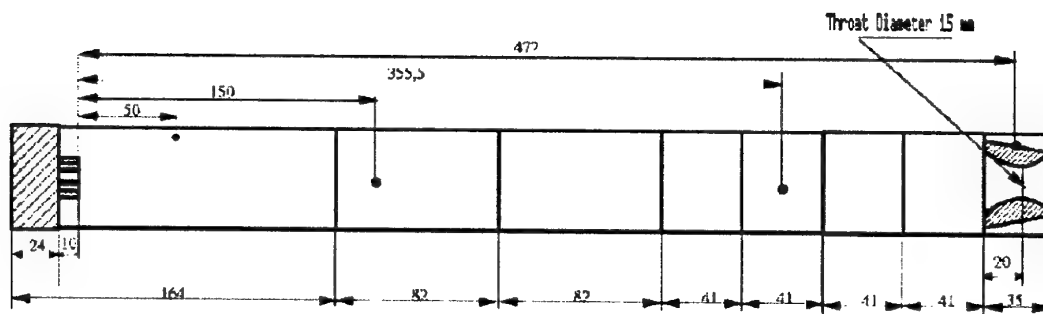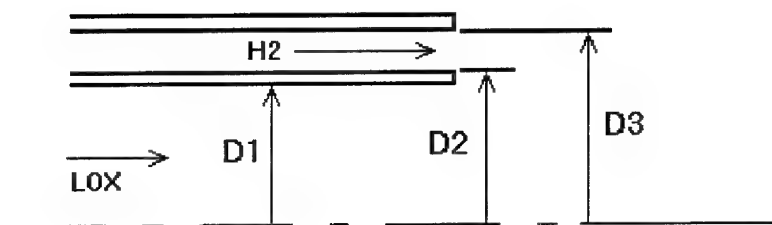

Figure 1: Mascotte Combustor

Figure 2: Combustor geometry (in mm) for the 10 bar case

Simulation were performed using a simplified injector geometry given below :

2

	D1	D2	D3
DIAMETER	5.0 mm	5.6 mm	12.0 mm

Numerical simulations were carried out either with a 2D (axisymmetrical geometry) or a 3D (slice of 5° with one cell in the tangential direction) geometry (Fig. 3). The oxygen liquid core is represented by a solid cone (Fig. 4) which length is 7.8 mm. The length Lc was determined using the following correlation[4]:

$$\frac{L_C}{D_1} = \frac{6}{\sqrt{J}}$$

D_1 being the inner LOX post diameter and J the hydrogen to oxygen momentum flux ratio. Droplets are injected along the cone. Although the chamber is square, we assumed an axisymmetrical geometry, presuming that the phenomena take place mainly in the centrepart of the chamber, therefore neglecting the boundary effects.
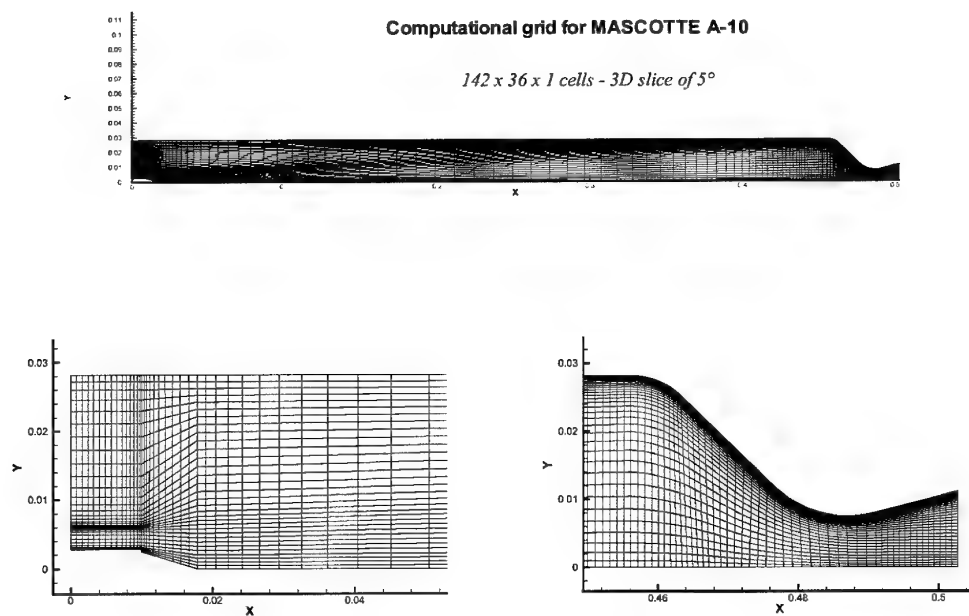

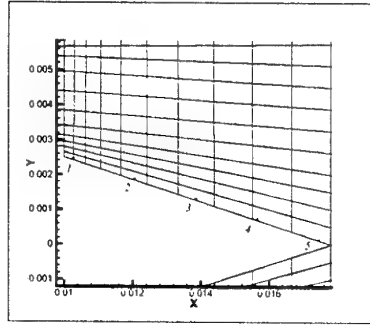Figure 3: Computational geometry and grid

3

Figure 4: Liquid core representation and injection points

4. Operating point and injection conditions

The operation point is A-10 which characteristics are :

PRESSURE	O/F	$\dot{m}$ (LOX)	$\dot{m}$ (H2)
10 bar	2.11	50 g/s	23.7 g/s

Hydrogen is injected gaseous at 287 K. Oxygen is supposed to be atomized and droplets are injected along the core in five locations as shown in figure 4. The injection velocity is 10 m/s and the direction of velocity is given by an empirical correlation[5] :

$$\theta(x) = \arctan[R_i(1 - x/L_c)/(x + R_i/\tan\theta_i)]$$

where $\theta_i = \theta(0)$, $\tan\theta_i = 0.68(U_{gas}/U_{liq} - 1)\sqrt{\rho_{gas}/\rho_{liq}}$,

$R_i = D_1/2$, L_c is the core length and x is the axial distance from the injector exit to the point of injection. Only one class of diameter has been considered.

To investigate the effect of the injection diameter, some computations were performed using three values of the diameter : 50 µm, 82 µm, 115 µm. In fact, flow visualisation showed that the atomisation process is very complex and far from being complete (presence of ligaments) in the near exit region. Nevertheless, some atomisation data could be obtained by means of a one-component PDPA (Phase Doppler Particle Analyzer) at 30 mm from the injector with an acceptable validation rate (47%). These measurements represent the droplet data at the closest location from the injector exit and could be used as inlet boundary condition. The diameter 115 µm corresponds to the Sauter mean diameter given by the PDPA at that location. 82 µm, which was the recommended value, is the Sauter mean diameter of the same distribution truncated at 250 µm by removing a small number of big droplets, and 50 µm was chosen for comparison.

5. Physical modelling

The two-phase turbulent reactive flow generated in the single-element Mascotte combustor is computed using the classical Eulerian-Lagrangian Method. Reynolds Averaged Navier-Stokes equations are solved for the gas and droplets are tracked using the Lagrangian solver DLS. A two-way coupling is performed between the liquid phase and the gas phase. Gas phase turbulence is computed with the $k - \varepsilon$ turbulence model. The turbulent dispersion is treated by the Gossman and Ionnides Eddy Life Time dispersion model with an additional spatial decorrelation criterion[6] to better account for crossing trajectory effect. Vaporization is computed with the standard "D^2" model with Ranz-Marshall correction to account for convection around the droplet. Four combustion models were used for these computations : two kinetic models (the Rogers and Chinitz model and

4

the Eklund model) and two turbulent models (the Magnussen's Eddy break-up model and the CLE model). Although experimental data including OH imaging and Coherent Anti-Stokes Raman Scattering (CARS) indicated a highly turbulent flame, kinetic combustion models were used for comparison. The CLE turbulent combustion model assumes an infinitely fast single scalar chemistry with a β-function pdf and a thermodynamical equilibrium limitation[7].

6. Results

Figure 5 shows radial temperature profile obtained with the two kinetic models at 200 mm from the injector exit. One can notice that both models predict a longer flame than expected and a still stratified temperature field at this location.
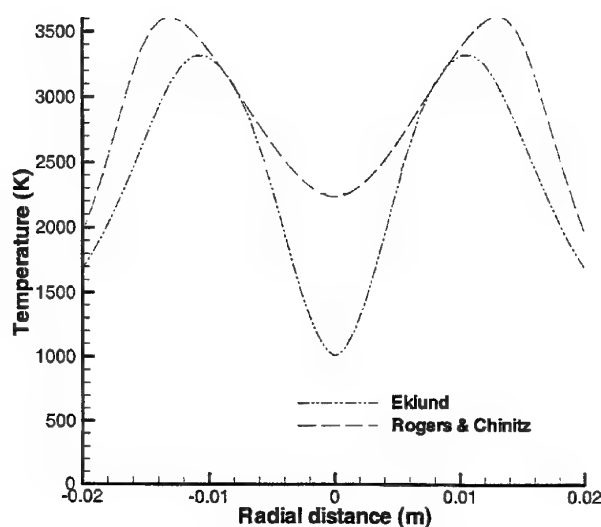

Figure 5 : Temperature profiles (x = 200 mm) – Kinetic models

Computations were also performed using the turbulent combustion models : the Magnussen model and the CLE model. Figure 6 shows a comparison of temperature field for both models. The flame shapes are similar but the Magnussen model gives a very high flame temperature (4500 K). This is due to the single step reaction used in the model that includes only three species O_2, H_2, and H_2O. Dissociation of these molecules into radicals (in particular OH) is ignored leading to an overestimation of the flame temperature.
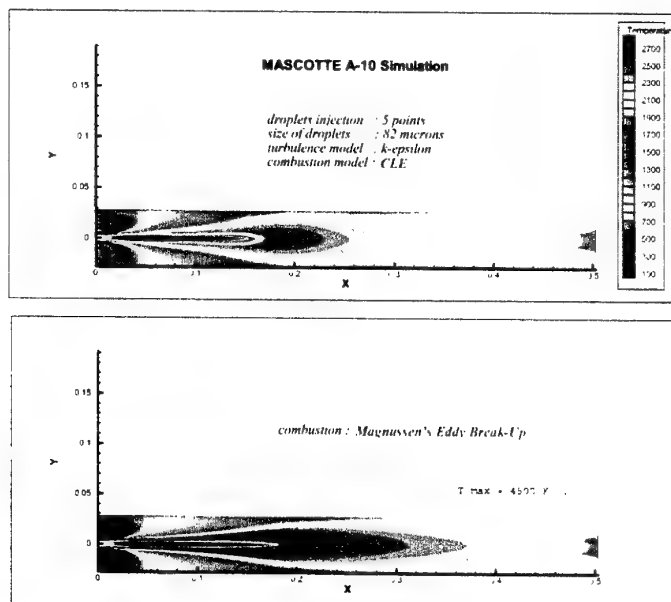
Figure 6 : Temperature field – The Magnussen and CLE models

After these first preliminary computations we choose the CLE model, which seems to give more representative results, to continue the analysis. Figure 7 shows the temperature field for three droplet sizes : the nominal value of 82 μm, a lower value (50 μm) and a higher value (115 μm). The three flames are similar in shape with a cold region at the center, corresponding to cold gaseous oxygen, and a flame zone around. The case with 115 μm injected droplet shows a long flame which expands more than the case with 50 μm for instance.
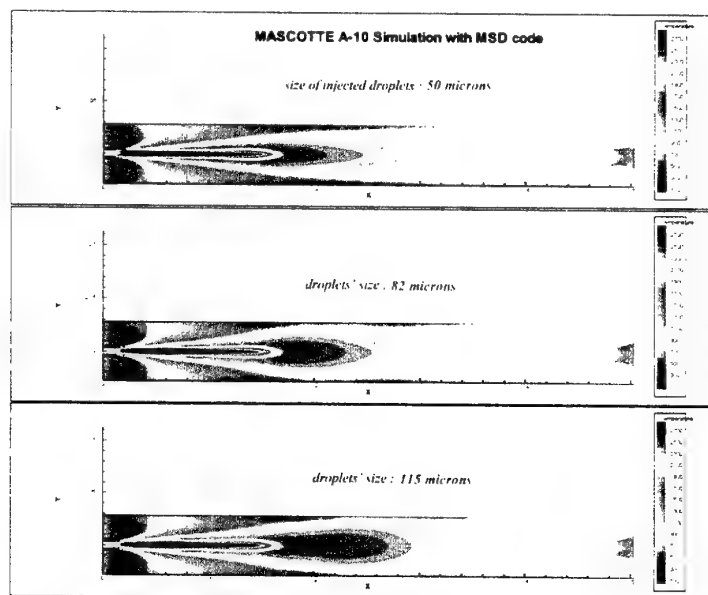

Figure 7 : Temperature field - Effect of droplet size diameter

The corresponding liquid presence and mixture ratio are displayed in figure 8. The figure shows (left) that big drops (82 μm and 115 μm) have crossed the flame.

6

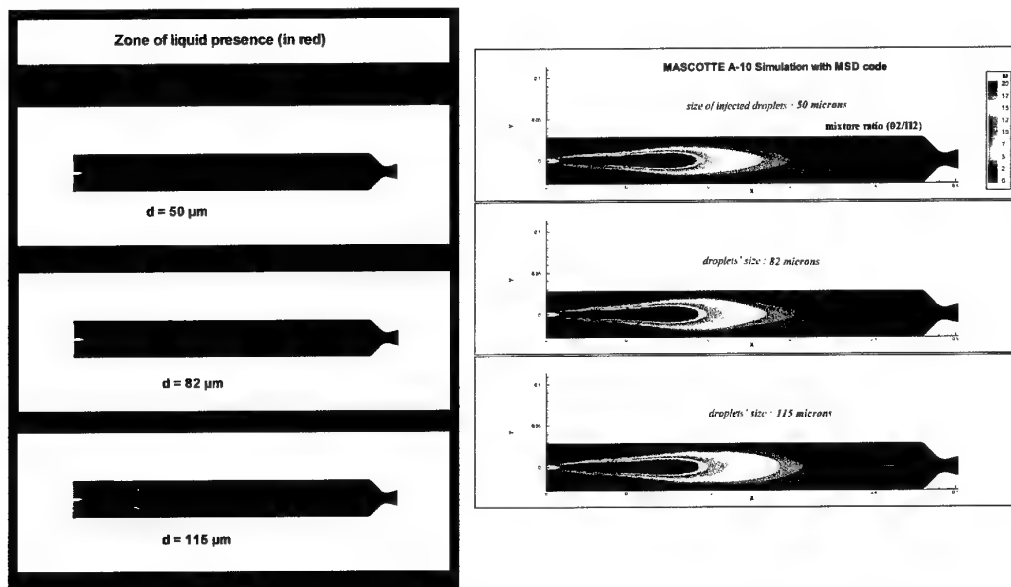Figure 8 : Liquid presence and mixture ration (O_2/H_2) - Effect of droplet size diameter

Results presented in the subsequent figures correspond to the 82 μm droplets. Figure 9 shows the temperature field and streamlines where the recirculation zone can be observed. Figure 10 shows hydrogen and gaseous oxygen mass fractions.
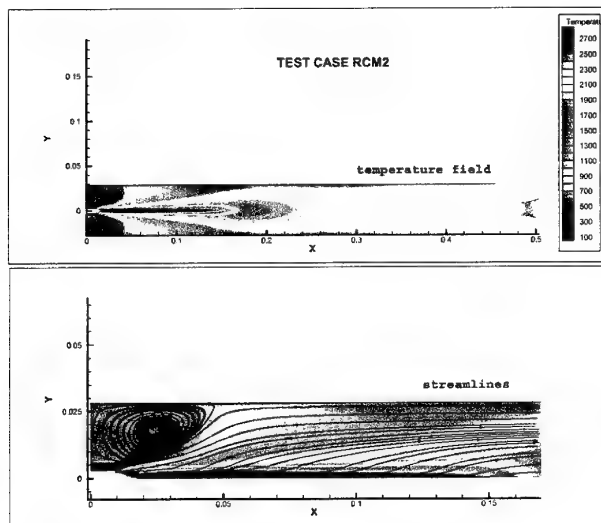

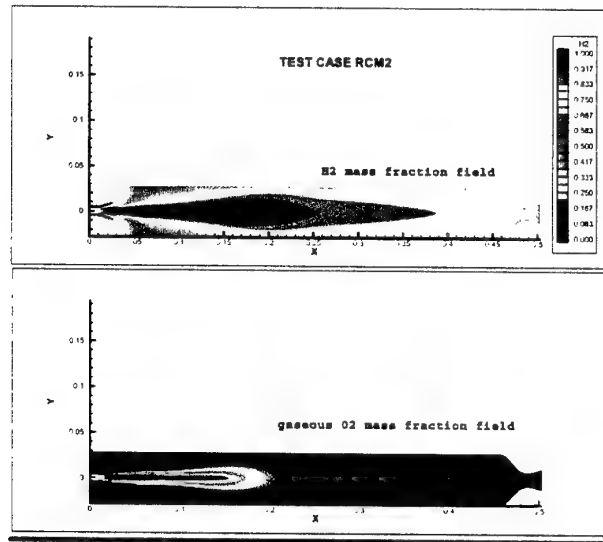Figure 9 : Temperature field and streamlines - CLE model, D = 82 μm.

Figure 10 : Mass fractions - CLE model, D = 82 μm.

Figure 11 shows velocity vectors, gas axial velocity, oxygen mass fraction, and hydrogen mass fraction in the near-injector region. One can notice particularly the high hydrogen axial velocity in the injection zone.
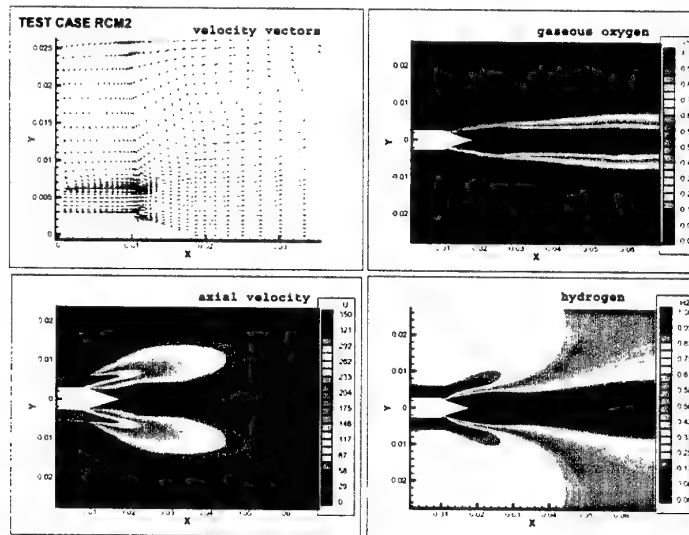

Figure 11 : Velocities and mass fractions in the near-injector zone - CLE model, D = 82 μm.

Figures 12 and 14 show a comparison of computed temperature profiles with experimental data obtained by means of the CARS technique. The CARS technique, using in this case hydrogen as a probe molecule, allows to measure instantaneous gas temperature at a given spatial location. The number on the experimental data (Figures 12 and 14) represents the validation rate which is the ratio of the number of CARS signals successfully processed to the total number of laser shots acquired during a Mascotte run. Nearly 100 laser shots are acquired during a run. At a fixed location, each CARS signal gives an instantaneous temperature. From the instantaneous values one can obtain a mean value and a standard deviation. Of course precision of the measurements depends on the validation rate, higher is this number, better are the statistics. The interval that bounds the experimental data (Figures 12 and 14) represents the standard deviation. The high values of the standard deviation indicate the turbulent character of the flow field.

Figure 12 compares temperature radial profiles at four axial locations : 10, 180, 250, and 410 mm from the injector exit. At 10 mm, one can observe a good agreement between computed results and experimental data.

8

This region corresponds to the recirculation zone with high concentration of hydrogen which also explains the observed high validation rate. As we move downstream, we have a relatively good agreement with the experimental data. It can be also noticed that the validation rate is low on the axis (x = 180 mm and x = 250 mm) and increases as we move to the chamber wall where more hydrogen in present. No hydrogen is detected on the axis at x = 10 mm.
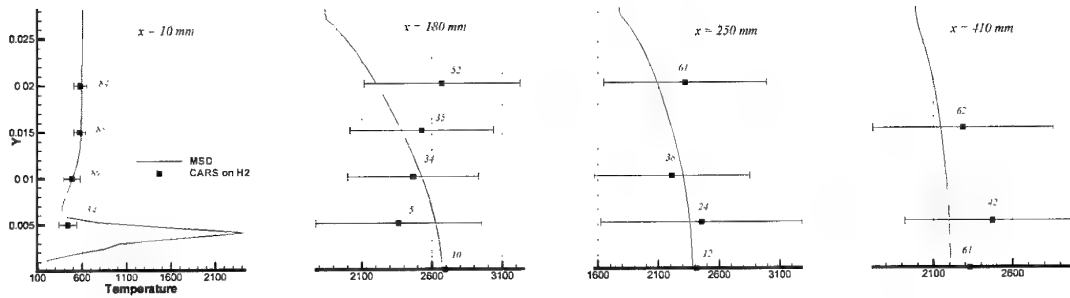
Figure 12 : Temperature radial profiles – Comparison of computations and experimental data

Figures 13 and 14 show temperature axial profiles at three radial locations. (y = 5, 10, and 15 mm). In figure 13, the temperature field is also presented. At 10 and 15 mm, computed profiles are compared with the experimental data. The agreement is fairly good.

Figure 13 : Temperature field and temperature axial profile at y = 5 mm.

Figures 15 presents temperature radial profiles at other intermediate locations between 10 mm and 410 mm. One can observe that the flame is closed at 200 mm which corresponds to the observed data. At 100 mm, the temperature on the axis seems too low, indicating a poor mixing at this location.
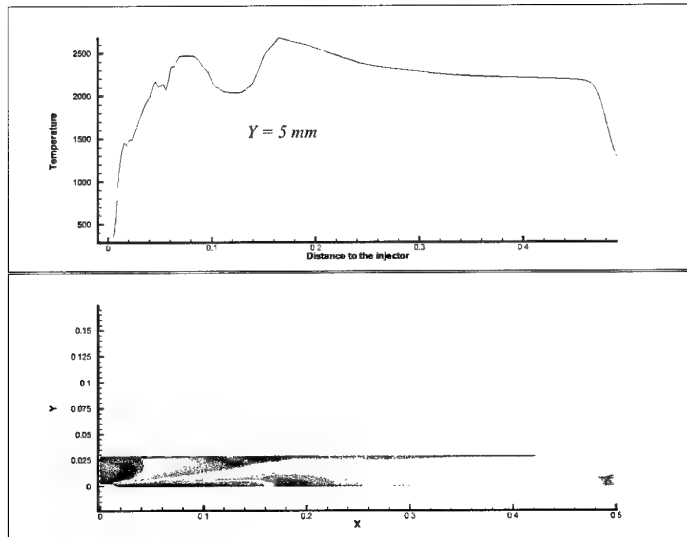
9
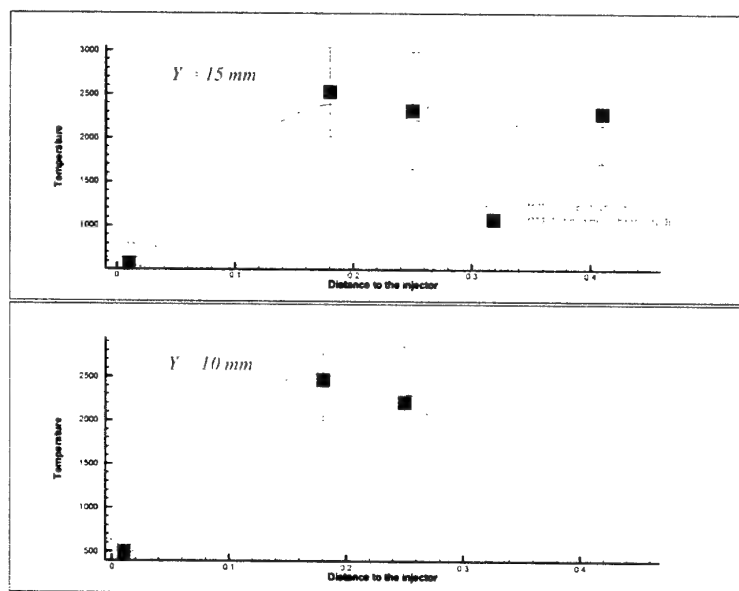
Figure 14 : Temperature axial profiles - Comparison of computations and experimental data
(y = 10 mm and y = 15 mm)
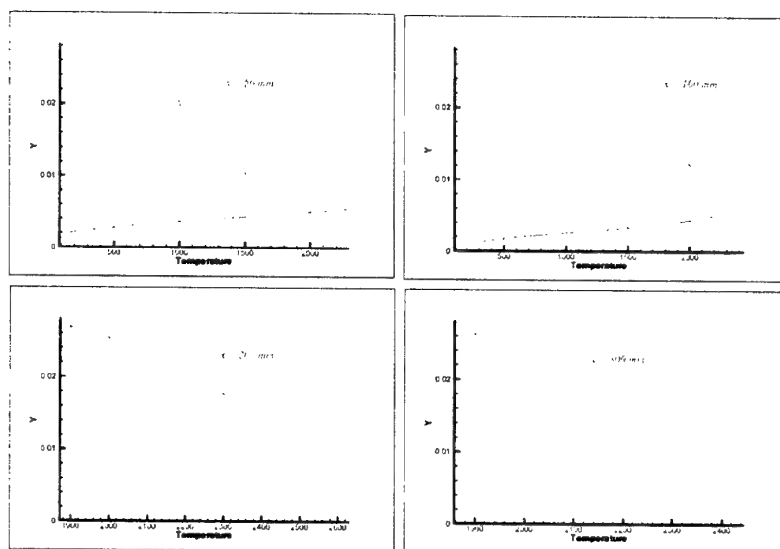
Figure 15 : Temperature radial profiles at other axial locations

7. Conclusion

Numerical simulations of the 10 bar Mascotte flow field performed using the ONERA MSD code have been presented. Droplets were injected along the liquid core represented by a solid cone. Only one class of droplets was injected which diameter was estimated from experimental data. Both kinetic and turbulence models were tested. The turbulent CLE model was found to be the most promising model for these computations. The flame was found to be anchored to the LOX post tip as observed experimentally.

Comparison with CARS data indicate a good agreement in the recirculation zone where temperature is relatively low with high hydrogen concentration. A relatively good agreement is observed on the radial profiles and axial profiles. The flame length could be estimated between 180 and 200 mm.

The flame development could be observed on temperature field and also on intermediate radial profiles of temperature. It seems that the flame does not expand very much compared to the observed data as OH imaging

10

for instance. Temperature on the axis remains low as far as 100 mm downstream indicating a poor mixing in that region.

Improvements could be searched for by considering a more realistic distribution with more drop sizes, effect of droplets on turbulence level, and other processes such as secondary atomisation and coalescence.

Of course, atomisation is one of the crucial points of this kind of computations as it constitutes the boundary condition for oxygen injection. More representative models have to be developed and used.

References

[1]   M. Habiballah, L. Vingert, J.-C. Traineau, P. Vuillermoz, "MASCOTTE : a test bench for cryogenic combustion research", IAF-96-S.2.03, *47th International Astronautical Congress*, (Beijing, China), October 7-10, 1996.

[2]   L. Vingert, M. Habiballah, J.-C. Traineau, , "MASCOTTE : a research facility for high pressure combustion of cryogenic propellants", 12th European Aerospace Conference, 3rd European Conference on Space Transportation Systems; November 29 – December 01, 1999, Paris.

[3]   L. Vingert, M. Habiballah, P. Vuillermoz, S. Zurbach, "MASCOTTE, a test facility for cryogenic combustion research at high pressure", IAF-00-S.3.06, *51th International Astronautical Congress*, (Rio de Janeiro, Brazil), October 2 - 6, 2000.

[4]   E. Villermaux, "Mixing and spray formation in coaxial jets", *Journal of Propulsion and Power*, Vol. 14, n°5, pp. 807-817, Sept-Oct. 1998.

[5]   Care, " Etude d'un injecteur coaxial assisté. ", PhD Thesis, Université de Rouen, Décembre 1990.

[6]   D. Bissière, " Modélisation du comportement de la phase liquide dans les chambres de combustion de statoréacteurs. ", PhD Thesis, Ecole Centrale, 1997.

[7]   G. Turpin, " Revue des modèles de combustion turbulente. Travaux de la 1ère année de thèse. ", Rapport Technique ONERA RT/2/6181 DSNA/Y, Mars 2000.

DIRECT NUMERICAL SIMULATIONS OF LOX/H_2 TEMPORAL MIXING LAYERS UNDER SUPERCRITICAL CONDITIONS

Nora Okong'o, Kenneth Harstad and Josette Bellan*
Jet Propulsion Laboratory
California Institute of Technology
4800 Oak Grove Drive
Pasadena, CA 91109-8099

Abstract

Direct Numerical Simulations (DNS) of a supercritical LOX/H_2 temporal three-dimensional mixing layer are conducted for the purpose of exploring the features of high pressure mixing behavior. The conservation equations are formulated according to fluctuation-dissipation (FD) theory which is not only totally consistent with non-equilibrium thermodynamics, but also relates fluxes and forces from first principles. According to FD theory, complementing the low-pressure typical transport properties (viscosity, diffusivity and thermal conductivity), the thermal diffusion factor is an additional transport property which may play an increasingly important role with increasing pressure. The Peng-Robinson equation of state with a correction for obtaining accurate molar volumes, in conjunction with appropriate mixing rules, is coupled to the dynamic conservation equations to obtain a closed system. The boundary conditions are periodic in the streamwise and spanwise directions, and of non-reflecting outflow type in the cross-stream direction. Following the DNS protocol, the studied temperature/pressure regime is one where both Kolmogorov and Batchelor scales can be resolved for pseudo-species (i.e. species with transport properties modified to allow the attainment of large enough Reynolds numbers). Correlations for the Schmidt and Prandtl numbers as functions of the thermodynamic variables, based on exact fluid properties, are used to ensure that correct relative transport processes are employed. To obtain rollup and pairing, the layer is perturbed similarly to heptane/nitrogen mixing layers that achieved transition in previous investigations. Due to the strong density stratification, the layer is considerably more difficult to entrain

*Corresponding author: josette.bellan@jpl.nasa.gov

1

than equivalent initial Reynolds number gaseous. droplet-laden or supercritical heptane/nitrogen layers. Simulations conducted with initial Reynolds numbers of 600 and 750, an initial convective Mach number of 0.4, an initial pressure of 100 atm. and freestream temperatures of 400 K in the lower LOX and 600 K in the upper H_2 stream. eventually exhibit distorted regions of high density gradient magnitude similar to the experimentally observed wisps of fluid at the boundary of supercritical jets. The temperature stratification was chosen such that the computation can be spatially resolved at these Reynolds numbers. accounting for memory constraints. In these simulations the layer does not exhibit transition to turbulence. although they are conducted with an initial Reynolds number and perturbation for which transition was obtained for a heptane/nitrogen mixing layer having a smaller initial density stratification. The cause of this occurrence is analyzed using global growth characteristics. vorticity and vorticity-magnitude budgets, instantaneous visualizations of the dynamic and thermodynamic variables and an inspection of the origins and spatial location of dissipation. The lack of transition is traced to two combined effects. First, the relatively large spanwise perturbation is responsible for the early creation of small turbulent scales which destroy the coherence of the vortices formed through pairing, resulting in a weakened ultimate vortex. Second, regions of high density gradient magnitude are formed due both to the distortion of the initial density stratification boundary and to the mixing of the two species: in these regions. the weakened vortex cannot create the small turbulent scales that are crucial to mixing transition.

1   Introduction

Liquid rocket propulsion relying on hydrogen/liquid-oxygen (LOX) combustion is not a mature technology in that improvements in design are still necessary to mitigate efficiency and stability problems. To solve these problems in a systematic manner, it is required to understand the fundamental processes occurring in liquid rocket chambers. A simplified description of the sequence of events in one of these combustion chambers is as follows: LOX enters the chamber through one of the many injection ports, and irrespective of the exact injection configuration, LOX disintegrates, mixes with H_2 in a highly turbulent manner while being ignited, with ensuing combustion producing water and other incomplete combustion products. From this description, it is immediately clear that LOX disintegration plays a crucial role in determining the size of the LOX parcels entering in contact with H_2, and further the efficiency of the combustion process.

    LOX disintegration is a process essentially different from the much studied spray atomization that involves the breakup of a liquid into a multitude of drops. Liquid breakup relies on physical mechanisms involving the surface tension, and therefore it is an appropriate concept only when a surface tension does indeed exist. In contrast, in liquid rocket chambers the mean pressure is about 20 MPa, with peaks as high

as 30 MPa, and therefore both LOX and H_2 are in a supercritical state (see Table 1). By definition [1], a substance is in a supercritical state when it is at a pressure, p, **or** temperature, T, exceeding its critical value (indicated here by a subscript c). What truly characterizes the supercritical state is the impossibility of a two phase region. Indeed, when the reduced pressure, $p_r \equiv p/p_c > 1$ **or** the reduced temperature $T_r \equiv T/T_c > 1$, in the (p, T) plane there is no longer the possibility of a two phase (i.e. gas/liquid) region, and instead there is only a single-phase region [2]. The general term for the substance is fluid, i.e. neither a gas nor a liquid. Noteworthy, since the critical locus of O_2/H_2 mixtures may include smaller or higher values of (p_c, T_c) than those of the pure species, it is possible that locally in space and time the mixture could be at subcritical conditions, but such a situation cannot be assumed to hold for any amount of time owing to the continuous change in the mixture composition. Moreover, Harstad and Bellan [3] concluded from their study of the evolution of an initial LOX fluid drop immersed in H_2 at pressures from 6 to 40 MPa, that nowhere in the fluid drop or in the fluid mixture surrounding it, are critical or subcritical conditions reached. The indications from this study as well as recent LOX/H_2 experimental evidence from Mayer et al. [4], [5] is that LOX disintegration assumes characteristics different from atomization, and that these characteristics reflect features associated with supercritical conditions. In contrast to the process of atomization, past the critical point of the fluid, disintegration assumes the aspect of what Chehroudi et al. [6] call 'fingers', or 'comb-like structures' at transcritical conditions, having an increasingly gaseous appearance with increasing pressure; their experiments were conducted with N_2/N_2, $N_2/(CO+N_2)$, He/N_2 and O_2/N_2. Related to the present study, Raman scattering measurements of the radial density in free N_2 jets at 4 MPa by Oschwald and Schik [7] show sharp profiles independent of the injection temperature, indicating the occurrence of sharp density gradients. These regions of sharp density gradients are indeed one of the distinctive optical features in environments at supercritical conditions. Not only have they been experimentally observed, but they have also been identified in simulations of heptane/nitrogen three-dimensional mixing layers (see Miller et al. [8], and Okong'o and Bellan [9]). Analysis of an enlarged database of Miller et al. [8] by Okong'o and Bellan [10] revealed that these regions of large density gradient magnitude play a crucial role in delaying transition to turbulence by acting similar to material surfaces in that they damp emerging turbulent eddies.

Because the behavior of a binary species system depends on the identity of the species, it is uncertain if our previous findings for heptane/nitrogen are immediately applicable to the LOX/H_2 system which is here of interest. For example, Harstad and Bellan [11] found that under supercritical conditions, compared to the heptane/nitrogen combination, the LOX/H_2 system displays an increased solubility, and also much larger effective Lewis numbers, Le_{eff}. The increased solubility results from the thermodynamic mixing rules [1], whereas the enhanced effective Lewis numbers were attributed to the considerably larger difference of the specific (i.e. mass based)

3

enthalpies of the components in the LOX/H_2 system compared to the equivalent difference for heptane/nitrogen.

The present paper is devoted to the study of LOX/H_2 three-dimensional (3D) mixing layers through Direct Numerical Simulations (DNS) as a means of obtaining information about its specific behavior. Since in DNS all scales of the flow are resolved, these simulations appear ideal for developing information to be used in modeling LOX disintegration, as well as turbulent LOX/H_2 mixing. In Section 2 below we briefly recall the conservation equations derived elsewhere [8], [9]. Section 3 is devoted to describing the particular aspects of the equation of state implemented in the model such as to obtain increased accuracy with respect to the typical Peng-Robinson formalism. Further, in Section 4 we address the choice of the transport coefficients. The configuration and boundary conditions are addressed in Section 5, whereas in Section 6 we discuss the numerics. Section 7 focuses on the initial conditions and presents results from a linear, inviscid stability analysis which is used to understand specific aspects of the LOX/H_2 mixing layer that are necessary for choosing initial conditions for the 3D simulations. In Section 8, we present two 3D simulations at different initial Reynolds numbers, Re_0. The global characteristics of the layers show that despite the relatively large momentum thickness based Reynolds number, Re_m, neither of these two layers reached transition. To understand the origin of lack of transition attainment, we concentrate on detailed studies of the layer with the larger Re_0 and present the results of this analysis. A summary and conclusions appear in Section 9.

2   Conservation equations

The conservation equations are briefly recalled, and the reader is referred for details to Miller et al. [8], Okong'o and Bellan [9] and Okong'o et al.[12]. For the binary mixture under consideration, the conservation equations are

$$\frac{\partial \rho}{\partial t} + \frac{\partial \left(\rho u_j\right)}{\partial x_j} = 0, \tag{1}$$

$$\frac{\partial \left(\rho u_i\right)}{\partial t} + \frac{\partial \left(\rho u_i u_j + p\delta_{ij}\right)}{\partial x_j} = \frac{\partial \tau_{ij}}{\partial x_j}, \tag{2}$$

$$\frac{\partial \left(\rho Y_O\right)}{\partial t} + \frac{\partial \left(\rho Y_O u_j\right)}{\partial x_j} = -\frac{\partial j_{Oj}}{\partial x_j}, \tag{3}$$

$$\frac{\partial \left(\rho e_t\right)}{\partial t} + \frac{\partial \left[\left(\rho e_t + p\right) u_j\right]}{\partial x_j} = -\frac{\partial q_{IKj}}{\partial x_j} + \frac{\partial \tau_{ij} u_i}{\partial x_j}, \tag{4}$$

4

where x is a Cartesian coordinate, t is time, ρ is the density, u_i is the velocity, $e_t = e + u_i u_i / 2$ is the total energy (i.e. internal energy, e, plus kinetic energy), p is the thermodynamic pressure (the temperature is T) and Y_O is the mass fraction of O_2 (the mass fraction of H_2 is $Y_H = 1 - Y_O$). Furthermore, $\mathbf{q}_{IK}$ is the Irwing - Kirkwood (subscript IK) form of the heat flux vector (see Sarman and Evans [13]), $\mathbf{j}_O$ is the heptane mass flux vector and τ_{ij} is the Newtonian viscous stress tensor

$$\tau_{ij} = \mu \left[\frac{\partial u_i}{\partial x_j} + \frac{\partial u_j}{\partial x_i} - \frac{2}{3} \frac{\partial u_k}{\partial x_k} \delta_{ij} \right], \tag{5}$$

where δ_{ij} is the Kronecker delta function, and μ is the mixture viscosity which is in general a function of the thermodynamic state variables. The mass flux and heat flux are given by

$$j_{Oj} = - \left[j'_{Oj} + (\alpha_{IK} - \alpha_h) Y_O Y_H \frac{\rho D}{T} \frac{\partial T}{\partial x_j} \right], \tag{6}$$

$$q_{IKj} = -\lambda'_{IK} \frac{\partial T}{\partial x_j} - \alpha_{IK} R_u T \frac{m}{m_O m_H} j'_{Oj}, \tag{7}$$

$$j'_{Oj} = \rho D \left[\alpha_D \frac{\partial Y_O}{\partial x_j} + \frac{Y_O Y_H}{R_u T} \frac{m_O m_H}{m} \left(\frac{v_{,O}}{m_O} - \frac{v_{,H}}{m_H} \right) \frac{\partial p}{\partial x_j} \right], \tag{8}$$

with

$$\alpha_h = \frac{1}{R_u T} \frac{m_O m_H}{m} \left(\frac{h_{,O}}{m_O} - \frac{h_{,H}}{m_H} \right). \tag{9}$$

The notation in eqs. 6 - 9 is as follows: D is the binary diffusion coefficient; α_D is the mass diffusion factor which is a thermodynamic quantity; m_α is the molar mass of species α; $m = m_O X_O + m_H X_H$ is the mixture molar mass where the molar fraction $X_\alpha = m Y_\alpha / m_\alpha$; $v_{,\alpha} = (\partial v / \partial X_\alpha)_{T,p,X_\beta(\beta \neq \alpha)}$ is the partial molar volume and $h_{,\alpha} = (\partial h / \partial X_\alpha)_{T,p,X_\beta(\beta \neq \alpha)}$ is the partial molar enthalpy; $v = X_H v_{,H} + X_O v_{,O}$, is the molar volume related to the density by $v = m/\rho$, $h = X_H h_{,H} + X_O h_{,O}$ is the molar enthalpy; R_u is the universal gas constant and λ'_{IK} is a thermal conductivity defined from the transport matrix

$$\lambda'_{IK} = \lambda + X_H X_O \, \alpha_{IK} \, \alpha_{BK} R_u \rho D / m, \tag{10}$$

where $\lim_{p \to 0} \lambda = \lambda_{KT}$ as discussed in [14], where the subscript KT refers to Kinetic Theory. The new transport coefficients associated with the Soret (in the molar fluxes) and the Dufour (in the heat flux) terms of the transport matrix are α_{BK} and α_{IK}, which are the thermal diffusion factors corresponding to the IK and the Bearman-Kirkwood (subscript BK) forms of the heat flux (see Sarman and Evans [13]). These

5

transport coefficients are characteristic of each particular species pairs and they obey the relationship

$$\alpha_{BK} = \alpha_{IK} - \alpha_h, \tag{11}$$

as shown by Harstad and Bellan [14]. Additionally, $\lim_{p\to 0} \alpha_{IK} \neq \alpha_{KT}$ and $\lim_{p\to 0} \alpha_{BK} = \alpha_{KT}$.

To solve the system of equations above, it must be closed by specifying the equation of state (EOS) and the transport properties.

3 Equation of state

The pressure can be calculated from the well-known Peng-Robinson (PR) EOS given the PR molar volume, v_{PR}, as

$$p = \frac{R_u T}{(v_{PR} - b_m)} - \frac{a_m}{(v_{PR}^2 + 2b_m v_{PR} - b_m^2)}, \tag{12}$$

where a_m, b_m are functions of T and X_α (see Appendix A). Due to the inaccuracy of the PR EOS at high pressures (see [1]), v_{PR} may differ significantly from the actual molar volume v. Therefore for improved accuracy, we use a modified PR EOS in which both v_{PR} and the volume shift

$$v_S = v - v_{PR} \tag{13}$$

are calculated from the PR EOS given p, T and X_α.

All the thermodynamic properties such as the molar enthalpy, $h = G - T(\partial G/\partial T)_{p,X}$, the constant-pressure molar heat-capacity, $C_p = (\partial h/\partial T)_{p,X}$, and the speed of sound, $a_s = \sqrt{1/\rho\kappa_s}$, are calculated in a consistent manner from the same EOS using the Gibbs energy, G:

$$G(T, p, X_\alpha) = \int_v^{v_u} p(v', T, X_\alpha) dv' + pv - R_u T + \sum_\alpha X_\alpha \left[G_\alpha^0 + R_u T \ln(X_\alpha) \right], \tag{14}$$

where the superscript 0 represents the 'low pressure' reference condition for the integration as generally used in the departure function formalism described by Prausnitz et al. [1]. The integral is ill defined for a zero pressure reference condition; hereinafter we choose $p^0 = 1bar$ such that $v_u = R_u T/p^0$. The volume shift v_S is calculated from G_α^0 (see Harstad et al. [15]) as

$$v_S = \sum X_\alpha \frac{\partial G_\alpha^0}{\partial p}. \tag{15}$$

The isentropic compressibility, κ_s is calculated from

$$\kappa_s = \kappa_T - vT\alpha_v^2/C_p, \tag{16}$$

6

where the expansivity (α_v) and the isothermal compressibility (κ_T) are given by

$$\alpha_v = -\frac{(\partial p/\partial T)_{v,X}}{v(\partial p/\partial v)_{T,X}} \, , \qquad \kappa_T = \frac{-1}{v(\partial p/\partial v)_{T,X}} \, . \tag{17}$$

The mass diffusion factor, α_D, is calculated from the fugacity coefficients, φ_α (which are related to the Gibbs energy), through

$$\alpha_D = 1 + X_\alpha \frac{\partial \ln(\varphi_\alpha)}{\partial X_\alpha} \tag{18}$$

and portrays departures from mixture ideality (i.e. $\alpha_D = 1$). Noteworthy, α_D is independent of the species chosen in the calculation of eq. 18.

These equations specify the entire thermodynamics of the binary mixture.

4 Transport coefficients

DNS are calculations where both the Kolmogorov and Batchelor scales must be resolved. To ensure that this requirement is satisfied, we produced contour plots (not shown) of the viscosity, and of Sc and the Prandtl number, Pr, based on accurate species transport properties calculated as in Harstad and Bellan [16]. Based on these contour plots in the range 200K to 800K, the transport properties were correlated as

$$\mu = \mu_R \left(\frac{T}{(T_1 + T_2)/2} \right)^{0.75} ; \qquad T \text{ in Kelvins,} \tag{19}$$

$$Sc \equiv \frac{\mu}{\rho \alpha_D D} = \left(1.334 - 0.668 Y_O - 0.186 Y_O^2 - 0.268 Y_O^6 \right) \left[1 + \left(\frac{88.6}{T} \right)^{1.5} \right], \tag{20}$$

$$\Pr \equiv \frac{\mu C_p/m}{\lambda} = \frac{1.335}{T^{0.1}}, \tag{21}$$

where μ_R is a reference viscosity and the reference temperatures T_1 (upper H_2 stream) and T_2 (lower O_2 stream) correspond to the free stream temperatures for mixing layer simulations.

The value of the reference viscosity is determined by the specified value of Re_0 (see below), chosen so as to enable the resolution of all relevant length scales.

The thermal diffusion factor is selected as in Harstad and Bellan [16] with $\alpha_{BK} = 0.2$, and α_{IK} is calculated from eq. 11.

7

5 Configuration and boundary conditions

The temporally developing mixing layer configuration is depicted in Fig. 1, which shows the definition of the streamwise (x_1), cross-stream (x_2) and spanwise (x_3) coordinates. The layer is not symmetric in extent in the x_2 direction, having found in our simulations that the layer growth is considerably larger in the hydrogen side. The freestream density $(\rho_1$ or $\rho_2)$ is calculated for each pure species at its freestream temperature $(T_1$ or $T_2)$ and at the initial uniform pressure (p_0). The vorticity thickness is defined as $\delta_\omega(t) = \Delta U_0 / (\partial < u_1 > /\partial x_2)_{max}$ where $< u_1 >$ is the $x_1 - x_3$ planar average velocity in the streamwise direction, and $\Delta U_0 = U_1 - U_2$ is the velocity difference across the layer. Miller et al. [8] explain the choice of the velocities of the two streams in a simulation initiated with four streamwise vortices pairing twice to produce an ultimate vortex. The choice of U_1 and U_2 for a real fluid

$$U_1 = 2M_{c,0}a_{s_1} \left[1 + \left(\frac{a_{s_1}}{a_{s_2}} \right) \sqrt{\frac{\rho_1 Z_1}{\rho_2 Z_2}} \right]^{-1}, \qquad U_2 = -\sqrt{\frac{\rho_1 Z_1}{\rho_2 Z_2}} U_1, \qquad (22)$$

was made with the intent of keeping the ultimate vortex stationary in the computational domain, although the success of this strategy was only partial. Here $M_{c,0}$ is the convective Mach number and $Z = p/(\rho T R_u/m)$ is the compression factor indicating departures from the perfect gas behavior (i.e. $Z = 1$). The specification of $M_{c,0}$ therefore determines ΔU_0. Given the initial streamwise velocity profile u_1 based on U_1 and U_2, $(\partial < u_1 > /\partial x_2)_{max}$ and hence $\delta_{\omega,0} \equiv \delta_\omega(0)$ are calculated.

The specified value of the initial flow Reynolds number,

$$Re_0 = \frac{0.5(\rho_1 + \rho_2)\Delta U_0 \delta_{\omega,0}}{\mu_R} \qquad (23)$$

is used to calculate μ_R.

The boundary conditions are periodic in the streamwise and spanwise directions, and of outflow type for real gas as derived by Okong'o et al. [12]. The outflow type conditions are essential to maintain stability since the initial perturbation causes large pressure waves which must be allowed out of the domain with minimal reflection.

6 Numerics

6.1 General method

The conservation equations are numerically solved using a fourth-order explicit Runge-Kutta time integration and a sixth-order compact scheme for spatial derivatives ([17]). Time stability is achieved by filtering the conservative variables every five time steps in the interior, in each spatial direction alternately, using an eighth-order filter. Since high-order boundary filters are unstable, no filtering is applied at the non-periodic

8

(x_2) boundaries. The computations were parallelized using three-dimensional domain decomposition and message passing. The tridiagonal solver for the compact derivative scheme was efficiently parallelized using the method of [18]. The simulations were performed on an SGI Origin 2000 supercomputer, using 64 processors.

In our solution protocol, once the pressure, temperature, and mole fractions are calculated, the density and energy are calculated from the EOS. To calculate the pressure and temperature from the known energy and mole fractions, we iterate at each time step, as described below.

6.2   Iterative solution for the pressure and temperature

Using the modified Peng-Robinson equation of state [15], once (p, T, X_α) are specified, one can calculate (ρ, e, Y_α). However, in the DNS the dependent variables are (ρ, e, Y_α) from which v and X_α are calculated as

$$m = \frac{1}{\sum_\alpha \dfrac{Y_\alpha}{m_\alpha}}, \quad X_\alpha = \frac{mY_\alpha}{m_\alpha}, \quad v = \frac{m}{\rho}. \tag{24}$$

This means that an iteration is necessary to obtain the values of (p, T) corresponding to the DNS (ρ, e). The procedure for this iteration is to update (p, T) at iteration level n, (p^n, T^n), using:

$$T^n = T^{n-1} + dT, \quad p^n = p^{n-1} + dp, \tag{25}$$

$$dT = \left(\frac{\partial T}{\partial v}\right)^{n-1}_{e,X_\alpha} dv + \left(\frac{\partial T}{\partial e}\right)^{n-1}_{v,X_\alpha} de + \sum_\alpha \left(\frac{\partial T}{\partial X_\alpha}\right)^{n-1}_{\substack{v,e,X_\beta \\ \beta \neq \alpha}} dX_\alpha, \tag{26}$$

$$dp = \left(\frac{\partial p}{\partial v}\right)^{n-1}_{v,X_\alpha} dv + \left(\frac{\partial p}{\partial e}\right)^{n-1}_{v,X_\alpha} de + \sum_\alpha \left(\frac{\partial p}{\partial X_\alpha}\right)^{n-1}_{\substack{v,e,Y_\beta \\ \beta \neq \alpha}} dX_\alpha. \tag{27}$$

Since X_α are known, $dX_\alpha = 0$. Also

$$de = e - e^{n-1}, \quad dv = v - v^{n-1}, \tag{28}$$

where

$$e^{n-1} = e\left(p^{n-1}, T^{n-1}, X_\alpha\right), \quad v^{n-1} = v\left(p^{n-1}, T^{n-1}, X_\alpha\right) \tag{29}$$

are computed from the EOS. The needed derivatives can be calculated from C_p, κ_T and α_v (where h, e in J/kg, C_p, C_v in J/mol K) as

$$\left(\frac{\partial T}{\partial v}\right)_{e,X_\alpha} = \frac{1}{v\alpha_v}\left(1 - \frac{C_p}{C_v}\right) + \frac{p}{C_v}, \quad \left(\frac{\partial T}{\partial e}\right)_{v,X_\alpha} = \frac{m}{C_v}, \tag{30}$$

9

$$\left(\frac{\partial p}{\partial v}\right)_{e,X_\alpha} = \frac{1}{\kappa_T}\left(-\frac{C_p}{C_v}\frac{1}{v} + \alpha_v \frac{p}{C_v}\right), \quad \left(\frac{\partial p}{\partial e}\right)_{v,X_\alpha} = \frac{m}{C_v}\frac{\alpha_v}{\kappa_T}. \tag{31}$$

The iteration is conducted by updating (p,T) until de and dv are within a desired tolerance, e.g. $de/e < 10^{-6}$, $dv/v < 10^{-6}$. The initial guess for (p,T) is from the previous time step, or the previous Runge-Kutta stage. For the O_2/H_2 regime under consideration, (p,T) converge in 2 iterations. It was also noted that if the initial guess for (p,T) is $(p_\infty,(T_1+T_2)/2)$, 4 or 5 iterations are required for convergence. Thus, there appears to be no need to store (p,T), therefore relaxing some of the computation overhead associated with this iteration. In fact, the memory overhead of the iterative method is the addition of the four arrays necessary to store e, v, e^{n-1}, v^{n-1}. Compared with the heptane/nitrogen simulations where a PR EOS for computing the pressure and an energy fit for temperature were employed [9], here an additional 50% CPU time per time step is used. However, for the O_2/H_2 mixture, the form of the energy fit for the temperature would be considerably more complicated than that of the heptane/nitrogen mixture, and the pressure can no longer be computed directly from the molar volume.

6.3   Resolution

The appropriate resolution of all scales is checked by visual inspection of the dilatation field, $\nabla \cdot u$, which is the most sensitive to numerical errors. The absence of small scale fluctuations in $\nabla \cdot u$ is well known to be a reasonable indicator of good resolution.

Generally, the flow field is extremely sensitive to having an appropriate resolution, and its lack is manifested by the code crashing. Another diagnostic of inadequate resolution is an increasing number of iterations for the convergence of the calculation involving the EOS, leading eventually to the code crashing as well.

7   Initial conditions

The appropriate initial conditions for simulating the evolution of mixing layers are notoriously difficult to choose, especially for density stratified situations (see a discussion in Miller et al. [8]). To this end, following Drazin and Reid [19], there are two issues that must be addressed: first, one must inquire about the basic (i.e. mean) flow, and then about the appropriate disturbance. Both of these issues were thoroughly investigated by Okong'o and Bellan [21] for real gases, and applied to the heptane/nitrogen system under supercritical conditions. The same formalism is applied here to explore the specific features of the O_2/H_2 system. Having determined here (by numerically solving the laminar equations) that the form of the basic flow for the O_2/H_2 system is that of an errorfunction-like profile (not shown), and thus that it has a single inflection point, a two-dimensional stability analysis is performed with the error function representing the mean flow; this is acceptable since according to

10

Drazin and Reid [19], for mean flows displaying a single inflection point the stability analysis is not sensitive to the exact form of the mean flow.

The freestream velocity is specified as

$$\bar{u}_1(\infty) = U_1; \quad \bar{u}_1(-\infty) = U_2 \tag{32}$$

and the mean velocity, temperature and mass fraction follow an error function profile, as listed below. Since the pressure is constant, the speed of sound and inverse of the density also assume approximately error function profiles. Therefore, the profiles used in the stability analysis are

$$\bar{u}_1(x_2) = \bar{u}_1(-\infty) + \frac{[\bar{u}_1(\infty) - \bar{u}_1(-\infty)]}{2} \left[\mathrm{erf}\left(\sqrt{\pi} \frac{x_2}{\delta_\omega} \right) + 1 \right], \tag{33}$$

$$a_s(x_2) = a_s(-\infty) + \frac{[a_s(\infty) - a_s(-\infty)]}{2} \left[\mathrm{erf}\left(\sqrt{\pi} \frac{x_2}{\delta_\omega} \right) + 1 \right], \tag{34}$$

$$\frac{1}{\bar{\rho}(x_2)} = \frac{1}{\bar{\rho}(-\infty)} + \frac{1}{2} \left[\frac{1}{\bar{\rho}(\infty)} - \frac{1}{\bar{\rho}(-\infty)} \right] \left[\mathrm{erf}\left(\sqrt{\pi} \frac{x_2}{\delta_\omega} \right) + 1 \right]. \tag{35}$$

Several mean flow conditions are listed in Tables 2 - 4. To find the stability characteristics of the layer, perturbations are imposed through

$$\Delta u_i = \hat{u}_i(x_2) \exp\left[i\alpha(x_1 - ct) \right], \tag{36}$$

$$\Delta p = \hat{p}(x_2) \exp\left[i\alpha(x_1 - ct) \right], \tag{37}$$

$$\Delta \rho = \hat{\rho}(x_2) \exp\left[i\alpha(x_1 - ct) \right], \tag{38}$$

where α is real and c is complex, and the hat denotes the perturbation amplitudes, all of which are functions of x_2 only. Within the protocol of the stability analysis, the physical quantities are obtained by taking the real part (subscript re) of the complex quantities.

Since the mean velocity, density and speed of sound have the same profiles as for heptane-nitrogen [21], the stability curves could be expected to be similar for the same initial density stratification and $M_{c,0}$. However, as illustrated in Fig. 2a where results are obtained for the conditions listed in Tables 2 and 3, discrepancies arise because, due to the different fluid properties, the freestream Mach numbers are different. Generally, the most unstable wavelengths are slightly longer for the O_2/H_2 mixture, as can be seen from Fig. 2a and from a comparison of Table IV in [21] with Table 5 herein, listing the most unstable wavelengths. More important and directly relevant to the strategy of conducting simulations for temperature ratios

11

$| T_2 - T_1 | / T_2$ as large as possible, even for values of $| T_2 - T_1 | / T_2$ quite smaller than unity, ρ_2/ρ_1 is here very large, and certainly much larger than for heptane/nitrogen. Equivalently, as listed in Table I of [21] and Table 3 herein, $\rho_2/\rho_1 = 12.88$ corresponds to $| T_2 - T_1 | / T_2 = 0.667$ for heptane/nitrogen and 0.2 for O_2/H_2, while $| T_2 - T_1 | / T_2 = 0.5$ returns $\rho_2/\rho_1 = 24.40$ for O_2/H_2 as shown in Table 4. For smaller freestream temperatures and $| T_2 - T_1 | / T_2 = 0.5$, the stratification is even larger, as shown in Fig. 2c for a range of T_1 and T_2 and at $p = 100$ and 400 atm. This indicates that as ρ_2/ρ_1 becomes larger, due to computational constraints associated with an increased number of nodes in the direction of the initial density gradient stratification (i.e. x_2) for the same resolution, the O_2/H_2 DNS must be restricted to smaller ratios $| T_2 - T_1 | / T_2$ than the equivalent simulations conducted for heptane/nitrogen [9], [21]. Therefore, all simulations conducted herein will be for the mean flow properties displayed in Table 4, and only Re_0 will be varied.

Following the arguments of Okong'o and Bellan [21] showing that 3D eigensolutions to the stability problem are not uniquely defined, the simulations are started with heuristic streamwise and spanwise vorticity perturbations [20],[22] superimposed on the mean initial velocity profile

$$\omega_1(x_2, x_3) = F_{3D} \frac{\lambda_1 \Delta U_0}{\Gamma_1} f_2(x_2) f_3(x_3) \qquad (39)$$

$$\omega_3(x_1, x_2) = F_{2D} \frac{\lambda_3 \Delta U_0}{\Gamma_3} f_1(x_1) f_2(x_2) \qquad (40)$$

where Γ_1 and Γ_3 are the circulations,

$$f_1(x_1) = A_0 \left| \sin\left(\frac{\pi x_1}{\lambda_1}\right) \right| + A_1 \left| \sin\left(\frac{\pi x_1}{2\lambda_1}\right) \right| + A_2 \left| \sin\left(\frac{\pi x_1}{4\lambda_1}\right) \right| + A_3 \left| \sin\left(\frac{\pi x_1}{8\lambda_1} - \frac{\pi}{2}\right) \right| \qquad (41)$$

$$f_2(x_2) = \exp\left[-\pi \left(\frac{x_2}{\delta_{\omega,0}}\right)^2 \right] \qquad (42)$$

$$f_3(x_3) = B_0 \sin\left(\frac{2\pi x_3}{\lambda_3}\right) + B_1 \sin\left(\frac{\pi x_3}{L_3}\right). \qquad (43)$$

We use $F_{2D} = 0.1$, $A_0 = 1$, $A_1 = 0.5$, $A_2 = A_3 = 0.35$ for the streamwise perturbations, and $F_{3D} = 0.05$, $B_0 = 1$ and $B_1 = 0.025$ for the spanwise perturbations. The wavelength of the perturbation is $\lambda_1 = 7.29\delta_{\omega,0}$ (the most unstable wavelength for incompressible flow) and $\lambda_3 = 0.6\lambda_1$, following [20]. Since this perturbation wavelength is smaller than the most unstable one, $\lambda_1 = 10.35\delta_{\omega,0}$, and the difference between the

12

two values is significant, based on the results of Okong'o and Bellan [21] with simulations perturbed at wavelengths smaller than the most unstable one, it is expected that even if a transitional state is here achieved, the structures will not be as convoluted as when the layer would be perturbed with the most unstable wavelength. The initial vorticity thickness $\delta_{\omega,0}$ is 6.859×10^{-3} m. The grid is chosen for all simulations so as to accommodate four wavelengths in the streamwise and spanwise directions, and the evolution of the layer is meant to encompass rollup and two pairings of the initial spanwise vortices. For these initial conditions, the grid sizes and the resolutions are displayed in Table 6.

8 Results

The results of the simulations listed in Table 6 are here discussed. For the first simulation, the value of Re_0 is chosen to be 600 to emulate a condition which led to a transitional state for the heptane/nitrogen mixing layer studied by Okong'o and Bellan [9]; however, that mixing layer had an initial density stratification of 12.88 instead of the much larger value of 24.40 employed in the present study. The larger $Re_0 = 750$ of the second simulation represents an effort to enhance the probability of reaching a transitional state; however, this more elevated Re_0 did not lead to transition either. To understand the physics associated with these results, we first focus on the global characteristics of the layer with special emphasis on the features indicative of transition. Further, we investigate the specific aspects of the instantaneous fields which are inherently absent from the measures given by the global characteristics. Finally, in order to understand some of the peculiarities of the instantaneous fields, we conduct a second order statistical analysis focussing on the dissipation.

8.1 Global growth characteristics

One of the essential characteristics of a mixing layer is its growth. Although many definitions of growth appear in the literature, Cortesi et al. [23] showed that several such measures, including the momentum thickness, are qualitatively similar. Here, we define the momentum thickness as

$$\delta_m = \frac{-1}{(\theta_1 - \theta_2)^2} \int_{-L_{2,\min}}^{L_{2,\max}} (\theta_2 + <\rho u_1>)(\theta_1 + <\rho u_1>) dx_2 \tag{44}$$

with $\theta_1 = <\rho u_1>_{x_2=L_{2,\max}}$ and $\theta_2 = <\rho u_1>_{x_2=L_{2,\min}}$, where $L_{2,\min} = -L_2/3$ and $L_{2,\max} = 2L_2/3$. While the growth is mostly a consequence of entrainment, the product thickness defined as $\delta_p = \int \int \int_V \rho Y_p dV$ in mass units, where $Y_p = 2\min(Y_O, Y_H)$, is a direct consequence of molecular mixing as also explained by Cortesi et al. [23]. Both of these quantities, non-dimensionalized, are illustrated versus the nondimensional time $t^* = t\Delta U_0/\delta_{\omega,0}$ in Fig. 3a, respectively, for the R600 and R750 simulations. The non-dimensional momentum thickness, $\delta_m/\delta_{\omega,0}$ of both layers is similar.

13

The R600 layer exhibits the first pairing at $t^* = 80$, but does not show promise of a second pairing by $t^* = 125$, at which time the simulation was terminated due to lack of further interest. In comparison, the R750 layer pairs first at $t^* = 80$ and finishes the second pairing at $t^* = 150$; this simulation was continued to $t^* = 190$ to explore the possible transition to turbulent mixing after the second paring. Despite the continuous growth of the layer, and the attainment of a relatively large $\mathrm{Re}_m = 1680$, the R750 layer does not reach transition for reasons discussed below. Compared to other initially density stratified layers such as drop laden layers (c.f. Miller and Bellan [24]; stratification of 1.5), or to supercritical layers of lesser initial stratification (c.f. Okong'o and Bellan [9]; stratification of 12.88), the present layers do not show the characteristic $\delta_m/\delta_{\omega,0}$ plateaux indicative of the influence of the forcing. This fact is attributed to the much larger present stratification, resulting in a resistance to entrainment. The nondimensional product thickness, $\delta_p/\delta_{p,0}$, displays a continuous growth indicating that despite the lack of transition, molecular mixing proceeds unabated.

Depicted in Fig. 3b are rotational global features of the layers: the non-dimensional positive spanwise vorticity, $<< \omega_3^+ >> (\delta_{\omega,0}/\Delta U_0)$, and the non-dimensional enstrophy, $<< \omega_i\omega_i >> (\delta_{\omega,0}/\Delta U_0)^2$, where $\omega = \nabla \times \mathbf{u}$ is the vorticity; here $<<>>$ denotes volume averaging. Since the initial mean velocity profile is such that the initial spanwise vorticity is negative, $<< \omega_3^+ >> (\delta_{\omega,0}/\Delta U_0)$ is an indicator of the development of small turbulent scales. Complementing this information, $<< \omega_i\omega_i >> (\delta_{\omega,0}/\Delta U_0)^2$ is a manifestation of stretching and tilting, the mechanism which is primarily responsible for the formation of small scales. For both simulations, $<< \omega_3^+ >> (\delta_{\omega,0}/\Delta U_0)$ increases from the null value once the layer rollup is completed; however, a reduced augmentation rate is displayed by the R600 simulation corresponding to the reduced layer growth. The peak in the curve portraying the R600 simulation, and the first peak in the corresponding curve for the R750 simulation occur at the first vortex pairing. Another peak, but of smaller magnitude is displayed by the R750 layer at the time station of the second pairing; the relative magnitude of these two peaks is a first indication of lack of mixing transition. Supporting evidence of lack of mixing transition evolves from examining the $<< \omega_i\omega_i >> (\delta_{\omega,0}/\Delta U_0)^2$ plots. The increase in enstrophy of the R600 is sporadic and modest, with two equivalent magnitude peaks evident at rollup and first pairing; past the first pairing, the enstrophy decays beyond its value at the initial condition. In contrast to the R600 results, for R750 the enstrophy culminates, with a substantial peak, at the first vortex pairing; subsequently, the plot displays a decay supporting the lack of transition. According to the detailed discussion in Okong'o and Bellan [21] analyzing the reasons for lack of transition in temporal mixing layers, in the R750 simulation we witness the early formation of substantial small turbulent scales which destroy the coherence of the vortices, thus impeding entrainment, pairing and further development of turbulent scales.

The analysis presented below is to ascertain that this physical picture is correct

and complete.

8.2 Vorticity production

To explore the global rotational state of the R750 layer, we examine the budget of the spanwise vorticity in the $(x_1 - x_3)$ homogeneous planes, and inspect both the average and the RMS. A parallel examination is conducted for the vorticity magnitude squared.

The vorticity equation for a compressible flow is

$$\frac{D\omega}{Dt} = (\omega \cdot \nabla)\mathbf{u} - (\nabla \cdot \mathbf{u})\omega - \nabla(\frac{1}{\rho}) \times \nabla p + \nabla \times (\frac{1}{\rho}\nabla \cdot \overline{\overline{\tau}}) \tag{45}$$

where D/Dt is the substantial derivative, and the equivalent equation for the vorticity magnitude squared follows

$$\frac{D(\omega^2)}{Dt} = 2\omega \cdot (\omega \cdot \nabla)\mathbf{u} - \mathbf{2}(\nabla \cdot \mathbf{u})\omega^2 - 2\omega \cdot \nabla(\frac{1}{\rho}) \times \nabla p + 2\omega \cdot \nabla \times (\frac{1}{\rho}\nabla \cdot \overline{\overline{\tau}}). \tag{46}$$

The first term in eqs. 45 and 46 represents the stretching and tilting contribution, the second term describes the effect of dilatation, the third term is the baroclinic participation to vorticity production, and the last term portrays the viscous contribution. Depicted in Figs. 4a and 4b are the non-dimensional average and RMS of the spanwise vorticity budget at $t^* = 80$, corresponding to the end of the first pairing. Most of the spanwise rotational activity of the layer, both average and RMS, is located in the H_2 side, where the lighter fluid is situated. The average spanwise vorticity budget is dominated by large peaks of the viscous term, while at some locations the stretching and tilting term competes with the viscous term. On the LOX side of the layer, the activity is dominated by the baroclinic term, while the positive dilatation contribution rivals in magnitude the negative stretching and tilting term. Compared to the average spanwise vorticity, the RMS displays a large culmination of the stretching and tilting term at the boundary between the two species, indicating that in this crucial region of small scale formation there is a considerable activity, explaining the large enstrophy peak at this time station. On the H_2 side of the layer, stretching and tilting and viscous terms contribute similarly to the RMS and dominate the dilatation and baroclinic term; on the LOX side of the layer, the viscous term dominates, although there is appreciable activity in all other terms. The indication is that in the LOX side, the formed turbulent scales are dissipated by the action of viscosity. The result of this dissipation is clearly seen in Figs. 4c and 4d, showing the non-dimensional average and RMS of the vorticity magnitude squared budget; the viscous term is larger in magnitude than all other terms, and negative while the second term in order of decreasing magnitude is the stretching and tilting term, which is positive thus indicating production of vorticity by this mechanism. Production through all mechanisms is negligible in the LOX side of the layer, and the

15

insignificant amount produced is dissipated by the dominating viscous effect. Finally, the RMS of the vorticity magnitude budget depicts the same ordering of terms as the RMS of the spanwise vorticity budget.

To understand the timewise evolution of the layer, illustrated in Figs. 5a and 5b are the non-dimensional average and RMS of the spanwise vorticity budget at $t^* = 150$. Similar to the $t^* = 80$ situation, most of the spanwise rotational activity of the layer, both average and RMS, is located on the H_2 side. Compared to the magnitude of the equivalent terms at $t^* = 80$, all terms are here reduced approximately by a factor of 2, indicating that vorticity production is abated; this finding is totally consistent with the global characteristics presented above. The dominant contribution to the average spanwise vorticity is from the stretching and tilting term which is negative, although at some cross-stream locations situated well into the H_2 side of the layer the viscous term rivals the stretching/tilting one in magnitude, and is positive. Both the averaged dilatation and baroclinic terms appear much smaller. This ordering of the relative magnitudes is even more dramatic in the RMS budget. Clearly, the RMS production is primarily due to stretching/tilting and viscosity effects which are essentially of similar magnitude; dilatation and baroclinic influences are smaller by approximately a factor of 4. In Figs 5c and 5d, a similar evaluation is presented for the vorticity magnitude squared. Although generally the same ordering of stretching/tilting and viscosity versus dilatation and baroclinic terms holds, viscous effects dominate the stretching/tilting activity, and the average viscous contribution seems to extend further into the LOX side of the layer. As expected, stretching/tilting is responsible for increasing the magnitude of the vorticity squared due to production of small scales, whereas the viscous term diminishes the magnitude of the vorticity through dissipation. The physical picture emerging is that production of small scales does not keep up with dissipation, therefore preventing the layer from reaching a transitional mixing state.

The analysis presented below is devoted to (i) corroboration of the above-derived conclusions based on the global characteristics and vorticity budgets of the layer at important time stations, (ii) a documentation of the specific aspects of LOX/H_2 mixing layers in the thermodynamic regime chosen herein, and (iii) an in-depth inquiry into the reasons responsible for the lack of transition. The R750 database is examined exclusively, but the conclusions pertain to the R600 simulation as well.

8.3 Visualizations of the dynamic and thermodynamic variables

Instantaneous aspects of the flow may reveal information that is unavailable from global characteristics. Such instantaneous aspects are best illustrated through contour plots at specific times and locations, chosen so as to highlight important features of the layer. Since two important times are $t^* = 80$ and 150, as explained above, the flow visualizations will depict the variables at one or both of those times.

16

Dynamic variables As discussed above, one of the most fundamental variables indicating the evolution of the flow is the spanwise vorticity. Shown in Figs. 6a and 6b are braid cross-section ($x_3 = L_3/16 = 0.0075$ m) distributions of the spanwise vorticity at $t^* = 80$ and 150, respectively; the between-the-braid plane cross-sections ($x_3 = L_3/2 = 0.06$ m) display an equivalent behavior. At $t^* = 80$, the two vortices remaining after the second pairing are clearly shown, whereas at $t^* = 150$ only a single vortex appears; however, some remnants of the second pairing process are obvious. The level of the positive spanwise vorticity, indicative of small scale formation decreases from $t^* = 80$ to 150, consistent with the global peak in positive spanwise vorticity as a function of time; however, the maximum positive spanwise vorticity increases in the between-the-braid plane as the layer evolves from the first to the second pairing. Noteworthy is the irregular, 'collapsed' aspect of the single vortex, similar to other such single vortices resulting from two pairings in simulations that did not achieve transition (see Okong'o and Bellan [21]). This is due to the early small scale formation induced by the relatively large value of F_{3D}, and results in the destruction of coherence of the vortex, impeding entrainment which is the crucial ingredient to growth.

The evolution of the streamwise vorticity in the mid-braid plane was documented by many investigators for gases at atmospheric conditions.(e.g. Rogers and Moser [25]). Of particular interest for qualitative comparison with the present results are the plots of Cortesi et al. [27] for gravitationally density-stratified temporal mixing layers; for such layers, the influence of gravity is measured by the value of the Richardson number. Presented in Figs. 7a and 7b are the present streamwise mid-braid plane ($x_1/\delta_{\omega,0} = 25.6$) contours at $t^* = 80$ and 150, respectively. These instantaneous plots may be compared with those in Figs. 9a and 9b of Rogers and Moser [25] corresponding to time stations after the first and second pairings, respectively. Both in Figs. 7a and 7b, distortions are observed in the cross-stream direction when comparing with the equivalent figures in [25] which display a definite symmetry. This symmetry of the structures both in the cross-stream and the spanwise direction no longer exists here due to the initial layer density stratification. The overwhelming activity is in the H_2 side of the layer, containing the lighter fluid. On the other hand, comparisons with Fig. 16a of Cortesi et al. [27] show that their streamwise vorticity also lacks symmetry; however, those calculations are not quantitatively comparable with ours because of the different forcing, among other different aspects. For example, Cortesi et al. [27] find that as the Richardson number is increased, the structures recover some symmetry (their Fig. 17a).

Thermodynamic variables In previous studies of supercritical mixing layers [8], [9], [21] for heptane/nitrogen at 60 atm and freestream temperatures of $T_1 = 1000$ K and $T_2 = 600$ K, the peculiarities of the layer were associated with departures from perfect gas behavior ($Z = 1$ for a perfect gas), and departures from mixture ideality (for an ideal mixture $\alpha_D = 1$). These associations were issued from quantitative as

well as visual correlations. Contour plots of Z and α_D for the present LOX/H_2 layer (freestream conditions of 100 atm, $T_1 = 600$ K and $T_2 = 400$ K) at different time stations, both in the braid and in the between-the-braid planes reveal that the fluid is extremely close to a perfect gas and the mixture is nearly ideal. For example, at $t^* = 150$ the compression factor varies between 1.009 and 1.035, whereas the mass diffusion factor varies between 0.9939 and 0.9996. Therefore, none of the features discussed below can be associated with specific real gas or non-ideal mixture behavior. It should, however, be noted that this thermodynamic state of the layer could not be foreseen *a priori*, and it is only a result of the calculation. (Moreover, it is expected that at the same pressure, with decreasing temperatures the mixture will increasingly exhibit departures from perfect gas and ideal mixture conditions.)

One of the most distinctive features of supercritical mixing layers examined so far is the existence of regions of high density-gradient magnitude (called further herein by the acronym HDGM). These regions have been identified in both pre-transitional [8], [21] and transitional [9], [21] supercritical mixing layers. Given the perfect gas and near ideal conditions of this layer, in retrospect these distinctive features could perhaps be better associated with the initial density stratification. However, movie animations of the $|\nabla\rho|$ timewise evolution show that the origin of these regions is not only from the distortion of the initial boundary between the two fluid species, but also from the mixing between the two species; this conclusion holds for all supercritical mixing layers studied so far, independent of the binary system of species. Illustrated in Figs. 8a and 8b is $|\nabla\rho|$ in the braid and the between-the-braid cross-sections located at $x_3 = 0.0075$ m and $x_3 = 0.06$ m, respectively, at $t^* = 150$. Compared to heptane/nitrogen mixing layers excited at the same wavelength and F_{3D} [9], the present regions of high $|\nabla\rho|$ are less convoluted and each such structure is more spread-out, particularly in the between-the-braid plane. The decreased convolution is the result of both lack of transition and the fact that the excitation wavelength is here further away from the most unstable wavelength found in the stability analysis (see Figs. 2a and 2b). The fact that each of the HDGM structures is more spread-out is attributed to the increased solubility in the LOX/H_2 system with respect to the heptane/nitrogen one. For example, in studies of heptane drops in nitrogen, Harstad and Bellan [14] found that the initial density discontinuity is maintained, although the location of the discontinuity changes during the drop evolution. In contrast, a LOX drop in H_2 displays a quicker relaxation of Y_O from unity inside the drop, indicating important H_2 solubility effects (see Harstad and Bellan [16]).

Since the existence of the HDGM regions cannot be here associated with real gas effects, or entirely due to the initial density stratification, the question arises as to their origin. Clearly, they are the result of mixing, without which they would not be formed. Parcels of heavy LOX are entrained into the lighter H_2 and they lose their identity only after mixing at the small scale. Before that time, the much larger molar weight of O_2 gives rise to a substantial density gradient. Therefore, the HDGM regions are here attributed to the very large molar weight ratio (a factor of

16) between O_2 and H_2. Contrary to the situation encountered for heptane/nitrogen where diffusion (which is a molecular scale process) was inhibited by the lower than unity mass diffusion factor, here such diffusion is efficient ($\alpha_D \sim 1$). Thus, we find that generally, HDGM regions may occur under quite different circumstances. For large molar weight ratio species, these regions may occur even if the species diffuse well (and we note again that this is a molecular scale process). For species having a modest to low molar weight ratio, HDGM regions may still occur if the species have difficulty in diffusing into each other.

To investigate the visual correlation between the HDGM regions and the distribution of Y_O, contour plots of the LOX mass fraction at $t^* = 150$ are displayed in Fig. 9a and 9b representing the braid and the between-the-braid planes. As inferred above, some parcels of LOX have broken off from the lower stream and are seen convected to the upper stream. Also, the layer consists of substantially inhomogeneous fluid composed of both LOX and H_2. An equivalent physical picture of non-homogeneities is obtained when examining the Y_O distribution at $t^* = 150$ in the streamwise mid-braid plane located at $x_1/\delta_{\omega,0} = 25.6$, shown in Fig. 9c. The characteristic 'mushroom' shapes typical of the streamwise plane of 3D simulations are evident; equivalent $| \nabla \rho |$ contours (not shown) are found. The disintegration of the lower O_2 stream and the migration of parcels of O_2 into the H_2 stream are manifest. Noteworthy, Cortesi et al. [23] also detected these mushroom structures (their Fig. 9a) evolving during the simulation of gravitationally density-stratified 3D mixing layers forced deterministically. These structures were less developed when a combined deterministic-random velocity field was used during the initialization.

To quantitatively assess the composition of the HDGM regions, conditional averages are listed in Table 7 representing the spatial distributions at $t^* = 150$; a similar calculation performed at $t^* = 80$ yielded similar results up to the third digit. The conditional averages are calculated over regions of $| \nabla \rho | > | \nabla \rho |_{cutoff} \equiv K | \nabla \rho |_{max}$ with $K = 0.1, 0.2, 0.3$ and 0.4. As higher values of $| \nabla \rho |$ are probed, the mass fraction of LOX increases, similarly to the findings with the heptane/nitrogen system [9]; however, for the same cutoff constant, the average mass fraction values are here higher. Nevertheless, because of the large ratio of O_2/H_2 molar weights, the average Y_O seems closer to stoichiometric than could be inferred for the heptane/nitrogen simulation for which directly equivalent evaluations are not possible owing to the lack of O_2 in the mixing layer simulations. Considering that the stoichiometric O_2 mass fraction is here $Y_{O,s} = 32/(32 + 4) = 0.89$, being calculated from the reaction

$$2H_2 + O_2 \rightarrow 2H_2O, \tag{47}$$

the present values of 0.906 to 0.956 found from conditional averages seem to indicate a globally favorable situation for combustion purposes. In contrast, for heptane/air the stoichiometric heptane mass fraction calculated from the reaction

$$C_7H_{16} + 11O_2 + (3.7 \times 11)N_2 \rightarrow 7CO_2 + 8H_2O + (3.7 \times 11)N_2 \tag{48}$$

19
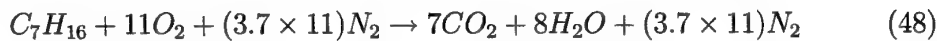
is $Y_{h,s} = 100/(11 \times 32 + 3.7 \times 11 \times 28) = 0.067$, which compares less favorably with values of 0.84 to 0.921 found from similar conditional averages with $K = 0.1, 0.2$ and 0.3 using the results of a heptane/nitrogen simulation[9]. This comparison is only qualitatively correct since the simulations in [9] were based on the heptane/nitrogen instead of the heptane/air system.

To further assess the correlation between $|\nabla\rho|$ and Y_O, listed in Table 8 are the global coefficients found in the braid and the between-the-braid planes at $t^* = 150$. The volume based correlation between two variables is defined by

$$\mathcal{R}_2(\mathcal{X}, \mathcal{Y}) = \frac{<< \mathcal{X}\mathcal{Y} >> - << \mathcal{X} >><< \mathcal{Y} >>}{\sqrt{(<< \mathcal{X}^2 >> - << \mathcal{X} >>^2)(<< \mathcal{Y}^2 >> - << \mathcal{Y} >>^2)}} \tag{49}$$

where $\mathcal{X}$ and $\mathcal{Y}$ are generic variables. The correlation in Table 8 is moderate and similar to that found in a previous study for heptane/nitrogen.

Because the temperature is directly related to the density through the EOS, the expectation is that the temperature distribution will be visually highly correlated with $|\nabla\rho|$ if the pressure is approximately constant. Indeed, examination of pressure contours in both the braid and the between-the-braid planes (not shown) reveals that the variations from the initial uniform pressure are small, at most 8%. Consistent with the almost uniform pressure, the braid and the between-the-braid temperature contours shown in Figs. 10a and 10b are visually well correlated with $|\nabla\rho|$. Hotter fluid from the upper stream is transported to the lower stream, and the HDGM regions generally contain fluid at higher temperature than their surroundings. This situation is very beneficial to combustion since it has been determined above that in these regions the composition is close to stoichiometric.

8.4 Irreversible entropy production (dissipation)

Okong'o and Bellan [10] have analyzed the reasons for the lack of transition in 3D supercritical heptane/nitrogen mixing layers, and found that it is due to the HDGM regions which acted similar to material surfaces and damped small turbulent scales formed through stretching and tilting. This conclusion was derived from an irreversible entropy production analysis (the irreversible entropy production is in fact the dissipation). Specifically, if Σ_j represents the reversible flux of entropy and g denotes the rate of irreversible entropy production, then

$$\Sigma_j = (q_{IK,j} - \mu_O j_{Oj}/m_O - \mu_H j_{Hj}/m_H)/T \tag{50}$$

where μ_H and μ_O are the chemical potentials (partial molar Gibbs free energy), $j_{Hj} = -j_{Oj}$, and g is the sum of viscous, Fourier heat flux and molar flux contributions

$$g = g_{visc} + g_{temp} + g_{mass}, \tag{51}$$

20

$$g_{visc} = \frac{\mu}{T} \left(2 S_{ij} S_{ij} - \frac{2}{3} S_{kk} S_{ll} \right), \quad g_{temp} = \frac{\lambda}{T^2} \frac{\partial T}{\partial x_j} \frac{\partial T}{\partial x_j}, \quad g_{mass} = \frac{1}{Y_H Y_O \rho D} \frac{R_u m}{m_H m_O} j_{Oj} j_{Oj},$$

$$(52)$$

$$S_{ij} = \frac{1}{2} \left(\frac{\partial u_i}{\partial x_j} + \frac{\partial u_j}{\partial x_i} \right), \tag{53}$$

where according to eqs. 6 - 8, g_{mass} contains the departure from mixture non-ideality (through j_{Oj}), $\propto \alpha_D$, and the Soret term, $\propto \alpha_{BK}$. One of the important issues determined was the contribution of each of the terms listed in eq. 52 to g, from $(x_1 - x_3)$ plane averages considering both the average and RMS, as well as an equivalent evaluation from volume averages. Analysis of the data at three time stations located before, at and after the culminating point of the global positive spanwise vorticity showed that whereas at all times the primary contribution to volume averages was from g_{visc}. At the time following the culminating global positive spanwise vorticity, visualizations showed that most of the g, as well as the g_{visc} and g_{mass} activity was concentrated at HDGM locations. This dissipation mechanism was considered responsible for the lack of transition, as formed small scales were damped by the region of large $| \nabla \rho |$ which acted similar to a material interface. These conclusions were consistent with those of Hannoun et al. [26] who experimentally investigated the turbulence structure near a sharp density interface.

A similar analysis was performed by Okong'o and Bellan [9] for a transitional supercritical heptane/nitrogen mixing layer, with somewhat different results. One of the important results was that the visual correlation between g and HDGM locations no longer existed.

Similarly to our previous work, we use here the inspection of the dissipation as a diagnostic determining the causes of the lack of transition. To this end, illustrated in Figs. 11a and 11b are the braid and the between-the-braid plane distributions of g at $t^* = 150$, respectively. A visual comparison with the $| \nabla \rho |$ plots of Figs. 8a and 8b leads to the conclusion that there is a lack of correlation between these two quantities. While there are some regions of common activity, few regions of very large dissipation correspond to locations of HDGM. The regions of highest g and $| \nabla \rho |$ activity are even more separated at $t^* = 80$. The difference between the present situation and that studied by Okong'o and Bellan [10] for heptane/nitrogen is that here the density stratification is much larger, inhibiting the formation of small scales in the LOX side of the layer. This explanation is supported by the vorticity budget analysis conducted above where the lack of activity of the crucial stretching and tilting term on the LOX side of the layer was noted, and by the striking visual lack of correlation between g and HDGM locations. In contrast, in [10] small scales were formed on the heptane side, but they were being damped by the action of viscosity in the HDGM regions.

Homogeneous-plane average plots of the g_{visc}, g_{mass} and g_{temp} contributions to g displayed in Figs. 12a (average) and 12b (RMS) at $t^* = 150$ are typical of the

situation at $t^* = 80$ as well. Contributions from g_{mass} and g_{temp} effects are about two orders of magnitude smaller than viscosity effects and this holds for both the average and the RMS. Consistent with the discussion on the lack of correlation between g and the HDGM regions which are primarily located in the LOX side of the layer, here the viscous activity is considerably stronger on the H_2 side of the layer, where the lighter fluid is located; this is true for both the average and the RMS. On the other hand, the dissipation due to the molar fluxes is stronger on the LOX side of the layer where the mass fraction and temperature gradients are larger. Finally, the much smaller g_{temp} is the result of the enhanced Le_{eff} at supercritical conditions, as shown by Harstad and Bellan [11]. The larger Le_{eff} causes the temperature to relax faster than the mass fraction (non-dimensional gradients are smaller), as the larger (than at low pressure conditions) thermal conductivity promotes heat transfer.

Based on this analysis, the lack of transition is due to two combined effects. Small scales are formed excessively early in the evolution of the layer, destroying the coherence of the ultimate vortex; this was elucidated by inspecting the global characteristics of the layer, by evaluating the vorticity and vorticity magnitude budgets, and by examining visualizations of the spanwise vorticity. As a result of the weakened vortex, entrainment is reduced and the small scales cannot develop. This effect is enhanced by the very large stratification which further prevents the formation of small scales. Evidence for this latter effect is found from exploring the development of the dissipation and its main contributions, as well as by scrutinizing visualizations of the dissipation and the density gradient magnitude.

9   Summary and conclusions

A Direct Numerical Simulation study has been performed of a three-dimensional temporal LOX/H_2 mixing layer in order to explore aspects of LOX disintegration under shearing conditions. The conservation equations were based on fluctuation-dissipation theory, having an enlarged transport matrix that includes Soret and Dufour effects. To close the system of equations, a real gas equation of state was coupled to the differential equations. Transport properties were accurate as much as possible in the chosen (p, T) regime to ensure the resolution of the Batchelor scales. This was accomplished by correlating the Schmidt and Prandtl numbers as functions of the thermodynamic variables, consistent with contour plots of these numbers based on accurate properties. The values of these numbers determined the thermal conductivity and diffusivity, while the viscosity was determined from the prescribed initial value of the Reynolds number. Boundary conditions were of periodic type in the streamwise and spanwise directions, and of outflow type, based on a real gas characteristic analysis of the differential equations, in the cross-stream direction. Additional to the Reynolds number, the initial conditions prescribed the Mach number, the temperatures of the two freestreams, the pressure, and the perturbation of the layer.

A stability analysis conducted for the O_2/H_2 system showed that at the same

density stratification, the stability curve is similar to the heptane/nitrogen system previously studied. However, at the enlarged stratifications characteristic of thermodynamic regimes of interest for the O_2/H_2 system, the density stratification is much larger and the most unstable wavelength is longer. It is shown that at high pressure, as the oxygen is at lower temperatures, the stratification increases dramatically.

Based on the stability analysis and previous experience with heptane/nitrogen supercritical mixing layers, the perturbation wavelength was chosen to be the most unstable incompressible one, and the amplitudes of the excitation were those that previously lead to transition in a similar heptane/nitrogen mixing layer simulation having albeit a smaller initial density stratification. The domain size was four times the perturbation wavelength to accommodate four vortices and two pairings. Two mixing layer conditions were simulated differing only by the initial Reynolds number. As the simulations are very computationally intensive, one simulation was pursued only past the first pairing, as it was obvious that transition would not be obtained. The second simulation, at a larger initial Reynolds number, evolved through two pairings, but also did not reach transition. To determine the causes leading to the lack of transition, a detailed analysis of the layer was conducted.

Global characteristics of the layer showed a momentum thickness and product thickness continuous growth, with a relatively large momentum thickness based Reynolds number reached. However, these aspects were not sufficient to induce transition. The evolution of the global positive spanwise vorticity and the enstrophy displayed a large peak following the first pairing, and continued to decay afterwards with only a minor increase following the second pairing. This information, interpreted in the context of a previous study examining the causes of lack of transition, was a first indication that the early formation of small turbulent scales destroyed the coherence of the vortices formed after the first pairing, impeding entrainment and the further formation of small scales.

To ascertain that this physical interpretation is correct, the vorticity and vorticity magnitude budgets were scrutinized at times following each pairing. Consistent with the global growth characteristics, very little vorticity is created on the oxygen side of the layer which contains the heavier fluid. Most of the vorticity is created on the hydrogen side of the layer by the action of the stretching and tilting term. However, even in those regions the negative viscous term dominates the budget of the vorticity magnitude squared, draining vorticity from the system.

Visualizations of the dynamic and thermodynamic variables revealed regions of high density gradient magnitude which mostly exist in the lower LOX stream. These regions are the result of both the distortion of the initial density stratification boundary and the mixing of the two fluids. Due to the very large molar weight ratio between oxygen and hydrogen, parcels of LOX detached from the lower stream will maintain their density identity while being entrained into the upper, lighter hydrogen, thereby creating these large density gradient magnitude regions prior to the complete mixing of the two fluids. Although regions of high density gradient magnitude were

23

identified also during the mixing of heptane/nitrogen, in that situation there were quantitatively correlated with locations of mixture non-ideality. In contrast, at the conditions of the present simulations the fluid behaves as a perfect gas and an ideal mixture.

Inspection of the irreversible entropy production, which is the dissipation, confirmed that most of the activity is concentrated in the lighter upper stream where most of the small scales are formed. In the lower stream, where most of the high density gradient regions reside, stretching and tilting activity is negligible resulting in the lack of small scales, explaining the inactive dissipation. At all locations, the viscous dissipation dominates both the mass flux and the heat flux dissipation by at least two orders of magnitude.

According to this analysis, two reasons contribute to the lack of mixing transition. First, the relatively large spanwise perturbation induces early small scale formation which destroys the coherence of the vortices formed through pairing, and impedes entrainment and the further formation of small scales. The ultimate vortex resulting from the second pairing is weakened during this process. Second, the regions of high density gradient magnitude formed through the distortion of the initial density stratification boundary and also through mixing of the two species contain very dense fluid in which small turbulent scales cannot form owing to the weakened ultimate vortex.

10 Appendix A

Miscellaneous relationships relevant to the EOS are

$$a_m = \sum_i \sum_j X_i X_j a_{ij}(T)$$

$$b_m = \sum_i X_i b_i$$

where indices here do not follow the Einstein notation, and

$$a_{ij} = 0.457236 \frac{(R_u T_{c,ij})^2}{p_{c,ij}} \alpha_i \alpha_j \tag{54}$$

$$\alpha_i \equiv 1 + C_i - C_i \sqrt{\frac{T}{T_{c,i}}}$$

$$C_i = 0.37464 + 1.54226 \Omega_i - 0.26992 \Omega_i^2$$

$$b_i = 0.077796 \frac{R_u T_{c,i}}{p_{c,i}}$$

24

$$T_{c,ij} = (1 - k_{ij}) \sqrt{T_{c,i} T_{c,j}} \quad \text{with } k_{ii} = 0 \qquad (55)$$

$$v_{c,ij} = \frac{1}{8} \left(v_{c,i}^{1/3} + v_{c,j}^{1/3} \right)^3$$

$$Z_{c,ij} = \frac{1}{2} \left(Z_{c,i} + Z_{c,j} \right)$$

$$p_{c,ij} = \frac{R_u T_{c,ij} Z_{c,ij}}{v_{c,ij}}$$

with $T_{c,i}$, $Z_{c,i}$ $v_{c,i}$ and $p_{c,i}$ being the pure species critical values. Ω_i is the species acentric factor and k_{ij} is an empirical mixing parameter. The values for hydrogen and oxygen are in Table 1, and for comparison the values for heptane and nitrogen are listed as well.

Most data references pertain to k'_{ij}, another mixing parameter related to a_{ij} through

$$k'_{ij} = 1 - \frac{a_{ij}}{\sqrt{a_{ii} a_{jj}}}. \qquad (56)$$

Replacing in eq. 56 a_{ij} and $T_{c,ij}$ from eqs. 54 and 55, yields a relationship between the parameters k_{ij} and k'_{ij}

$$(1 - k_{ij}) = (1 - k'_{ij}) \frac{Z_{c,ij}}{v_{c,ij}} \left(\frac{v_{c,i} v_{c,j}}{Z_{c,i} Z_{c,j}} \right)^{1/2} .$$

Given the lack of information regarding the values of k_{ij} or k'_{ij}, in the simulations herein $k_{ij} = 0$.

Acknowledgment

References

[1] Prausnitz, J., Lichtenthaler, R. and de Azevedo, E., *Molecular Thermodynamics for Fluid-phase Equilibrium*, Prentice -Hall, Inc., 1986

[2] Hirshfelder, J. O., Curtis, C. F. and Bird, R. B., *Molecular Theory of Gases and Liquids*, John Wiley and Sons, Inc., 1964

25

[3] Harstad, K. and Bellan, J., The D^2 Variation for isolated LOX drops and poly-disperse clusters in hydrogen at high temperature and pressures, *Combustion and Flame*, 124, 2000

[4] Mayer, W., Schik, A., Schweitzer, C. and Schaffler, M., Injection and mixing processes in high pressure LOX/GH2 rocket combustors AIAA 96-2620, 1996

[5] Mayer, W., Ivancic, B., Schik, A. and Hornung, U., Propellant atomization in LOX/GH2 rocket combustors AIAA 98-3685, 1998

[6] Chehroudi, B., Talley, D. and Coy, E. Initial growth rate and visual characteristics of a round jet into a sub- to supercritical environment of relevance to rocket, gas turbine and Diesel engines AIAA 99-0206, 1999

[7] Oschwald, M. and Schik, A., Supercritical nitrogen free jet investigated by spontaneous Raman scattering *Experiments in Fluids*, 27, 497-506, 1999

[8] Miller, R. S., Harstad, K. and Bellan, J., Direct Numerical Simulations of supercritical fluid mixing layers applied to heptane-nitrogen, *J. Fluid Mech.*, 430, 1-39, 2001

[9] Okong'o, N. and Bellan, J., Direct Numerical Simulation of a transitional supercritical mixing layer: heptane and nitrogen, submitted for publication to the Journal of Fluid Mechanics, 2000

[10] Okong'o, N. and Bellan, J., Entropy production of emerging turbulent scales in a temporal supercritical n-heptane/nitrogen three-dimensional mixing layer, *Proc. Comb. Inst.*, Vol. 28, 497-504, 2000

[11] Harstad, K. and Bellan, J., The Lewis number under supercritical conditions. *Int. J. Heat and Mass Transfer*, 42, 961-970, 1999

[12] Okong'o, N., Bellan, J. and Harstad, K., Consistent boundary conditions for multicomponent real gas mixtures based on characteristic waves, submitted for publication to the Journal of Computational Physics, 2000

[13] Sarman, S. and Evans, D. J., Heat flux and mass diffusion in binary Lennard-Jones mixtures, *Phys. Rev.*, A45(4), 2370-2379,1992

[14] Harstad, K. and J. Bellan, J., An all-pressure fluid-drop model applied to a binary mixture: heptane in nitrogen, *Int. J. Multiphase Flow*, 26(10), 1675-1706, 2000

[15] Harstad, K. Miller, R. S. and J. Bellan, J., Efficient high-pressure state equations. *A.I.Ch.E. J.*, 43(6), 1605-1610, 1997

[16] Harstad, K, and J. Bellan, J., Isolated Liquid Oxygen Drop Behavior in Fluid Hydrogen at Rocket Chamber Pressures, *Int. J Heat and Mass Transfer*, 41, 3537-3550, 1998

[17] Kennedy, C. A. and Carpenter, M. H., Several new numerical methods for compressible shear-layer simulations *App. Num. Math.* 14, 397-433, 1994

[18] Muller, S. M. and Scheerer, D., A method to paralleleize tridiagonal solvers, *Parallel Computing*, 17, 181-188, 1991

[19] Drazin, P. G. and Reid, W. H., *Hydrodynamic Stability* Cambridge University Press, 1981

[20] Moser, R. D. and Rogers, M. M., Mixing transition and the cascade to small scales in a plane mixing layer, *Phys. Fluids* A 3(5), 1128-1134, 1991

[21] Okong'o, N. and Bellan, J., Linear stability analysis of supercritical two- and three-dimensional mixing layers, submitted for publication to Physics of Fluids, 2001

[22] Moser, R. D. and Rogers, M. M., The three-dimensional evolution of a plane mixing layer: pairing and transition to turbulence, *J. Fluid Mech.*, 247, 275-320, 1993

[23] Cortesi, A. B., Smith, B. L., Yadigaroglu, G. and Banerjee, S., Numerical investigation of the entrainment and mixing processes in neutral and stably-stratified mixing layers, *Phys. Fluids* **11**(1), 162-185, 1999

[24] Miller, R. S. and J. Bellan, J., Direct Numerical Simulation and Subgrid Analysis of a Transitional Droplet Laden Mixing Layer, *Phys. Fluids*, 12(3), 650-671, 2000

[25] Rogers, M. M. and Moser, R. D., Spanwise scale selection in plane mixing layers, *J. Fluid Mech.*, 247, 321-337, 1993

[26] Hannoun, I., Fernando, H. and List, E. 1988 Turbulence structure near a sharp density interface *J. Fluid Mech.* 189, 189-209, 1988

[27] Cortesi, A. B., Yadigaroglu, G. and Banerjee, S., Numerical investigation of the formation of three-dimensional structures in stably-stratified mixing layers, *Phys. Fluids* **10**(6), 1449-1473, 1998

Species	m (g/mol)	T_c (K)	p_c(MPa)	v_c(cm^3/mol)	Z_c	Ω
Hydrogen	2.0159	33.0	1.2838	64.284	0.306	-0.216
Nitrogen	28.013	126.26	3.399	89.8	0.290	0.039
Oxygen	31.9988	154.58	5.0430	73.368	0.288	0.025
Heptane	100.205	540.2	2.74	432.0	0.263	0.35

Table 1: Pure species properties.

Mean quantity	$x_2 = -\infty$ (Oxygen)	$x_2 = \infty$(Oxygen)
$\bar{u}_1$(m/s)	-193.732	193.732
a_s(m/s)	484.329	484.329
$\bar{\rho}$(kg/m^3)	63.191	63.191
p(atm)	100	100
T(K)	600	600
Y_O	1	1

Table 2: Mean flow properties ρ_2/ρ_1=1.

Mean quantity	$x_2 = -\infty$ (Oxygen)	$x_2 = \infty$(Hydrogen)
$\bar{u}_1$(m/s)	-187.287	666.798
a_s(m/s)	467.045	1671.193
$\bar{\rho}$(kg/m^3)	68.271	5.298
p(atm)	100	100
T(K)	556	444
Y_O	1	0

Table 3: Mean flow properties ρ_2/ρ_1=12.88.

Mean quantity	$x_2 = -\infty$ (Oxygen)	$x_2 = \infty$ (Hydrogen)
$\bar{u}_1$(m/s)	-158.004	770.983
a_s(m/s)	397.517	1915.376
$\bar{\rho}$(kg/m^3)	96.764	3.965
p(atm)	100	100
T(K)	400	600
Y_O	1	0

Table 4: Mean flow properties ρ_2/ρ_1=24.40.

Case	Flow type	$\dfrac{\rho_2}{\rho_1}$	$\alpha\delta_\omega$	$\alpha\delta_\omega\dfrac{c_i}{\bar{U}}$	$\dfrac{c_{re}}{\bar{U}}$	$\dfrac{\lambda_1}{\delta_\omega}=\dfrac{2\pi}{\alpha\delta_\omega}$
1	Variable density[1] $(a_s = 10^6)$	1.00	0.860	0.3830	0.6598	7.31
2	Variable density[2]	1.00	0.797	0.3151	0	7.88
3	Variable density[2]	12.88	0.670	0.1756	-0.0747	9.38
4	Variable density[2]	24.40	0.607	0.1284	-0.0745	10.35

[1]Same velocity profile as for Case 4.
[2]Velocity profile from Equation 32, $M_{c,0} = 0.4$.

Table 5: Most unstable wavelength, two-dimensional analysis.

Run	Re$_0$	$L_1 \times L_2 \times L_3$	$N_1 \times N_2 \times N_3$	max Re$_m$	t^*_{max}	Timesteps	CPU(h)
R600	600	0.2×0.232×0.12	288×336×176	1014	127.45	3730	5472
R750	750	0.2×0.2×0.12	352×352×208	1680	190.44	6860	13214

Table 6: Listing of the simulations and associated resolution. L_i is in meters.

$\mid\nabla\rho\mid_{cutoff}=$ $K\mid\nabla\rho\mid_{max}$	Braid plane: $\mid\nabla\rho\mid_{max}= 2.440 \times 10^4 kg/m^4$	Between-the-braid plane: $\mid\nabla\rho\mid_{max}= 1.955 \times 10^4 kg/m^4$
$K = 0.4$	0.954	0.956
$K = 0.3$	0.945	0.951
$K = 0.2$	0.930	0.949
$K = 0.1$	0.906	0.923

Table 7: Conditional averages over regions where $\mid \nabla\rho \mid$>cutoff. The calculations are made at $t^* = 150$ for R750.

	Braid plane	Between-the-braid plane	Global
$Y_O, \mid\nabla\rho\mid$ Correlation	0.34	0.37	0.35

Table 8: Correlations with $\mid \nabla\rho \mid$ at $t^* = 150$ for R750.
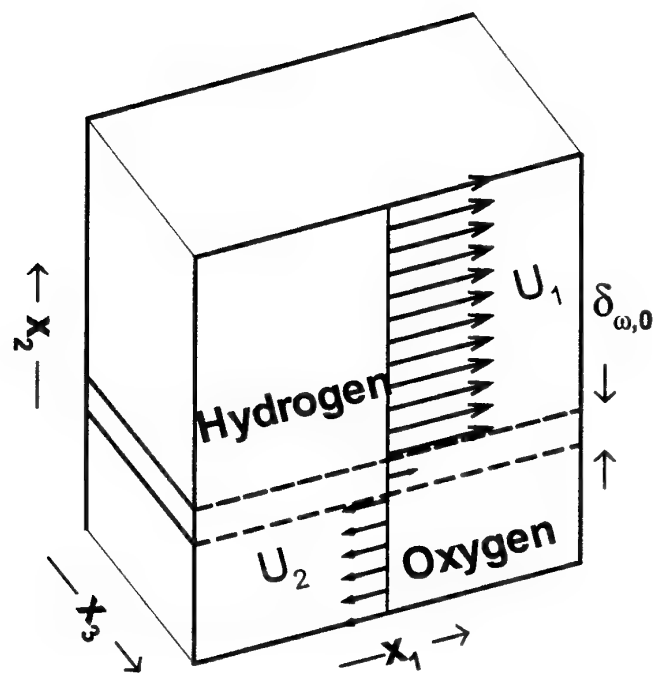
Figure 1: Sketch of the mixing layer configuration.
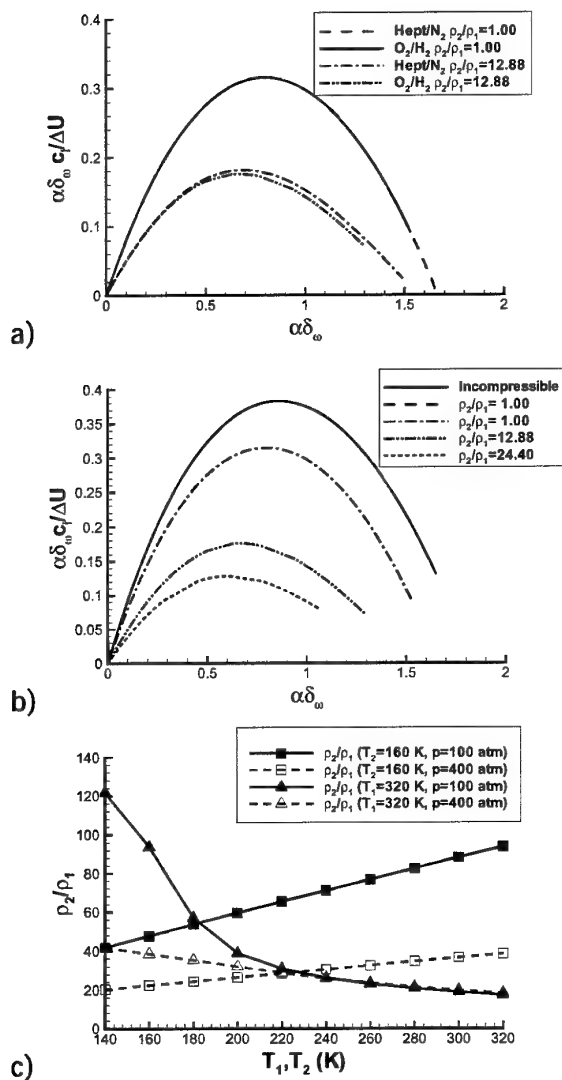
Figure 2: a) Comparison of the stability curves for heptane/nitrogen (at 60 atm) and oxygen/hydrogen (at 100 atm), b) stability curves for oxygen/hydrogen (at 100 atm) and c) density ratio versus temperature for oxygen/hydrogen.
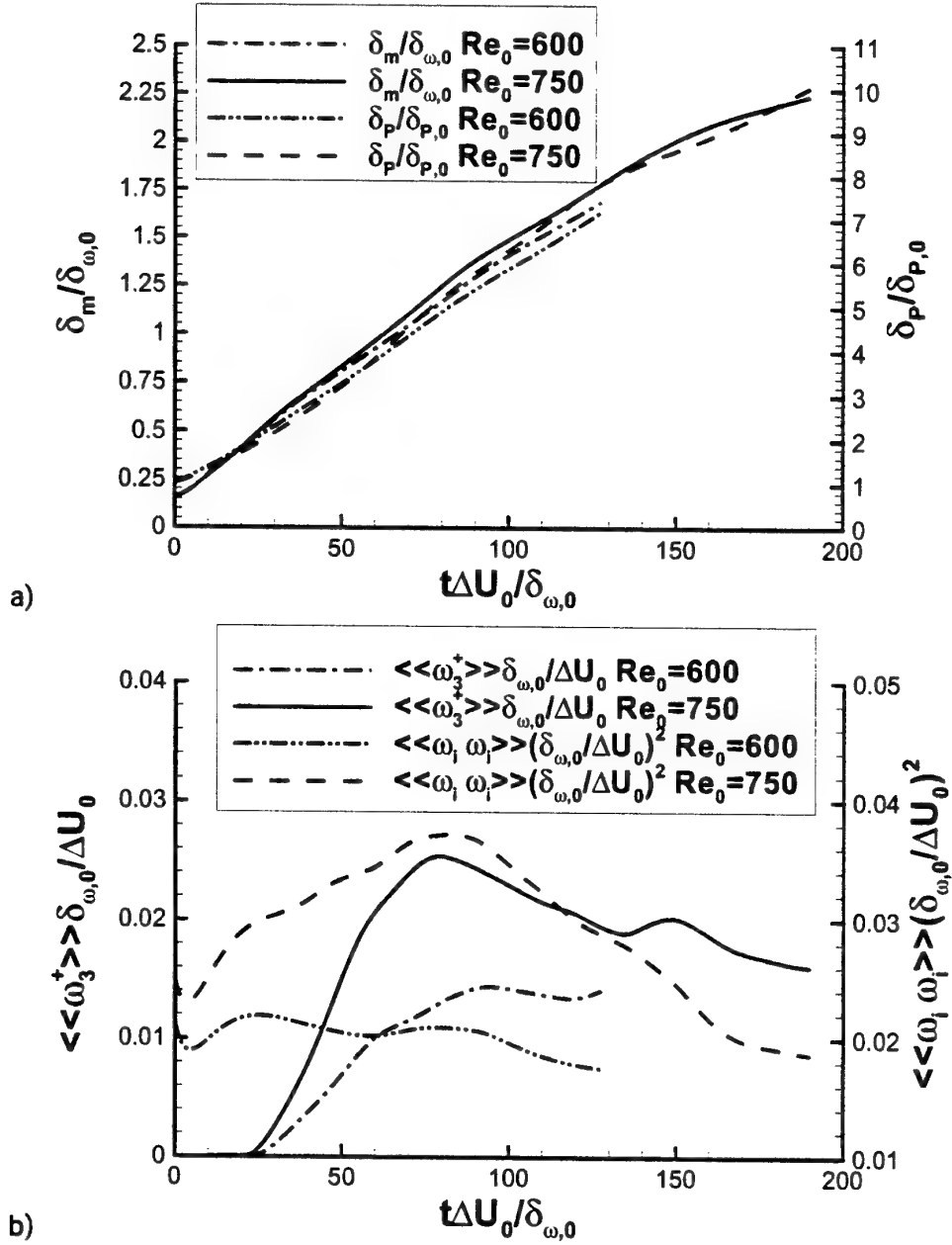
Figure 3: Time evolution of a) momentum and product thicknesses and b) global spanwise vorticity and enstrophy.
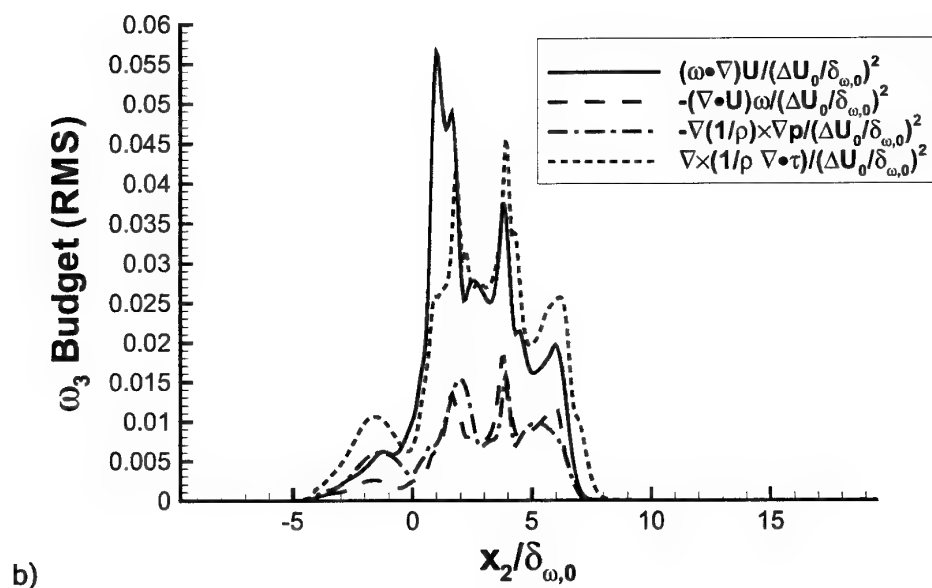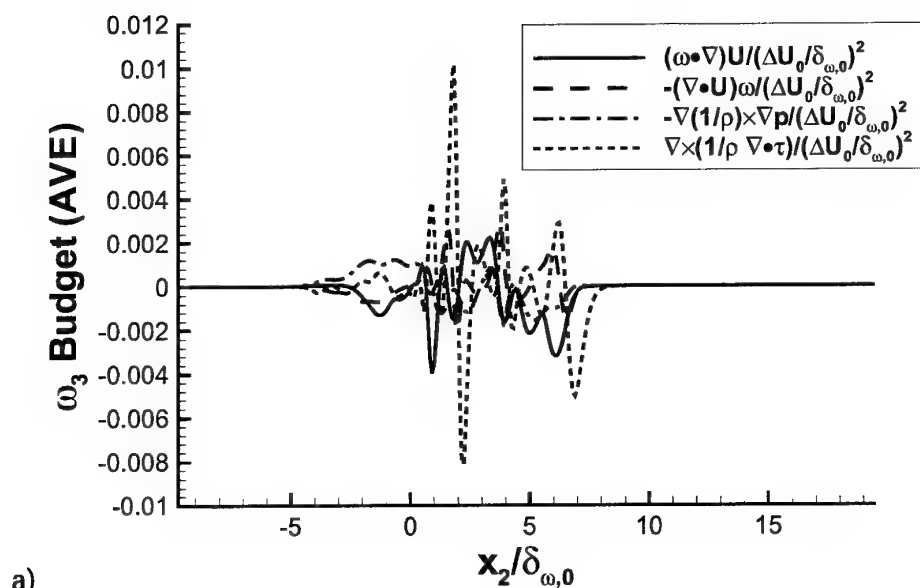
Figure 4: Vorticity budget for R750 at t^*=80: Spanwise vorticity, a) plane average and b) plane RMS, and vorticity magnitude, c) plane average and d) plane RMS.
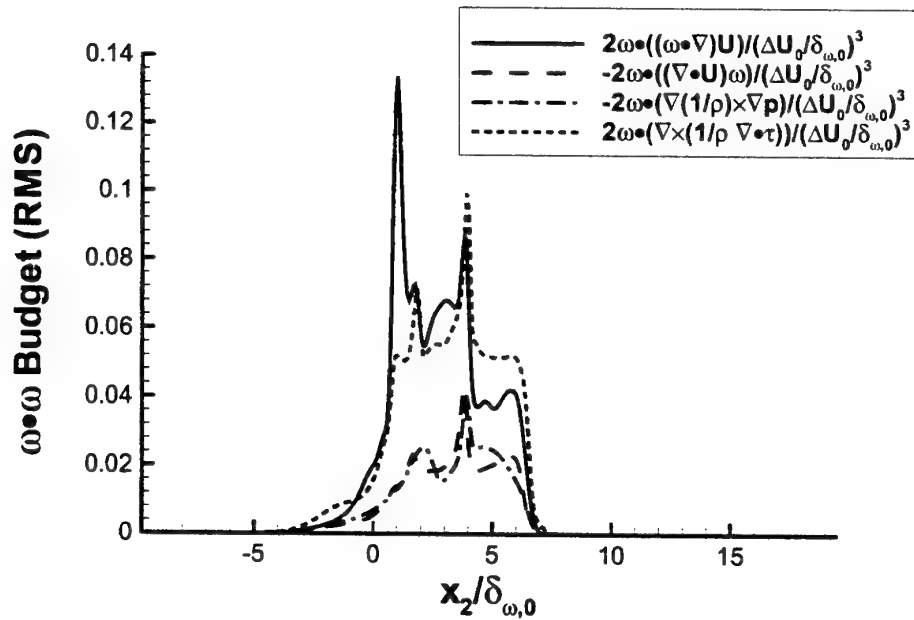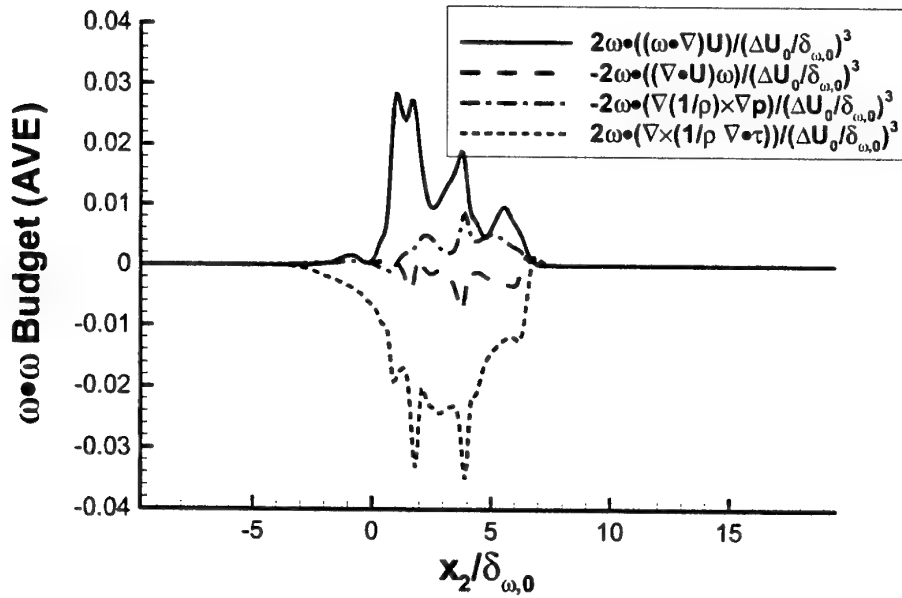
Figure 4: (continued) Vorticity budget for R750 at $t^*=80$: Spanwise vorticity, a) plane average and b) plane RMS, and vorticity magnitude, c) plane average and d) plane RMS.
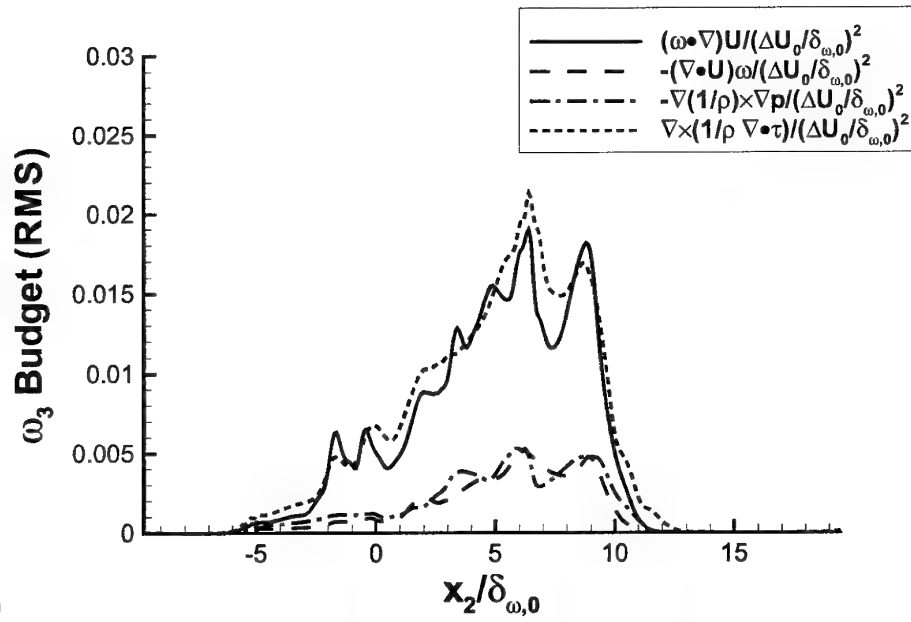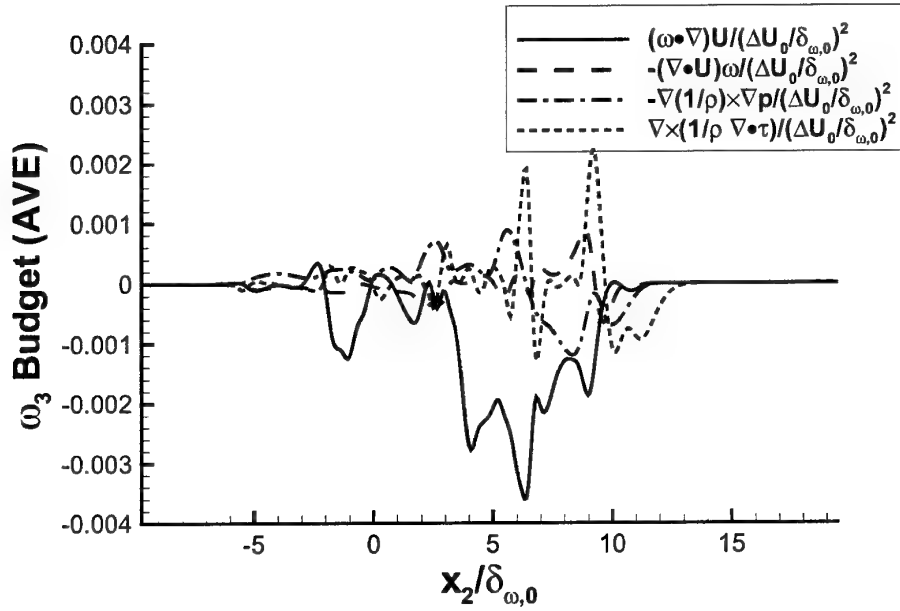
Figure 5: Vorticity budget for R750 at $t^*=150$: spanwise vorticity, a) plane average and b) plane RMS, and vorticity magnitude, c) plane average and d) plane RMS.
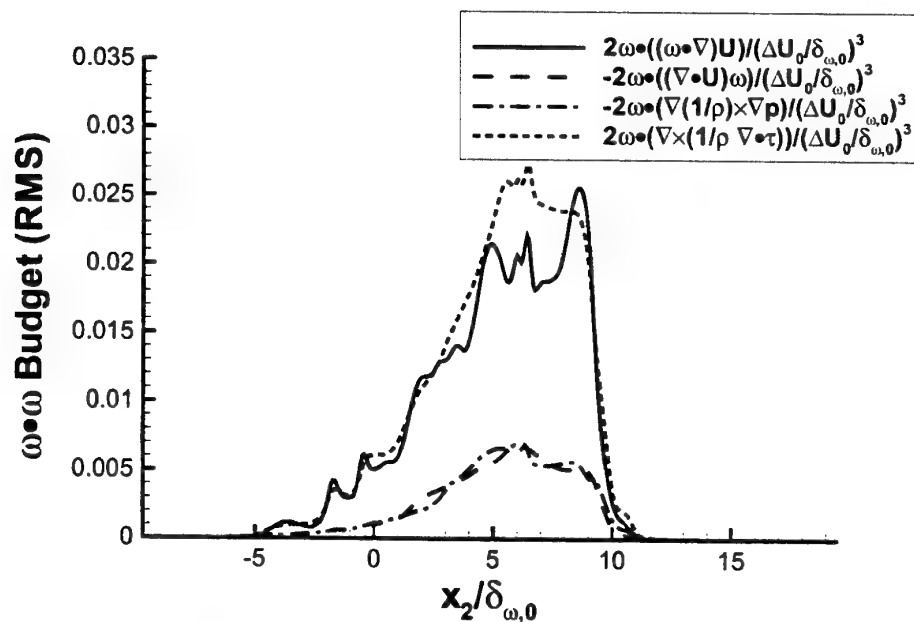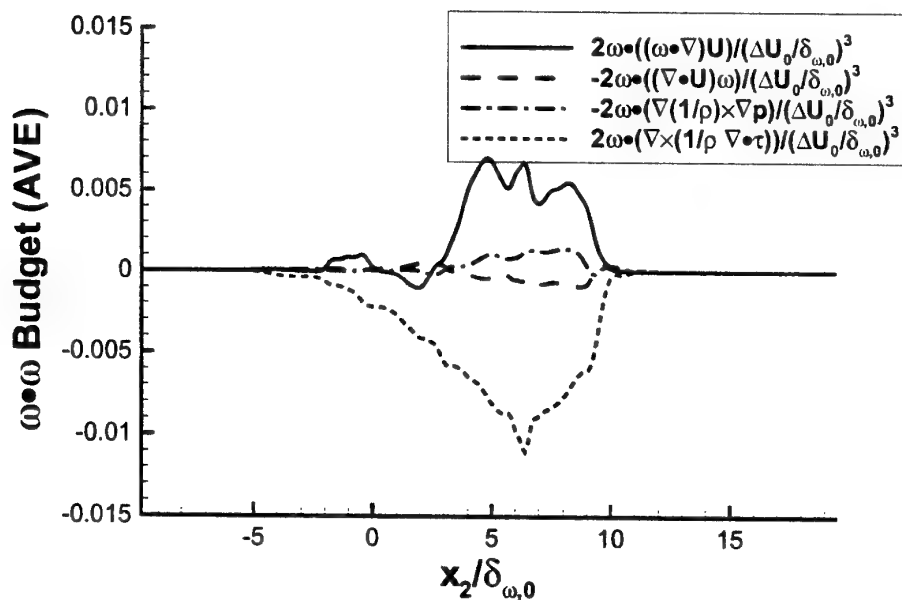
Figure 5: (continued) Vorticity budget for R750 at t^*=150: spanwise vorticity, a) plane average and b) plane RMS, and vorticity magnitude, c) plane average and d) plane RMS.
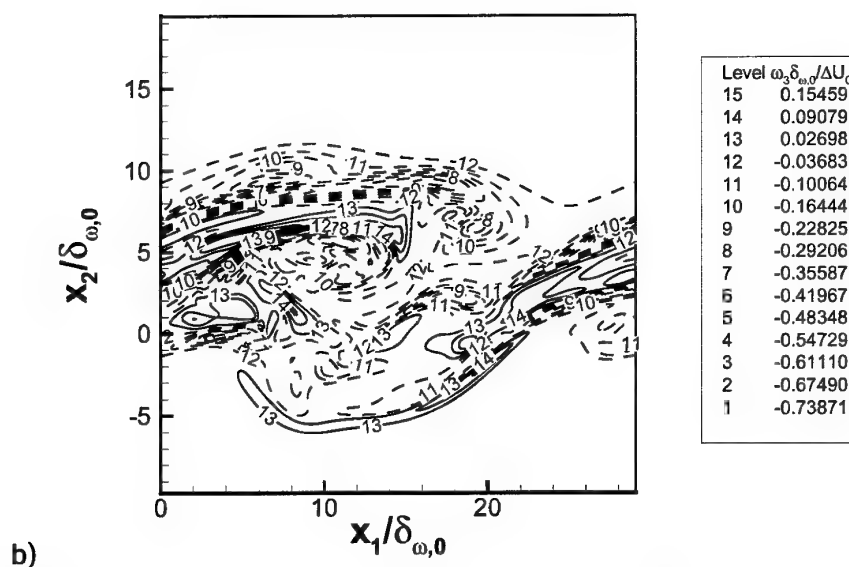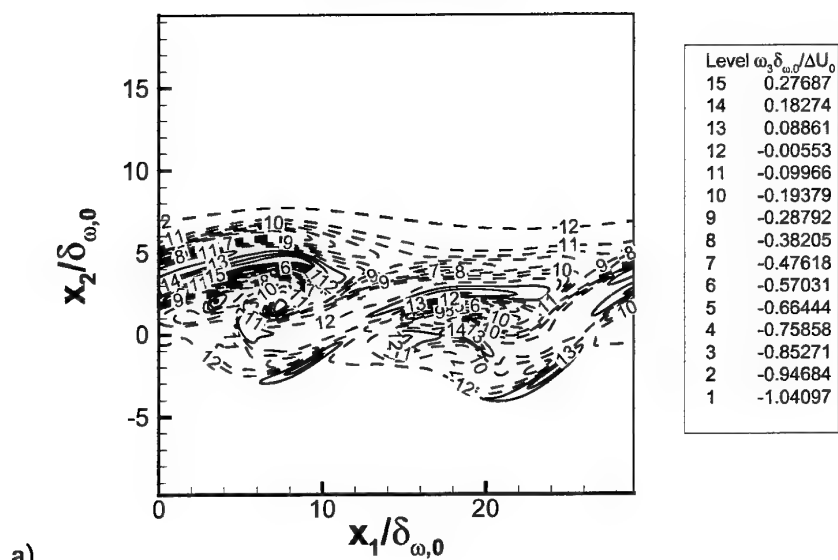
Figure 6: Nondimensional spanwise vorticity for R750 in the braid plane ($x_3 = L_3/16$) at a) t^*=80 and b) t^*=150.

Legend (a):

Level	$\omega_1\delta_{\omega,0}/\Delta U_0$
15	0.61479
14	0.52553
13	0.43628
12	0.34702
11	0.25776
10	0.16850
9	0.07924
8	-0.01002
7	-0.09927
6	-0.18853
5	-0.27779
4	-0.36705
3	-0.45631
2	-0.54556
1	-0.63482

a)

Legend (b):

Level	$\omega_1\delta_{\omega,0}/\Delta U_0$
15	0.56055
14	0.47411
13	0.38767
12	0.30123
11	0.21479
10	0.12835
9	0.04191
8	-0.04454
7	-0.13098
6	-0.21742
5	-0.30386
4	-0.39030
3	-0.47674
2	-0.56318
1	-0.64962

b)
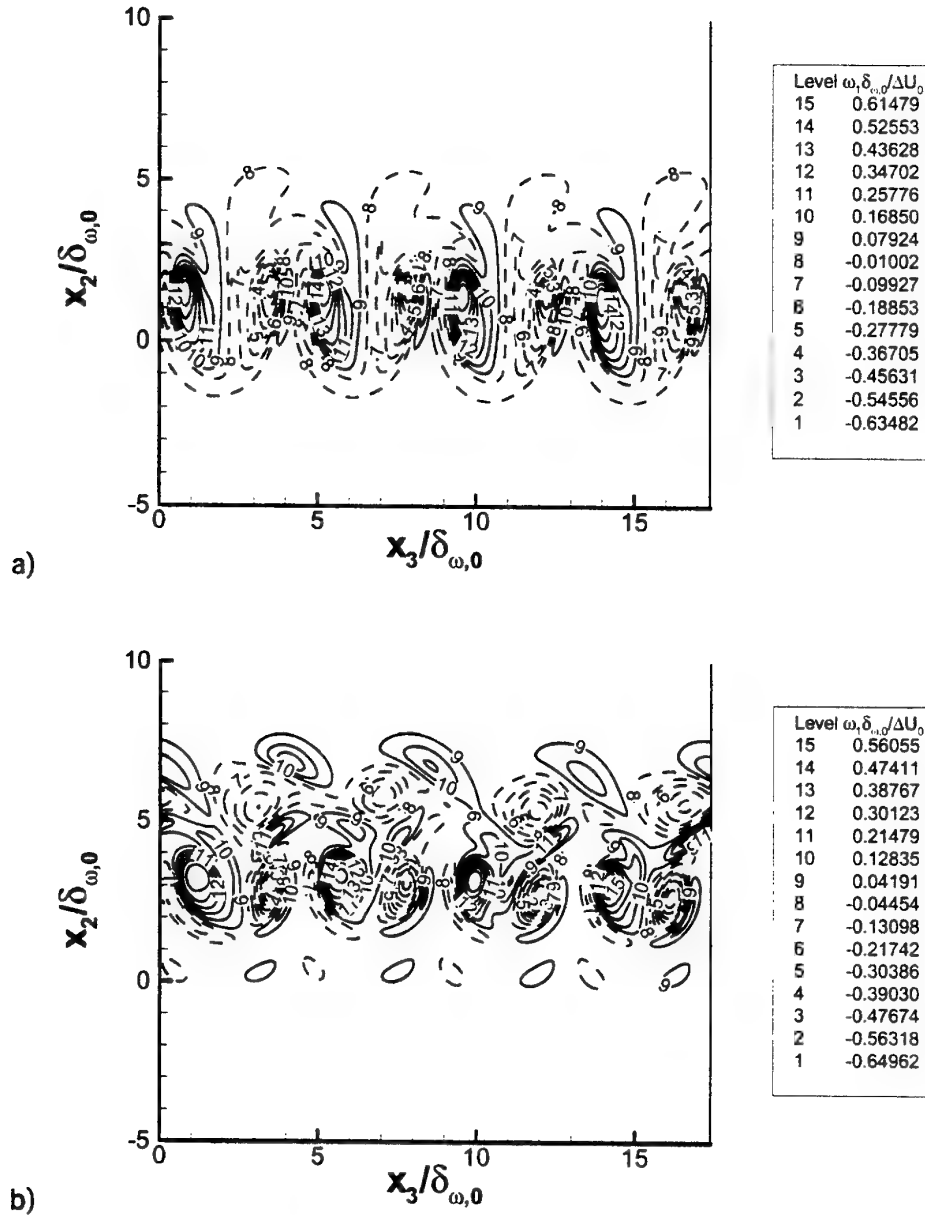
Figure 7: Nondimensional streamwise vorticity for R750 in the streamwise mid-braid plane ($x_1/\delta_{\omega,0}$=25.6) at a) t^*=80 and b) t^*=150.

a)

b)
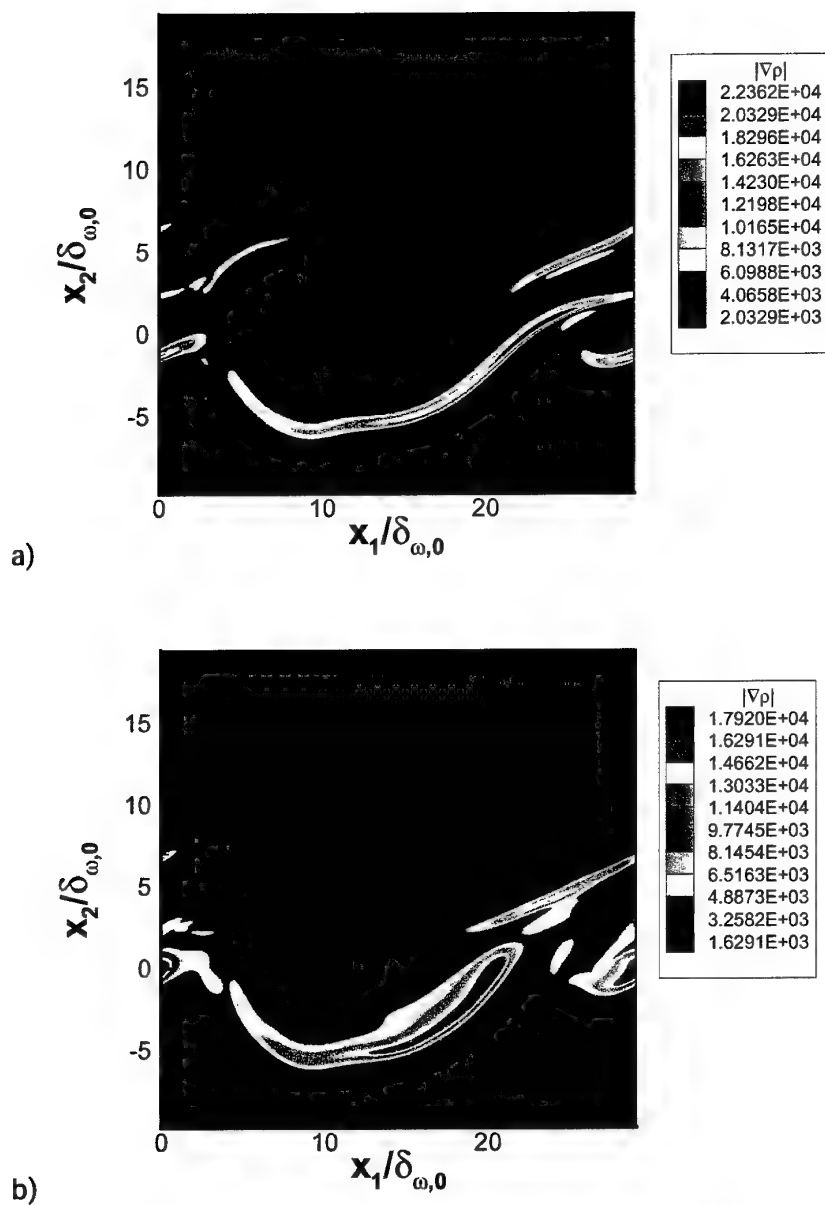
Figure 8: Density gradient magnitude (in kg/m⁴) for R750 at $t^*=150$, a) in the braid plane ($x_3 = L_3/16$) and b) in the between-the-braid plane ($x_3 = L_3/2$).
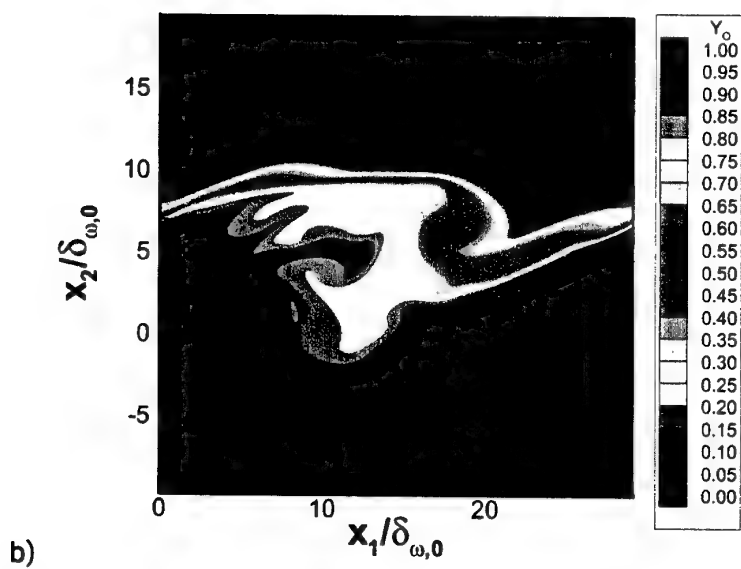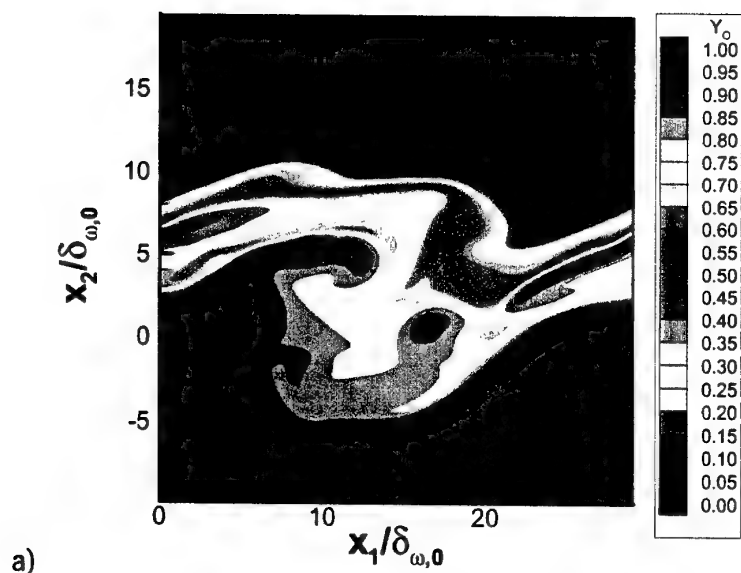
Figure 9: Oxygen mass fraction for R750 at t^*=150, a) in the braid plane, b) in the between-the-braid plane and c) in the streamwise mid-braid plane.

c)
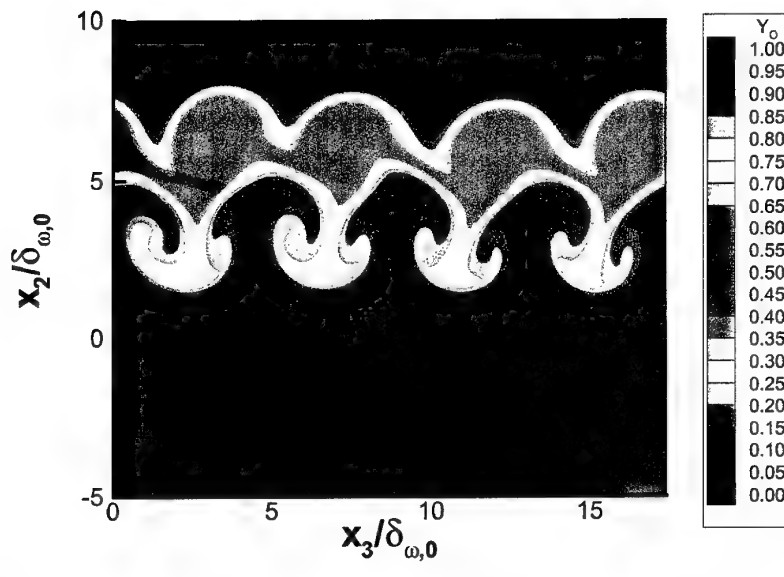
Figure 9: (continued) Oxygen mass fraction for R750 at t^*=150, a) in the braid plane, b) in the between-the-braid plane and c) in the streamwise mid-braid plane.
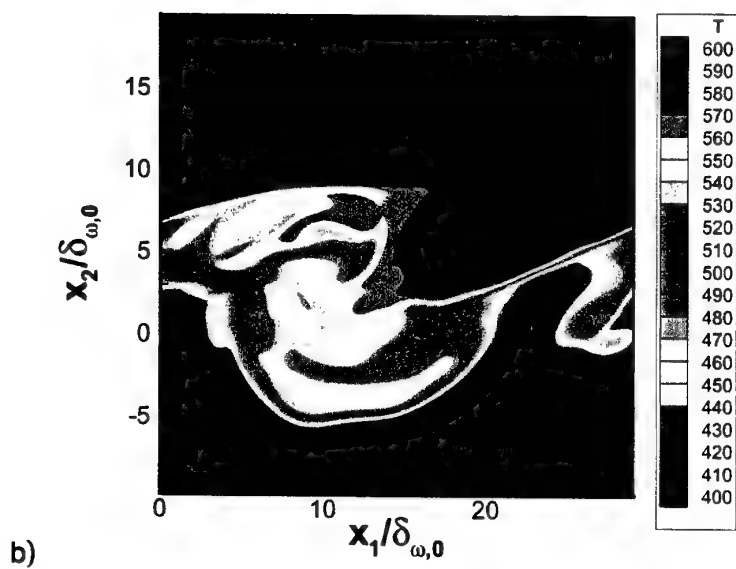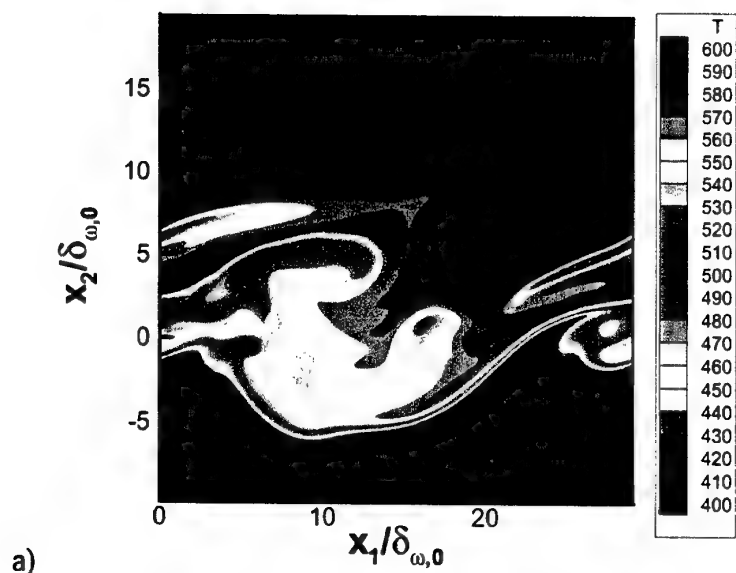
Figure 10: Temperature (in Kelvin) for R750 at $t^*=150$, a) in the braid plane and b) in the between-the-braid plane.

a)

b)
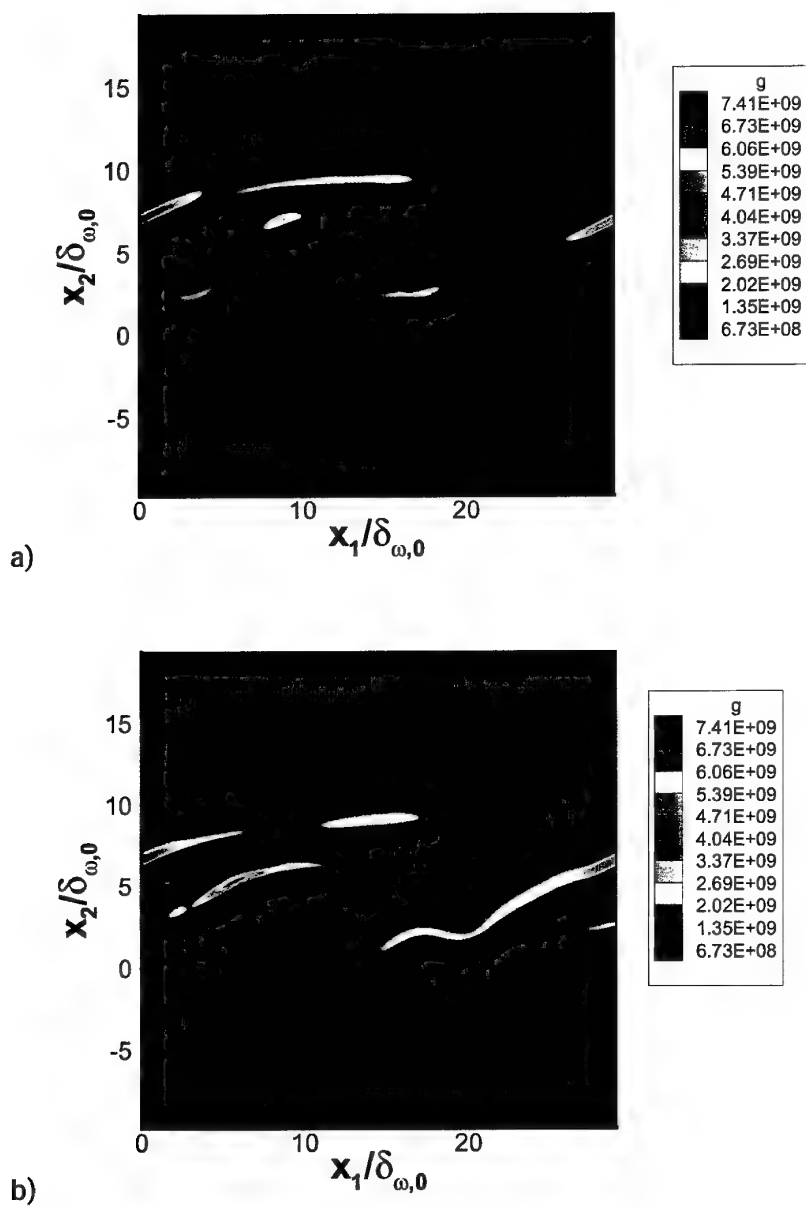
Figure 11: Dissipation (in J/m^{3}K) for R750 at t^*=150, a) in the braid plane and b) in the between-the-braid plane.
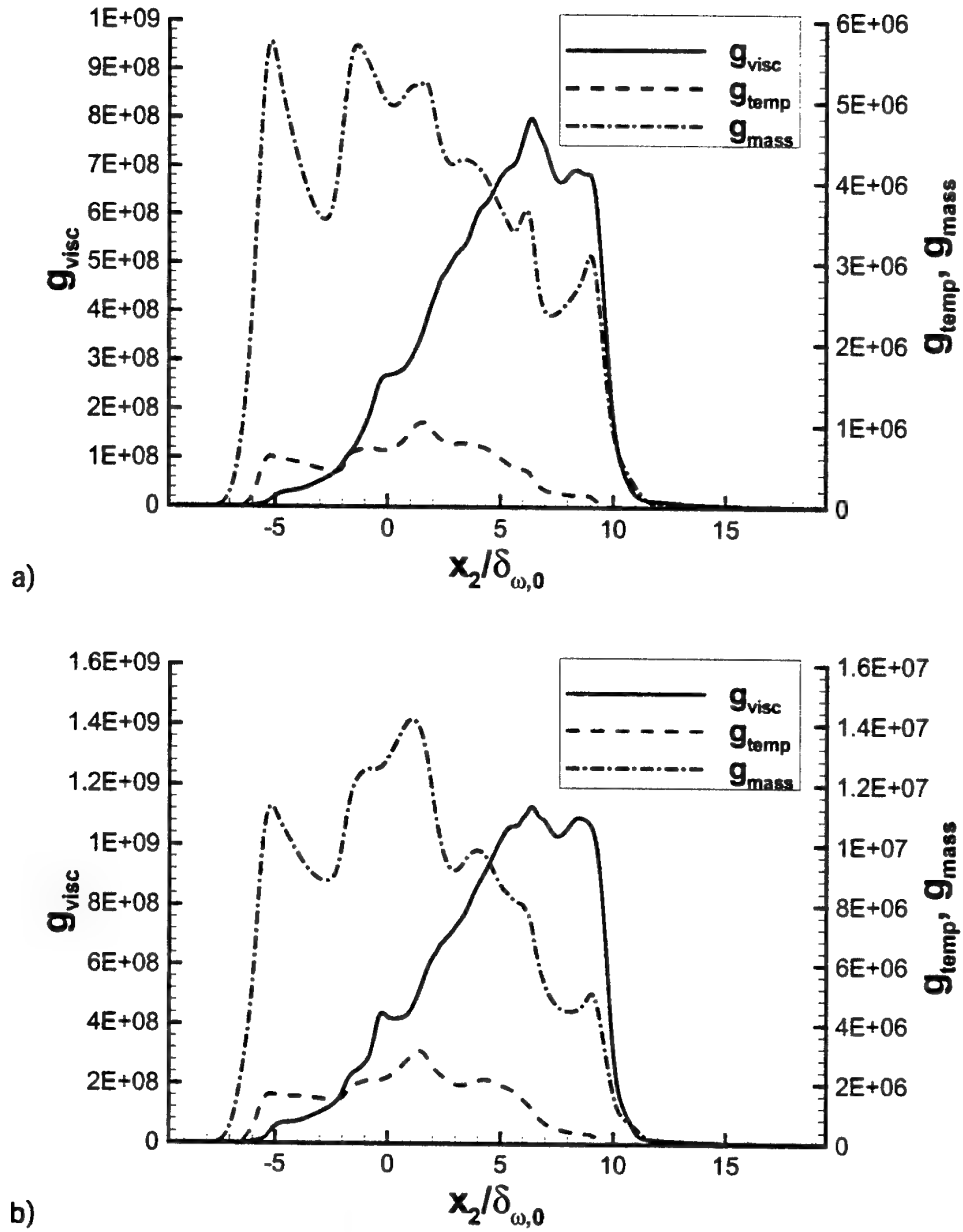
Figure 12: Contributions to the dissipation (in J/m^3K) for R750 at $t^*=150$, a) plane average and b) plane RMS.

2nd International Workshop

2nd International Workshop

ROCKET COMBUSTION MODELING
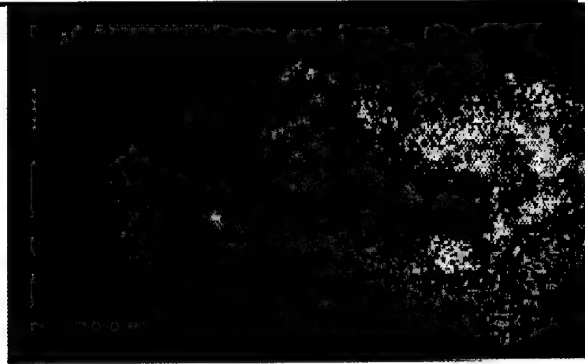
TEST CASE RCM-3
Mascotte single injector
- 60 bar -

March 25 –27, 2001
DLR, Lampoldshausen

French-German Research on Liquid Rocket Combustion

I- GENERAL PRESENTATION

The MASCOTTE cryogenic combustion test facility was developed by ONERA to study fundamental processes which are involved in the combustion of cryogenic propellants, namely liquid oxygen (LOX) and gaseous hydrogen (GH2). Three versions of this test facility have been built since the project was started in 1991. The first tests at atmospheric pressure were performed in January 1994, while pressures up to 10 bar were achieved in fall 1995.

A number of additional test data has been recently obtained at chamber pressure of 60 to 70 bar, which is higher than the critical pressure for LOX (50,4 bar). This range of pressure is thought to be representative of the chamber pressure encountered in a real engine like the Ariane 5 Vulcain Engine. Due to the difficulties met in running those high pressure experiments, the data base is smaller than for the 10 bar case, but some experiments will soon provide more data.

Test case RCM3 will thus consist of modeling the MASCOTTE combustor at a chamber pressure of 60 bar. The details for both the test facility geometry and the operating conditions required for the numerical simulations are listed below.

II- GEOMETRY

a) Test combustor

The MASCOTTE test combustor has a square section of 50 mm x 50 mm (Figure 1).

The injector head consists of a single coaxial injector element.

Combustion is initiated by using an H2/O2 igniter (O/F = 4) for roughly 2 seconds.

Figure 2 summarizes the geometry of the combustion chamber used for tests at 10 bar . The black dots indicate the locations of wall temperature transducers.

b) Injector

The MASCOTTE injector is a coaxial element consisting of a core of liquid oxygen surrounded by a high speed flow of gaseous hydrogen to provide good atomization properties.
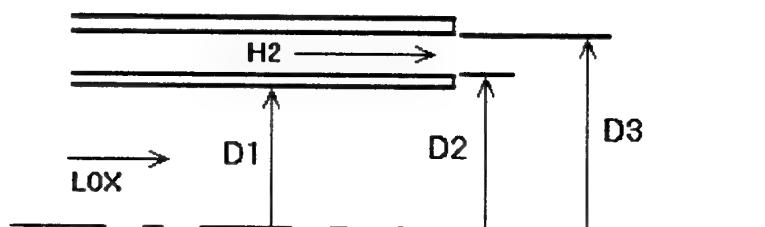
The dimensions of the injector are listed below.

	D1	**D2**	**D3**
DIAMETER	5.0 mm	5.6 mm	10.0 mm

Figure 3 shows a sketch of injector head geometry.

III- TEST OPERATING CONDITIONS

a) Operating point

The operating point chosen for this test case is a 60 bar case, called A-60 case. The operating conditions are defined in the following table:

PRESSURE	O/F	$\dot{m}$ (LOX)	$\dot{m}$ (H2)
60 bar	1.4	100 g/s	70 g/s

b) Propellants

Oxygen is injected under liquid conditions at 85 K, while hydrogen is injected under gaseous conditions at a temperature of approximately 287 K.

The physical properties of the propellants are summarized below:

Conditions	H2	O2
Pressure	6 MPa	6 MPa
Massflow	70 g/s	100 g/s
Temperature	287 K	85 K
Density	5.51 kg/m^3	1177.8 kg/m^3
C_p	15110 J/kg/K	1660.9 J/kg/K
Velocity	236 m/s	4.35 m/s
Viscosity	8.67E-4 kg/m/s	2.34E-4 kg/m/s
Surface tension	-	Cf § 4.

c) Turbulence

No data are yet available regarding the turbulence level at the injector exit. However, in order to make the comparison between various computations easier, we propose fixing the kinetic energy level at $\iota = 5$ % ($\iota^2 = 2/3 \ k \ / \ U^2_{inj}$). In addition, we recommend deriving the value of turbulence dissipation ε at the inlet using a turbulence length of 4 mm as a representative scale of the GH2 injection ring. The length of the GH2 inlet duct can be chosen by the participant, as well as the wall boundary condition. It is preferred to have fully developed velocity and turbulence profiles.

IV- GENERAL DATA FOR COMPUTATIONS

The list below describes the methods which should be used for this simulation.

- Computational Domain

  - A computation of the entire chamber (i.e., including the nozzle) is preferred. The nozzle, if any, will be chosen in order to have 60 bar static chamber pressure.

  - If there are problems, computations may be performed for a shorter chamber (without the nozzle) with the following characteristics:

    - Chamber length = 400 mm

    - Exit boundary condition: Constant pressure, p = 60 bar

- Droplet Injection

Given the lack of data in this pressure range, which is above the theoretical critical pressure for LOX, a rather simple representation will be chosen for LOX injection conditions.

  - Droplet size distribution:

    - One droplet size: D32 = 50 micron, initial velocity of drops, Vinj = 4.35 m/s

    - The droplets will be injected in the axial direction, with a uniform mass flow on the LOX post exit area.

- Physical Models

  - Combustion, turbulence, and evaporation models (also treatment of surface tension) are not specified. Participants are free to choose these models as they see fit.

V- FREE CASE

Given the physical uncertainties concerning the presence of LOX droplets in this pressure range, an additional case will be calculated with no specifications concerning the conditions of LOX injection (for example, eulerian atomisation model or real gas model can be used instead of a lagrangian description).

VI- EXAMPLES OF AVAILABLE DATA

Each test run performed on MASCOTTE provides a set of standard temporal data, such as propellant mass flow rate, pressures, wall temperatures, and propellant temperature at the inlet.

As of today, only one test campaign is available for test data at 60 bar chamber pressure: OH emission (figure 4 a)). Abel transform of the shots were performed in order to have an axisymetrical view of the flame (figure 4 b)). Other diagnostics are currently under investigation but the data is not yet available.

VI- REQUESTED RESULTS

Despite of the few information available at 60 bar, the results of numerical computations must be presented in such a way that they can be compared to future experimental data, and to calculations performed in the same combustor at 10 bar. The participants are requested to provide the following information (to the extent possible depending on the output of the numerical code):

- Radial profiles of mean temperature and standard deviation at CARS measurement locations (x/D1 = 10; 20; 30; 40; 50; 60). x represents the axial distance from the injector exit (see Figure 2), D1 = 5 mm.

- Mean temperature as a function of distance from the injector at three radial locations (y/D1 = 1; 2; 3).

- OH mass fraction contours in the near field of the injector (up to 150 mm downstream); see Fig. 4.

- Gaseous oxygen contours in the near field of the injector (up to 150 mm downstream).

- Axial profile of mean wall temperature (adiabatic wall temperature).

VII- REFERENCES

[1]   Habiballah. M, Vingert. L, Traineau. JC, Vuillermoz. P, "MASCOTTE : a test bench for cryogenic combustion research", IAF-96-S.2.03, *47th International Astronautical Congress*, (Beijing, China), October 7-10, 1996.

[2]   Bazile. R, Guerre. S and Stepowski. D, "Planar Laser Induced Fluorescence of Hot O2 in MASCOTTE", *Second French-German Colloquium on Research on Liquid Rocket Propulsion*, (Aachen, Germany), 1996.

[3]   Herding. G, Snyder. R, Scouflaire. P, Rolon. C and Candel. S, "Emission and Laser Induced Fluorescence Imaging of Cryogenic Propellant Combustion", *Conference on Propulsive Flows in Space Transportation Systems*", (Bordeaux, France), pp 1-14, 1995.

[4]   Brummund. U et al, Péalat. M et al and Candel. S et al "Laser Diagnostics for Cryogenic Propellant Combustion Studies*, Proceeding of the 2nd International Symposium on Liquid Rocket Propulsion*" (Châtillon, France), 1995, pp. 19.1-19.22.

[5]   Candel. S, Herding. G, Snyder. R, Scoufflaire. P, Rolon. C, Vingert. L, Habiballah. M, Grish. F, Péalat. M, Bouchardy. P, Stepowski. D, Cessou. A, Colin. P, "Experimental investigation of shear-coaxial cryogenic jet flame*, Third International Symposium on Space Propulsion*, (Beijing, China), August 11-13, 1997.

In case of further questions, you may contact:

mohammed.habiballah@onera.fr or stephan.zurbach@sep.snecma.fr
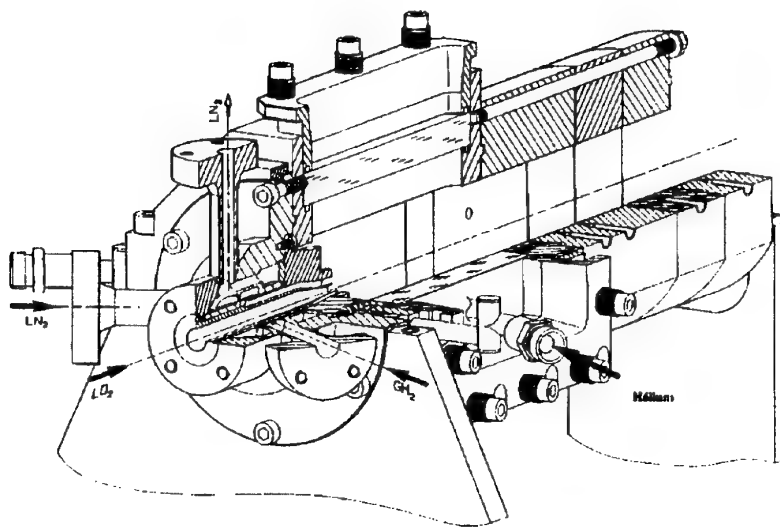
Figure 1: MASCOTTE Combustor
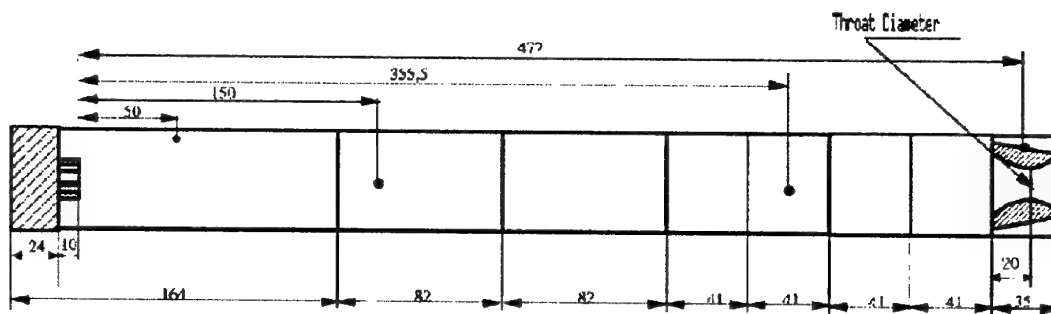
Figure 2: Combustor geometry (in mm): Throat diameter is **9 mm** for the 60 bar case
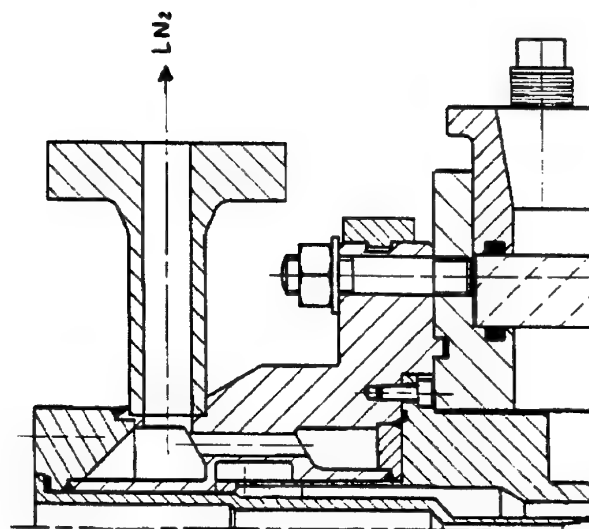
Figure 3: Injector head
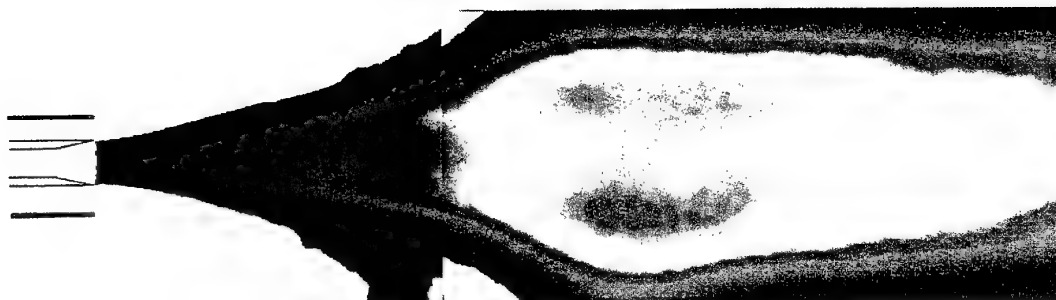
(a)

(b)

Fig. 4: Average emission image a) and Abel-transformed emission image b) for
operating point A-60, p = 60 bar.

TEST CASE RCM-3 USING CPS

B. Legrand, P. Durand, P. Vuillermoz

CNES - DLA
Rond point de l'Espace
91023 EVRY Cedex

1. GENERAL PRESENTATION

1.1. Introduction

The test case RCM-3 consists of modeling the MASCOTTE combustor at a pressure chamber of 60 bar, which is higher than the critical pressure of liquid oxygen (50.4 bar). This range of pressure is thought to be representative of the chamber pressure encountered in real engine.

The CPS code (version 1.3) was used to model this test case. Various models have been compared between them and to the experimental results available.

1.2. Geometry of MASCOTTE

The MASCOTTE test combustor has a square section of 50 x 50 mm. The chamber length is fixed at 400 mm.

The injector head consists of a single coaxial injector element (Figure 1).
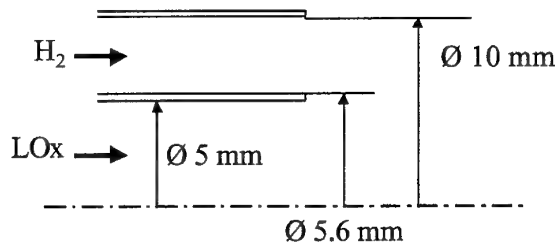
Figure 1 : injector geometry

1.3. Operating condition

The operating point is the A-60 case. It is defined in the following table:

Pressure	O / F	$\dot{m}$ (LOx)	$\dot{m}$ (H$_2$)
60 bar	1.4	100 g/s	70 g/s

1

In this case [1], liquid oxygen is injected at 85 K, while gaseous hydrogen is injected at approximately 287 K. The physical properties of the propellants are summarized in the following table:

Conditions	H_2	O_2
Pressure	6 Mpa	6 MPa
Mass flow	70 g/s	100 g/s
Temperature	287 K	85 K
Density	5.51 kg/m^3	1177.8 kg/m^3
Cp	15110 J/kg/K	1660.9 J/kg/K
Velocity	236 m/s	4.35 m/s
Surface tension	8.67 10^{-4} kg/m/s	2.34 10^{-4} kg/m/s

1.4. Experimental results

Available data for this test case is OH emission. Abel transform permit to have an axisymetrical view of the flame (Figure 2)

Average OH* emission image for operating point A-60

Abel transform emission image for operating point A-60

Figure 2 : Experimental result for operating point A-60

1.5. Physical phenomena

The phenomena involve in such case are summarize in the Figure 3.
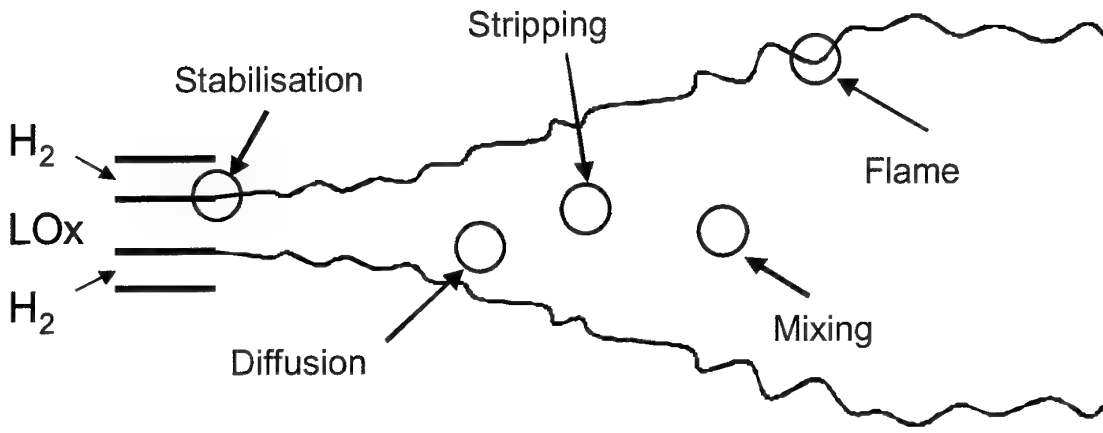
Figure 3 : Physical phenomena in supercritical condition.

1.6. Oxygen thermodynamics properties

Various thermodynamics properties of oxygen at 60 bar are plot on Figure 4. We observe important variation between injection temperature (85 K) and boiling temperature (119 K).
Critical temperature and pressure are respectively 154 K and 5.04 MPa.
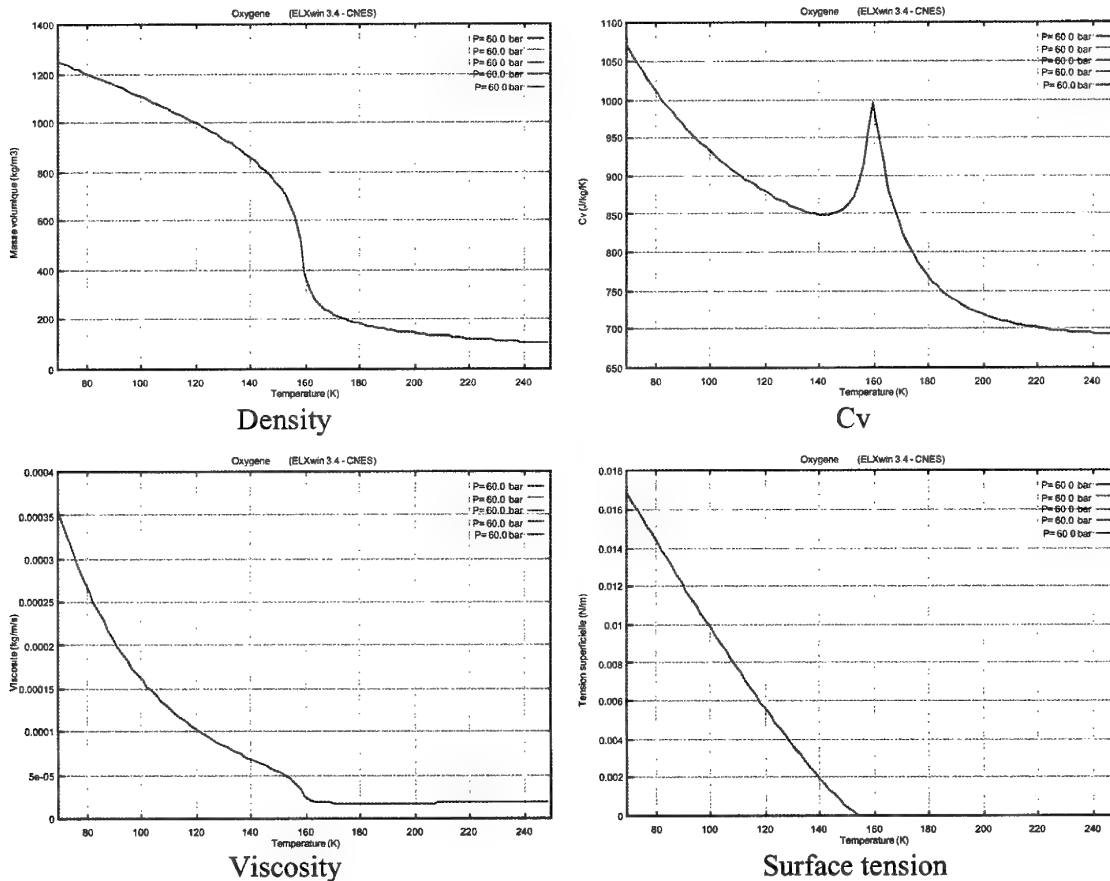
Figure 4 : Evolution of oxygen thermodynamics properties between 70 et 250 K at 60 bars.

2. MODELING

2.1. Mesh

The mesh is composed of 37 x 58 cells as represented in Figure 5.
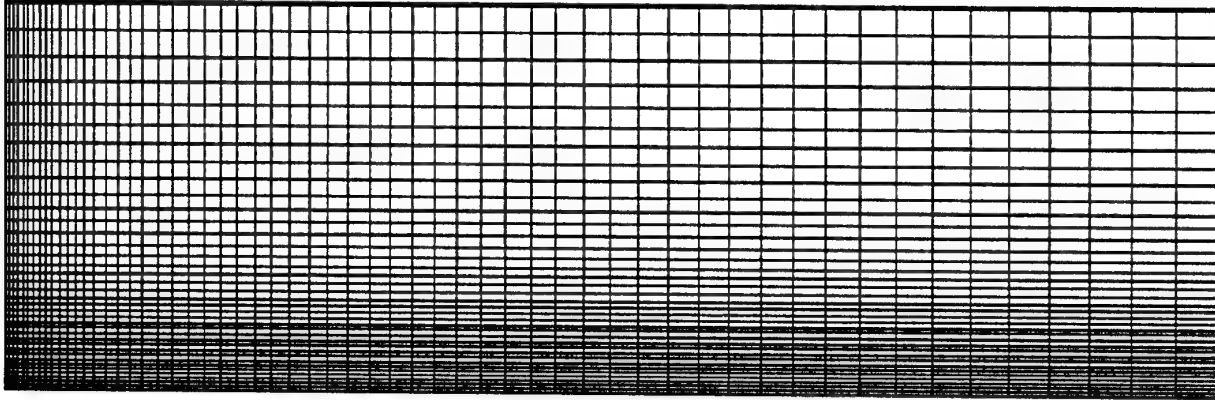
Figure 5 : Mesh (representation dilated by 5 on vertical direction)

2.2. Conditions

Calculation have been made with constant parameter and model as:
- Lagrangian approach
- Explicit scheme
- Droplet fragmentation model (TAB)
- Droplet vaporization model
- Without droplet collision
- Initial droplet diameter (50 μm)

Other parameter and model have been compared:

2.2.1. Injection condition

Injection of liquid in critical condition is not well known. It's clear that injection of one size droplet is not representative. So we have used different injection condition for oxygen:
- Gas
- Liquid
- Mixture with Gas / Liquid ratio variable

2.2.2. Turbulence model

Two turbulence model have been used:
- q-ω Coakley
- k-ε Jones-Launder

q-ω Coakley	k-ε Jones-Launder
$\mu^t = C_\mu f_d \dfrac{\rho k}{\omega}$	$\mu^t = C_\mu f_d \dfrac{\rho k}{\omega}$
$s_1 = q = k^{1/2}$	$s_1 = k = q^2$
$s_2 = \omega = \dfrac{\varepsilon}{k}$	$s_2 = \varepsilon = \omega k$
$H_q = \dfrac{1}{2}\left[C_\mu f_d \dfrac{S}{\omega^2} - \dfrac{2}{3}\dfrac{D}{\omega} - 1\right]\rho\omega q$	$H_k = \left[C_\mu f_d \dfrac{S}{\omega^2} - \dfrac{2}{3}\dfrac{D}{\omega} - 1\right]\rho\omega k$
$H_\omega = \left[C_1\left(C_\mu \dfrac{S}{\omega^2} - \dfrac{2}{3}\dfrac{D}{\omega}\right) - C_2\right]\rho\omega^2$	$H_\varepsilon = \left[C_1\left(C_\mu f_d \dfrac{S}{\omega^2} - \dfrac{2}{3}\dfrac{D}{\omega}\right) - C_2 f_e\right]\rho\omega\varepsilon$

2.2.3. Combustion model

Two combustion model have been used:
-   Coherent flame model (CFM)
-   Eddy Break Up model (EBU)

CFM	EBU
$S^c_{\rho S_f} = \alpha\rho\varepsilon_S S_f \dfrac{\dot{Q}_h}{\dot{Q}_{h0}} - \beta\rho S_f^2 \dfrac{\dot{Q}_{k\lim}}{Y_{k\lim}}$	$\dot{\omega} = \dfrac{\rho}{Stoemas_{k\lim}} C_{EBU} Y_{k\lim}\left(Y^0_{k\lim} - Y_{k\lim}\right)$
with $\quad \varepsilon_S = C_S \dfrac{\varepsilon}{k}$	$S^c_{\rho Yk} = Stoemas(k)\dfrac{\Delta t\dot{\omega}}{\rho}$

2.2.4. Oxygen thermodynamics properties

   The oxygen thermodynamics properties have take constant in our calculus. To take into account the droplet temperature increase we have take different thermodynamics properties for the oxygen.

	Injection (85K)	Boiling (119K)
Density (kg/m^3)	1177.8	1004.4
Viscosity (kg/m/s)	$2.34\ 10^{-4}$	$1.05\ 10^{-4}$
Surface tension (N/m)	$1.32\ 10^{-2}$	$5.82\ 10^{-3}$
Cv (J/kg/K)	987.5	880.6

2.3. Different case

The different case test are summarize in the following table (the variable parameter are in italic):

Injection	Combustion model	Turbulence model	Oxygen thermodynamics properties
Gas / *Liquid*	EBU	q - ω	Injection (85 K)
Liquid / *Mixture*	CFM	q - ω	Injection
Mixture ratio	CFM	k - ε	Boiling (119 K)
Liquid	*CFM* / *EBU* / *EBU/Arrhénius*	q - ω	Injection
Mixture	*EBU* / *CFM*	k - ε	Injection
Mixture	CFM	*q - ω* / *k - ε*	Injection
Liquid	CFM	q - ω	*Injection* / *Boiling* / *Cv / ρ / enthalpy / μ*
Mixture	CFM	k - ε	*Injection* / *Boiling* / *Surface tension*

3. RESULTS

3.1. Injection influence

We observe an important variation of the flame length with the ratio gas / liquid injected (Figure 6 and Figure 7). The flame length increases with the liquid fraction (Figure 6). This phenomenon is due to the time increased necessary to vaporize all the droplets. We also observe a modification of the reactive zone on the near field of the injector due to the presence of gaseous oxygen.

Injection Gas – Liquid (1:1)

Injection Liquid

Figure 6 : Reactive rate (mol/kg/s) : CFM, q - ω; oxygen (injection)
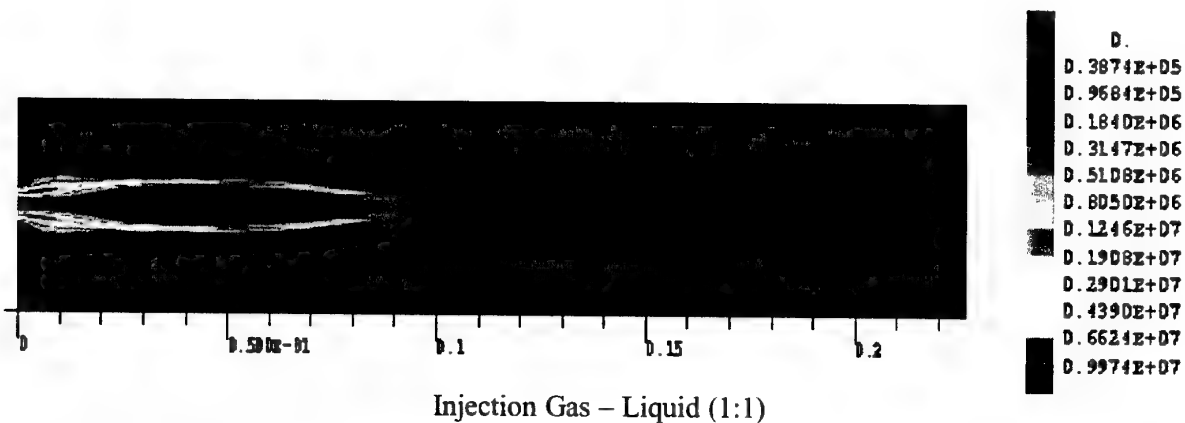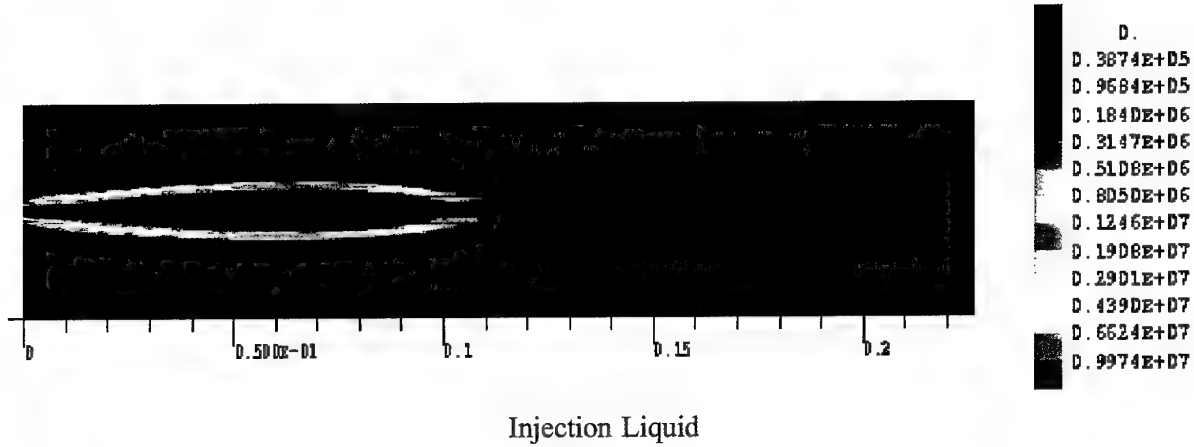
If we decrease drastically the liquid fraction, the flame length increases (Figure 7). This is due to the increase of the oxygen injection speed to obtain the correct amount of oxygen injected.

Injection Gas – Liquid (4:1)

Injection Gas – Liquid (1:1)
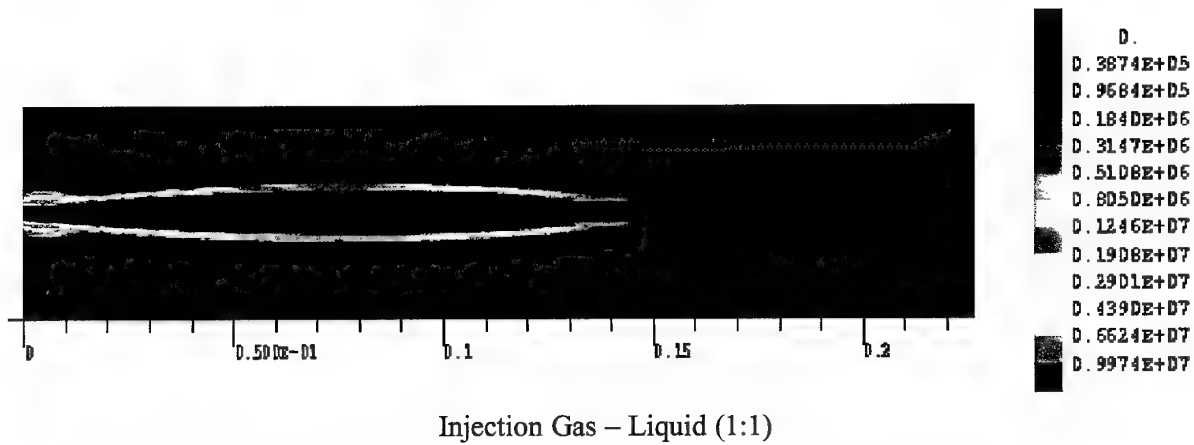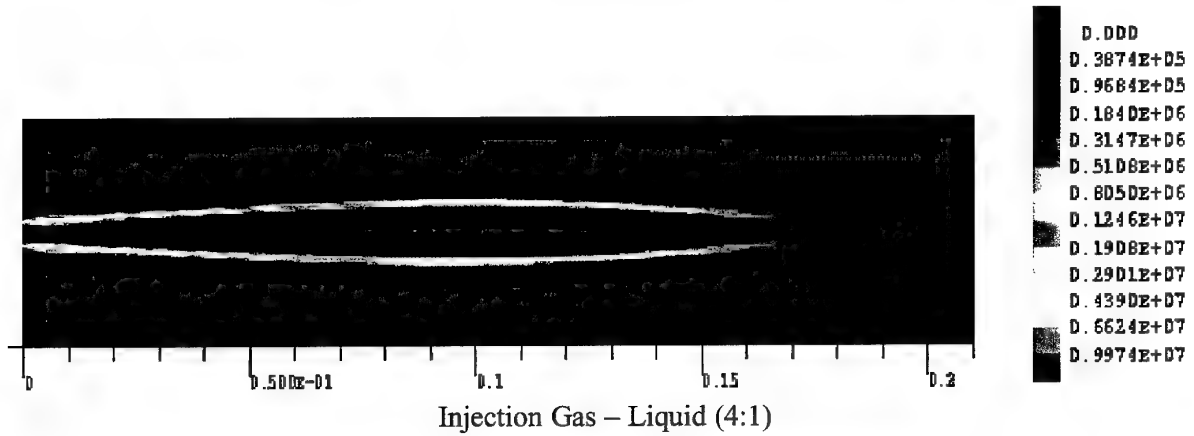
Figure 7 : Reactive rate (mol/kg/s) : CFM, k - ε; oxygen (injection)

We observe on Figure 8 that liquid oxygen volume fraction can be find greater that one (red part on the figure). This is physically incorrect and due to the fact that CPS neglect the volume of the droplet. To minimize this effect, in most case, we have take a gas-liquid mixture for oxygen injection.

7

Figure 8 : Liquid oxygen volume fraction
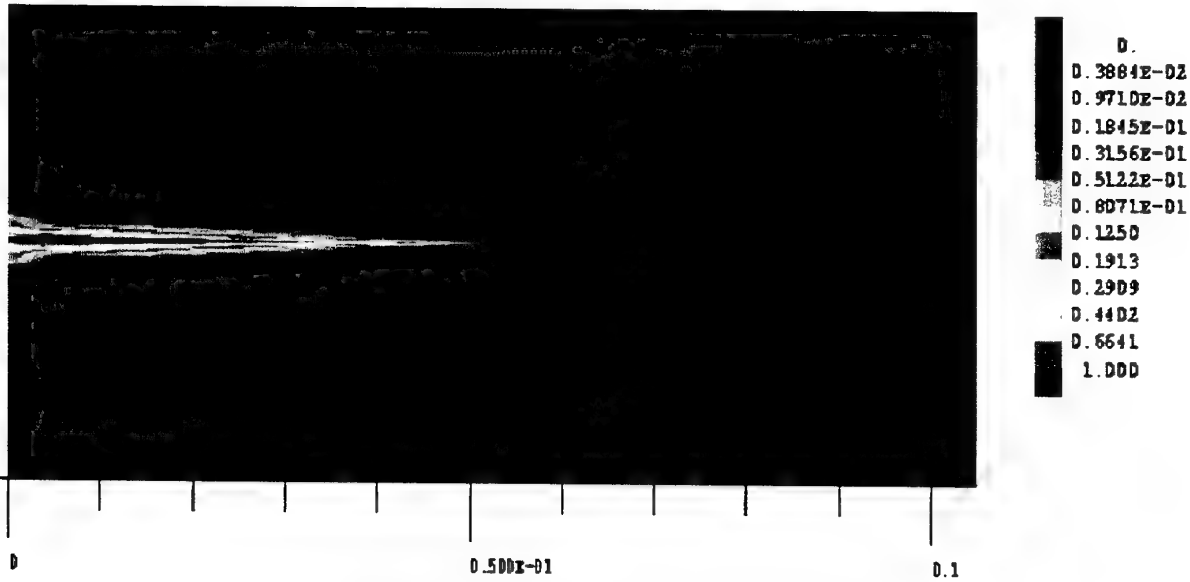
3.2. Turbulence model influence

k - ε

q - ω

Figure 9 : Reactive rate (mol/kg/s) : CFM, Gas – Liquid (1:1), oxygen (injection)
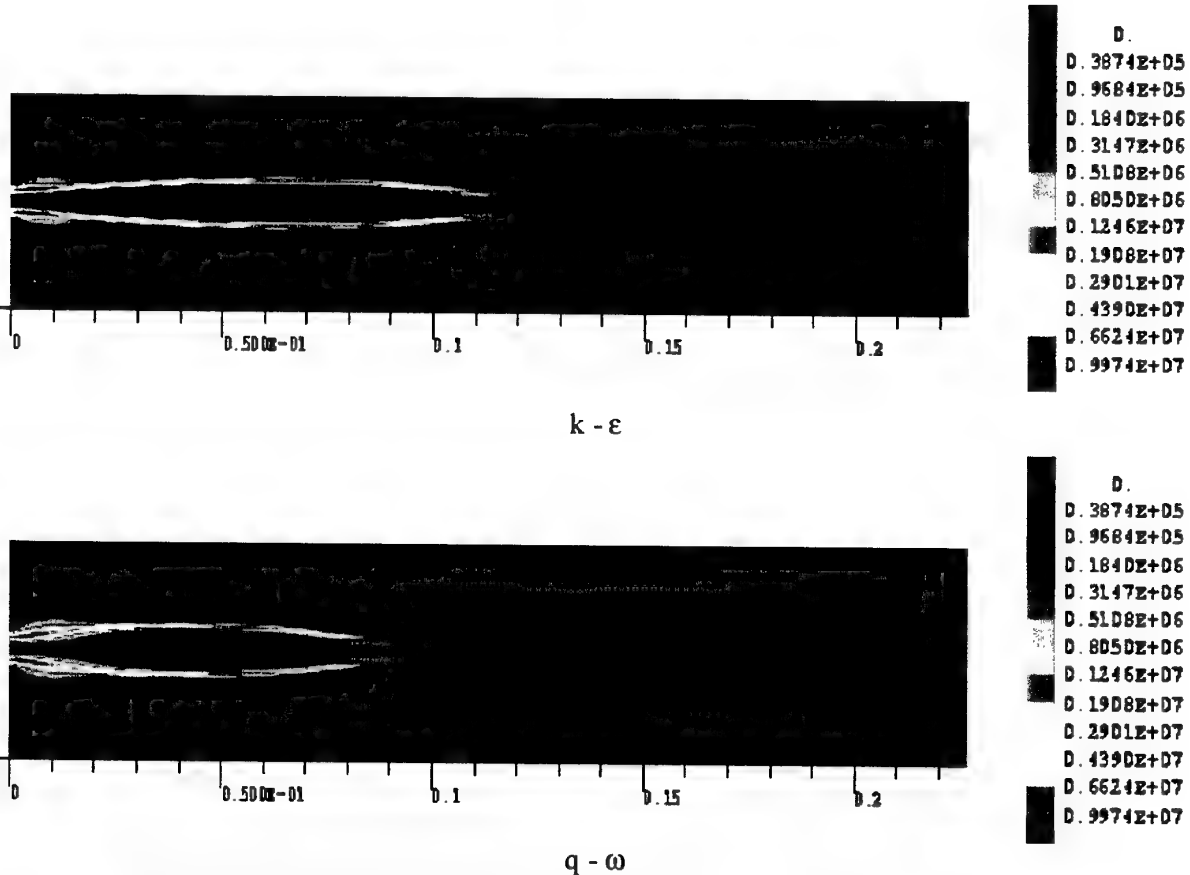
3.3. Combustion model influence

We observe important variation of the flame structure between the two models (Figure 10 and Figure 11). With Gas+Liquid injection: EBU model gives a better flame structure in the injector near field. But the CFM gives better results for:
- Temperature value (Figure 12)
- Flame structure

CFM

EBU
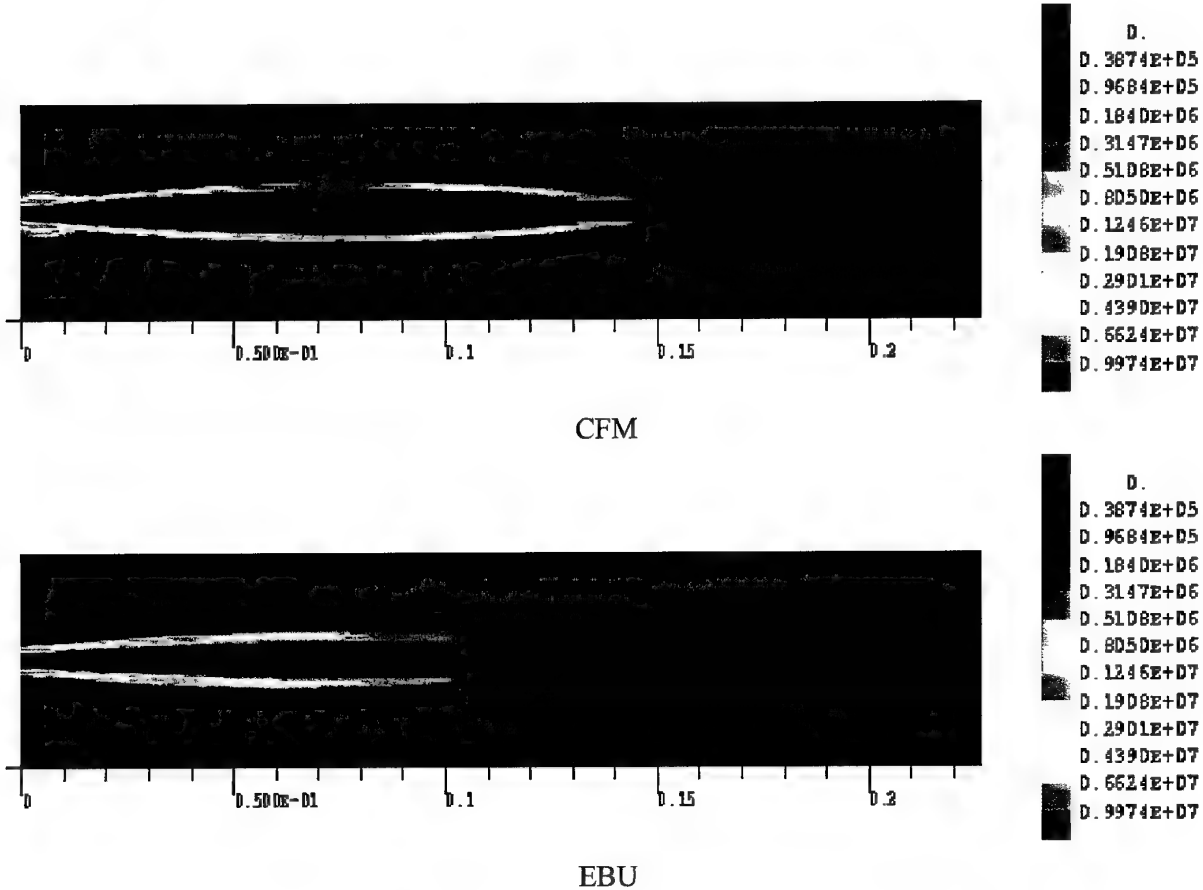
Figure 10 : Reactive rate (mol/kg/s) : Gas – Liquid (~1:1), k - ε, oxygen (injection)

CFM

9

EBU
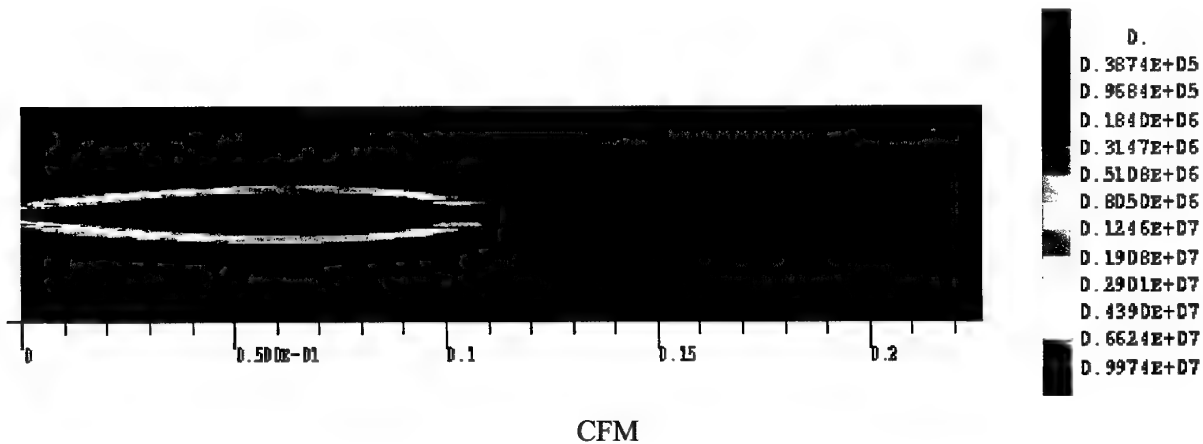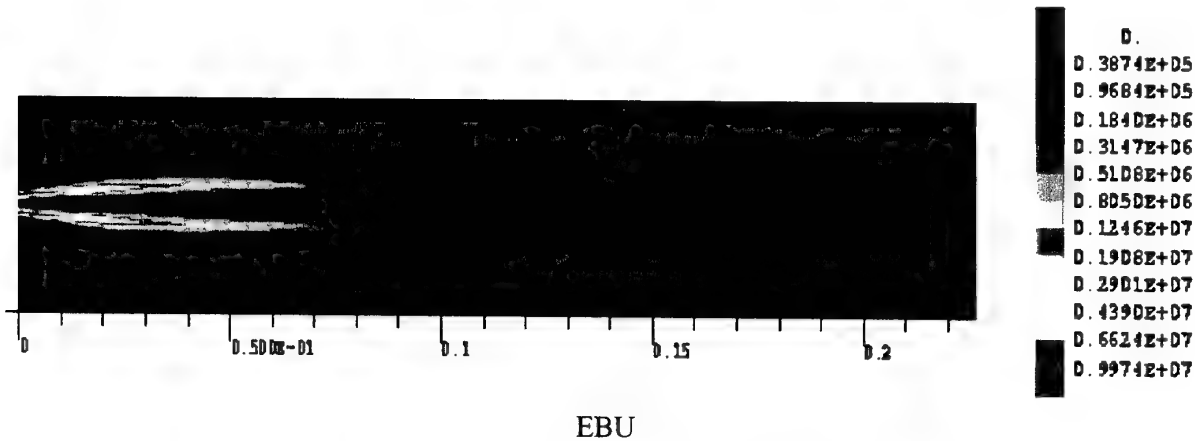
Figure 11 : Reactive rate (mol/kg/s) : Liquid, q - ω, oxygen (injection)

EBU   CFM
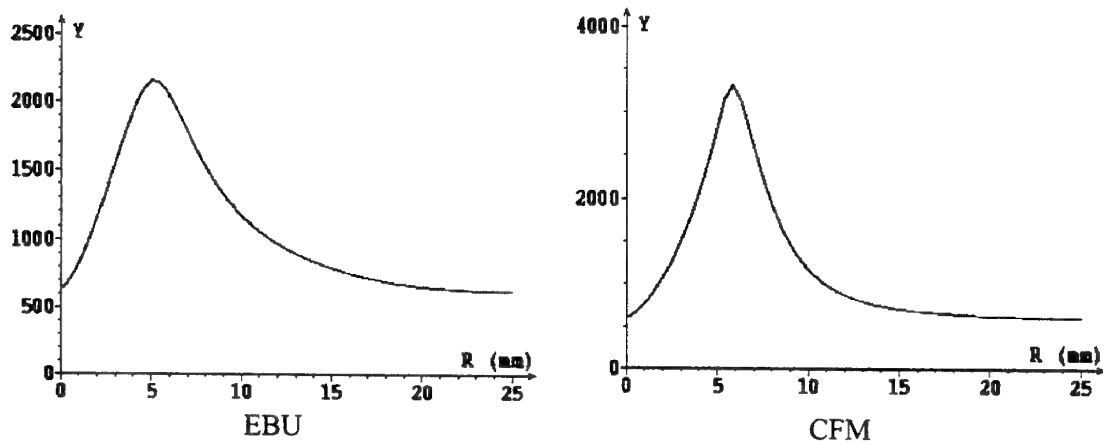
Figure 12 : Temperature radius profile (x = 50 mm) : Liquid, q - ω, oxygen (injection)

3.4. Oxygen thermodynamics properties influence

When we change oxygen thermodynamics properties, we don't observe difference in the results except in the near field of the injector. This is due to the modification of the surface tension and the increase of breakup with decreasing σ ($\sigma = 1.32 \; 10^{-2}$ N/m at 85K et $5.82 \; 10^{-3}$ N/m at 119K).

Thermodynamics properties at 85 K (Injection)
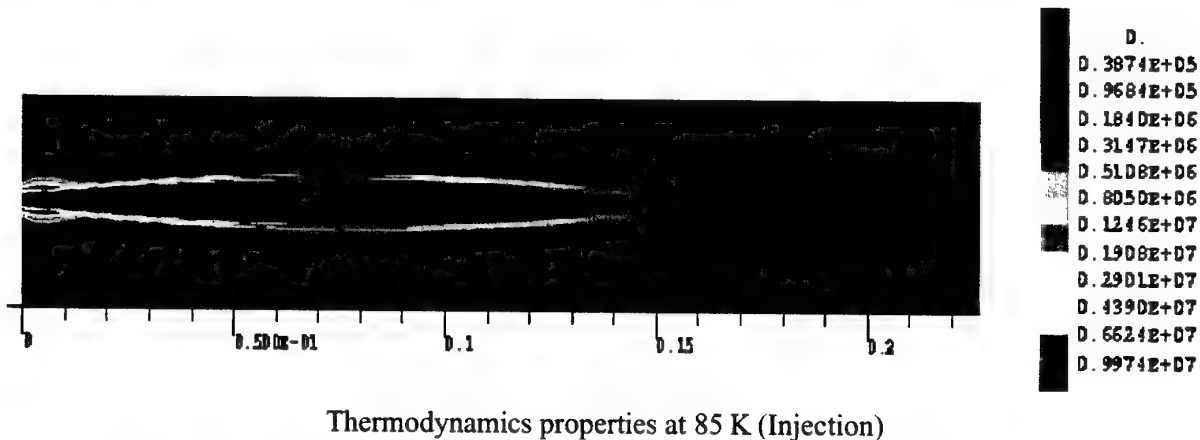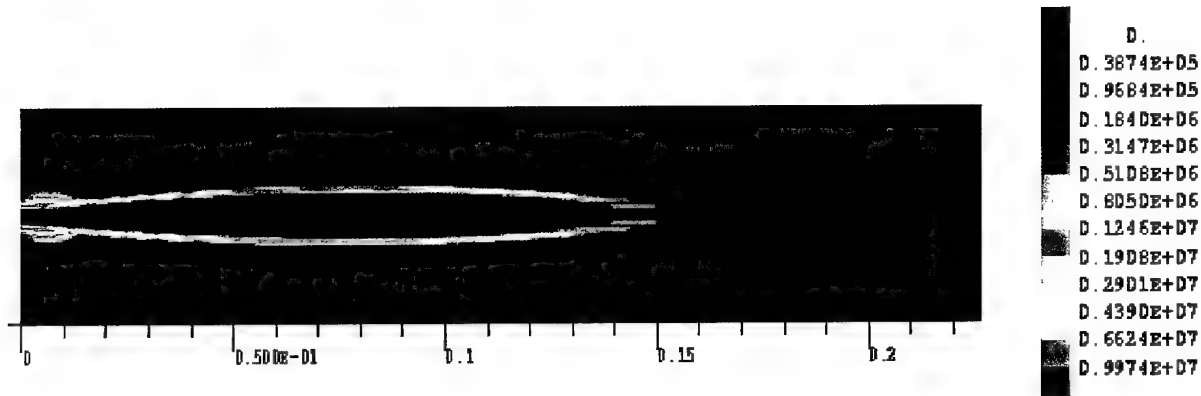
Thermodynamics properties at 119 K (Boiling)
Figure 13 : Reactive rate (mol/kg/s) : CFM, k - ε, Gas – Liquid (~1:1)

In supercritical condition the surface tension drastically decrease. To observe the influence of σ, with have made calculation with an arbitrary value for σ witch is 10^{-6} N / m. The flame length decrease with the surface tension (Figure 14).
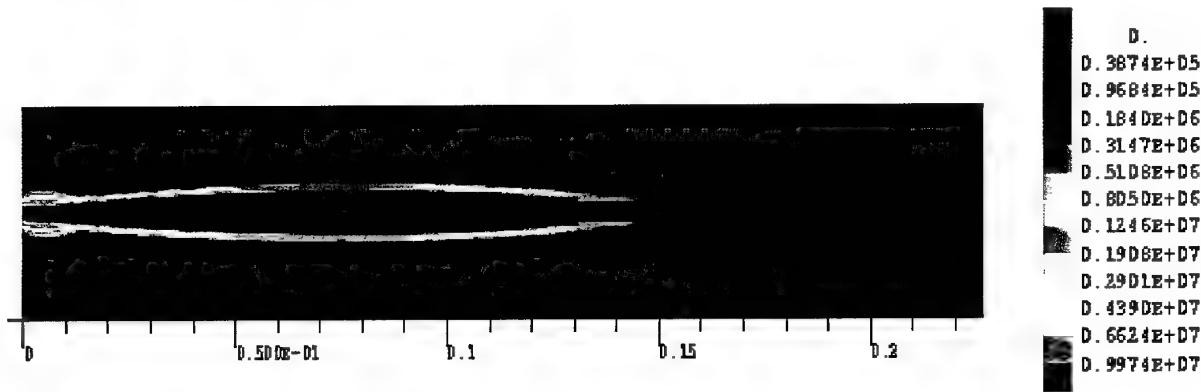
$$\sigma = 1.32 \; 10^{-2} \; N / m$$
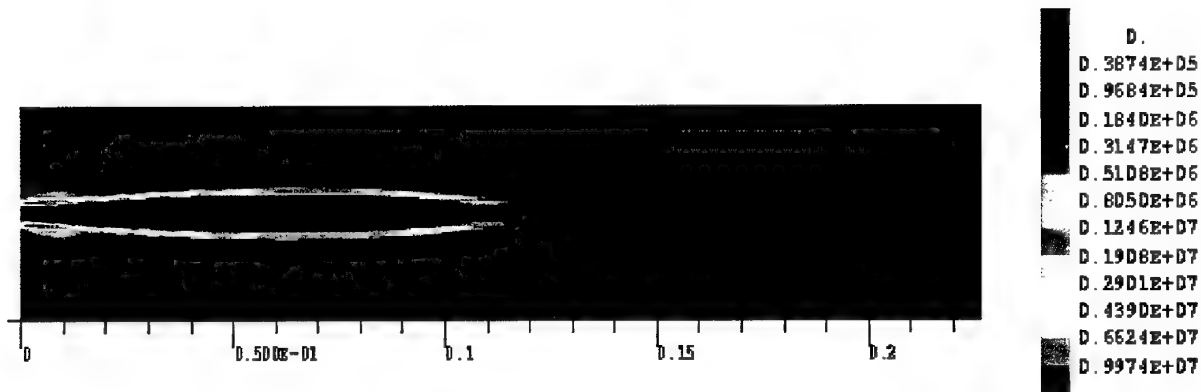
$$\sigma = 1 \; 10^{-6} \; N / m$$

Figure 14 : Reactive rate (mol/kg/s) : Liquid, q - ω, oxygen (injection except σ)

3.5. Global case result

This case correspond to the following condition:
- Liquid injection for oxygen
- Turbulence model: q - ω
- Combustion model: CFM
- Surface tension σ = 1 10⁻⁶ N/m
- Oxygen thermodynamics properties take at 85 K (injection)
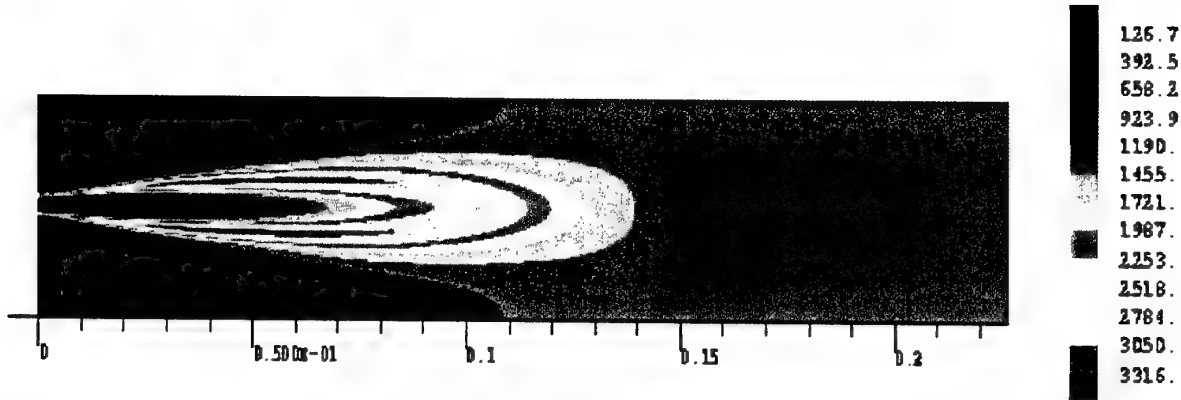
Figure 15 : Temperature (K)
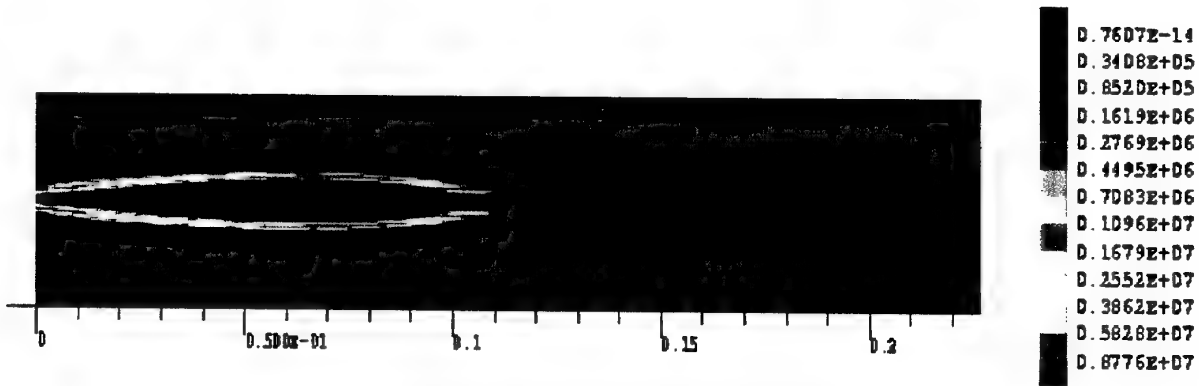
Figure 16 : Reactive rate (mol/kg/s)
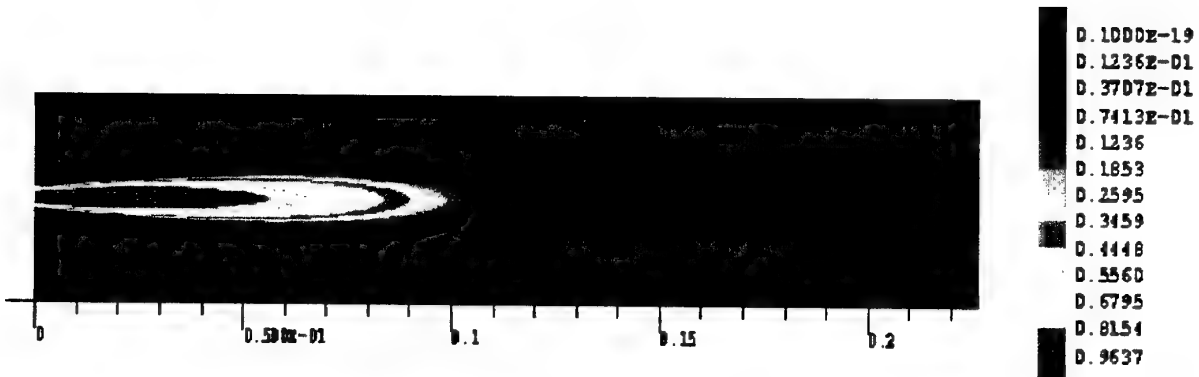
Figure 17 : O₂ mass fraction

12
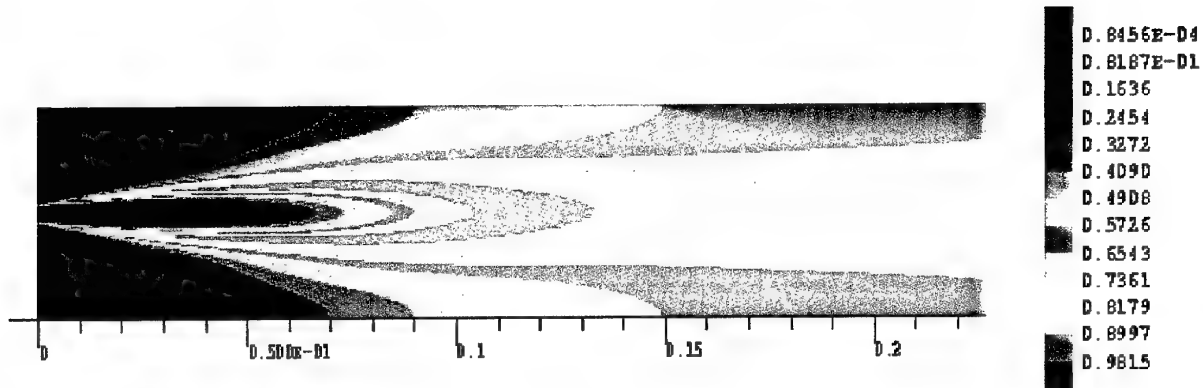
Figure 18 : H₂O mass fraction

<u>*3.6. Comparison with experimental results*</u>

If we compare the axisymetrical OH* emission image obtained experimentally with the most comparable calculated variable (the reactive rate), we obtain Figure 19. We observe a good agreement in the near field of the injector, but the second part of expansion of the flame is not obtained with calculation.

Axisymetrical average OH* emission image

Calculated reactive rate
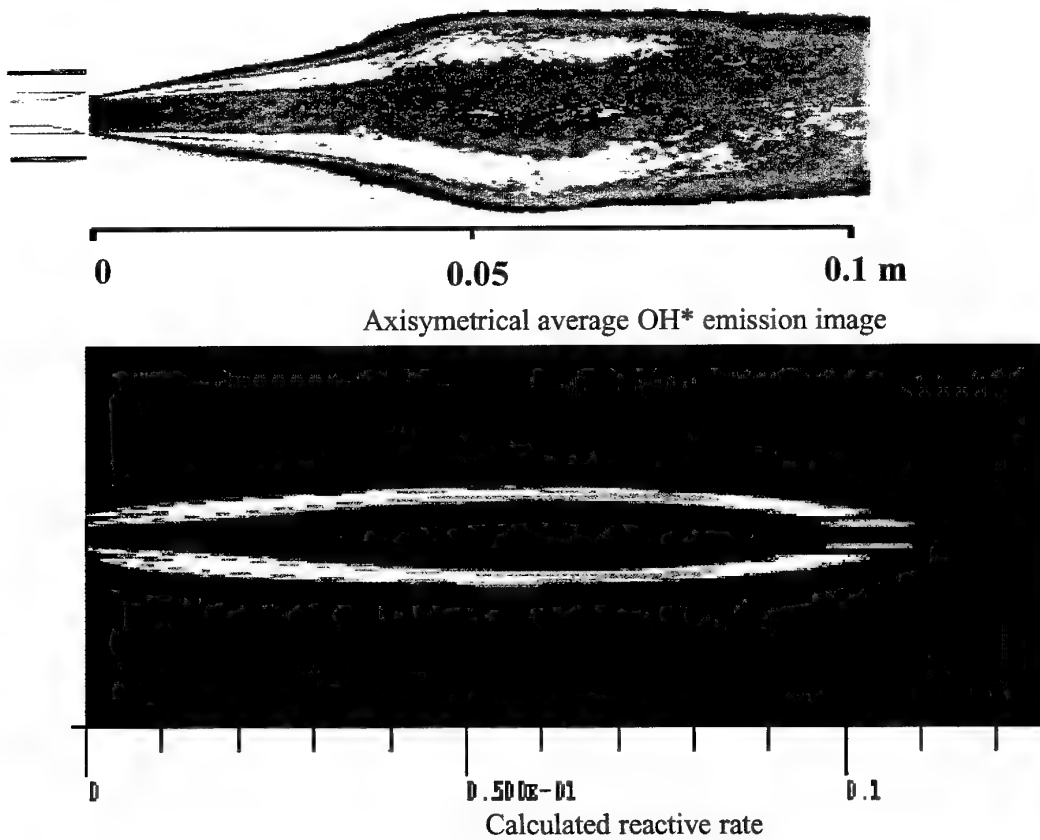
Figure 19 : Comparison experiment – calculation

Experimentally [2] observe an expansion angle of 3.4° for OH* emission and 5.1° for H_2O emission. If we measure the reactive rate angle obtained by calculation, we have 4.0° (Figure 20). This value is coherent with experimental result.

Figure 20 : Calculated reactive rate expansion angle

4. CONCLUSION

The calculations performed for this test case RCM-3 show important difference on obtained results. Nevertheless, they are in good agreement with experimental results even if they are few for this operating point (A-60).

The lagrangian approach for oxygen generates some interrogation when it's used in supercritical condition. It appears that a real gas law for oxygen should be interesting for eliminates all the problems relative to droplet injection.

RÉFÉRENCES

[1] Test cas RCM-3, Mascotte single injector – 60 bar-, Test case specification for the *2nd International Workshop on Rocket Combustion Modeling*.
[2] Tripathi A., Structure de flammes cryotechniques à haute pression, *Thèse École Centrale Paris*, (2001)

Application of Astrium's CryoROC Code to a Single Injector Problem

A contribution to the RCM-3 Mascotte Test Case (60 bar)

Josef Görgen, Oliver Knab

Astrium GmbH, Space Infrastructure, IP34, 81663 München, Deutschland

Introduction, Motivation and Objectives

This paper presents a numerical analysis of the RCM-3 Mascotte test case (60 bar) with CryoROC, Astrium's advanced multiphase Navier-Stokes solver. The CryoROC spray combustion CFD-code was developed and intended to simulate the flowfield and the heat exchange within existing and future cryogenic rocket thrust chambers. For that purpose, the computational approach so far excluded too much effort on precise modelling the vicinity of the injector head with its single elements. It's rather a question of whether the code's predictions are efficient, fast and precise enough regarding the whole thrust chamber and its global characteristics. The CryoROC code is an important tool used in the thrust chamber layout process at Astrium.

The motivation for this work thus came from two points: on one hand, it would be an interesting question, whether the code is capable to resolve the complex combustion phenomena in detail near the injector head, when the computational mesh is adequately refined in that area. One the other hand allows the workshop a further assessment of the CryoROC computation results by comparison with experimental data and other computations. This procedure is intended to analyse and to evaluate the impact of the injector-nearfield flow evolution on the overall combustion process, i.e. answering the question whether it is necessary to resolve the injector-nearfield flow phenomena *en détail* to predict global engine characteristics as the wall heat transfer accurately? Or if that is only of minor importance because there are only negligible differences a short distance further downstream the injector head, which are anyway included in the spray initialisation process?

The numerical code CryoROC

Thrust chamber flows of cryogenic hydrogen/oxygen rocket engines are characterised by the coexistence and complex interaction of various physical phases. A reactive multi-species gas mixture (1st phase), together with a dispersed oxygen droplet phase (2nd phase) have to be resolved efficiently. CryoROC treats the gaseous phase by solving the Favre-averaged Navier-Stokes equations extended by the species continuity and k-ε turbulence

Capabilities	Capabilities (cont.)
• compressible - sub-, trans- and supersonic	• viscous heating, species diffusion
• turbulence models - standard k - ε with wall functions - 2 layer model - compressibility effects	• standard Jannaf property data base for gaseous combustion species (Gordon & McBride)
• multi-gaseous species consideration (H_2, O_2, H_2O, H, OH, N_2, CO_2, CO, ...etc.)	• porous walls and crack simulation • coupling with Astrium's RCFS (Regenerative Coolant Flow Simulation) code
• chemical reaction models - turbulence controlled (Eddy Dissipation Concept) - kinetically controlled (Arrhenius) - multi-step global reaction schemes * hydrogen/oxygen	**Numerics** • 2D, axisymmetric, finite volume • Favre-averaged • SIMPLE algorithm (pressure correction) • implicit Stone solver
• Lagrangian particle tracking (Stochastic Separated Flow model) - multi-class, bi-propellant, discrete particle injection and sequential tracing approach - mass, momentum and heat coupling with gas phase - supercritical LOX gasification model	**Grid** • structured • non-orthogonal • curvilinear

Table 1:   Specification of CryoROC (*Cryo*genic *RO*cket *C*ombustion) Code

equations. The latter include appropriate modifications accounting for compressibility effects and handle the near wall region optionally by a logarithmic wall function approximation or by a two-layer approach. The set of equations is discretized according the finite-volume methodology for non-orthogonal, boundary fitted grids and solved by an implicit algorithm. Hereby, both central and upwind differencing schemes are applied. The reaction mechanism of cryogenic hydrogen/oxygen systems is represented by 5 species (H_2, O_2, H_2O, H and OH). Up to now, a single-step, global reaction scheme is employed ($H_2 + xO2 \Rightarrow aH_2O + bH + cOH$) basing on a turbulence (EDC) and/or kinetically (Arrhenius) controlled combustion model.

In addition to solving transport equations for the continuous gas phase, CryoROC allows to simulate multiple discrete phases in a Lagrangian frame of reference. These second phases consist of spherical particles representing propellant droplets of different sizes being dispersed in the continuous gaseous phase. CryoROC computes the trajectories of these discrete phase entities by integrating their force balance. In particular for LH2/LOX systems, CryoROC allows for transient LOX droplet heat-up, supercritical LOX gasification, as well as droplet-to-gas phase turbulent interaction.

Gaseous and dispersed phase calculations are coupled in a loosely manner, i.e. source terms in the respective governing equations are not updated simultaneously. As a thumb rule, oxygen droplet tracking is performed every 70 to 200 gas phase iterations. Table 1 gives a survey on the most important modelling features of the CryoROC software. For a more detailed description of the models the reader is referred to [1], [2],[3].

Computational Results

Since the CryoROC code so far has only been applied to entire thrust chamber configurations, see e.g. [4], some simplistic assumptions are necessary to take, in order to receive a certain degree in reliability and efficiency. Firstly, the spray initialisation has to get adapted, because a detailed resolution of the single injector elements is not possible within that context. In particular, primary atomisation processes and 3-dimensional effects have to be excluded to enable an efficient handling. The approach chosen corresponds with concept #1 in Figure 1 and is referred as standard in the following. Here the H_2 and LOX are perfectly mixed throughout the injector element diameter so that the global mixture ratio fits exactly. Because of the finite number of injector elements inside an injector row, this approach is assumed to be rather appropriate and realistic for axisymmetric thrust chamber computations. It might not be quite as appropriate for single element calculations, as already hinted in Figure 1.
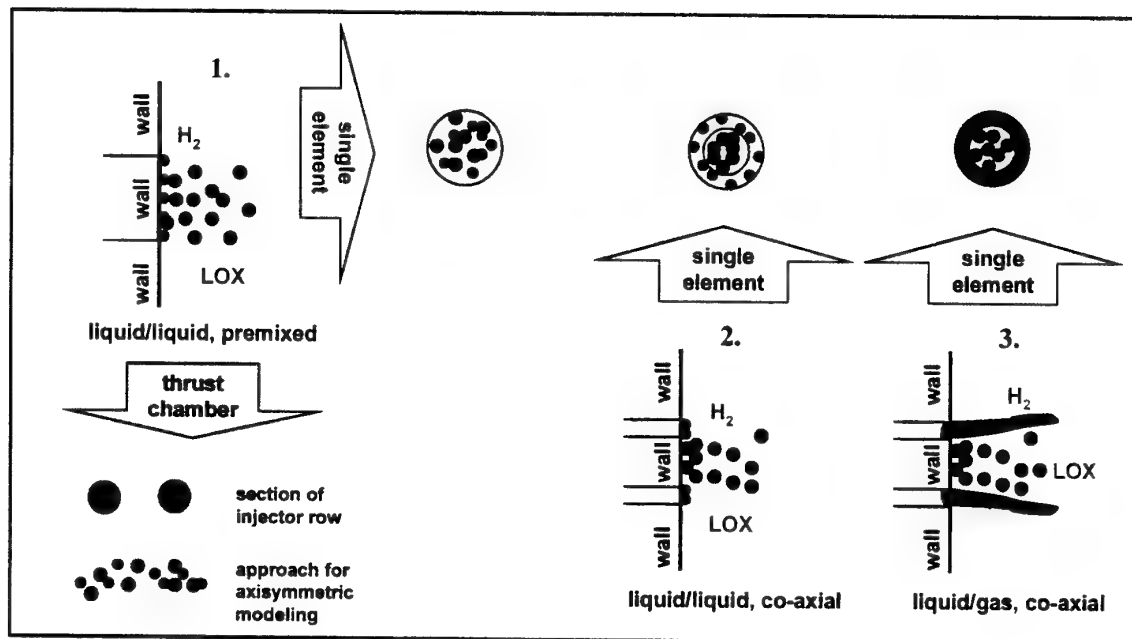

Figure 1:   Spray Initialisation Concepts 1. - 3. Applied to the "Single Element Problem"

The other major assumption made for standard thrust chamber computations lies in the fact that both, oxygen as well as hydrogen, are injected in the chamber as dispersed and liquid droplets. The hydrogen, of course, is eva-porated instantly. This has several advantages, but above all does that enable CryoROC to simplify the

boundary condition at the injector head. Propellant inflow is realised solely by spray initialisation, so that the wall remains closed and only an adaptation of the conservation equations' source terms is needed.

As one can recognise from Figure 1, in order to contribute to the Mascotte test case and to apply the CFD code to a single injector problem, different methods have been elaborated and applied. Apart from the standard concept #1, the concept #2 gives room to a more detailed resolution of the injector-nearfield, i.e. H_2 and LOX are now initialised co-axial but still as droplet sprays with instantaneously evaporating H_2. Concept #3 at last removes that restriction too, the way that now gaseous H_2 and dispersed O_2 are injected co-axial in accordance with the injector geometry (Figure 1). Concept #2 and #3 are assumed to be more realistic approaches to simulate axisymmetric single injectors, but less appropriate to simulate axisymmetric spray combustion within a multi-element combustor.

The Figures 2 and 3 show the computational mesh. After all, the mesh resolution still isn't fine enough to resolve the LOX post and the taper geometry and this, by the way, is assumed to be responsible for the fact that the onset of the combustion process, i.e. the anchoring of the flame front, is not captured closer to the wall in neither computation (see Figure 4).

Figure 4 reveals the temperature flowfield for all three initialisation concepts. As expected, concept #1 is not suited to resolve the flowfield phenomena in the vicinity of the injector. Best results, as far as we think to know, delivers us concept #2. Here, the flame front is clearly resolved and the flame angle coincide fairly well with that resulting from Abel-transformed emission imaging ($\approx 4°$). Moreover, the flame length seems to be realistic and compares well with what is known from experimental observations.

The alternative concept #3 looks alike, but mixture happens much sooner which leads to a much smaller combustion zone compared to concept #2. This is probably due to the specified inflow turbulence (5%), which could be too high. Reducing the incoming turbulence should lead to less diffusion and therefore to a flow field similar to concept #2. But what is more important here, is the fact that changing boundary conditions from wall to incoming mass flux condition, in order to simulate the gaseous H_2 inflow, have a dramatic effect on numerical stability and convergence behaviour. Especially the convergence criterion is only reached about a factor 10 later. Since we have to keep in mind the accessibility of the code to actual design problems with "overnight" reaction times demanded, it can be stated that this approach is far too time consuming and therefore ruled out for complex thrust chamber design applications.

As illustrated by other test case contributions, injection concept #3 is the standard for spray combustion codes. To elongate the (unrealistic) combustion zone, therefore, different correcting measures are applied. The most popular are to increase the LOX droplet injection velocities (SNECMA) or to split up the oxygen inflow into a liquid and a gaseous portion (CNES). Both measures, however, violate the inflow momentum ratio between fuel and oxidiser when a real gas approach is not taken into account. With concept #2, these boundary condition infringements could be avoided.

The OH mass fraction contours (Figure 5) give the same tendency. The development of the temperature profiles along the chamber towards the throat is shown in Figure 6. One can recognise different patterns at the start due to the different spray initialisation, which is not so much a surprise. The important point here to notice is the fact that these discrepancies will vanish after a certain distance. This becomes even more clear in Figure 7, where the (cross sectional averaged) axial temperature profiles are shown: the discrepancies exist at the start-up, but after about 0.2 m downstream, the temperature levels became very similar in all three computations. This ensures the applicability of the concept #1, i.e. it proves that one can satisfy industrial needs without resolving the flow phenomena in the injector near-field. Besides, to overcome the delayed combustion onset in concept #1, it may be suitable to reduce the O_2 - mass mean diameter and hence to adopt the spray characteristics to the assumed pre-mixed conditions.

Conclusion

The single element Mascotte test case RCM-3 has been calculated with Astrium's multi-phase Navier-Stokes code CryoROC. To take into account for thrust chamber applications' unusual single element configuration, three different propellant initialisation concepts, characterised by gaseous or dispersed hydrogen, pre-mixed or co-axial injection, have been applied and their results compared.

The concept #3 (gaseous H_2, co-axial) showed the worst convergence behaviour (about a factor 10) and is therefore ruled out for complex thrust chamber simulations. The flame could be resolved best by the concept #2 (dispersed H_2, co-axial), but as it is shown, the far-field of the injector is only slightly affected by the individual

spray initialisation concept and this outlines the applicability of concept #1 (dispersed H_2, pre-mixed) to complex thrust chamber simulations.

Note, that since there aren't any reliable experimental results available yet, a thorough assessment of the CFD results seems to be obsolete at this point.

References

[1] Knab O., Fröhlich A. and Wennerberg D.
Design Support for Advanced Storable Propellant Engines by ROCFLAM Analyses,
AIAA 99-2459, 1999.

[2] Preclik D., Estublier D. and Wennerberg D.
An Eulerian-Lagrangian Approach to Spray Combustion Modelling for Liquid Bi-Propellant Rocket Motors, AIAA 95-2779, 1995

[3] Preclik D., Wiedmann D., Oechslein W. and Kretschmer J.
Cryogenic Rocket Calorimeter Chamber Experiments and Heat Transfer Simulations,
AIAA 98-3440, 1998

[4] Wennerberg D., Knab O.
Effective Calculation of Multiphase flow Fields in Liquid Rocket Thrust Chambers,
AIAA-2001-3407, 2001
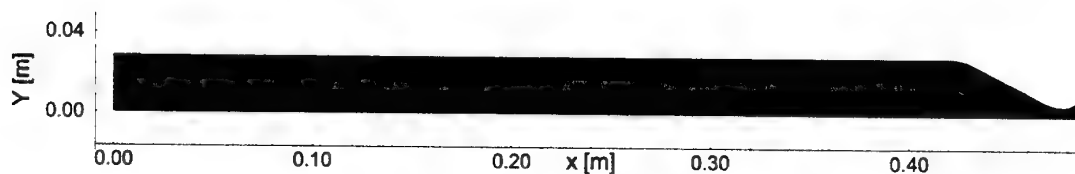
Figure 2:   Computational Mesh 512x101
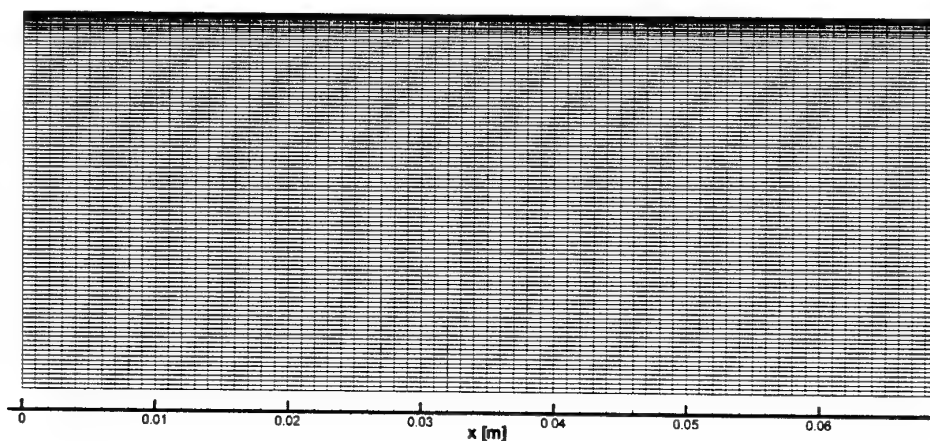
Figure 3:   Zoom of the Computational Mesh, Injector Near-Field and Boundary Layer
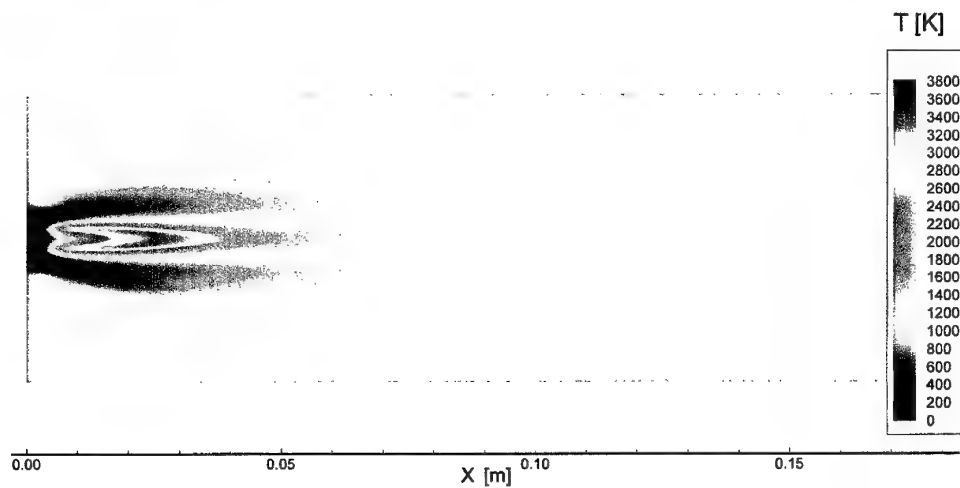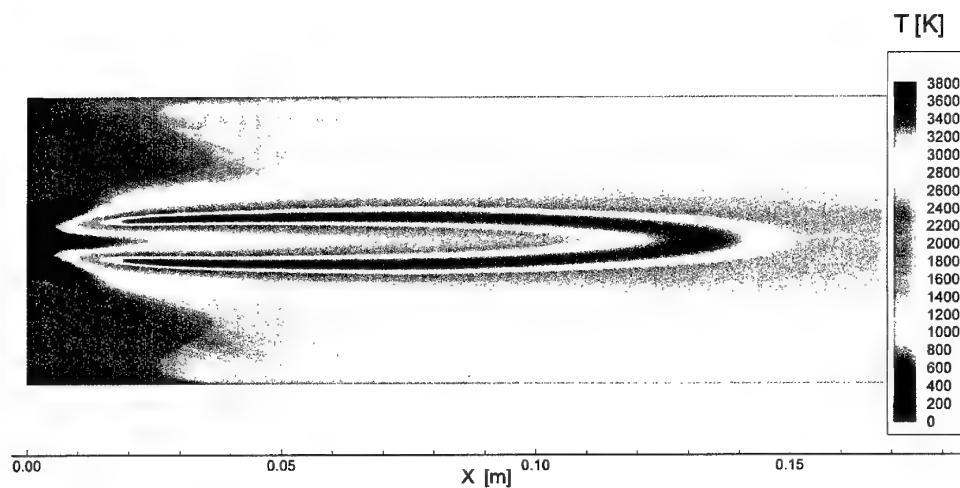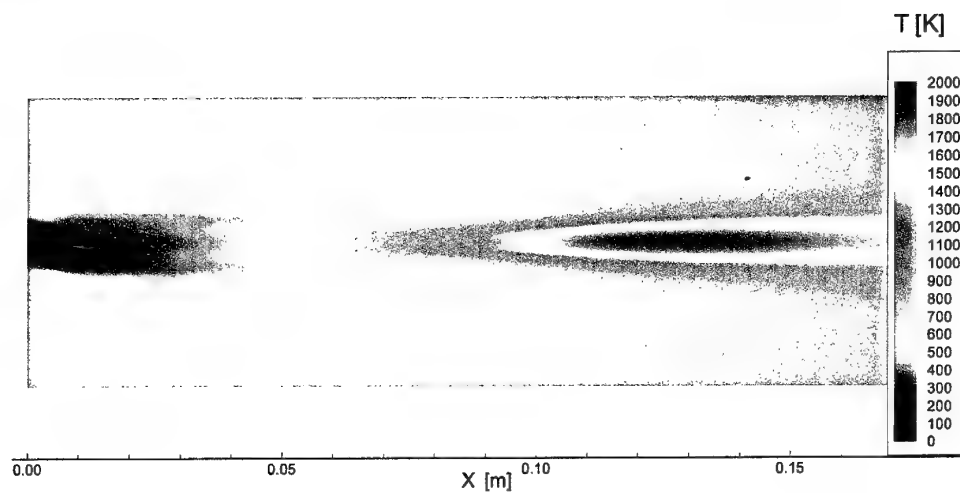
Figure 4: Temperature Contours for Spray Initialisation Concept 1 (top), 2 (middle) and 3 (bottom)
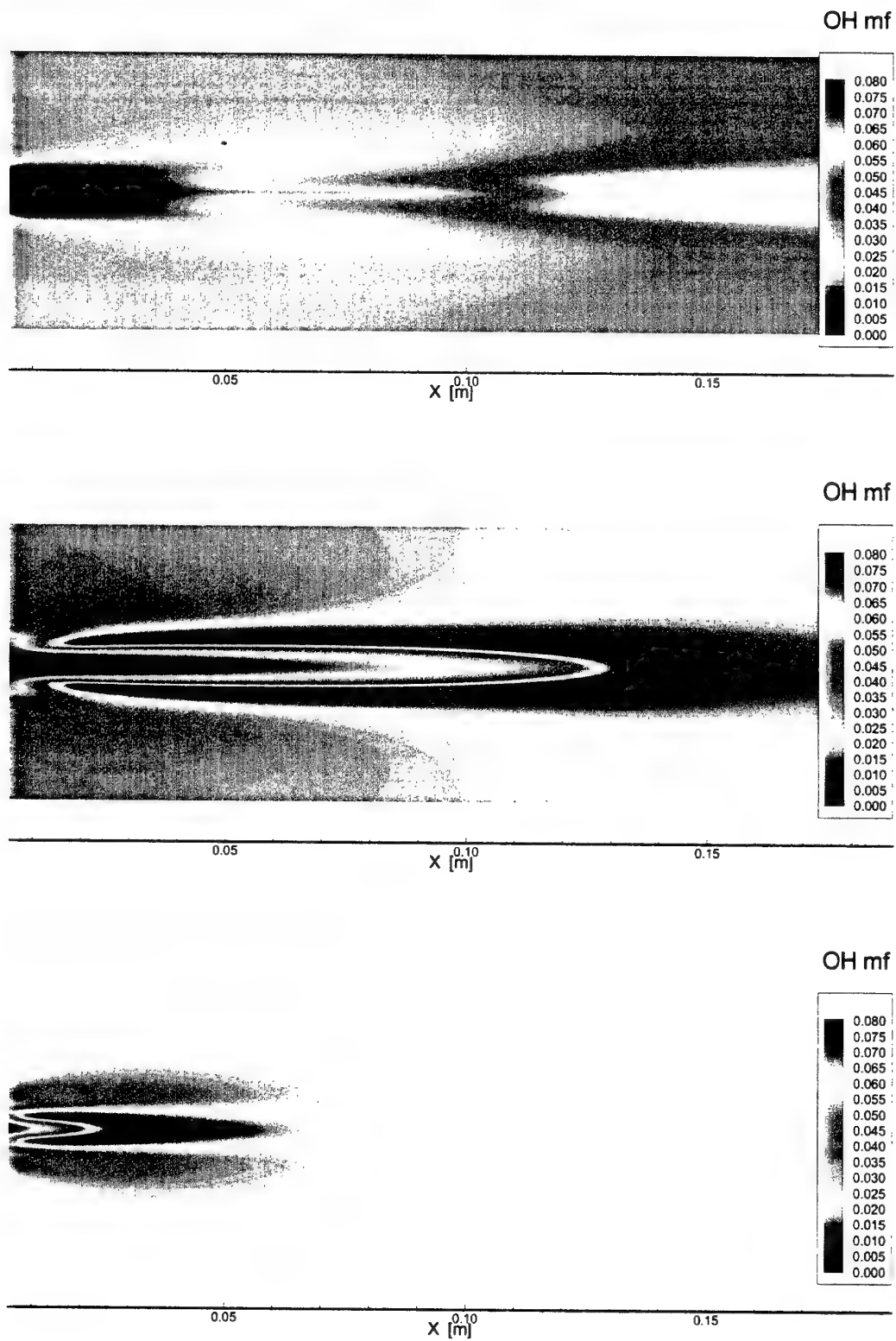
Figure 5:   OH Mass Fraction Contours for Concept 1 (top), 2 (middle) and 3 (bottom)
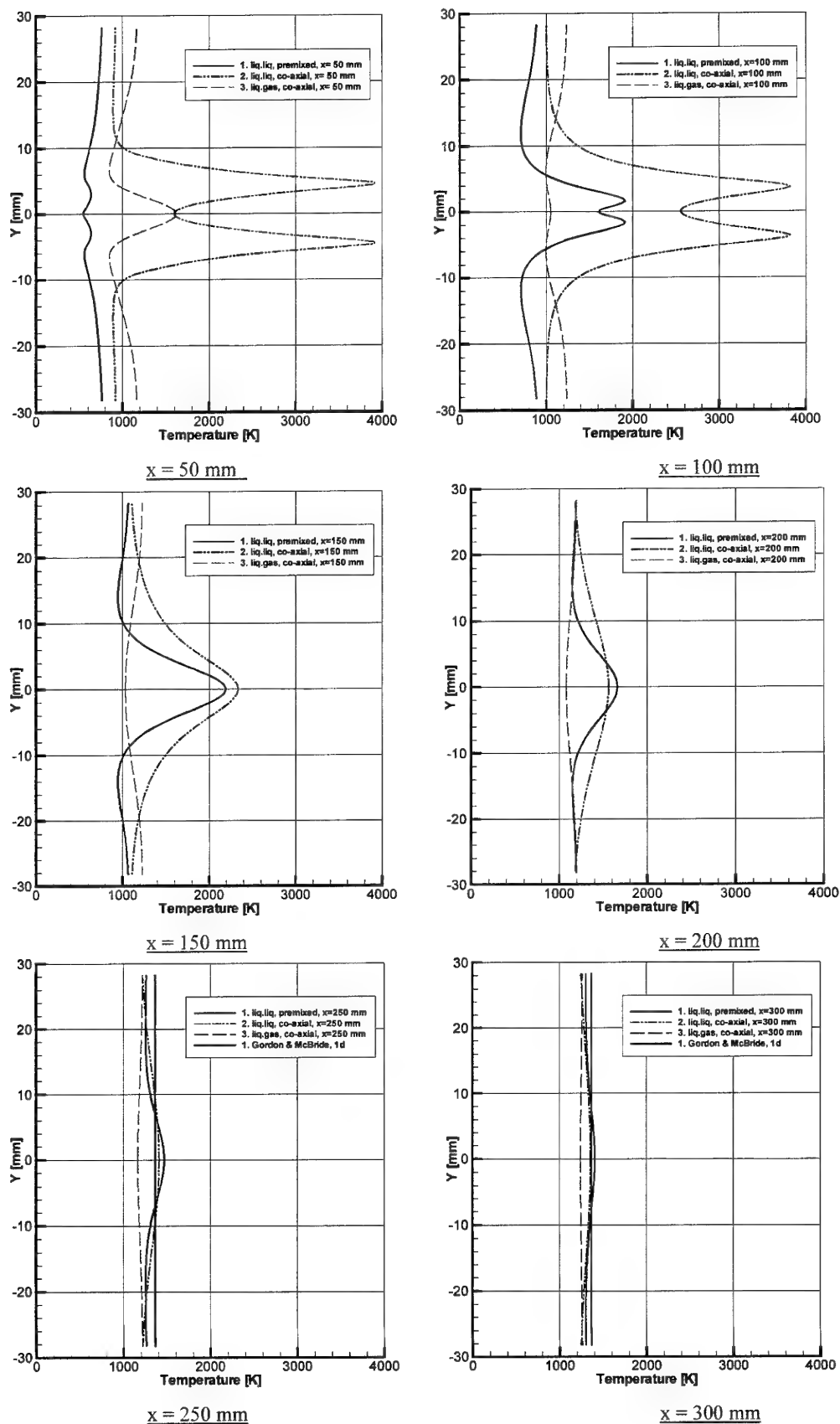
x = 50 mm

x = 100 mm

x = 150 mm

x = 200 mm

x = 250 mm

x = 300 mm

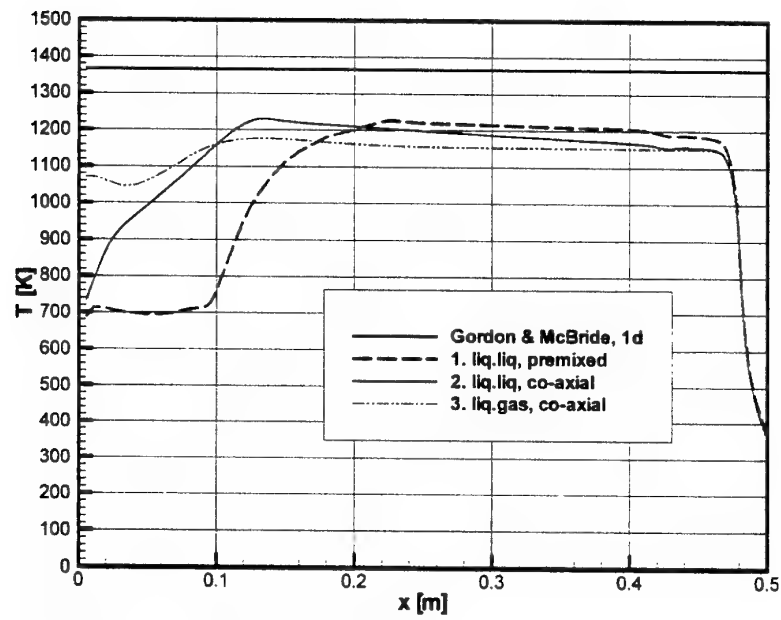Figure 6:   Temperature Profiles at Different Axial Locations

Figure 7: Cross Sectional Averaged Temperature Profiles

Rocket Combustion Modelling
Test Case RCM-3
*

Numerical calculation of MASCOTTE 60 bar case with THESEE

A. Depoutre, S. Zurbach, D. Saucereau, J.P. Dumont
SNECMA Moteurs

E Bodèle, I. Gökalp
LCSR

Introduction

This paper presents the numerical simulation of the RCM-3 test case done by Snecma and LCSR. The specified inlet conditions and computational options are described in the paper. A brief discussion about the main results is also given.

Operating point

The MASCOTTE operating point to be simulated was given by the workshop specifications. It is defined in the following table:

RCM-3			
Pressure	RM	$\dot{m}$ (LOX)	$\dot{m}$ (GH2)
60 bar	1,4	100 g/s	70 g/s

Numerical simulation

The code used to perform the calculation is a RANS code called THESEE. This solver enables the computation of 2D or 3D geometries with unstructured multi-element meshes. It can predict multiphase, multispecies turbulent reactive flows under steady or unsteady condition. The numerical scheme is based on a finite volume formulation for the Navier-Stokes equations.

The calculation was performed with the following assumptions:
- Compressible reactive flow
- Standard k - ε turbulence model
- EBU combustion model
- Unsteady and fully coupled lagrangian droplet tracking
- Evaporation rate estimated by the Delplanque-Sirignano model
- Ideal gas law with variable thermodynamics
- Variable thermodynamic properties for the droplets

Three different gaseous species were considered: H_2, O_2, H_2O and one liquid specie: liquid oxygen. The gaseous phase and the liquid phase are solved in the same time, in a coupled manner. We assumed variables thermodynamic properties for the four species and a single chemical reaction (H_2O):

$$H_2 + 1/2\ O_2 \rightarrow \text{Products } (H_2O + \text{dissociation})$$

It should be noticed that the Cv of the third specie H2O was corrected to take into account the dissociation processes occurring at high temperature in order to avoid an overestimation of the adiabatic flame temperature.

All gaseous properties, μ (viscosity) and λ (conductivity) are functions of the temperature. For the liquid oxygen, the variations due to the temperature for the Cp, μ, Hvap (enthalpy of vaporisation) , ρ (density), σ (surface tension) and Yos (gaseous oxygen mass fraction on the droplet surface) were also taken into account.

The numerical options are the following :
- 2D axi symmetric computation
- Unstructured hexahedrons mesh
- ALE scheme for the two-phase flow
- Explicit convection 2nd order

Geometry and grid

The computation was performed on a 2D axisymmetric geometry consisting of a 20° slice (length 400 mm, radius 25 mm) of the chamber. The nozzle was not modelled and so we assumed a constant pressure in the chamber. The computational domain ends at the exit of the cylindrical combustor at x = 400 mm.
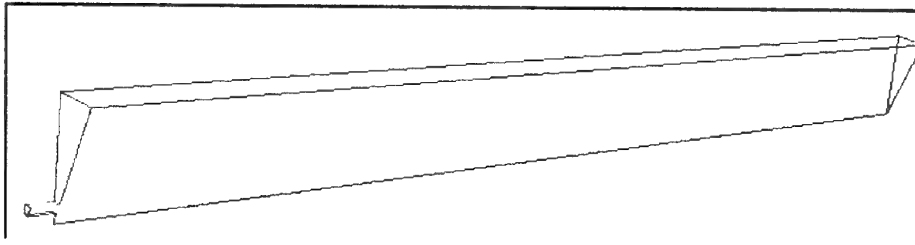
Geometry of the simulation

We use an unstructured hexahedrons mesh of 5373 cells.

Unstructured hexahedrons mesh

Inlet boundary condition

GH2

LOX
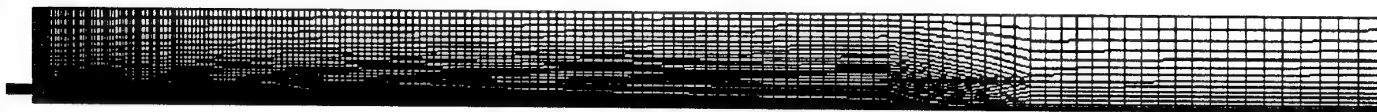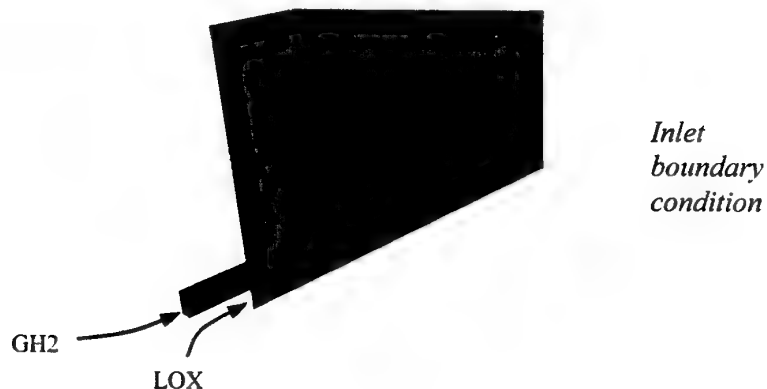
Boundary conditions

Hydrogen injection: Gaseous hydrogen was injected through the annular injector. This inflow is subsonic and the total temperature and mass flow rate were specified.

Oxygen injection: Droplets were injected in the axial direction through a porous wall, with a random position, as required in the RCM3 specification. The injection droplet velocity was increased to 20 m/s to avoid droplet accumulation in the recirculation zone behind the lox inlet. We chose a macro-droplet weight equal to 10 to reduce the total number of physical droplets.

Exit area: As the nozzle was not considered, the outflow is subsonic and the outlet conditions are determined by fixing the static pressure.

Boundary conditions		
Hydrogen inlet	Droplet injection	Outlet
$\dot{m} = 70$ g/s T = 287 K P = 60 bar V = 236 m/s	$\dot{m} = 100$ g/s T = 85 K V = 20 m/s Macro-droplet weight = 10 Size D32 = 50 µm	P = 60 bar $Y_{H_2} = 0.344$ $Y_{O_2} = 0$ $Y_{H_2O} = 0.656$

Walls : Slip conditions were used and the combustion chamber walls are assumed to be adiabatic.

Initial condition

The combustion chamber is initialised with hydrogen at 287 K.

Results

The total CPU time necessary to obtain the converged was about 180 hours. The calculation was performed with the Delplanque-Sirignano evaporation rate model without stripping.

The velocity fields in Fig.1 and 2 exhibit a deviation of the hydrogen jet due to atomisation and combustion. A recirculation zone is located between the injector and the upper and lower walls. This recirculation contains about 70% of gaseous hydrogen, 30% of water vapour and no gaseous oxygen (see Fig. 5, 6 and 7). The temperature in the recirculation is about 900 K (Fig. 3).

Figures 9 and 10 show the mean reaction rate field. The flame length is about 230 mm. Figure 10 shows three characteristic structures of a cryogenic flame :

- A first expansion cone of length $L_1 = 15 \times$Dlox. This zone is the longest one and its expansion is weak.
- A second expansion zone of length (L2-L1) with L2 = 19×Dlox. This zone is shorter than the first one, but its expansion is higher due to the recirculation zone and the attachment point.
- A confining zone where the flame ends and parabolic temperature profiles.

The temperature fields (Fig.3) give an estimation of the flame position and length. Assuming a "mixed is burnt" type model, the flame is attached to the injector tip. The maximum mean temperature is about 3600 K and the outlet averaged temperature is about

1600 K. This result can be compared to the temperature computed by an equilibrium code , minimising the Gibbs free energy ;for RM 1.4,the equilibrium temperature is equal to the 1580 K.

The mean mass fraction fields are presented on figures 5, 6 and 7. The outlet H2O fraction integrated on the outlet is about 0.66 (Fig.8). This value is similar to the equilibrium one at RM 1.4 and equal to 0.656.

Figures 11, 12 and 13 are the prediction of the velocity, temperature and droplet diameter fields.

Compared to the available experimental data of fig 14 and 15, the global structure of the flame is therefore correctly represented, particularly on the observed attachment point due to the combustor confinement and the corresponding recirculation effect. Also, the initial angle of the flame is close to the experimental data. However, there is a discrepency between the calculation and the observed length of the flame, certainly due to the choice made on the drop size and initial velocity.

Conclusion

The numerical computation of the 2D axisymmetric MASCOTTE configuration at RCM-3 operating point was presented.

At 60 bars, the liquid oxygen is fully consumed in the chamber and the global structure of the flame is correctly represented. However, the computed flame length is longer than the experimental data. This phenomenon is due to the droplets injection velocity which has been increased to 20 m/s to avoid accumulation of droplets downstream of the porous wall injection. It was the biggest difficulty we have encountered in our simulations and a solution would be to simulate the droplets injection boundary condition from a potential cone.

Moreover, we don't consider stripping in the evaporation rate model, and this approach could affect the length of the flame. It is also clear that a lagrangien model is not ideal for such type of high pressure simulation and that a real fluid modelization would be better suited. Finally, more experimental measurements should be available and compared in detail with calculation results.
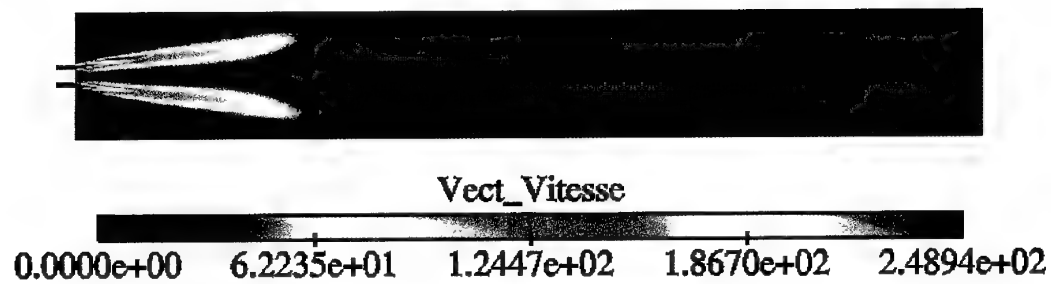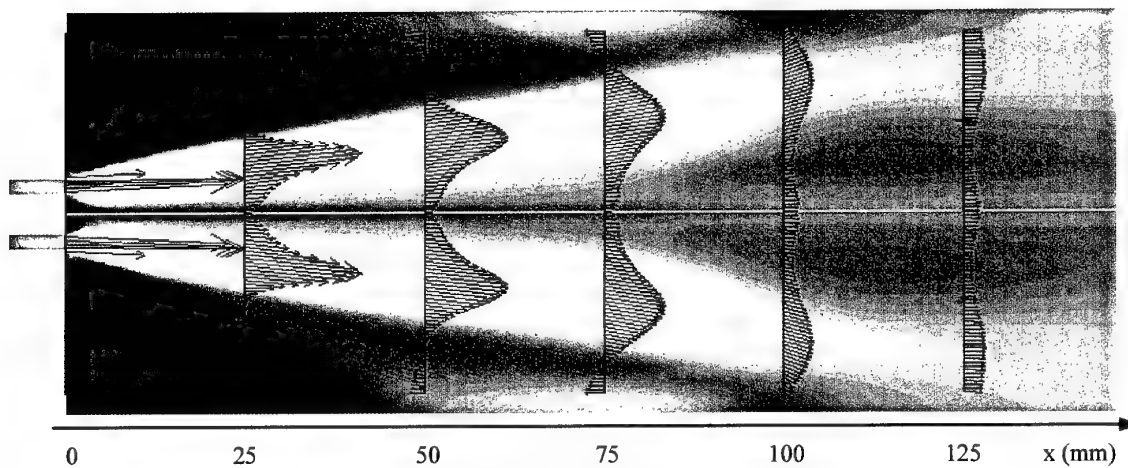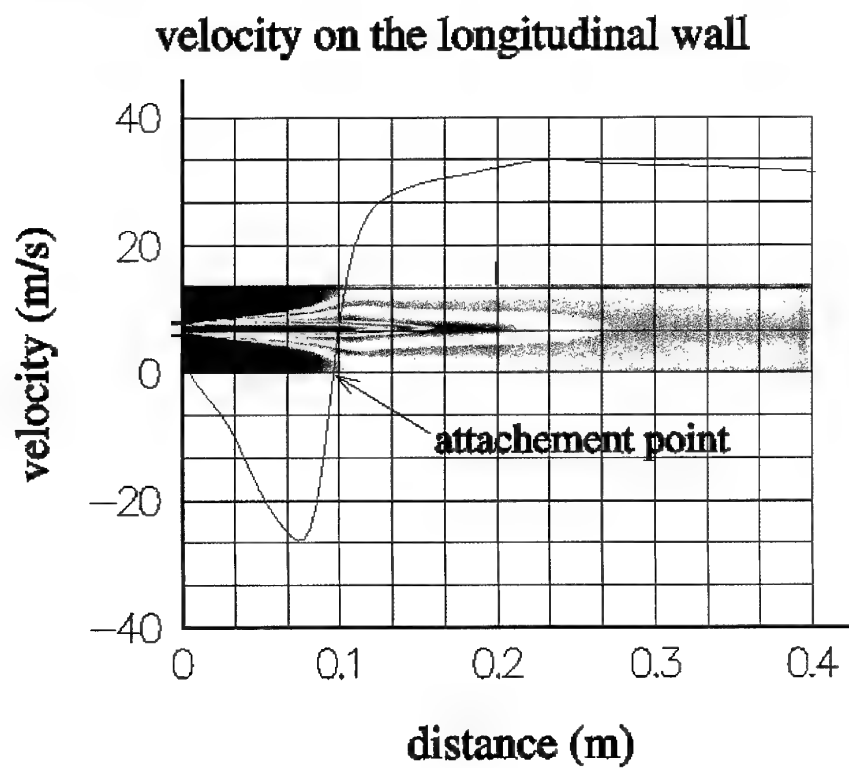
Vect_Vitesse

0.0000e+00   6.2235e+01   1.2447e+02   1.8670e+02   2.4894e+02

Fig. 1: Contours of velocity (m/s)
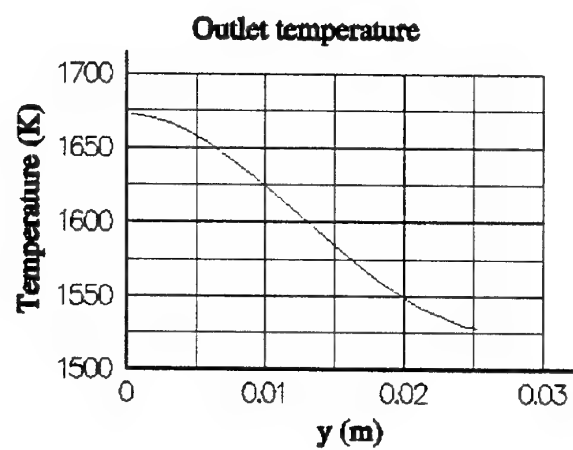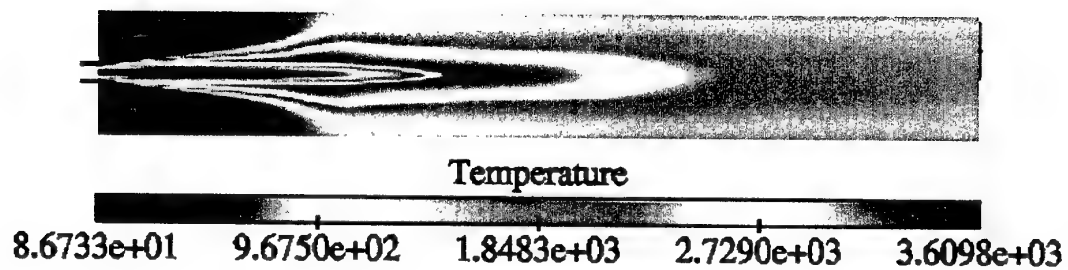

Fig. 2: Field and profiles of velocity vectors

velocity on the longitudinal wall

attachement point

distance (m)

Temperature

8.6733e+01   9.6750e+02   1.8483e+03   2.7290e+03   3.6098e+03

Fig. 3: Mean temperature fields (K)

10 mm   50 mm   100 mm   150 mm   200 mm
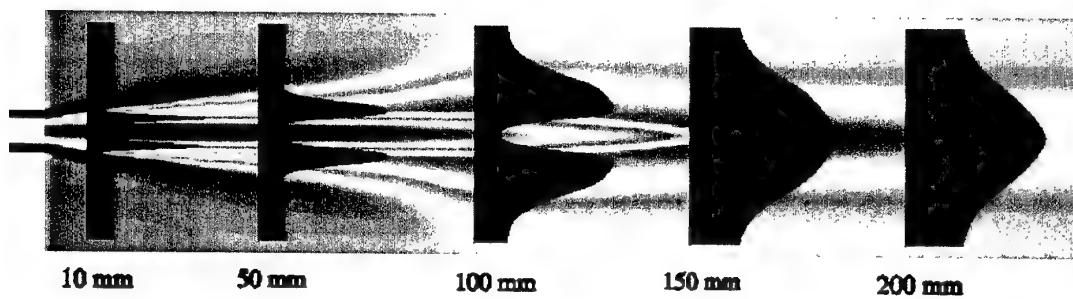
Fig. 4: Field and Radial Temperature profiles
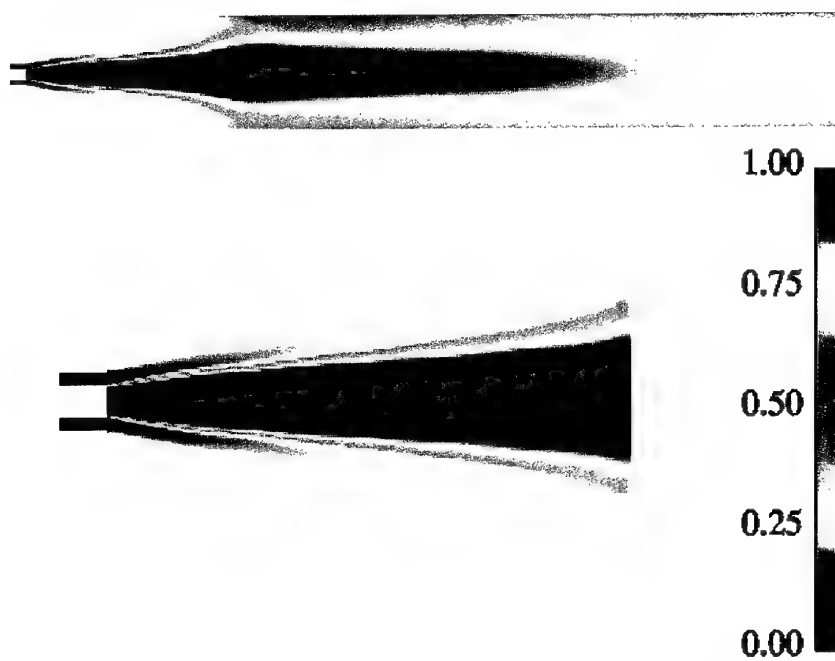
Fig. 5: Gaseous Hydrogen mass fraction fields
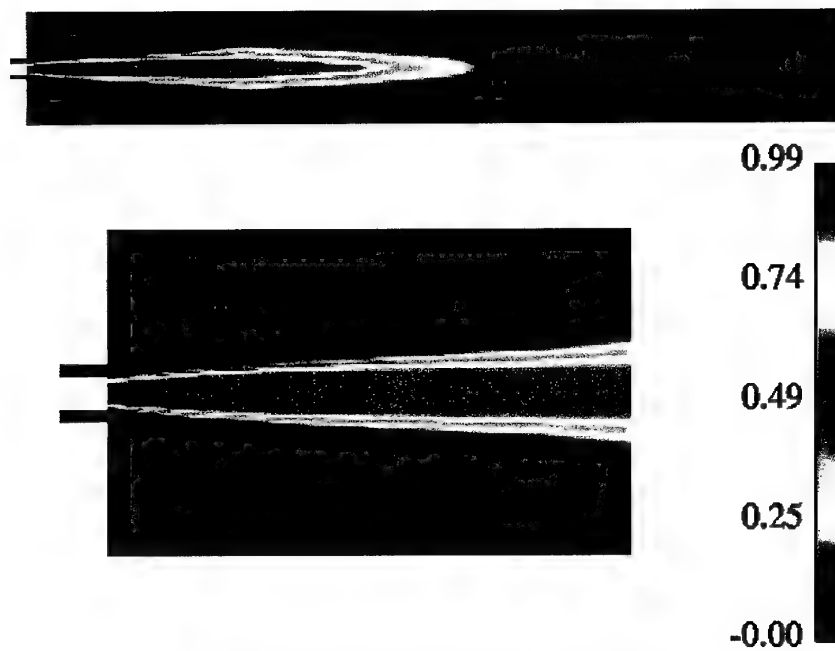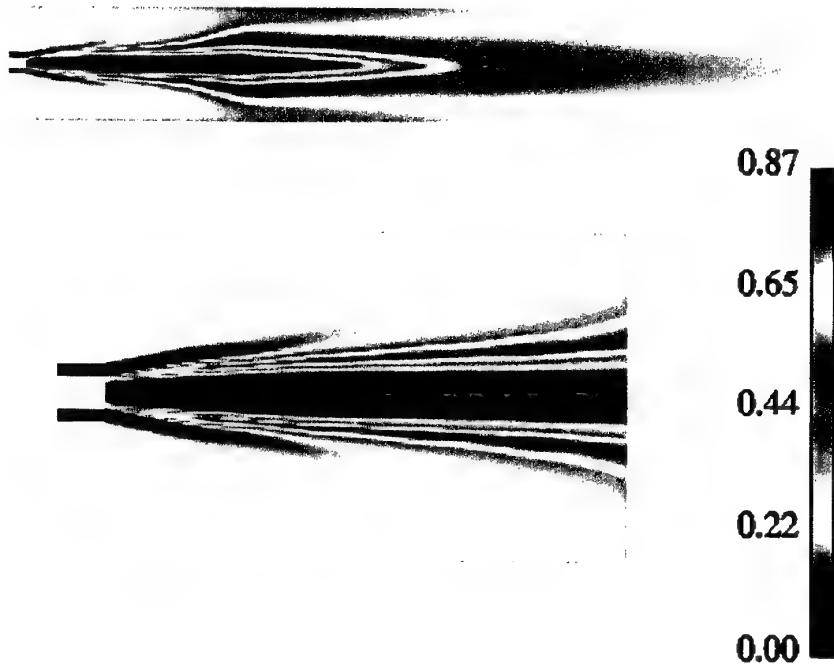

Fig. 6: Gaseous Oxygen mass fraction fields

Fig. 7: Water Vapour mass fraction fields
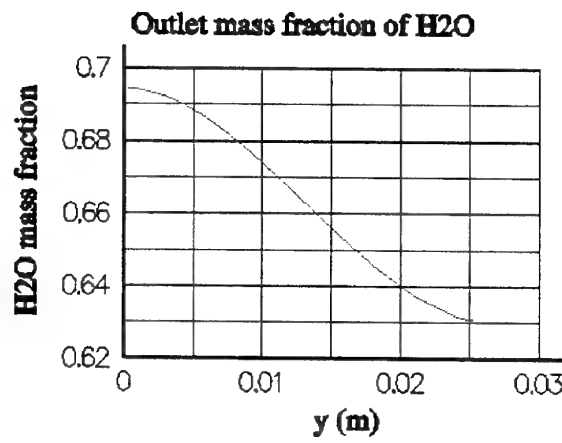

Fig. 8: Axial Water mass fraction at the outlet plane
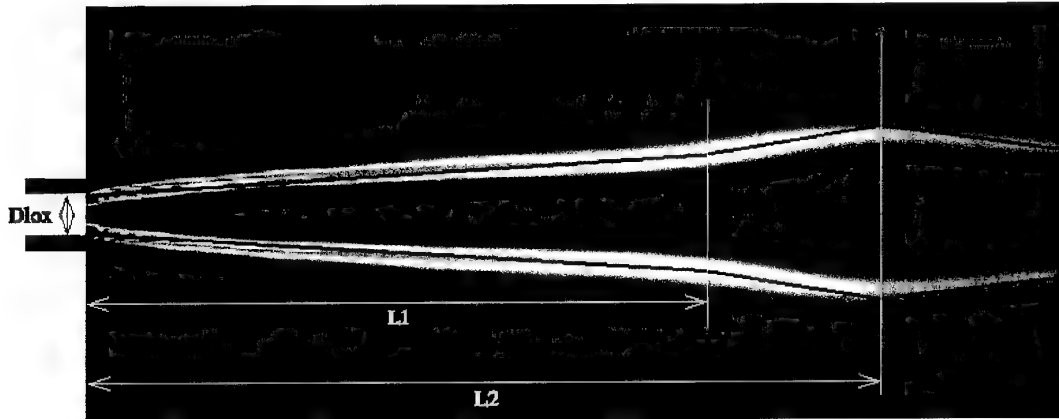
Fig. 9: Mean reaction rate fields

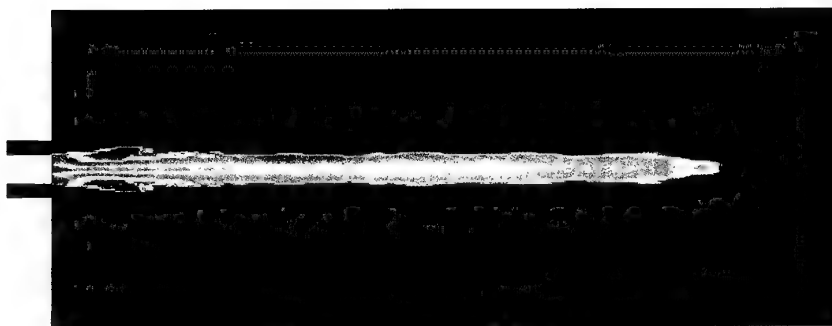*Fig. 10: Characteristic Flame Structure*

Fig. 11: Droplet Velocity field (m/s)

0.000E+00
2.198E+00
4.396E+00
6.868E+00
9.066E+00
1.126E+01
1.374E+01
1.593E+01
1.813E+01
2.061E+01
2.280E+01
2.500E+01
2.747E+01
2.967E+01
3.187E+01
3.407E+01
3.654E+01
3.874E+01
4.121E+01
4.341E+01
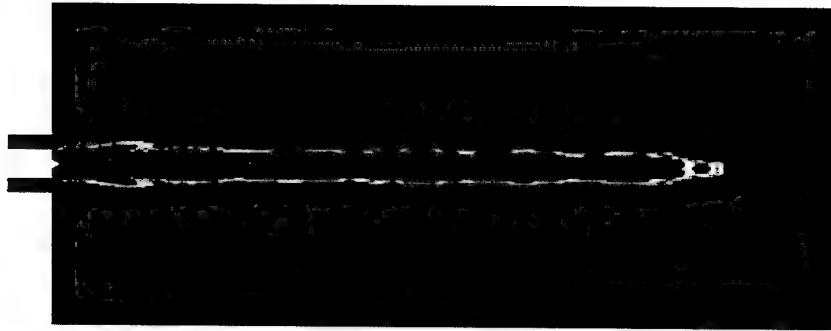4.561E+01
4.808E+01
5.028E+01
5.247E+01

Fig. 12: Droplet Temperature field (K)

0.000E+00
6.215E+00
1.243E+01
1.942E+01
2.564E+01
3.185E+01
3.884E+01
4.506E+01
5.127E+01
5.827E+01
6.448E+01
7.070E+01
7.769E+01
8.390E+01
9.012E+01
9.633E+01
1.033E+02
1.095E+02
1.165E+02
1.227E+02
1.290E+02
1.360E+02
1.422E+02
1.484E+02
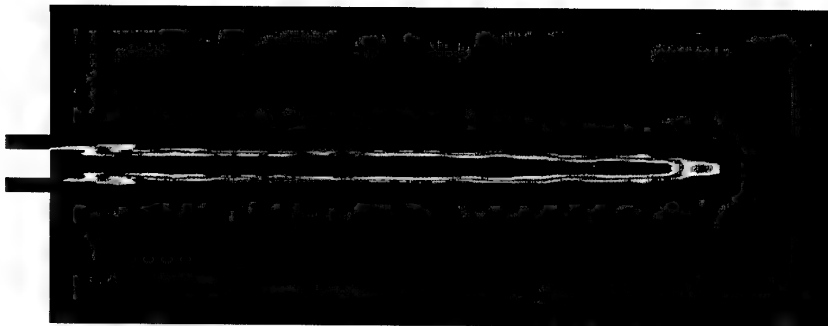
Fig. 13: Droplet Diameter field (m)

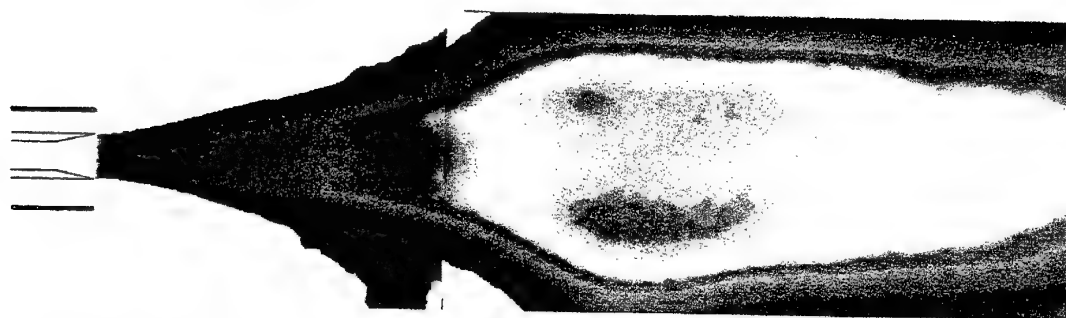| |
|---|
| 0.000E+00 |
| 2.349E-06 |
| 4.697E-06 |
| 7.339E-06 |
| 9.688E-06 |
| 1.204E-05 |
| 1.468E-05 |
| 1.703E-05 |
| 1.938E-05 |
| 2.202E-05 |
| 2.437E-05 |
| 2.672E-05 |
| 2.936E-05 |
| 3.171E-05 |
| 3.405E-05 |
| 3.640E-05 |
| 3.905E-05 |
| 4.139E-05 |
| 4.404E-05 |
| 4.638E-05 |
| 4.873E-05 |
| 5.138E-05 |
| 5.372E-05 |
| 5.607E-05 |

Figure 34: Image d'émission du radical OH^* dans l'UV. 11/03/99, 1er tir et 25/03/99. 1er tir. Point de fonctionnement A. Pression 69 bars. Injecteur sans retrait. Ouverture = 4,5.Gain = 150. Filtrage = 1 UG5, 1 WG305, 1 FNQ027, 1 FNQ015. 1 FNQ007. Durée d'exposition = 3760 μs. Image non normalisée

Fig.14: Experimental data OH emission

Figure 40: Image par la transformée d'Abel d'émission du radical OH^* dans l'UV. 11/03/99, 1er tir et 25/03/99, 1er tir. Point de fonctionnement A. Pression 69 bars. Injecteur sans retrait. Ouverture = 4,5.Gain = 150. Filtrage = 1 UG5, 1 WG305, 1 FNQ027, 1 FNQ015, 1 FNQ007. Durée d'exposition = 3760 μs. Image non normalisée

Fig.15: Experimental data OH emission (Abel transformed)

CFD SIMULATION OF LIQUID ROCKET ENGINE INJECTORS
Part 3. SIMULATIONS OF THE RCM-3 EXPERIMENT

Richard Farmer & Gary Cheng
SECA, Inc.

Yen-Sen Chen
ESI, Inc.

INTRODUCTION

Detailed design issues associated with liquid rocket engine injectors and combustion chamber operation require CFD methodology which simulates highly three-dimensional, turbulent, vaporizing, and combusting flows. The primary utility of such simulations involves predicting multi-dimensional effects caused by specific injector configurations. SECA, Inc. and Engineering Sciences, Inc. have been developing appropriate computational methodology for NASA/MSFC for the past decade. CFD tools and computers have improved dramatically during this time period; however, the physical submodels used in these analyses must still remain relatively simple in order to produce useful results. Simulations of clustered coaxial and impinger injector elements for hydrogen and hydrocarbon fuels, which account for real fluid properties, is the immediate goal of this research. The spray combustion codes are based on the FDNS CFD code[1] and are structured to represent homogeneous and heterogeneous spray combustion. The homogeneous spray model treats the flow as a continuum of multi-phase, multicomponent fluids which move without thermal or velocity lags between the phases. Two heterogeneous models were developed: (1) a volume-of-fluid (VOF) model which represents the liquid core of coaxial or impinger jets and their atomization and vaporization, and (2) a Blob model which represents the injected streams as a cloud of droplets the size of the injector orifice which subsequently exhibit particle interaction, vaporization, and combustion. All of these spray models are computationally intensive, but this is unavoidable to accurately account for the complex physics and combustion which is to be predicted. Work is currently in progress to parallelize these codes to improve their computational efficiency.

These spray combustion codes were used to simulate the three test cases which are the subject of the 2nd International Workshop on Rocket Combustion Modeling. Such test cases are considered by these investigators to be very valuable for code validation because combustion kinetics, turbulence models and atomization models based on low pressure experiments of hydrogen air combustion do not adequately verify analytical or CFD submodels which are necessary to simulate rocket engine combustion.

We wish to emphasize that the simulations which we prepared for this meeting are meant to test the accuracy of the approximations used in our general purpose spray combustion models, rather than represent a definitive analysis of each of the experiments which were conducted. Our goal is to accurately predict local temperatures and mixture ratios in rocket engines; hence predicting individual experiments is used only for code validation. To replace the conventional JANNAF standard axisymmetric finite-rate (TDK) computer code[2] for performance prediction with CFD cases, such codes must posses two features. Firstly, they must be as easy to use and of comparable run times for

conventional performance predictions. Secondly, they must provide more detailed predictions of the flowfields near the injector face. Specifically, they must accurately predict the convective mixing of injected liquid propellants in terms of the injector element configurations.

HOMOGENEOUS SPRAY COMBUSTION MODEL

The homogeneous spray combustion CFD codes utilize very general thermodynamics in a conventional CFD code. The heterogeneous codes (described in Part 2) use tabulated properties for the liquid phase and ideal gas properties for the vapor phase. Thermal and caloric equations of state, vapor pressure, heat of vaporization, surface tension, and transport properties are modeled with the equations of state proposed by Hirshfelder, et al[3,4] (we term these the HBMS equations of state) and with conventional correlations,[5] for the other properties. The property correlations used were not chosen for their absolute accuracy, but for their validity over a wide range of temperatures and pressures and for requiring a minimum of data to describe a particular species. These correlations are explicit in density and temperature.

HBMS thermal equation of state:

$$\frac{P}{P_c} = \sum_{j=1}^{4} T_r^{j-2} \sum_{i=1}^{6} B_{ij} \; \rho_r^{i-2} \; ; T_r = \frac{T}{T_c} \; ; \rho_r = \frac{\rho}{\rho_c}$$

HBMS caloric equation of state:

$$\frac{H - H_0}{RT} = Z_c \int_0^{\rho_r} \left[\frac{P}{T_r} - \left(\frac{\partial P}{\partial T_r} \right)_{\rho_r} \right] \rho_r^{-2} \, d\rho_r \; + \; Z_c \; \frac{P}{\rho_r T_r} \; - \; 1$$

These equations are based on the "theorem of corresponding states" for real fluids, which essentially means that the p-v-T relations for all species are similar if these variables are normalized with their values at the critical point, i.e. if reduced values are used. The reduced values in these equations are indicated with a subscript r. H_0 is the ideal gas species enthalpy. Z_c is the compressibility for a given species at the critical point. The HBMS equations are attractive to use because arbitrary correlations for vapor pressure, heat of vaporization, and liquid densities can be used. Since multi-component fluid/vapor mixtures may be present in the flowfield, the mixture properties are calculated by the additive volume method. This means that multiphase mixtures are treated as ideal solutions. For H_2/O_2 propellants under conditions where the species become ideal gases, the thermodynamic data from the CEC code[6] were used.

The combustion reactions used in the simulations reported herein are shown in Table 1. Not all of the reactions were used in all of the combustion simulations. Elementary rate data for these reactions are reported by Gardner, et al[7,8]. Such data are empirical and were obtained for hydrogen/air combustion, under conditions far different from those encountered in rocket engines.

2

Table 1. Combustion Model for H_2/O_2 Reaction

Chain initiation:
$H_2 + O_2 = 2OH$
$1.86\ H_2 + O_2 = 1.645\ H_2O + 0.067\ O + 0.142\ H + 0.288\ OH$
Chain Branching:
$H_2 + OH = H_2O + H$
$2\ OH = H_2O + O$
$H_2 + O = H + OH$
$O_2 + H = O + OH$
Chain termination:
$O + H + M = OH + M$
$2\ O + M = O_2 + M$
$2\ H + M = H_2 + M$
$OH + H + M = H_2O + M$

The CFD solver used was the Finite-Difference Navier-Stokes code with provision for using real fluid properties, the FDNS-RFV code. This code is pressure based; it differs from an ideal gas code in the methodology used to relate the pressure correction to the continuity equation and of course in the properties subroutines used. The pressure correction (p') equation used in the FDNS-RFV code is:

$$\frac{\beta_p\ p'}{\Delta T}\ \Delta \bullet (u_i \beta_p p')\ -\ \Delta \bullet (\rho^* D_p \Delta\ p')\ =\ -\Delta \bullet (\rho^* u_i)\ -\ \frac{\rho^* - \rho^n}{\Delta t}$$

$$p^{n+1} = p^n + p'\ ;\quad \beta_p = \gamma\!\big/\!{a^2}\quad ;\quad u_i \approx -D_p\ \Delta p'$$

where the superscripts * and n denote the value at the intermediate and previous time steps, respectively. D_p is the inverse of the matrix of the coefficients of the convective terms in the finite-difference form of the inviscid equations of motion. This is not an obvious definition, but is one which has made the FDNS-RFV code a useful solver. The sound speed used in the pressure correction equation is that calculated for the real fluid multi-component mixture.

In all cases simulated, a k-ε turbulence model was used to close the mass averaged transport equations solved by the code. Our experience is that this incompressible turbulence model overestimates the mixing in a combusting flowfield. However, since the liquid propellants are also mixed by this model, we concluded that there are currently insufficient data to better tune the turbulence model. The homogeneous spray model has been used to simulate: (1) a single element like-on-like (LOL) impinger injector element and a single element unlike impinger element for the configuration and flow conditions used in the cold-flow experiments; (2) an ensemble of injector elements in the Fastrac engine; and (3) several configurations of the vortex engine currently being developed.[9]

RESULTS

The super-critical combustion case, RCM-3, was simulated with the homogeneous spray combustion model. Any drops present will be highly unstable; therefore, this model should represent the flow rather well. Local equilibrium and simplified finite-rate combustion submodels were used and the results for the two simulations compared well. More detailed combustion submodels were attempted, but proved to behave too poorly for successful simulations.

The preponderance of super-critical spray combustion models which have been reported have been extensions of sub-critical models. Such models encounter a basic problem in over emphasizing the role of surface tension. Since surface tension is zero for super-critical conditions, drops should not exist. Although such drops can be observed experimentally, they are extremely unstable and do not survive very long. The homogeneous CFD model was developed to account for the major physical effects which do exist. Namely, the large density and momentum differences which exist in multi-phase super-critical flows. Such a model allows one to accurately relate the inlet conditions at the injector face to boundary conditions for the CFD simulation. This relationship is essential to predicting the effects of injector element configuration and inlet momentum vector on the convective mixing and cross winds which occur in practical rocket engines. Otherwise, one is forced to use the historical method of creating costly experimental data bases from which to choose designs.

The injector configuration and flow conditions for the supercritical combustion of the RCM-3 test case are presented in Fig. 1. This is uni-element shear coaxial injector with LOX and GH_2 propellants. The numerical simulation was conducted with some simplification because, initially, detailed information was unavailable; such as: (1) the flare of LOX injector near the exit was neglected; (2) the injector was flush at the chamber head-end instead of protruding into the chamber because the outer diameter of hydrogen tube and distance between the chamber head-end and the injector exit were not known; (3) the nozzle was not included because of insufficient information about the chamber tail-end and nozzle geometry; and (4) the coolant (later found to be helium) for the chamber wall was not included because its flow rate and properties were not specified. As can been seen, the chamber pressure (60 bar) is well above the critical pressure of oxygen; hence, the homogeneous real-fluid model was used to simulate this test case. A two-zone mesh system (61x39 and 301x101) was used to model the injector section and the combustion chamber.

The combustion reactions in this high pressure experiment are expected to be in local thermodynamic equilibrium and were simulated as such. To demonstrate the methodology, two finite-rate simulations were also made with a subset of the reactions in Table 1. The single global reaction which produces radicals as well as water provides a good estimate of the temperature field. Its rate was set to attach the flame near the injector tip. Since the radicals are not rigorously simulated with the single reaction, a second finite-rate simulation was made with the 2-body reactions. Backward reaction rates are determined with equilibrium constants. A third finite-rate/equilibrium model was also tested. The finite-rate effects were described with the 9 elementary reactions in Table 1 with the combustion assumed to be in local equilibrium when the temperature was greater than some specified value. Temperatures of 1000 and 1500K were used for this switch point. Thus, the finite-rate effects would be considered near the injector and in the expansion section of the nozzle. This combustion model did not require an extremely tight grid near the injector tip to hold the flame. The simulation of the RCM-3 case with this model was very similar to the equilibrium combustion

4

model For high pressure cases such combustion modeling is essential to keep the computation stable.

The chemistry and turbulence models used in our simulations do not make use of probability density functions (PDFs) because most of the shear layers formed by the injector element should be continuum. The only regions for which this might not be the case are the intermittent edges of the shear layers. Pope[10] terms these regions the "viscous superlayer". The thickness of these layers are inversely proportional to the Reynolds number to the 0.75 power. For these high speed coaxial jets, they should be very thin.

The flow predicted at the injector tip is shown in Figure 2. The radial temperature profiles predicted at several axial stations are shown in Figure 3. The axial profiles at several radial locations are shown in Figure 4. The temperature and oxygen and OH concentration profile fields are shown in Figure 5. The combustion models used do not predict chemiluminescent OH, which might be observed in the experiments. These results are shown for the equilibrium combustion model. Results for the finite-rate equilibrium combustion simulations are very similar, hence they are not shown. The wall temperature distributions for all four cases are compared in Figure 6, and as noted the results are very similar.

CONCLUSIONS

The following conclusions were drawn from performing CFD simulations of the three RCM test cases for the 2nd IWRCM.

1. A homogeneous and a heterogeneous spray combustion CFD models have been developed to simulate combustion in rocket engines. Since neither of these models is expected to be accurate until critical parameters are evaluated from test data, simulation comparisons to the MASCOTTE type experiments are needed.

2. The utility of either CFD model cannot be determined until values of critical parameters are determined and efforts to optimize the computational efficiency of the models are performed.

3. Although the CFD rocket engine models provide much more detailed information concerning the vaporization, mixing, and combustion process, their place in the design process is yet to be identified. Older more approximate rocket "performance" models are difficult to displace. Furthermore, every physical process thought to be present in the engine does not have to be modeled to create a useful design code. There are more knobs to adjust in the code than there are experimental data to justify their turning.

4. The experiments conducted in preparation for the 2nd IWRCM appear to be a significant first step in providing test data valuable to CFD modelers. However, blind comparisons of CFD model predictions to such data are premature. The CFD modelers have not previously had sufficient test data properly specify the many assumptions which are necessary to simulate such complex flows.

5. Better communication between analysts and experimenters needs to be accomplished. Can the modeler simulate the experiments which are being performed? Can the data obtained from the experiment critically test the model?

ACKNOWLEDGEMENTS

REFERENCES

1. Chen, Y.S., "Compressible and Incompressible Flow Computations with a Pressure Based Method," AIAA Paper 89-0286, 1989.

2. Nickerson, G.R., et al, "Two-Dimensional Kinetics (TDK) Nozzle Performance Computer Program," Vols. I-III, Rpt. No. SN91, Software and Engineering Associates, Inc., mar. 1989.

3. Hirschfelder, J.O., et al, "Generalized Equations of State for Gases and Liquids," IEC, 50, pp.375-385, 1958.

4. Hirschfelder, J.O., et al, "Generalized Excess Functions for Gases and Liquids," IEC, 50, pp.386-390, 1958.

5. Reid, R.C., et al, The Properties of Gases & Liquids, 4th ed, McGraw-Hill, 1987.

6. Gordon, S., and B.J. McBride, "Computer Program for Calculation of Complex Chemical Equilibrium Compositions, Rocket Performance, Incident and Reflected Shocks, and Chapman-Jouget Detonations," NASA-SP-273, 1971.

7. Gardiner, W.C., Jr., Combustion Chemistry, Springer-Verlag, 1984.

8. Gardiner, W.C., Jr., Ed., Gas-Phase Combustion Chemistry, Springer, 1999.

9. Farmer, R.C, G. Cheng, H. Trinh, and K. Tucker, "A Design Tool for Liquid Rocket Engine Injectors," AIAA 2000-3499, 2000.

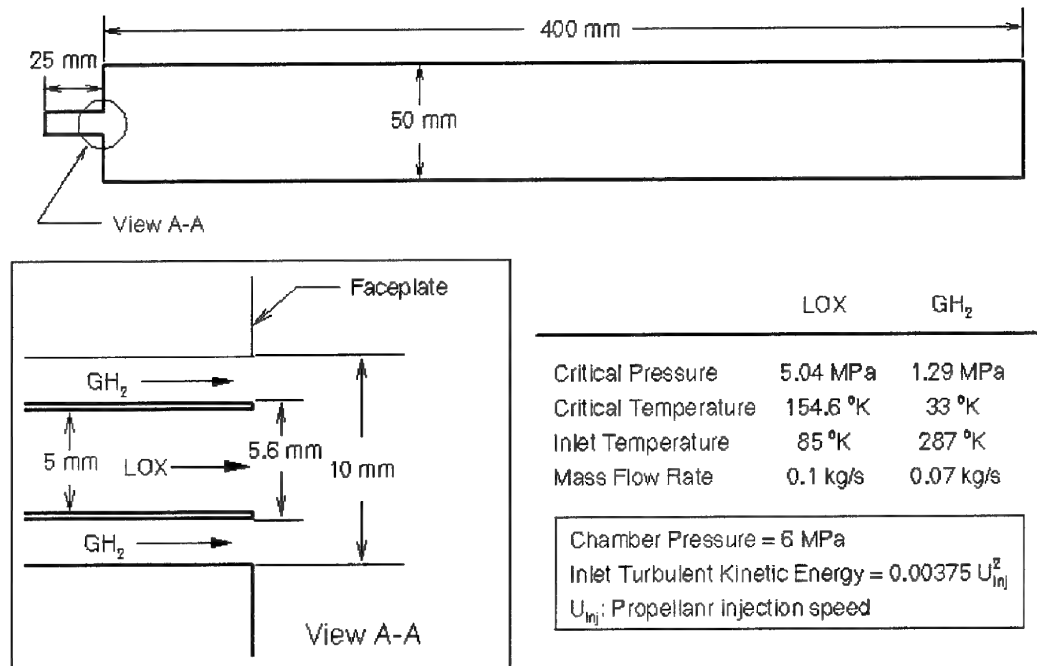10. Pope, S.B., Turbulent Flows, Cambridge, 2000.

Figure 1. Configuration of the RCM-3 Case (Homogeneous Spray Model).

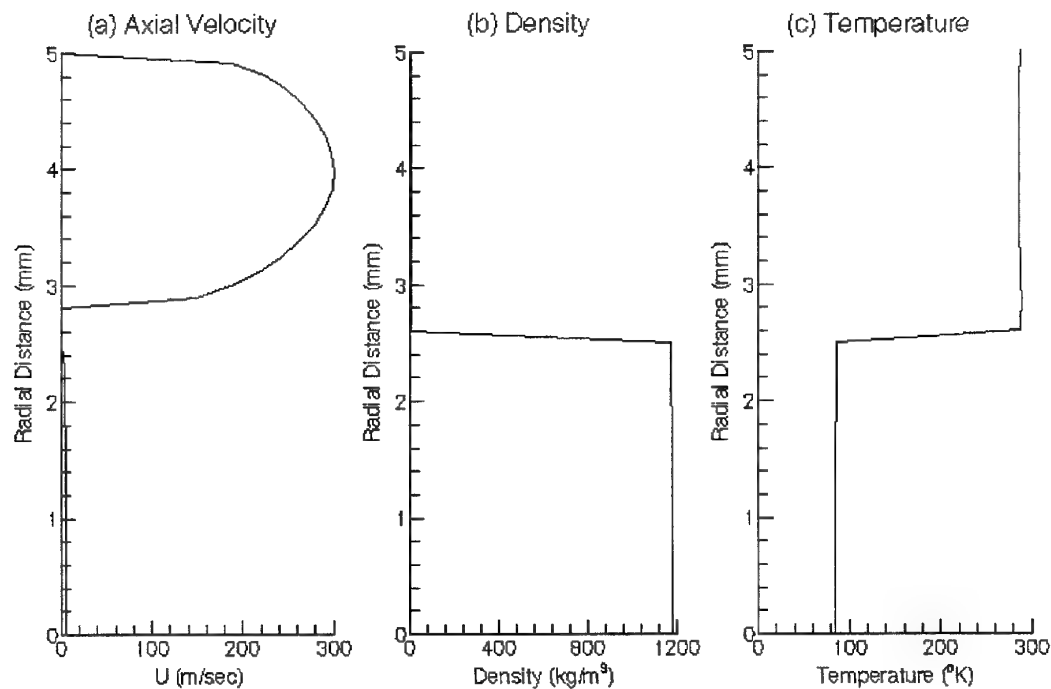(a) Axial Velocity (b) Density (c) Temperature

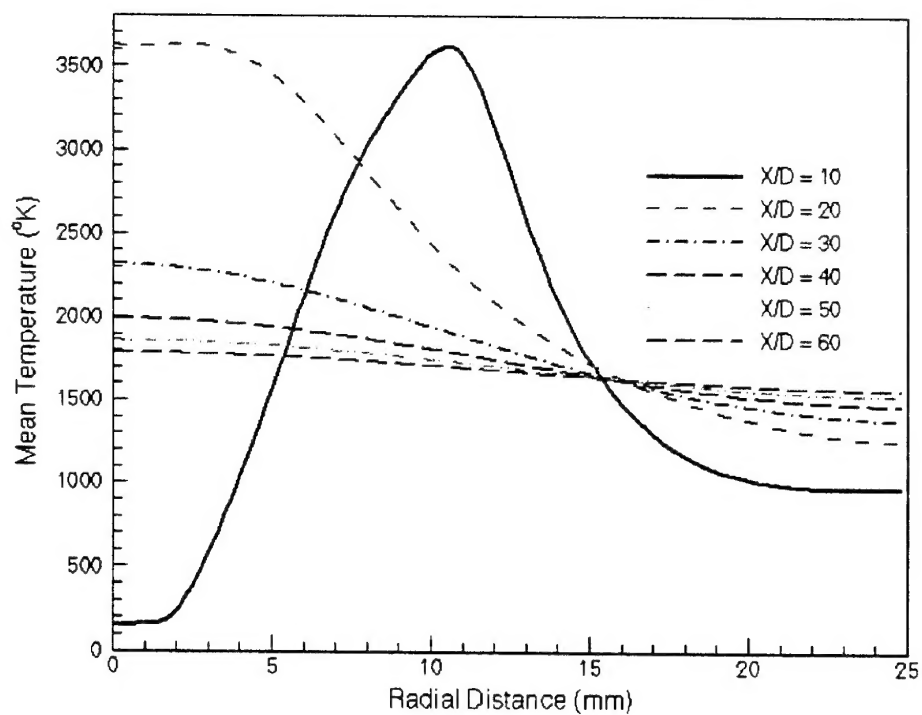Figure 2. Flow Properties at the Injector Exit of RCM-3 (Homogeneous Spray Model).

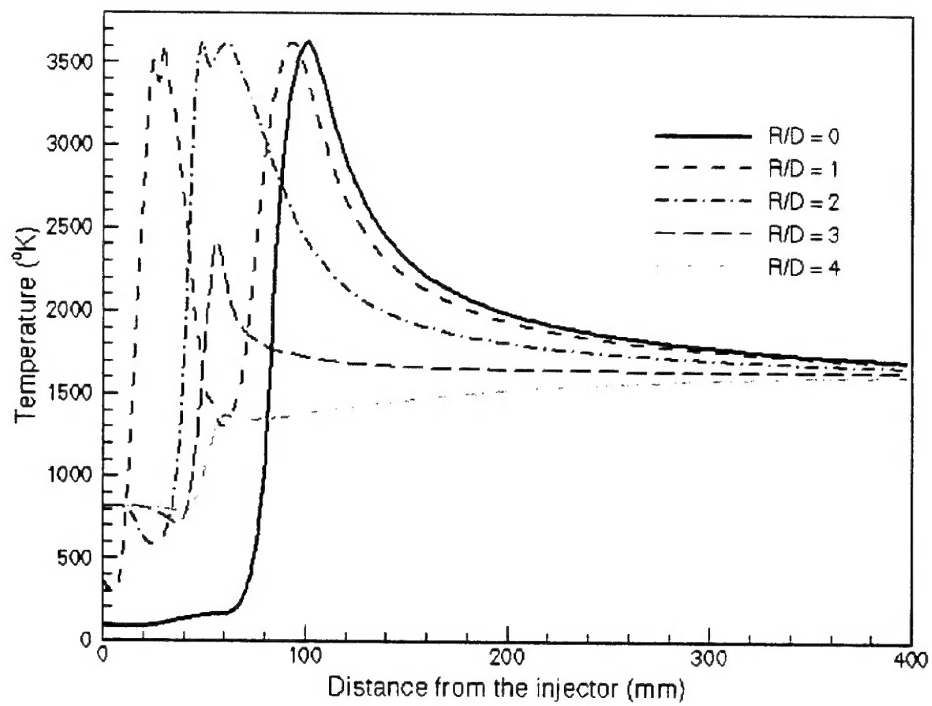Figure 3. Radial Profiles of Mean Temperature at Various Axial Locations of RCM-3.

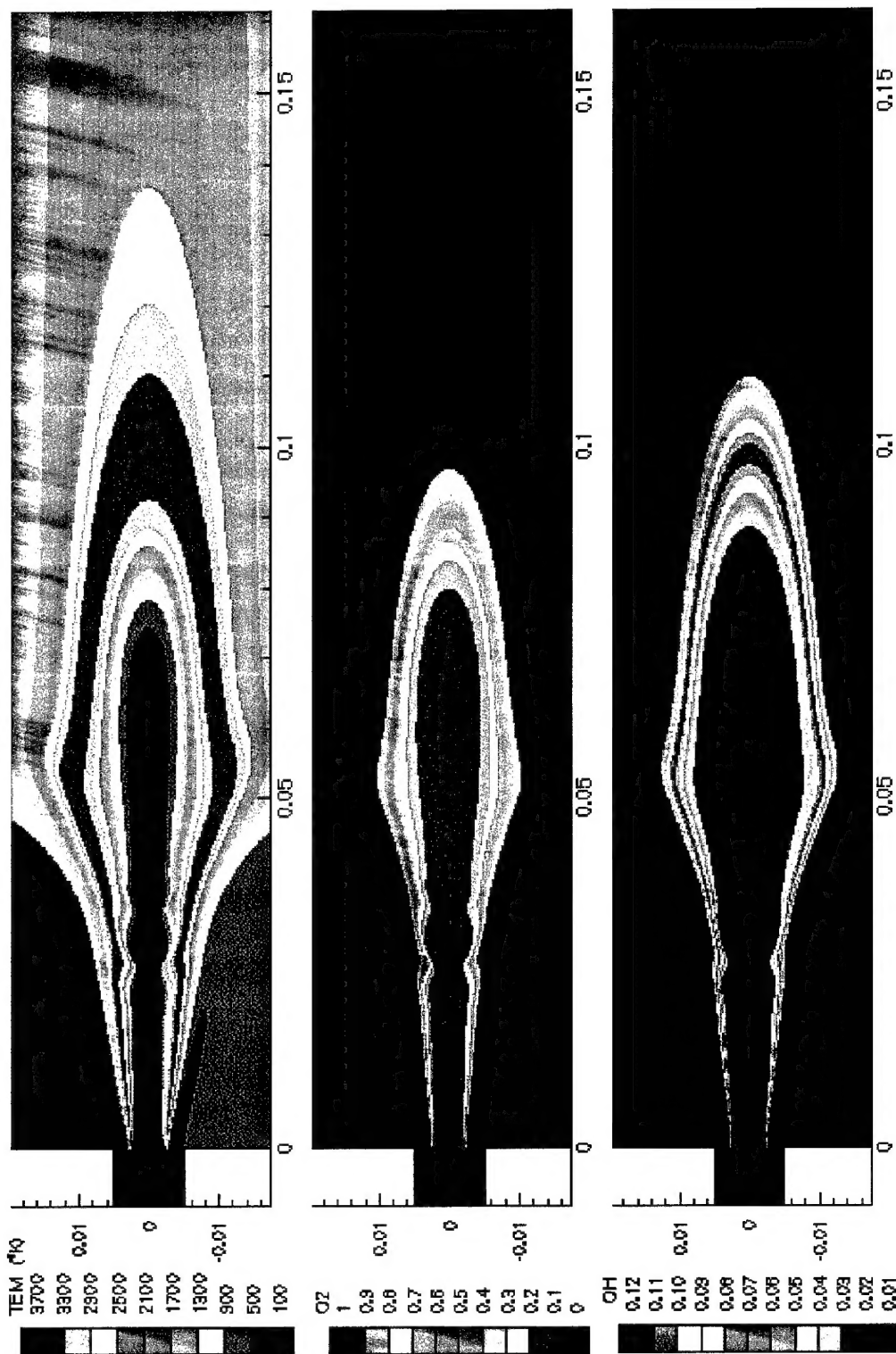Figure 4. Axial Profiles of Mean Temperature at Various Radial Locations of RCM-3.

8

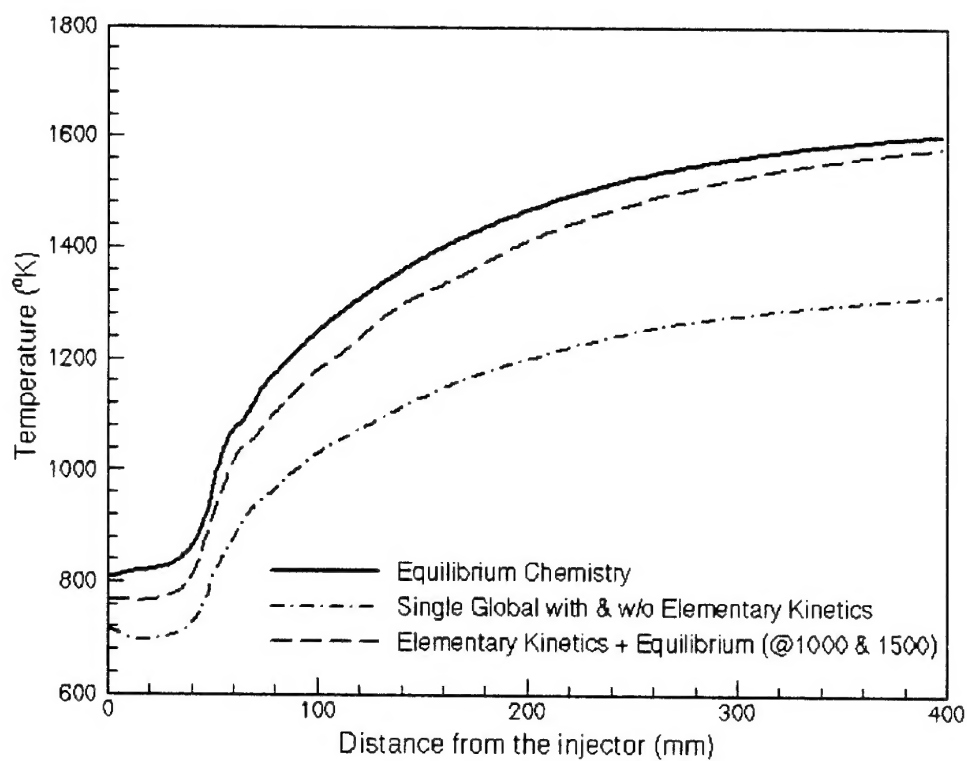Figure 5. Temperature and Species Concentrations Near the Injector of RCM-3.

Figure 6. Near Wall Temperature Distributions for Various Chemistry Model of RCM-3.

2nd International Workshop
Rocket Combustion Modeling

This collection of presentations from the second workshop on rocket combustion modeling, resembles the current status of the numerical tools available today for the prediction of atomization, combustion and heat transfer in rocket engines applied to the following three simplified but well defined test cases typical for cryogenic liquid rocket engines: Cryogenic Super-critical Single Injection, Cryogenic Sub-critical Single Injector Spray Combustion and Cryogenic Super-critical Single Injector Combustion.

The more fundamental contributions aim at giving an overview on the current research trends in the field and show what is on the horizon for design engineers of rocket engines in the near future.